Novel organic semiconductors for light-emitting diodes

Alexandros Georgios Rapidis

Thesis submitted for the degree of
Doctor of Philosophy

Department of Physics & Astronomy

University College London

Novel organic semiconductors for light-emitting diodes

Alexandros Georgios Rapidis

Thesis submitted in fulfilment of the requirements for the degree of *Doctor of Philosophy* at the University College London

Department of Physics & Astronomy and
London Centre for Nanotechnology
University College London

Declaration

I, Alexandros Georgios Rapidis, confirm that the work presented in this thesis is my own. Where information has been derived from other sources, I confirm that this has been indicated in the thesis.

A. G. Rapidis
London, 30th September 2019

Principal Supervisor: Prof. Franco Cacialli
Department of Physics & Astronomy and London Centre for Nanotechnology
University College London

Subsidiary Supervisor: Dr. Oleg Mitrofanov
Department of Electronic & Electrical Engineering
University College London

To my brother, Ιάσων (Iáson) and
To my parents Ιφιγένεια και Αλέξανδρο (Ifigéneia and Aléxandro)...

"I was born not knowing and have only a little time
to change that here and there."
R. P. Feynman

Acknowledgements

While the journey of my Ph.D. arrived to its end, the friendships with so many people seem only to have just begun. Too many just to mention at the Acknowledgements page of this thesis, and for some, too small their contribution to be fully appreciated! With its ups and downs, this journey has given me some incredible memories to remember for life! And to use the words of A. A. Milne in Winnie the Pooh:

"*How lucky I am to have something that makes saying goodbye so hard*"

First and foremost, the warmest ***Thank you*** goes to my family, my brother Iáson and my parents, Iphigéneia and Aléxis. Without their influence, guidance, help and support this journey, to say the least, wouldn't be possible!

(F)Alex was the most frequent of the receivers of the worst aspects the Ph.D.-life can outcome and has always stood by me, putting up with all that I could throw at her! Suffering with me, supporting me and believing in me! Her love has fuelled my passion to try to excel in every aspect of my life. And I thank her dearly for that.

The hurdles that arise from the research world wouldn't be copped without the moral support from the social interactions with so many different people! One of the most important, Panos. A dear-old friend, a companion and an ideal flatmate, so many late nights discussing with a gin&tonic in our hands! Hatton Garden will always be our little love-nest! And with him, Akis and the rest of the Greek society in London!

Met through work, we supported each other on various occasions! From a birthday cake and some pieces of toasted bread in Hatton Garden to a fantastic weekend in Puglia, a "*rafinato*" moment in Genova, a "*communist*" lunch in Warsaw, Pippo has been an inspiring colleague and a valuable friend!

Most of this thesis, and for that matter a big chunk of all our research, wouldn't be possible without the "supervision", help, support and scientific input

from Dr. Minnio! Questionable haircuts, fantastic financial advices and excellent science companion! With him, the other "Dr." of the group (during my era), Dr. Zampe, they both offered us excellent support throughout our research, embarking on countless DIY solutions to mend and keep our equipment alive!

Setting about a world outside of physics might have been smoother have I heard Gianfri a bit earlier and tackled the "*pythoning*" side of things! His stress is really not going to be missed, unlike his character and humour! I must say, after spending two years a meter apart, it seems weird to sit in a desk and not have someone on your side mumbling in an incomprehensive Italian dialect (of course) or listening to white noise on his headphones!

All in all, research couldn't be any more pleasant without the members of the Organic Semiconductors and Nanostructures group on my side! Giu (Lucarelli), Tecla (Arcidiacono), Vale (Robbiano), Andre (Zampetti), Ale (Minotto), Fra (Silvestri), Giovanni (Francesco Cotella), Beppe (M. Paternò), Luca (Santarelli), Ioannis (Ierides) and Peppe (Carnicella)! You guys have proven that *una fazza, una razza* is more than true! Endless discussions that showed me that we share more than just a similar face and a sea to bathe in during summer! F9 was an academic temple for all kinds of discussions, from research to... (put politely) controversial talks, even dancing and watching Italy on the World Cup!

Further to the "permanent" members of our group, a special thanks is due to the visiting researchers and master students that were hosted in our labs; Rose Scowen, Peter Aruffo, Jonathan Barsotti, Nikos Fotias, Leonardo Fumarina, Jessica Miller, Bradley Douglas, Gianluigi Albano and Simone Poddi amongst many!

Condensed Matter and Material Physics (CMMP) in UCL Physics was a welcoming place, where a small Greek community existed once upon a time: A Cypriot and a Greek-German that where completely incompetent to form a sentence in faultless Greek, Marios & Stefanos and the "*Salonik*" Kostas, now spread around Europe, once we enjoyed a cup of CMMP tea or a beer in a pub! Joined by Christian, Mitch, Callum and Jack, among many others, we managed to exchange a few ideas and devour some biscuits in E3/7 during the usual Thursday 3pm appointment!

Outside UCL, I couldn't forget the 15 fellow Early Stage Researchers at the SYNCHRONICS network that carried out our research and met in Italy, France, UK and Poland to exchange experiences and form a tightly-bond group! Also, a big "thank you" is due to the two synthetic chemistry groups that helped me: Prof. Harry L. Anderson, FRS and Dr. Hugo Bronstein and their groups for synthesising the materials that are presented in this thesis and their valuable

contributions for the papers prepared, submitted and published, and numerous useful discussions.

I would also like to thank Dr. G. M. Paternò and Prof. G. Lanzani for hosting me during my secondment in IIT-Milan and for their help with the pump-and-probe and lasing experiments, and Dr. I. Bulut and Prof. H. L. Anderson for hosting me during my secondment in Oxford University and for showing me how the world of synthetic organic chemistry works!

A big thank you also goes to the "unsung heroes" of the department; the support and admin staff at UCL, where James, Khadija, Nadia to name a few, made our research so much easier.

Part of my professional and personal life was shaped during the three years I spent in Montpellier, France. During those years I had the chance to meet some wonderful people that became dear friends. Charléne, Brice and Renaud, with a beer and a burger at a local pub, or exploring the mountains on a mountain bike, they made my time there as pleasant as it could be! Je vous remercie Messieurs-dame pour toujours me casser les bonbons! But, being impossible for a Greek not to finds fellow Greeks, Dr. Tsili and Dr. Melissa were always there to share a glass of wine in park or discuss the political turmoil of that era, before both of them abandoning the beauties of the South of France to cross the Atlantic, in search of other Greeks there (and maybe some science)!

Last, and certainly not least, a huge **thank you** to Prof. Franco Cacialli. A superb supervisor, a mentor and a guide in the difficult world of the academic research! An excellent teacher of the organic semiconductors physics, and on occasions of Greek (!) grammar! Thank you for believing in me, and trusting me with the role in the group, and for providing a deep understanding of the carbon world!

And finally, I would like to thank *you*, the reader, for taking the time to read this thesis, giving it some value.

Και επειδή είμαστε 'ΑΙΛΙΝΑΙΣ', δεν θα μπορούσαν να λείπουν και οι ευχαριστίες στην μητρική.

Αν και η συμβολή στην ολοκλήρωση του διδακτορικού ήταν μηδενική (ευτυχώς), η ψυχολογική τους υποστήριξη και η βαθειά και χρόνια φιλία τους πάντα ενοχλεί και δεν λέει να χαθεί: Αλέκος, Βίκ, Λις! Αιώνια και αθεράπευτα καθυστερημένοι, αλλά οι πιο αγαπημένοι φίλοι, όσα χρόνια και αν περάσουν, όσα χιλιόμετρα και ας μας χωρίζουν πάντα θα βρίσκουν τον τρόπο να γίνουν ανυπόφοροι!

Με τις αποστάσεις και τα χρόνια είχα την τύχη να γνωρίσω αρκετούς ανθρώπους στην ζωή μου που είχαν σημαντική επιρροή πάνω μου. Από το 2004 και ύστερα, παρόλο που ήταν η αίτια μιας 7-ετίας καπνίσματος, θα είναι πάντα στην καρδιά μου ως ο άνθρωπος που κυνήγησε τα όνειρά του όπως λίγοι... Μανωλιώ, εγώ κατάφερα να γίνω πραγματικός Δρ., παρόλο που πήγες και σπούδασες ιατρική!

Επίσης, νομίζω ότι υποσυνείδητα επηρεάστηκα πολύ από τον έταιρο τεχνολογικά-καμμένο της οικογένειας, Μάικ, και μιας και έβαλα πλώρη για άλλες θάλασσες πέρα από τον κόσμο της φυσικής, οφείλω να τον ευχαριστήσω και επίσημα!

Ιδιαίτερη μνεία (και στην ελληνική, γιατί της αξίζει) μιας και φυσικά όλα θα ήταν τοοόσο ευκολότερα χωρίς την παρουσία, υποστήριξη και διαρκή ενόχληση από την Φάλεξ, πάρτνερ ιν λάιφ αντ ιν κράιμ, να δυσκολεύει με κάθε δυνατό τρόπο το διδακτορικό!

Όπως αρχίσανε οι ευχαριστίες, έτσι και θα τελειώσουν, με ένα μεγάλο ευχαριστώ για τη διαρκή υποστήριξη στα γονίδια, και ένα μεγάλο μπράβο που κατάφεραν να με ανεχτούν τόσα χρόνια! Και φυσικά στον χαϊδεμένο της οικογένειας, τον μικρό Ιάσονα!

Funding acknowledgements

This dissertation is based on the work carried out at the Organic Semiconductors and Nanostructures Group at the Department of Physics & Astronomy and the London Centre for Nanotechnology, University College London, London, U.K. between 11/2015 and 11/2018. During this period, two secondment placements took place at the Chemical Research Laboratory of the University of Oxford, Oxford, U.K. and the Italian Institue of Technology CNST@POLIMI in Milan, Italy.

This work was supported from the European Community's Horizon 2020 Research and Innovation Programme under the Grant Agreement No. 643238 (SYNCHRONICS).

SYNCHRONICS

EU MSCA ETN on SupramolecularIY eNgineered arCHitectures for optoelectRonics and photONICS

Publications

Work presented in this thesis or carried out in parallel has led to the following publications and conferences presentations.

Peer reviewed journals:

- D. M. Freeman, A. J. Musser, J. M. Frost, H. L. Stern, A. K. Forster, K. J. Fallon, A. G. Rapidis, F. Cacialli, I. McCulloch, T. M. Clarke, R. H. Friend, H. Bronstein. Synthesis and Exciton Dynamics of Donor-Orthogonal Acceptor Conjugated Polymers: Reducing the Singlet–Triplet Energy Gap, *J. Am. Chem. Soc.*, 2017, 139 (32), pp 11073–11080
- A. Leventis, J. Royakkers, A. G. Rapidis, N. Goodeal, M. Corpinot, D.-K. Bučar, M. Blunt, F. Cacialli, H. Bronstein, Highly Luminescent Encapsulated Narrow Bandgap Polymers Based on Diketopyrrolopyrrole, *J. Am. Chem. Soc.*, 2018, 140 (5), pp 1622–1626

Manuscripts in preparation:

- A. Minotto, I. Bulut, A. G. Rapidis, G. Carnicella, M. Patrini, E. Lunedei, H. L. Anderson* and F. Cacialli*, Porphyrin oligomers beat the energy-gap law in near-infrared fluorescent light-emitting diodes, *submitted*.
- L. Tejerina#, A. G. Rapidis#, M. Rickhaus, P. Murto, E. Wang, A. Minotto, H. L. Anderson*, F. Cacialli*, A Porphyrin Pentamer as a Bright Emitter for NIR OLEDs, *submitted*.
- A. G. Rapidis, A. Minotto, I. Bulut, G. Carnicella, R. Scowen, H. L. Anderson, F. Cacialli, Zinc porphyrin oligomers as efficient emitters in NIR OLEDs, *in preparation*

Conferences contributions:

- A. G. Rapidis, A. Minotto, I. Bulut, H. L. Anderson, F. Cacialli Near-Infrared Organic Light Emitting Diodes based on Porphyrin Oligomers, *European Optical Society Bi-Annual Meeting (EOSAM)*, Berlin, Germany September 2016, poster presentation
- A. G. Rapidis, A. Minotto, I. Bulut, H. L. Anderson, F. Cacialli. Highly Efficient Near-Infrared Organic Light Emitting Diodes based on Porphyrin Oligomers, *European Material Research Society (E-MRS)*, Warsaw, Poland September 2017, poster presentation
- A. G. Rapidis, Flexible Electronics, Festival of Science, Genova, Italy October 2017, poster presentation
- A. G. Rapidis, R. Scowen, A. Minotto, G. Carnicella, I. Bulut, H. L. Anderson, F. Cacialli. Highly Efficient Near-Infrared Organic Light Emitting Diodes based on Porphyrin Oligomers, *European Material Research Society (E-MRS)*, Strasbourg, France June 2018, poster presentation
- A. G. Rapidis, A. Leventis, J. Royakkers, N. Goodeal, M. Corpinot, D.-K. Bučar, M. Blunt, F. Cacialli, H. Bronstein, Highly Luminescent Encapsulated Narrow Bandgap Polymers Based on Diketopyrrolopyrole, *European Material Research Society (E-MRS)*, Strasbourg, France June 2018, poster presentation

All the posters can be found in Appendix D.

Abstract

The intriguing properties of organic semiconductors in various optoelectronic applications, ranging from molecular wires for integrated circuits, to organic photovoltaics (OPV), organic transistors (OFET) and organic light-emitting diodes (OLEDs) have motivated the work presented in this thesis. More precisely, this thesis focuses on narrow energy gap materials, suitable for OLEDs emitting in the red and near-infrared (NIR) regions. Conjugated materials emitting at low energies face great challenges to have efficient light emission. This thesis proposes two very interesting and novel strategies to cope with the limiting factors of efficient light-emission from conjugated compounds.

Firstly, a series of porphyrin oligomers is presented. With emission ranging from red to pure NIR, three architectures of these oligomers were studied. Zinc oligomers at various length that allowed for fine tuning of the emission, five hexamers with different coordinating metals at the centre of each unit, allowing for phosphorescence emission, and a pentamer, with single acetylene instead of butadiyne bonds connecting porphyrin units, resulting in a shorter oligomer with an extended π-conjugation and a bathochromic shift of the emission. Two limitations can be identified for efficient NIR emission, the so-called "energy-gap law" and aggregation quenching. Both limitations are addressed, resulting in unprecedented external quantum efficiencies when the oligomers are used in OLEDs and remarkable devices lifetimes, considering the non-optimised diodes.

Secondly, three diketopyrrolopyrrole-based copolymers are presented and their photophysical properties discussed. These polymers represent a different strategy to prevent aggregation; by engineering covalent bonds, the conjugated core is sheathed within its cyclic sidechains. The strategy is proven highly successful and the three polymers are compared with their unprotected counterparts, where emission is severely quenched. The advantages of the encapsulation are more pronounced when the polymers are incorporated in OLEDs, where the encapsulated ones achieved up to 16 times higher external quantum efficiencies compared to the unprotected ones.

Impact Statement

The present thesis is focused on novel organic semiconductors, suitable for applications in organic light-emitting diodes (OLEDs) emitting in the lower energies of the electromagnetic spectrum, *i.e.* near-infrared (NIR). OLEDs are well studied devices, and are used in commercial applications for over two decades, primarily in digital displays such as TVs and smartphones, mainly utilising materials emitting in the red, green and blue, *i.e.* visible, to make the pixels.

However, NIR OLEDs are attracting significant attention thanks to a wide range of applications, ranging from biomedical, in photodynamic therapy and blood oxymetry, to defence and security, in night-vision applications, to communications, as a candidate for the substitute of Wi-Fi. Further to these, the organic NIR emitters offer flexibility, conformability and bio-compatibility compared to inorganic ones, expanding the range of their applications.

There are two main limitations in achieving efficient NIR emitters, the so-called "energy-gap law" and aggregation quenching. The energy-gap law for radiationless transitions predicts an exponential increase of the rate of non-radiative transitions with a decreasing energy gap. Secondly, to achieve a sufficiently small energy gap as to have NIR emission, an extended conjugation is required that dictates a very planar molecular conformation, which favours π-π stacking and the formation of non-emissive aggregates.

In this thesis two different approaches are presented in overcoming the limitations mentioned above. Firstly, the effects of the so-called "energy-gap law" are suppressed by modifying the length of the molecule. By increasing the length of the porphyrin oligomers, intersystem crossing is reduced by increasing the mismatch of the spatial extent of singlet and triplet excitons. Further to this, the radiative rate is increased by enhancing the strength of the oscillator strength. Secondly, the detrimental intermolecular interactions can be minimised and suppressed by molecular engineering the materials. Two approaches of different molecular engineering were studied, the use of bulky sidechains and sheathing the conjugated core within cyclic sidechains. The porphyrin oligomers limit the

formation of dark aggregates thanks to steric hindrance by the bulky sidechains, while the diketopyrrolopyrrole-based (DPP) polymers are encapsulated using covalently-linked cyclic sidechains that protect the conjugated core.

The result of the aforementioned approaches is unprecedented external quantum efficiencies for NIR OLEDs, emitting at wavelengths $> 850\,\mathrm{nm}$ with efficiencies $> 4\,\%$, while the encapsulated DPP OLEDs showed 16 times higher efficiencies than the non-encapsulated ones. Fabricated NIR OLEDs based on porphyrin oligomers, while not optimised for long lifetimes, showed impressive performance under continuous operation, remaining $> 80\,\%$ of the initial performance for $> 30\,\mathrm{h}$.

These results pave the way for efficient NIR emitters and are a proof of concept that conjugated polymers and oligomers, that omit the use of toxic, heavy metals, are feasible.

Contents

List of Figures

List of Tables

1 | Organic semiconductors

"Physics is like sex: Sure, it may give some practical results, but that's not why we do it."

R. P. Feynman

In this chapter, a short review of the history of the general field of organic semiconductors is presented and the forces that drive the research carried out in this field. What are the emerging technologies and how do they influence every day lives.

1.1 Introduction - why Organics?

We can define as organic semiconductors (OS) the class of materials that are based on carbon, ranging from small molecules to polymers, and are able to conduct electricity. Organic semiconductors have attracted significant interest since the second half of the 20th century. Among the long list of advantages of OS are found the ease of handling and low cost of manufacturing, the possibility to cover large surfaces and substrates that are mechanically flexible and conformable, the fact that their energy gap sits well in the visible spectrum as to allow for applications such displays, the facts that they can create, transmit, modulate and detect light when embedded in low-cost and light architectures and also that they can be inkjet printed, all contribute to the infiltration in the field of optoelectronics, traditionally dominated by inorganic III-V and II-IV materials. [1–3] Techniques and architectures that are typically oriented towards optoelectronic applications have also been proved to be biocompatible, when an organic photovoltaic module restored the vision in a rat. [4] It is such the versatility that organic semiconductors offer in terms of physical, optical and electrical properties, that the chemical synthesis can now be accelerated by the use of Machine Learning techniques. [5, 6]

A very early report by André Bernanose *et al.* in 1952 [7] describes electroluminescence (EL), the process of producing light by applying a voltage. Bernanose used crystalline films of acridine orange and quinacrine, an organic phosphorescent compound, to observe electroluminescence. The work published in 1955 [8], unofficially making him the *"father of the organic light-emitting diode"*. Notable work on the study of EL was carried out by Pope *et al.* at New York University and was reported in 1963, when the authors described light emission from anthracene single crystals, though unusable due to the very high voltages applied. [9] Research in the field was not very active until 1977, when Shirakawa, MacDiarmid and Heeger reported the electrical conductivity in synthesised doped polyacetylene. [10, 11] It was this discovery that was later rewarded with the Nobel Prize in Chemistry in 2000 "*for the discovery and development of conductive polymers*". *Plastics* ceased to be simply insulators.

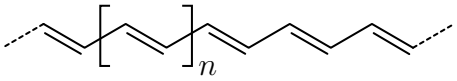

Figure 1.1 | Chemical structure of *trans*-polyacetylene. The discovery of electrical conductivity in polyacetylene was the stimulus for the expansion of organic electronics.

1.1.1 Organics in renewable energy sources

While physics and chemistry behind carbon can be fascinating, practical applications in devices in everyday life are necessary to push research to be commercialised. Two main pillars can be identified where organic electronics have the capacity to contribute: light generation and light harvesting, with electrically-conductive devices being a possible third. The field of organic semiconductors is, therefore, partially fuelled by the field of renewable energy sources as the light harvesting pillar. While the Earth's population is growing, so is the hunger for energy. Inevitably, the energy consumption has more than double in the past 40 years, with an expected increase of 37 % by 2040. [12]

Currently we remain completely dependent on fossil fuels, we know that these resources are not limitless and we see the destructive consequences they have on our planet. This has lead to the search of alternative, renewable energy sources. The greatest of the them all is the Sun, with wind, tidal, hydro and geothermal powers as other sources. A large number of solar photons bombard Earth's surface, making solar energy the primary point of focus for harvesting to substitute fossil fuels and photovoltaic devices as the most promising mean of doing it.

Photovoltaic devices are structures that convert photons to electrical power. It is estimated that only $0.3-0.4$ % of the Earth's surface covered with photovoltaic devices of an average 20 % efficiency would suffice to cover our energy demands. [12, 13] There are many examples of photovoltaics with efficiencies around or above this value as shown in Figure 1.2 below. A theoretical maximum for organic dye-sensitised solar cells of just over 20 % [14], with values of 29.3 % reported for gallium arsenide devices, 27.6 % for single crystal silicon and up to 46.0 % for multijunction cells [1], show this potential is feasible.

[1] Values sourced from NREL, accessed September 2018.

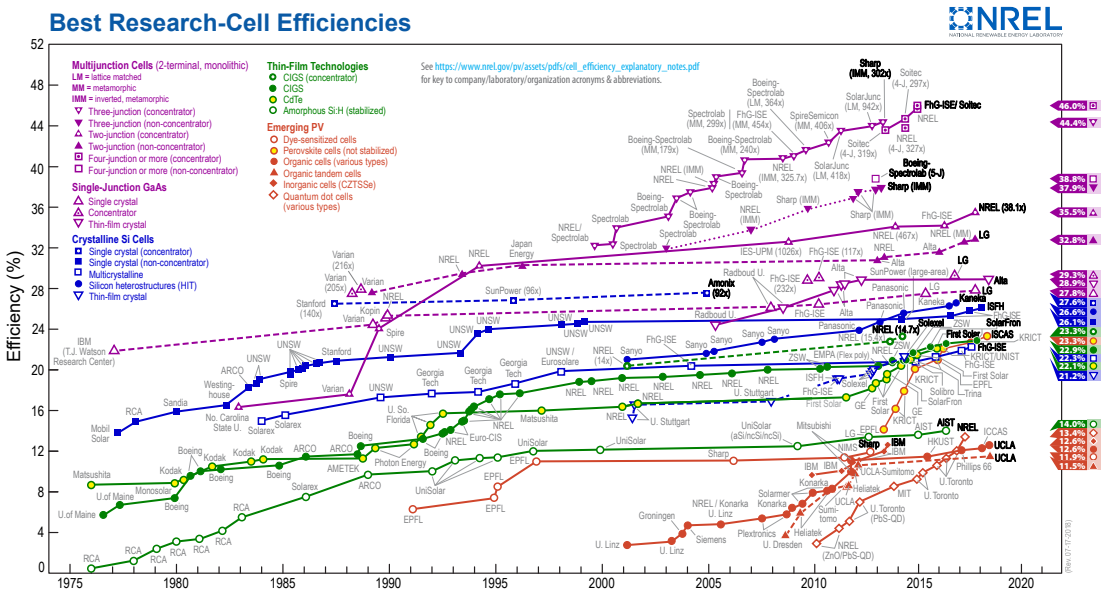

Figure 1.2 | Figure illustrating the highest confirmed power conversion efficiencies for photovoltaic solar cells from a range of different technologies. Image reproduced from National Center for Photovoltaics (NCPV) at the National Renewable Energy Laboratory (NREL), accessed September 2018.

The active material of most commercial solar panels installed is silicon. While silicon is abundant on Earth, high temperatures and various toxic and expensive processes are needed to fabricate high quality solar panels. This results in expensive and non-environmentally friendly production that requires at least a few years to pay back the initial investment, an estimated >1 year for the sunnier Southern Europe. [2] Light-emitting diodes that are widely used in various lighting and display applications, also require similar expensive and complicated processes. This is where the organic semiconductors provide a promising alternative. With processes that do not require high temperatures and vacuum are faster, simpler and cheaper than the ones for processing silicon, while still providing efficiencies that are comparable to the inorganic alternatives.

The need of a simpler, cheaper method of fabrication has pushed towards solution processing. Solution processing means that the fabrication, or deposition of the materials, starts from a solution, followed a by a process of spin coating, spray coating, slot-dye coating, dip-coating or inkjet printing and resulting in uniform, thin, and, if needed, semi-transparent films. There are many reports from various research groups that very high efficiencies from solution-processed organic materials have been achieved, with a very recent record efficiency of 17.3 % for organic solution processed solar cells. [15] Solution processing has driven research throughout the field of organic semiconductors with applications

[2] Source: Fraunhofer Institute for Solar Energy Systems, ISE.

found also in light-emitting diodes, [16, 17] lasers, [18–20] photodiodes [21] and thin-film transistors. [22]

One class of photovoltaics that emerged from this solution-processed drive, were the dye-sensitised solar cells, first reported by O'Regan and Grätzel in 1991, [23] with the latest results reporting a record efficiency of 13 %. [24] In the last years, a new class of hybrid organic-inorganic solar cells has emerged, the perovskite solar cells. They are solution processed, cheap and have a huge tolerance over impurities and imperfections, contrary to silicon. [25] Though the field has seen an unprecedented explosion since the publication of the seminal paper of Snaith and co-workers [26] in 2012, the first reports were from Miyasaka and co-workers, reporting a 2.2 % efficiency in 2006 [27] that was increased to 3.8 % in 2009. [28] Since then, perovskites have attracted significant attention in understanding the physical processes. However, a big drawback of perovskites remains the use of heavy and very toxic metals, such as cadmium and lead and their environmental and human toxicity, though there are studies on the life cycle of a perovskite solar cell [29], as well as lead-free perovskites. [30] Much effort has been focused on researching different materials composition, processing conditions and device architecture as to stabilise them for over 25 years, as required for real-life applications. [25] However, in only a few years, building on the technology and know-how obtained from the dye-sensitised solar cells, perovskite solar cells have been reported achieving efficiencies up to 22.9 %, as shown in Figure 1.2 above. A remarkable increase from the 10.9 % reported in 2012. [26]

1.1.2 Light-emitting organic semiconductors

Organic photovoltaics, including perovskites, are part of the driving force for the research in organic semiconductors. And as it was put by Yablonovitch and co-workers, a material suitable for photovoltaics should be an efficient emitter. [31] Looking at the second pillar, that of light generation, then, we look at the organic light-emitting diodes. After the discovery of the conductivity in polyacetylene [10, 11] and the reports of electroluminescence from organic compounds [8, 9], research continued to thrive, resulting in the reports of Roger Partridge using poly(N-vinylcarbazole) (PVK) and making an OLED. [32] Though the efficiency made it unusable, it showed the potential of organic material to produce light.

It was not until a few years later, in 1987, when Tang and Van Slyke from Kodak reported the first organic light-emitting diode (OLED) with true functional potential, and efficiency of 1 % photon/electron, using the thermally evaporated small molecule tris(8-hydroxyquinolinato)aluminium (Alq_3). [33] Shortly after this report, Adachi *et al.* reported a multi-layer architecture, closer to today's standards for OLEDs, though significantly lower photon/electron efficiency of 0.04 %. [34] Fast forward to 1990, the Cambridge group lead by Burroughes, Bradley and Friend were the first to report a solution processed high-efficiency polymer-based OLED with poly(p-phenylene vinylene) (PPV) as emissive material [16], with Heeger validating this discovery with the PPV derivative MEH-PPV [35] and a noteworthy work on flexible solution-processed light emitting diodes. [36] This ignited a research field that for the last 30 years has an average of almost 2 scientific papers per day,[3] while there are more than 224,000 patent documents.[4]

Over the 30 past years of intense research in the field, there has been a wealth of materials with excellent optoelectronic properties, resulting in very efficient OLEDs. [37, 38] As already mentioned, a good material for OPVs is a good emitter, and perovskites are not an exception. [38, 39] Perovskite based OLEDs have been demonstrated to have have excellent electroluminescence external quantum efficiency (η_{EL}) values, and with easily tunable emission wavelength. Further to OLEDs, perovskites are a good candidate for organic lasers. To achieve electrically excited lasing, several ingredients are necessary: a high-quality gain medium with slow non-radiative decay pathways at the carrier density levels required for population inversion, large mobilities and free-carrier densities to minimise resistive heat loss, good thermal stability, a large gain cross-section at

[3] *Scopus* results based on the keyword "*OLED*" for the period 1987-2018, accessed 04/09/2018.

[4] *Scopus* results for the period 1987-2018 for patent documents with the keyword "*OLED*", accessed 04/09/2018.

the lasing wavelength and sharp band tails marked by a low Urbach energy. Perovskites have demonstrated all of these properties except for high carrier densities and thermal stability, making them an exciting candidate for electrically-driven lasing. [38, 40, 41]

Either from dye-sensitised [23], polymer [15, 42, 43], perovskite [25, 26] or small molecule solar cells [44], organic field effect transistors [3, 22, 45, 46], light-emitting diodes [16, 33] or lasers [18, 19], organic semiconductors is vast field, covering and showing applications in every day life on many different sectors, shows also huge potential of improving many aspects of everyday life.

1.2 Optical and electronic properties

All the exciting properties that make organic semiconductors such a fascinating field to conduct research in, arise from a simple principle of alternating single and double bonds of their carbon-based atoms. By repeating this over a number of units, one forms long linear chains that we call "conjugated polymers". It is this fact of alternating singe and double bonds that can lead to electrical conductivity in organics and that allows light emission and absorption. It was such the significance of "*the discovery and development of conducting polymers*" that made it the subject of the 2000 Nobel Prize in Chemistry.

1.2.1 Molecular orbitals and π-conjugation

A carbon ($^{12}_{6}$C) atom has 6 electrons and its electronic structure is $1s^2\,2s^2\,2p^2$ in the ground state. Therefore, there are two electrons unpaired in the outer shell. However, the small energy difference between $2s$ and $2p$ states allows one electron to be excited to the $2p$ state, resulting in a total of four electrons to form chemical bonds. A spherically symmetric $2s$ orbital and three dumbbell-shaped $2p$, as illustrated in Figure 1.3 below. These orbitals can hybridise in three different configurations, sp^1, sp^2 and sp^3 and form covalent bonds:

- Four sp^3-orbitals: all three p-orbitals are hybridised with the s-orbital.
- Three sp^2-orbitals hybridised between the s-orbital and the p_x- and p_y-orbitals and one unhybridised p_z-orbital
- Two sp-orbitals hybridised between the s-orbital and the p_x-orbital, leaving the p_y- and p_z- orbitals unperturbed.

The sp^3 hybridised forms mainly "saturated" polymers and diamonds, where all four electrons are confined in σ-bonds (single) with neighbouring atoms, therefore becoming an insulator that lacks interesting electronic or optical properties.

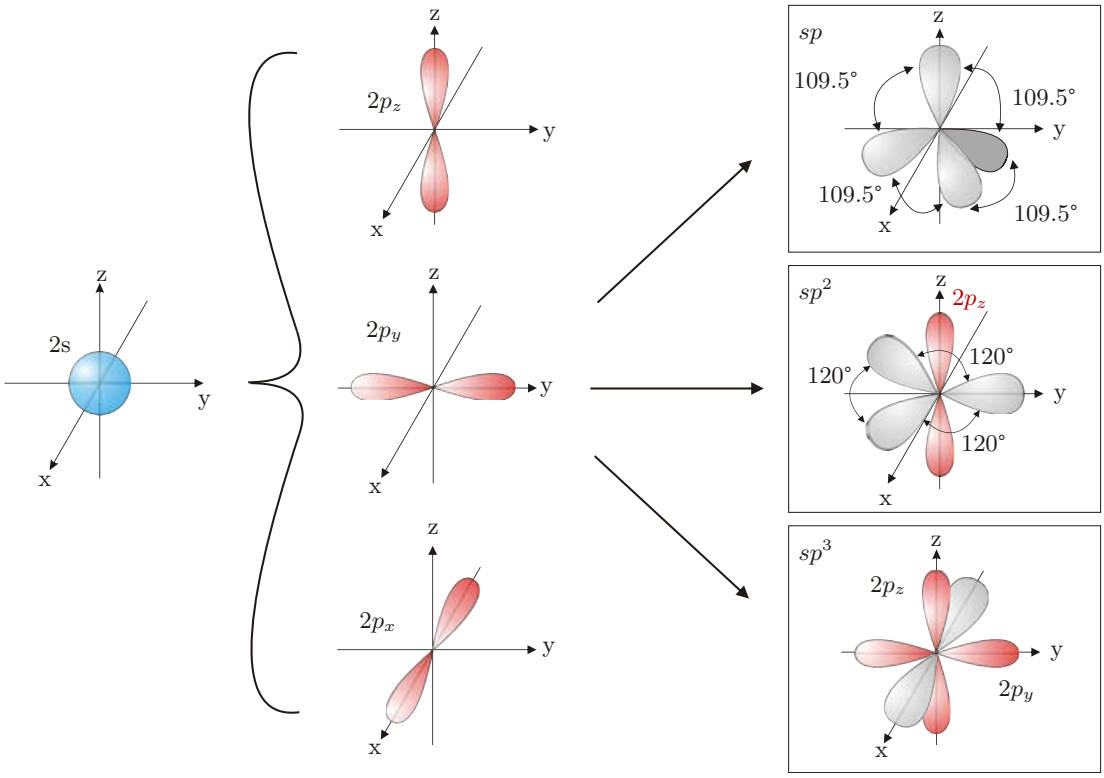

Figure 1.3 | The outer orbitals of carbon. The spherically symmetric $2s$ and the three dumbbell-shaped $2p$ ($2p_x$, $2p_y$ and $2p_z$). The combination of the orbitals result in three hybridised orbitals, sp, sp^2 and sp^3, that form σ- and π-bonds with neighbouring atoms. Image adapted from [13].

However, sp^2 hybridised atoms form three coplanar, 120 ° to each other, σ-bonds with neighbouring atoms. The remaining p_z orbital, perpendicular to the plane of the σ-bonds, is free to delocalise and overlap with neighbouring orbitals to form π-bonds. This π-bond is a double bond and is illustrated in Figure 1.4a below. The overlapping π-bond is extended below and above the plane of the σ-bond. This overlapping of the orbitals leads to the formation of a molecular bond and the subsequent splitting into two distinct energy levels, a bonding molecular π-orbital and an anti-bonding π^*-orbital (Figure 1.4b). The bonding π-orbital sits in lower energy level than the original p_z, while the π^*-orbital is in a higher energy level. Similarly, the overlapping sp^2 orbitals lead to the formation of a bonding σ-orbital and an anti-bonding σ^*-orbital, that sit higher and lower than the π & π^*-orbitals respectively, as illustrated in the Figure 1.4b below.

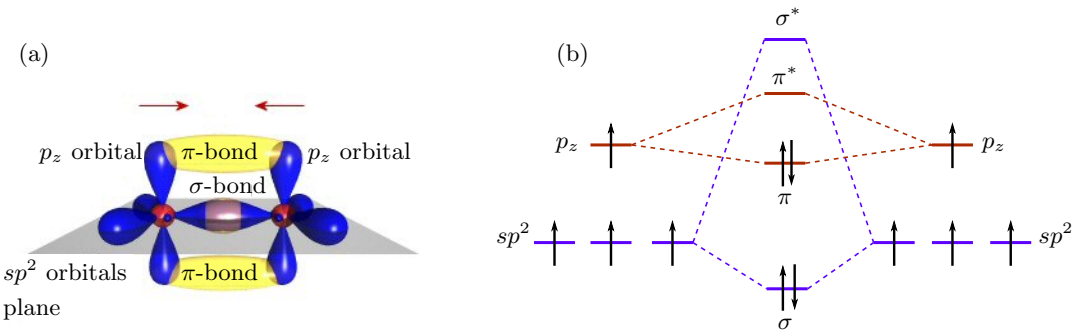

Figure 1.4 | **(a)** Illustration of the sp^2 orbitals (blue) forming the σ-bonds and the perpendicularly-standing p_z orbital that forms a π-bond (double bond) with a second carbon atom. **(b)** Distinct energy levels of π- and π^*- orbitals of two neighbouring carbon atoms. Image reproduced from orgworld.de, accessed September 2018.

By increasing the number of these sp^2 hybridised carbon atoms, the distinct energy levels of the π & π^*-orbitals degenerate into quasi-continuous bands where the low-energy π-orbital is referred to as highest occupied molecular orbit (HOMO) and the higher energy π^*-orbital as lowest unccupied molecular orbit (LUMO). This is depicted in Figure 1.5b below. The degeneration takes place in polymers, such as PPV presented in Figure 1.5a below, the same polymer that was used as the active layer in the first ever reported polymer OLED. [16] The energy difference between HOMO and LUMO is defined as the energy gap (E_G) of the molecule. The analogous of the HOMO and LUMO in inorganic semiconductors is the valence and conduction bands (VB and CB respectively). The energy gap is typically $1.4 - 3.5\,\text{eV}$ for organic molecules and is the origin of the optical properties of organic semiconductors, allowing transition in the range $\sim 350 - 900\,\text{nm}$, although there are reports from OS emitting in wavelengths up to $2\,\mu\text{m}$. [47–49]

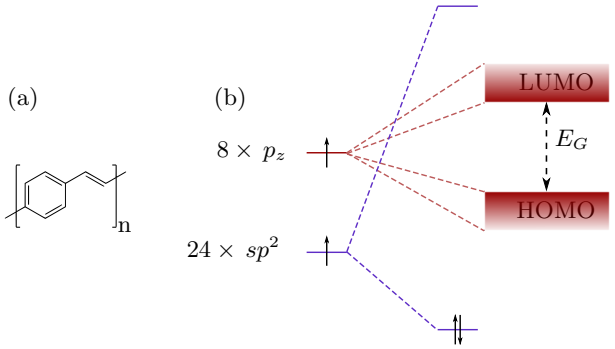

Figure 1.5 | Chemical structure of poly(p-phenylene vinylene) (PPV) and the degeneration of the energy levels into quasi-continuous bands, highest occupied molecular orbit (HOMO) and lowest unccupied molecular orbit (LUMO), which are the equivalent valance and conduction bands met in inorganic semiconductors.

For the *sp* hybridised carbon atoms, the two *sp*-orbitals overlap with two adjacent co-linear atoms to form two σ-bonds. The remaining p_x- and p_y- orbitals will be perpendicular to the σ-bond and overlap with the respective orbitals of the adjacent atoms to form a triple bond.

Lastly, as mentioned above, the exciting properties of the organic semiconductors are owed to the alternating single and double bonds. A system with such alternation is called a π-*conjugated* system and can be either a small molecule or a polymer. The π-conjugation is characterised by a spatial extension of the π-orbitals over the backbone of the carbon atom chain that leads to delocalised electrons. Such a system is *trans*-polyacetylene and the PPV polymer shown in Figures 1.1 and 1.5a above. The molecules and polymers, that are going to be presented below in Chapters 3 and 4 and form the core of this thesis, are also π-conjugated. It is these delocalised electrons that are responsible for the electrical conductivity of organic semiconductors. It is evident that the length of the delocalised orbitals has an important effect on the optical and electrical properties of the materials.

1.2.2 Optical properties

There are two main processes arising from the energy gap of a molecule involving photons: **(a)** absorption, when a photon is absorbed by the excitation of an electron from the ground state (HOMO) to an excited state (LUMO), **(b)** spontaneous emission when the excited electron returns to the ground state (HOMO) by emitting a photon, basically the inverse process of absorption. Process (a) is the main process occurring in photodetectors and solar cells and (b) in LEDs. Processes (a) and (b) can be visualised with the help of the Jablonski diagram shown in Figure 1.6. [50] There is a third process that can occur, named stimulated emission and involves the emission of another similar photon by recombination, resulting in the emission of two coherent photons and is the main process in a laser.

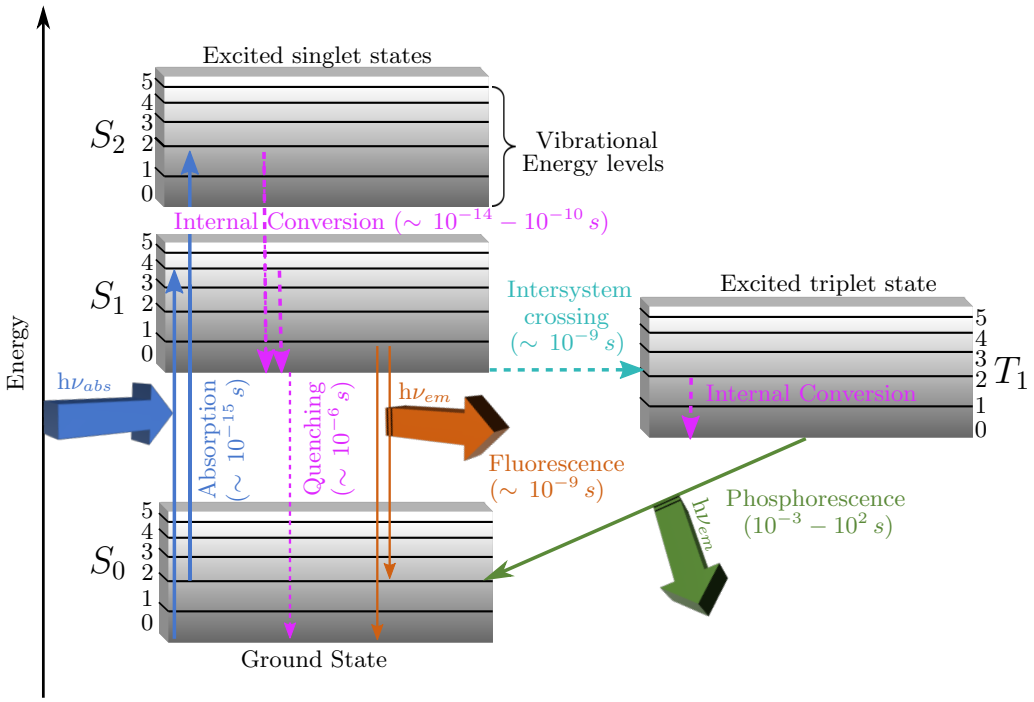

Figure 1.6 | The Jablonski diagram. Illustrates the optical transitions between the ground state (S_0) and the excited single states (S_1, S_2) and triple state (T_1), and typical time scales for each transition. With **blue** is noted the absorption of a photon, with **orange** fluorescent relaxation, with **cyan** the intersystem crossing and with **green** phosphorescence. With **pink** are noted the non-radiative relaxation processes (quenching and internal conversion). Solid lines indicate radiative processes while dashed indicate non-radiative. Each of the ground and excited states is split into further vibronic states 0, 1, ..., 5.

The diagram depicts the energy levels of a molecular system, arranged vertically by energy and horizontally by spin number. The ground state S_0 and

the two excited states S_1 and S_2 are singlet states, *i.e.* states with total spin number $s = 0$, as shown in Equation 1.2 below, while T_1 is a triplet excited state, *i.e.* a state with total spin number $s = \pm 1$, as shown in Equation 1.1 below.

$$\left.\begin{aligned} |1,1\rangle &= \uparrow\uparrow \\ |1,0\rangle &= \frac{(\uparrow\downarrow + \downarrow\uparrow)}{\sqrt{2}} \\ |1,-1\rangle &= \downarrow\downarrow \end{aligned}\right\} s = 1 \tag{1.1}$$

$$\left.\begin{aligned} |0,0\rangle &= \frac{(\uparrow\downarrow - \downarrow\uparrow)}{\sqrt{2}} \end{aligned}\right\} s = 0 \tag{1.2}$$

Conjugated polymers exhibit strong electron-lattice coupling, and therefore all states are split into further vibrational energy levels, 0, 1, ..., n. The processes that involve absorption and emission of photons are noted with solid lines while non-radiative relaxations are noted with dashed lines.

The vertical transition from the ground state S_0 to an excited state S_1 or S_2 is termed absorption and takes place in $\sim 10^{-15}$ s ($h\nu_{abs}$ in Figure 1.6). An electron excited to S_2 relaxes non-radiatively to S_1 in a process called internal conversion (IC), process with a typical timescale of $\sim 10^{-12}$ s. Kasha's rule states that a return to the ground state S_0 is more likely to occur from the lowest excited state, *i.e.* S_1. [51] A return from S_1 to S_0 is a radiative process called fluorescence that occurs in a $\sim 10^{-9}$ s regime (orange $h\nu_{em}$ in Figure 1.6). This is a *spin-allowed* process where the electron in the S_1 and the electron in the S_0 have opposite spin.

However, a *spin-forbidden* relaxation to S_0 can occur, when the excited electron has the same spin as the one in S_0. This happens when an electron from S_1 "jumps" to T_1 by intersystem crossing (ISC), a non-radiative spin conversion process between two electronic states of different multiplicity, and later relaxes to the ground state. For ISC to occur, spin-orbit coupling is required. Spin-orbit coupling (SOC), or the heavy atom effect as it has been termed, is a relativistic effect mixing the singlet and triplet wave functions. [52, 53] If the spin angular momentum s and the orbital angular momentum l of an electron couple, then a change in spin angular momentum can be compensated by an opposite change in orbital angular momentum. This is because only the total angular momentum $j = s + l$ has to be conserved during an optical transition. [54] Organic semiconductors are usually characterised by weak spin-orbit coupling, unless there is a heavy atom present, such as platinum. However, as it is examined below, this can be more favourable, and is observed, in the presence of heavy metals. This process takes place in the order of $\sim 10^{-6}$ s to several s and is

called phosphorescence (green $h\nu_{em}$ in Figure 1.6). Photoluminescence (PL) is defined as the emission of photons, either fluorescence or phosphorescence, due to photoexcitation.

Absorption and emission should be, theoretically, mirror images of one another since the same energy level transitions are involved. In practise, they are significantly broadened and many differences can be observed. The shapes of the absorption and emission spectra can be described with the help of the Frank-Condon diagram, illustrated in Figure 1.7 below.

The *Frank - Condon principle* derives from the Born-Oppenheimer approximation. According to the approximation, electronic transitions and nuclear motions are independent. The Frank-Condon principle states that the electrons, being much lighter, are excited on a much faster time scale ($\sim <$ fs) than the motion of the heavier nuclei ($\sim$ 100 fs). [55] Hence, electronic transitions are represented by vertical lines. Because the electronic transitions take place in a time scale much faster than the time scale of the nuclear motions, a transition has higher probability of occurring between the two vibrational levels with the most significant wavefunction overlap, in the example shown in Figure 1.7 is between $\nu = 0$ and $\nu = 2$ that shows the highest intensity in the spectrum.

The more realistic absorption and emission spectra are shown in Figure 1.7 with solid lines overimposed to the transitions. This broadening is attributed to various inhomogeneities in the exciton energies arising from different conjugation lengths in polymers, different vibrational energies and general disorder in the system. These differences can have physical origins, such as torsional vibrations.

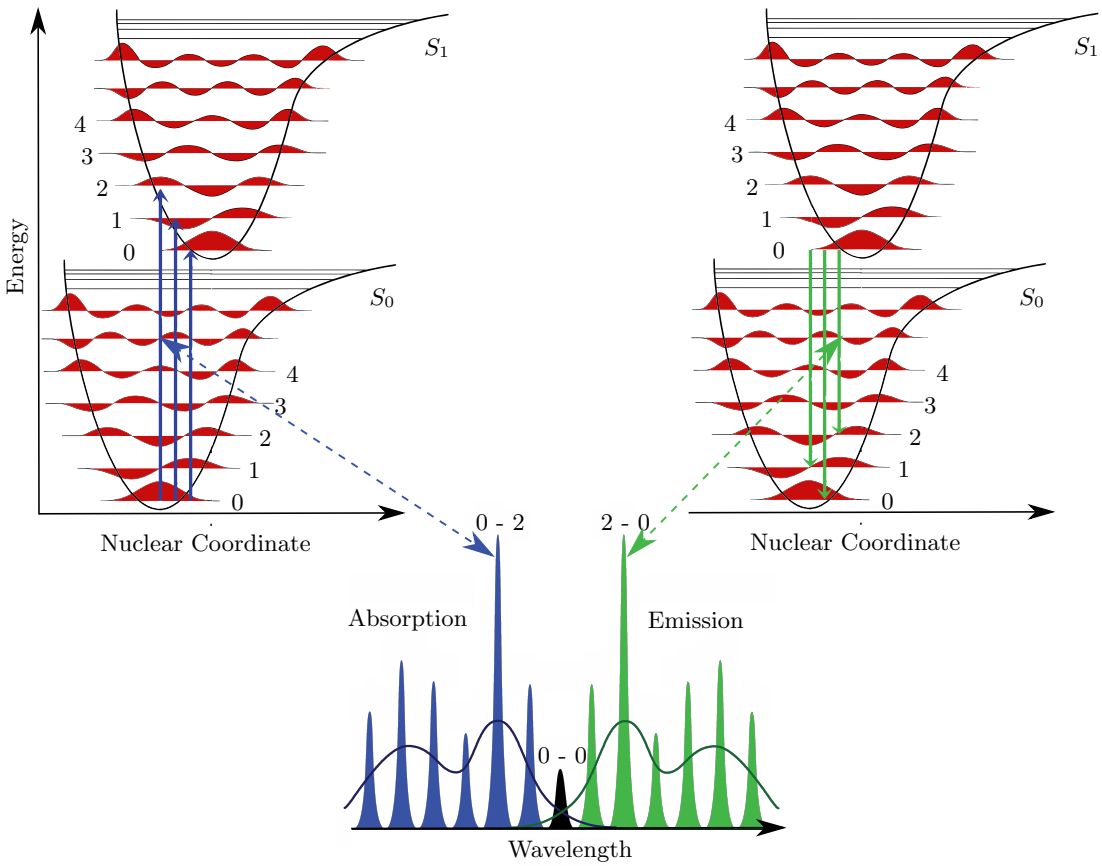

Figure 1.7 | (a) Franck-Condon Energy Diagram. Morse-like potential energy curves for the ground (E_0) and first excited (E_1) states. The vibrational wavefunctions are display with orange. The most favourable transitions are indicated with arrows. **(b)** Illustration of the spectra of the same vibronic transitions that are shown in (a) as absorption and emission. Usually observed in dilute gases, while the solid lines represent the broadening of the spectra in solids and solutions. Figure adapted from M. Samoza under the Creative licence.

The energetic difference between the $0-0$ transition in absorption and emission is defined as *Stokes' shift*. In the example presented in Figure 1.7 above there is no Stokes' shift as the $0-0$ transition in absorption and emission are perfectly overlapping. An example that this can occur is for individual chromophores in the gas phase. However, typically in dense molecular systems, such as amorphous molecular film or conjugated polymers, electronic coupling between different chromophores will be observed, that leads to energy transfer populating tail states of the density of states distribution and a large Stokes' shift will be exhibited. Smaller, more rigid molecules have smaller shifts due the absence of conformational change due to excitation. Stokes' shift can also be split in true and apparent, with true owing to geometric relaxations and the apparent to spectral diffusion.

After defining what photoluminescence is, shown in the Jablonski diagram

in Figure 1.6 above, the efficiency of an emitter can be determined by the photoluminescence quantum efficiency (η_{PL}). It simply the ratio of the number of photons emitted to the number of the photons absorbed. [56] Experimentally this is measured using an integrating sphere (absolute method) or comparing it to a standard (relative method), but more details about the experimental determination are discussed in Section 2.3 below.

Assuming an initial number of fluorophores in the excited state N_0, after the excitation there are N fluorophores that will leave the excited state S_1 according to the rate:

$$dN(t) = -(k_r + k_{nr})N(t)dt \tag{1.3}$$

where t is the time, k_r is the *radiative rate* for the $S_1 \rightarrow S_0$ transition and k_{nr} is the non-radiative rate. Integrating Equation 1.3 and considering that the intensity of the fluorescence $I(t)$ is proportional to the excited state population $N(t)$ yields:

$$I(t) = I_0\, e^{-t/\tau} \tag{1.4}$$

where τ is the fluorescence lifetime, I_0 is the fluorescence intensity at $t = 0$, *i.e.* the number of the photons absorbed, and can be experimentally determined. The process of determining τ is described in Section 2.5 below.

η_{PL} can, therefore, be defined as:

$$\eta_{PL} = \frac{\int_0^\infty k_r n(t)dt}{N_0} \tag{1.5}$$

However, the η_{PL} can be also expressed using the radiative and non-radiative rates as the fraction of the radiative rate to the total decay rate of an excited state using the formula:

$$\eta_{PL} = \frac{k_r}{k_r + k_{nr}} \tag{1.6}$$

This is an equation with two unknowns, assuming that η_{PL} is experimentally determined. To solve it, a second formula combining k_r and k_{nr} is the one for the lifetime of the excited state τ, also termed natural lifetime, *i.e.* the time a molecule spends in the excited state before, radiatively or non-radiatively,

returning to the ground state. The expression is:

$$\tau = \frac{1}{k_r + k_{nr}} \tag{1.7}$$

Once τ and η_{PL} are measured, the two rates can be calculated.

It can also be argued that, while there is only one radiative path, and therefore a singe k_r, there are multiple non-radiative paths, such as IC, ISC and energy transfer. In that case a summation factor $\sum_i k_{nr_i}$ would be used, of all the different rates.

The study of conjugated polymers is carried out using the exciton model. When a photon is absorb by a π-electron, the electron is excited to higher lying orbital. This leaves behind a hole and an electron-hole system is formed. Coulomb interaction between the two results in a bound state, a bosonic quasiparticle called *exciton*. There are two types of excitons that are formed in semiconductors, Wannier-Mott and Frenkel excitons. The former are typically met in inorganic semiconductors, with lower binding energies and larger radii. In conjugated polymers, the excitons are strongly-bound, owing to the difference of the permittivity of the two media, with small radii and indicate the latter, Frenkel-type excitons, with binding energies $\sim 0.1 - 1.5\,\text{eV}$. [57, 58] Depending on the total spin S, excitons are defined as singlet and triplet excitons, where singlets have $S = 0$ and triplets $S = 1$. Excitons, both triplets and singlets can exist both in photoluminescence and electroluminescence, *i.e.* following excitation by photons or electrons respectively. Triplets radiative recombination will lead to phosphorescence, as described above, while singlets lead to fluorescence.

1.2.3 Energy transfer

A substantial part of the results presented in this thesis, and the entirety of Chapter 3 is based on energy transfer. Energy transfer, as stated by its name, is the transfer of an excited state's energy from a donor to an acceptor. The *trivial* or *cascade* energy transfer is the process involving a photon emitted from a donor molecule D that and is reabsorbed by an acceptor molecule A. It usually involves long distances ($\sim$ tens of nm) and is typically met in dilute solutions. This process can be expressed as:

$$\begin{aligned} D^* &\rightarrow D + h\nu \\ h\nu + A &\rightarrow A^* \end{aligned} \tag{1.8}$$

A different process, prevailing in dense media, that can take place is a non-radiative energy transfer occurring via quantum chemical coupling between electronic transitions, and is expressed as:

$$D^* + A \rightarrow D + A^* \tag{1.9}$$

where D is the donor, A is the acceptor and * denotes excited states. This mechanism of transfer is called Förster resonant energy transfer (FRET), depends on the spectral overlap of the donor's emission and acceptor's absorption. It involves only spin-allowed transitions, *i.e.* singlets, and therefore only fluorescence is involved in the process. This was first formulated by the Perrin brothers and is referred to as a through-space mechanism. [59, 60]

A final energy transfer mechanism is that of Dexter transfer and is an electron exchange interaction. In Dexter transfer, an excited donor electron is transferred to the acceptor excited state and an electron from the acceptor ground state is transferred to the donor ground state. Since Dexter transfer is independent from the electrons spin, both singlets and triplets are involved.

The quantum chemical coupling for energy transfer between donor and acceptor is weak, the rate constant for the energy transfer is derived using Fermi's Golden Rule:

$$k_{FRET} = \frac{2\pi}{\hbar} \mid \langle \Psi_f | \hat{H}' | \Psi_i \rangle \mid^2 \rho_E \tag{1.10}$$

where:

ρ_E : The density of final states

$\hat{H}'$: The coupling Hamiltonian, comprising the electrostatic interaction between the charge distributions on the donor and acceptor

As noted, FRET is related to the spectral overlap between donor emission and acceptor absorption which is expressed as:

$$J = \int I_D(\lambda)\, \varepsilon_A(\lambda)\, \lambda^4\, d\lambda \tag{1.11}$$

where:

$I_D(\boldsymbol{\lambda})$: Donor emission (dimensionless)
$\varepsilon_A(\boldsymbol{\lambda})$: Extinction coefficient expressed in $\mathrm{M^{-1}\,cm^{-1}}$

and the donor emission in normalised as $\int I_D(\lambda)\, d\lambda = 1$. The resulting J is therefore expressed in $\mathrm{M^{-1}\,cm^{-1}\,nm^4}$.

To evaluate the electronic interaction energy $\beta = \langle \Psi_f | \hat{H}' | \Psi_i \rangle$, the donor and acceptor molecules are considered as a system. The initial and final state wavefunctions are $\Psi_i = \hat{A}\Psi_D^*\Psi_A$ and $\Psi_f = \hat{A}\Psi_D\Psi_A^*$, with $\hat{A}$ being the antisymmetrisation operator and Ψ containing both electronic and spin wavefunction. Considering that the system has two indistinguishable electrons, the two wavefunctions for the initial and final states can be constructed as:

$$\begin{aligned} \Psi_i &= \frac{1}{\sqrt{2}} \left[\Psi_D^*(1)\Psi_A(2) - \Psi_D^*(2)\Psi_A(1)\right] \\ \Psi_f &= \frac{1}{\sqrt{2}} \left[\Psi_D(1)\Psi_A^*(2) - \Psi_D(2)\Psi_A^*(1)\right] \end{aligned} \tag{1.12}$$

Substituting Ψ_i and Ψ_f into $\beta = \langle \Psi_f | \hat{H}' | \Psi_i \rangle$ leads to:

$$2\beta = \left\langle [\Psi_D(1)\Psi_A^*(2) - \Psi_D(2)\Psi_A^*(1)] \middle| \hat{H}' \middle| [\Psi_D^*(1)\Psi_A(2) - \Psi_D^*(2)\Psi_A(1)] \right\rangle \Rightarrow \tag{1.13}$$

$$\begin{aligned} 2\beta = &\left\langle \Psi_D(1)\Psi_A^*(2) \middle| \hat{H}' \middle| \Psi_D^*(1)\Psi_A(2) \right\rangle - \left\langle \Psi_D(1)\Psi_A^*(2) \middle| \hat{H}' \middle| \Psi_D^*(2)\Psi_A(1) \right\rangle \\ &- \left\langle \Psi_D(2)\Psi_A^*(1) \middle| \hat{H}' \middle| \Psi_D^*(1)\Psi_A(2) \right\rangle + \left\langle \Psi_D(2)\Psi_A^*(1) \middle| \hat{H}' \middle| \Psi_D^*(2)\Psi_A(1) \right\rangle \end{aligned} \tag{1.14}$$

In first and last term of Equation 1.14, the electrons remain in the respective molecules before and after the interaction changing to the excited state (or the ground state) and make up a coulomb term. In the two middle terms, the

electrons change between the two molecules and retain their status of being in an excited or ground state molecule before and after the interaction. These two terms make up an exchange term. Equation 1.14 can be written as:

$$\beta = \beta^C + \beta^E \tag{1.15}$$

with:

$$\begin{aligned} \beta^C &= \left\langle \Psi_D(1)\Psi_A^*(2) \middle| \hat{H}' \middle| \Psi_D^*(1)\Psi_A(2) \right\rangle \\ \beta^E &= \left\langle \Psi_D(1)\Psi_A^*(2) \middle| \hat{H}' \middle| \Psi_D^*(2)\Psi_A(1) \right\rangle \end{aligned} \tag{1.16}$$

Assuming that the distance between acceptor and donor is large compared to their size, it suffices to consider only the dominant dipole-dipole interaction and is the approximation that Förster used, termed point-dipole interaction. In this case, the Coulomb interaction energy β^C follows an inversely proportional relation to the donor-acceptor distance R, such as:

$$\beta^C \propto \frac{|\mu_D|\,|\mu_A|}{R^3}\,\kappa \tag{1.17}$$

where:

$|\mu_D|$ & $|\mu_A|$: The transition dipole moments for the donor and acceptor
κ : An orientation parameter for the relative orientation between the dipole moments that $\kappa = cos(\phi) - 3\,cos(\theta_D)\,cos(\theta_A)$

In a sample where the transition dipoles are isotropically oriented, $\kappa^2 = \frac{2}{3}$ is used, while a collinear arrangements results in $\kappa^2 = 4$, a parallel in $\kappa^2 = 1$ and a perpendicular $\kappa^2 = 0$. As a result of Equation 1.17, the energy transfer rate for FRET depends inversely on the sixth power of the distance between donor and acceptor:

$$k_{FRET} \propto \frac{|\mu_D|^2\,|\mu_A|^2}{R^6}\,\kappa^2 \tag{1.18}$$

Taking into account spectroscopically measurable quantities for the transition dipole moments, such as the fluorescence lifetime τ and the photoluminescence efficiency η_{PL}, through the Einstein coefficients and the density of states, the formula for k_{FRET} can be derived [54]:

$$k_{FRET} = \frac{9 \cdot ln10}{128\,\pi^5\,N_A}\,\frac{\kappa^2\,\eta_{PL}}{n^4\,\tau_D^0\,R^6}\,\underbrace{\int I_D(\lambda)\,\varepsilon_A(\lambda)\,\lambda^4\,d\lambda}_{J} \tag{1.19}$$

where:

N_A : Avogadro's number, $N_A = 6.02 \times 10^{23}\,\mathrm{mol}^{-1}$
n : Refractive index in the medium around the donor and acceptor
η_{PL} & τ_D^0 : Donor's photoluminescence quantum yield and lifetime, respectively, without the presence of the acceptor

The same equation can be simplified into:

$$k_{FRET} = \frac{1}{\tau_D^0}\left[\frac{R_0}{R}\right]^6 \tag{1.20}$$

R_0 is the *Förster radius*. Assuming $\varepsilon_A(\lambda)$ is expressed in $\mathrm{M}^{-1}\,\mathrm{cm}^{-1}$ and λ in nm:

$$R_0^6 = 8.77 \cdot 10^{-5}\,\eta_{PL}\,\kappa^2\,J \tag{1.21}$$

Typical values for Förster radii are in the order of $1 - 10\,\mathrm{nm}$, while Dexter energy transfer dominates smaller distances. [54, 56]

However, when estimating a Förster radius in an organic semiconductor, care must be taken as the classic Förster theory implies a single step process from donor to acceptor. In condensed phases, such as thin films, energy transfer is often a multi-step process including a random walk among donor chromophores. Furthermore, as noted above, Förster approximation assumes a large distance between donor and acceptor compared to their size and when the coupling is provided by electromagnetic dipole–dipole interaction. This holds true in solutions but not in thin films. This results in failure of the point-dipole approximation in extended π-conjugated molecules and polymers. [54, 56]

Finally, in the case where distances are very short ($R < 1\,\mathrm{nm}$), Dexter energy transfer is predominant. The rate of Dexter transfer is expressed as:

$$k_{Dexter} \propto J\,e^{-\frac{2R}{L}} \tag{1.22}$$

where L is a constant that relates the effective average orbital radius of the acceptor and the donor states.

1.3 Organic light-emitting diodes

While relatively young, the field of OLEDs has greatly expanded and matured by the quality and innovative research that has focused, both from the academic world but also from the private sector. Since the first OLED was reported from the Kodak labs, companies such as Hewlett-Packard, Pioneer, Panasonic, Konica Minolta use OLEDs in their products. Most known in the recent years for the commercial application in televisions are Sony, Samsung and LG and since 2015 Apple. Two major suppliers of materials for those applications are Cambridge Display Technology (CDT) and Universal Display Corporation (UDC). Impressively, the latter holds exclusively, co-exclusively or sole licence right to more than $5,000+$ patents for applications of phosphorescent OLEDs. [5] Some of the major OLED producers worldwide, such as Samsung, LG, Pioneer and Panasonic, are all supplied by UDC.

While the best-known applications for OLEDs are imaging (screens) and lighting, where visible light emission is necessary, near-infrared (NIR) OLEDs have not been equally studied, albeit their niche applications in healthcare, defence and security and telecommunications.

A typical diode structure comprises of a glass or other transparent substrate on which the electrodes and functional layers are deposited. The simplest OLED has a transparent anode, the active (emissive) layer and a reflecting metal as cathode. A structure of this single-layer OLED is shown in Figure 1.8. Active layer may include any emissive small molecule or polymer, such as PPV [16] or polyfluorenes (PFO or F8) [61, 62]. The cathode usually is a thermally evaporated metal such as calcium (Ca), aluminium (Al), silver (Ag), magnesium (Mg), etc. [63] Further to pure metals, lithium fluoride (LiF) is widely used as a μ-layer of a few nanometres with aluminium. [64] Current OLEDs typically consist of four or more layers of different materials. Such multilayer structures allow for the separation of the charge-injecting, charge transporting and light-emitting functions to the different layers, thus leading to increased efficiency and lifetime [65]

[5] As noted on the company's website oled.com

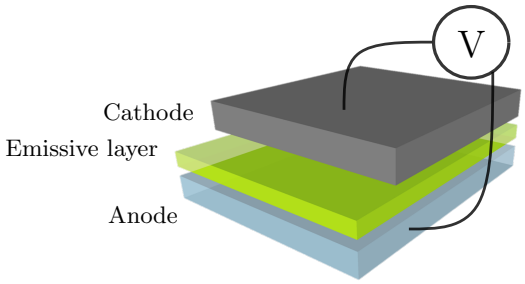

Figure 1.8 | Exploded view of the structure of an OLED with a transparent anode (bottom blue layer), emissive layer (central green layer) and a metal cathode (top grey layer). Voltage is applied via the two contacts.

The single layer device efficiency has been improved over the course of the years following its discovery. This improvement was partially the result of insertion of more layers to act as Electron/Hole Transport Layer (ETL/HTL), Electron/Hole Injection Layers (EIL/HIL), Electron/Hole Blocking Layers (EBL/HBL) according to the energy bands and purpose, while chemical design and engineering progressed and the synthesis of very efficient materials was achieved. A typical diode architecture that has been widely studied, and is also the part of the research presented in this report in Chapter 3, is ITO/PEDOT:PSS/F8BT/Ca/Al. [66, 67] Such architecture is reported in Figure 1.10.

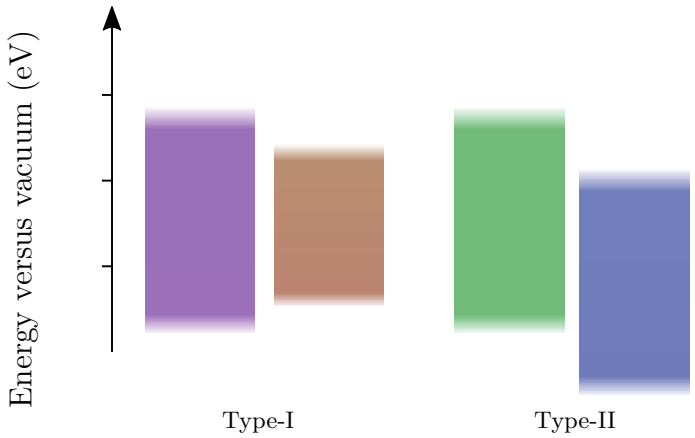

Figure 1.9 | Illustration of type-I and type-II heterojucntions.

In the case of a multilayer architecture, or an architecture employing a host-guest strategy, similar to the one that is investigated in the Chapter 3 below,

there are two possible heterojunctions that can form. Type-II heterojunction is a system where the HOMO and LUMO levels of the first semiconductor are both energetically higher than the second, a staggered architecture, illustrated in Figure 1.9. Such systems are largely employed by organic photovoltaic (OPV) devices, as they can efficiently dissociate formed excitons. In OLEDs, however, such system can be utilised to serve as an electron or hole blocking layer. However, in the case of emissive layers, such as the blends in Chapter 3, type-I heterojunction is employed. In such a system, the energy gap of one semiconductor is within the second one, as depicted in Figure 1.9, resulting in charge trapping at the smaller energy gap material.

This multilayer architecture utilises indium tin oxide (ITO) as the anode electrode, a very common material used for the anode, formed by a solid solution of Indium Oxide (In_2O_2) and $10\,w/w\,\%$ of Tin Oxide (SnO_2) as dopant. ITO has a high conductivity (sheet resistance in the order of $\sim 20\,\Omega/\square$), a high work function ($\sim$ 4.6 eV), low roughness (~ 1.8 nm RMS measured by Atomic Force Microscopy (AFM) from the supplier) and transparency to a range of wavelengths from visible to NIR. [68] Further modification to the sheet resistance ($\sim 15\,\Omega/\square$) and work function ($\sim$ 4.8 eV) comes from oxygen plasma treatment, [69] but increases up to $1.3 - 1.6$ eV reported by Brown *et al.* [70]. Interestingly, the duration of the oxygen plasma treatment doesn't seem to strongly affect the work function modification, nor does the intensity. However, Brown *et al.* showed a rapid decrease of the work function when the samples were left in air, a range of $100-400$ min, with a rather slower decrease for larger time scales, while remaining >5 eV. [70]

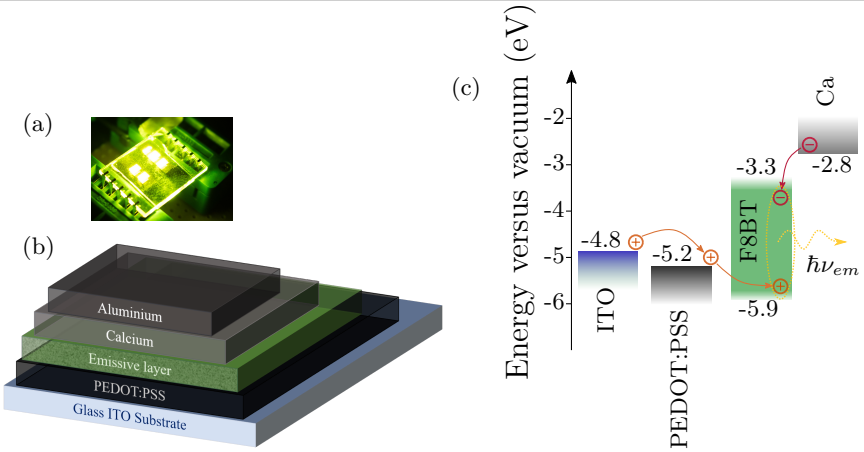

Figure 1.10 | (a) Photograph of an F8BT-based organic light-emitting diode (OLED) under operation. **(b)** Illustration of the F8BT OLED architecture used. **(c)** Energy diagram of the isolated materials used for the F8BT OLED and illustration of the operation principle. Holes are represented with the orange "+" sign, electrons with the red "-" sign. The resulting emitted photon is illustrated with the yellow arrow. Holes move from the indium tin oxide (ITO) to the lower-sitting PEDOT:PSS to the highest occupied molecular orbit (HOMO) of the polymer, while electrons are injected from the Ca to the lowest unccupied molecular orbit (LUMO). The recombination of electron-hole pair leads to electroluminescence, with a photon emitted.

The following step includes spin coating poly(3,4-ethylenedioxythiophene)-poly(styrenesulfonate) (PEDOT:PSS) from a water dispersion on top of the ITO to act as a Hole Transport Layer (HTL). [64] PEDOT:PSS has a higher work function than ITO ($\sim -5.2\,\text{eV}$), therefore better matching the HOMO of the active layer, usually around $5 - 6\,\text{eV}$. On top of the PEDOT:PSS is deposited, usually via spin-coating process, the active layer, the conjugated polyfluorene derivative poly[(9,9-di-n-octylfluorenyl-2,7-diyl)-*alt*-(benzo[2,1,3]thiadiazol-4,8-diyl)] (F8BT). F8BT is a widely studied polyfluorene derivative with a wide energy band-gap, two strong absorption bands with maxima at $\sim 325\,\text{nm}$ and $\sim 450\,\text{nm}$ and green emission, with maximum at $\sim 550\,\text{nm}$ (absorption and emission spectra are illustrated in Figures 3.13 and 3.50b & 3.12a below).

The low work function material that injects the electrons in the cathode is calcium (Ca). Ca is thermally evaporated under high vacuum ($\sim 10^{-6}\,\text{mbar}$) and has a work function of $\sim -2.8\,\text{eV}$. [71] On top of Ca a protection layer of aluminium (Al) is evaporated without breaking the vacuum to prevent oxidation of the Ca layer. A schematic representation of a multilayer device, carrier injection, as well as the band diagram of the aforementioned materials (isolated) can be seen in Figure 1.10.

Further details about the device fabrication can be found in Section 2.6.

1.3.1 Device operation

The operational principle of an OLED, when is under forward bias, starts with the injection of the carriers. Holes from the ITO, and electrons from the cathode metal are injected to the emissive layer HOMO and LUMO respectively. These carriers are then transported through the emissive polymer where they are attracted by Coulomb interaction, forming a bound state, an *exciton*. This exciton can recombine radiatively, with emission of light from the emissive layer, or non-radiatively. This phenomenon of light emission due to charge injection is called electroluminescence (EL). This principle is illustrated in Figure 1.11. [16]

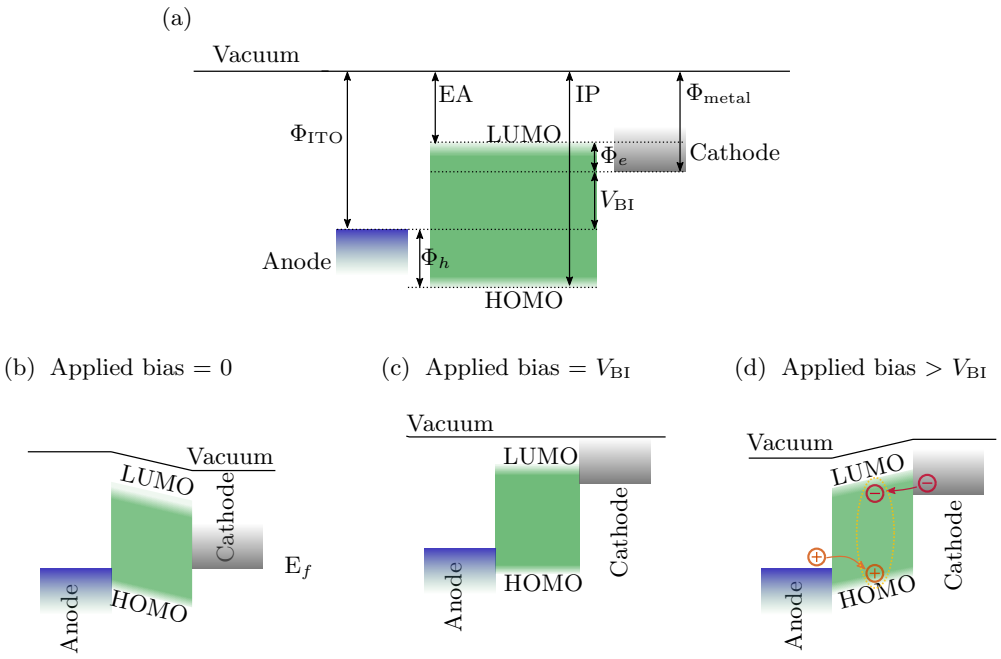

Figure 1.11 | Illustration of the energy level alignment in an organic light-emitting diode (OLED) with an architecture of ITO/Emissive Layer/Calcium. **(a)** Isolated materials (before contact), **(b)** materials in contact, **(c)** flat band condition, *i.e.* when the applied bias is $V = \mathrm{V_{BI}}$ and **(d)** materials under forward bias, *i.e.* when $V > \mathrm{V_{BI}}$.

The choice of materials with proper work functions, Φ, used as electrodes is important as to minimise the the energy barriers, notably Φ_h for the holes and Φ_e for the electrons. As shown in Figure 1.11, it is unlikely for electrons to be injected from the anode electrode (ITO) and holes from the cathode (calcium) due to the high energy barriers. The energy barriers for holes and electrons are defined as:

$$\begin{aligned} \Phi_h &= E_{\mathrm{HOMO}} - \Phi_{\mathrm{ITO}} \\ \Phi_e &= \Phi_{\mathrm{calcium}} - E_{\mathrm{LUMO}} \end{aligned} \tag{1.23}$$

As it is illustrated in Figure 1.11, $\Phi_{\text{ITO}} \neq \Phi_{\text{calcium}}$. Consequently, once the different materials are brought into contact, charges move from the cathode to the anode creating a built in voltage, V_{BI}, until $\Delta E = 0$ where the Fermi level of the structure (E_f) is aligned. V_{BI} is defined as

$$V_{\text{BI}} = \Phi_{\text{ITO}} - \Phi_{\text{calcium}} \tag{1.24}$$

Contrarily to other semiconductors, electronic structures in polymers are accurately illustrated with rigid bands as the depletion region is $\gg$ thickness (hundreds of μm versus $\sim 100\,\text{nm}$). [72] Therefore, bands are illustrated tilting rigidly by the V_{BI}, with negligible band bending. As illustrated in Figure 1.11, the energy gap (E_G) can be express as:

$$E_G = e\,V_{\text{BI}} + \Phi_h - \Phi_e \tag{1.25}$$

With the materials being in contact, the Fermi energy is constant. In the case of conjugated polymers, E_f is within the energy gap, as illustrated in Figure 1.11, not corresponding to an actual energy level. Given a thermodynamic equilibrium, the Fermi-Dirac distribution, $f(\epsilon)$, expresses the probability of an electronic state with energy ϵ being occupied at a temperature T:

$$f(\epsilon) = \frac{1}{e^{\frac{(\epsilon - \text{E}_f)}{kT}} + 1} \tag{1.26}$$

Therefore, when $\epsilon = \text{E}_f$, the probability of occupancy is 50 %. This is called the Fermi level.

As illustrated in Figure 1.11c, when the applied bias $V_0 = \text{V}_{\text{BI}}$, the is a flat-band case. The applied voltage V_0 is the minimum voltage required for charge carrier injection. By increasing the forward applied bias, more charges are injected. The injection occurs via thermally assisted tunneling through the thin Coulombic barriers of the depletion regions at the metal contacts. In the case of the forward applied bias, the charge carriers propagate through the various layers, overcoming small energy barriers at the interfaces, ending up to the emissive layer where they can recombine. The large energy barriers offered confine the carriers to the emissive layer, preventing further propagation.

For low energy barriers between electrodes and emissive layer, the current flowing can be described by the Richardson-Schottky model and is not injection limited. When the energy barriers are higher, the current is injection limited, and the charge injection is better described by a Fowler-Nordheim model. However,

upon injection, charge transport takes place through the thermally assisted tunnelling, *i.e.* hopping. [73] For low energy barriers, hole current is space charge limited (SCLC) while electron current is trap limited. This is a result of the low hole mobility that causes an accumulation of charges close to the anode interface and generate an opposite electric field. Electrons instead are more affected by trap states caused by defects.

1.3.2 Efficiency

As mentioned above, there are two different states possible, singlet states with spin $s = 0$ (Equation 1.2) and triplet states with $s = 1$ (Equation 1.1). As already discussed, the ratio of singlet to triplet (r_{st}) is 3:1, *i.e.* 75 % triplets and 25 % singlets, assuming an equal formation probability. [74] Radiative recombination is fully allowed from singlet states only, and with a high energy barrier between singlet and triplet energies, intersystem crossing (ISC) is unlikely and emission is mainly due to singlet excitons. There are, however, cases where triplet emission is the main source, such as heavy-metal containing material with phosphorescent emission, or purely organic materials that are engineered in such a way that the energy difference of singlet and triplet (ΔE_{st}) is small and reverse ISC is possible, resulting in purely fluorescent thermally activated delayed fluorescence (TADF).

The efficiency of an OLED device incorporating a fluorescent emissive layer, termed electroluminescence external quantum efficiency (η_{EL}), is summarised by a single expression of the product of the internal quantum efficiency and the light outcoupling efficiency (ξ):

$$\begin{aligned} \eta_{EL} &= \xi * IQE \\ \eta_{EL} &= \xi * \gamma \left[r_{st} * \eta_{PL_{\mathrm{FL}}} + (1 - r_{st}) \eta_{PL_{\mathrm{PH}}} \right] \end{aligned} \tag{1.27}$$

Where:

η_{PL} is the photoluminescence quantum efficiency (η_{PL}) contribution for $\eta_{PL_{\mathrm{FL}}}$ fluorescence and $\eta_{PL_{\mathrm{PH}}}$ phosphorescence

r_{st} is the ratio between singlets to the total number of excitons

γ is the excitons formation efficiency or charge balance factor, *i.e.* a factor taking into account the carrier population imbalance (the ratio of minority to majority carrier populations)

ξ is the outcoupling efficiency, *i.e.* the amount of light escaping the device

As η_{PL} is defined the ratio between the number of photons emitted to the number of photons absorbed by a material in solution or in thin film.

$$\eta_{PL} = \frac{photons\ emitted}{photons\ absorbed} \tag{1.28}$$

Further details about the experimental setup for the evaluation of η_{PL} are given in Chapter 2.

From Equation 1.27 is appreciated that it is important to have a high η_{PL}, a property affecting the material, but also a balanced charge injection (γ_{cap}). However, an improvement of a factor of 3 can be achieved by leveraging triplet states, and it is the reason for the intense research that is carried out by the organic semiconductors community and the use of heavy metals, rare earth elements and lately thermally activated delayed fluorescent materials. Lastly, η_{out} proves another limiting factor, with significant room for improvement. Typical values of η_{out} are reported in the order of $0.2 - 0.3$. [75] This is limited by the difference in the refractive indices of the various layers, total internal reflections at the interface of substrate/air, waveguided light in the various layers and substrate, etc. Approaches in improving this could be modifying the substrate by employing microlenses to extract more light, or changing the shape of the light output face, something has proven to be successful in high-energy physics with scintillating crystals. [76–78]

1.3.3 Near-infrared emitting organic light-emitting diodes

With near-infrared (NIR) is defined conventionally the spectral region above $\lambda = 700\,\text{nm}$ and below $\lambda = 1000\,\text{nm}$. Following the significant reports of OLEDs by Partridge in 1983 [32], Kodak in 1987 [33] and the Cambridge group in 1990 [16], the field of organic NIR emitting dyes was also ignited. As a result, since 1990 there have been $> 1,200$ reports in the literature. [6] As shown in Figure 1.12, the field has shown an increasing trend of published papers, therefore an increased interest over the last years.

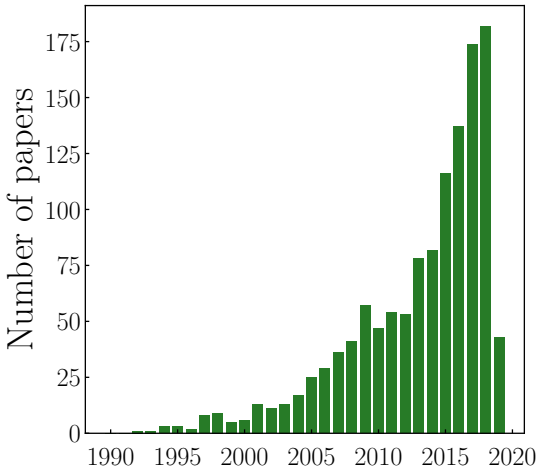

Figure 1.12 | Number of papers published since 1990 based on a search of "near-infrared", "emission" and "organic" as reported from the Web of Science, as of March 19$^{\text{th}}$, 2019. Image adapted from [79].

Despite this increase of reports and interest, the field of NIR organic materials is relatively underdeveloped compared to the visible range, owing to the difficulty of achieving very high luminescence and electroluminescence external quantum efficiency (η_{EL}) values. This can be attributed to two major factors. Firstly, the necessary small energy gap to achieve NIR emission ($< \sim 1.77\,\text{eV}$) results in a need to have very planar π-conjugated systems. These systems have the tendency to π-π stack and form non-emissive (dark) H-aggregates that are detrimental for the emissive properties of the material. [80] Secondly, it has been shown that NIR emitting organic materials obey the so-called "energy-gap" law. The energy-gap law predicts that chemically similar compounds have an exponentially increasing non-radiative (k_{nr}) with decreasing energy gap due to the vibrational overlap of the manifolds of the ground and excited states. [81, 82] This means that while the emission red-shifts, the internal conversion (IC) (non-radiative process, *vide*

[6] These results are based on the Web of Science reports for the keywords "near-infrared", "emission" and "organic". Accessed March 19$^{\text{th}}$, 2019.

infra) of $S_1 \rightarrow S_0$ becomes more efficient. The energy-gap law is summarised in the expression [56]:

$$k_{nr} \propto exp\,(-\frac{\gamma\,\Delta E}{\hbar\,\omega}) \tag{1.29}$$

where:

ω : maximum vibrational frequency
γ : is a quantity expressible in terms of the molecular parameters

Several approaches have been reported in an attempt to minimise and overcome the limitations of the two factors mentioned above. One approach is by molecularly engineering the materials, such as rotaxanes [83, 84] and similar structures [85], that sheath the conjugated core protecting it from π-π stacking. A second approach is to increase the distance between the emitters, by diluting the NIR emitting chromophores in a polymer matrix, typically with a wider energy gap. [86–95] Further to organic materials, inorganic metal complexes and quantum dots have also been reported in the literature as efficient NIR emitters. This thesis, dealing with narrow energy gap emitters, has employed both approaches to achieve efficient emission. Figure 1.13 presents the the η_{EL} of NIR emitting OLEDs published to date, including the results presented in this thesis. [91, 96]

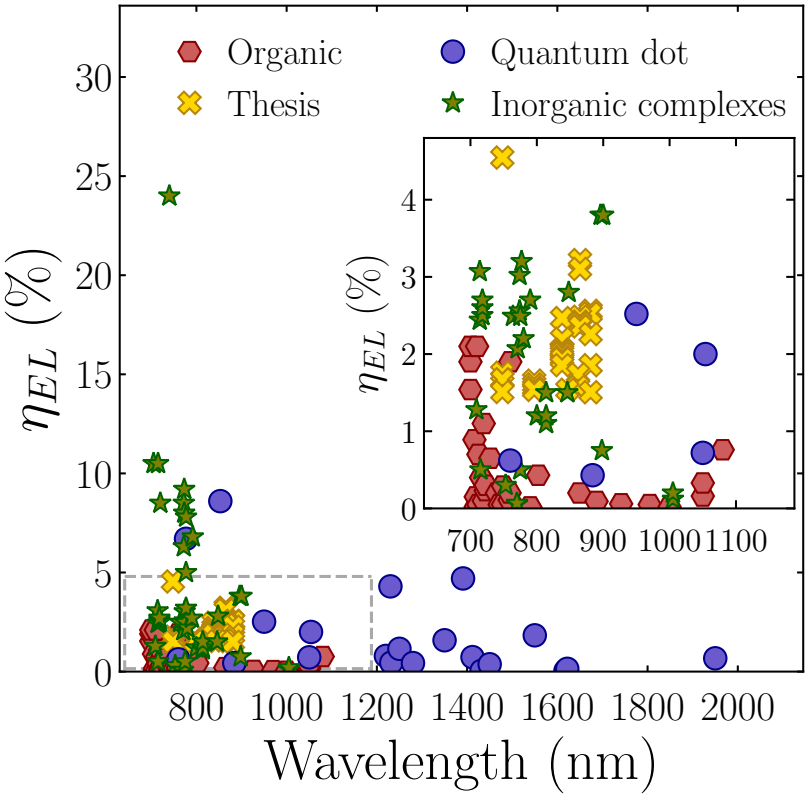

Figure 1.13 | Electroluminescence external quantum efficiency (η_{EL}) as a function of emission wavelength for near-infrared (NIR) organic light-emitting diodes (OLEDs) published to date including the results presented in this thesis. [96] The grey dashed box in the bottom left corner is the area that has been magnified in the inset. There are no TADF results in this figure.

As shown in the Figure 1.13 above, there are many organic-inorganic metal complexes that have exhibited impressively high η_{EL} values, but the "record holder" for the highest η_{EL} reported so far is by Tuong Ly *et al.* that achieved an impressive $\eta_{EL} = 24\,\%$ in a normal planar OLED structure that was further boosted to $55\,\%$ when using a light-outcoupling hemisphere. [97] The diode emission peaks at 740 nm and was based on platinum metal organic complexes as the emissive layer. The NIR emitting phosphorescent porphyrins reported by the groups of Forrest [78, 92, 98, 99] and Reynolds [100–102] are also among the highest efficiencies reported for NIR organic materials containing, however, toxic heavy metals. Furthermore, perovskites have also been shown to achieve high values of $\eta_{EL} \sim 5.0\,\%$. [37, 38, 103]

Bridging the gap between triplet emission and toxic heavy metals are materials that can leverage triplet excitons without the use of heavy elements needed by phosphorescent materials, such as platinum, lead, iridium, etc. Such materials were first reported by Adachi *et al.* in 2012 and their emission is referred to as thermally activated delayed fluorescence (TADF). [104]. By employing reverse

intersystem crossing (rISC) thanks to the engineered small energy difference between singlets and triplets (ΔE_{ST}), highly efficient spin up-conversion from non-radiative triplet states to radiative singlet states is promoted. This results in materials that are possible to achieve 100 % internal quantum efficiency, but avoid the use of toxic and heavy metals. By employing TADF, Adachi was able to report a very impressive η_{EL} of $\sim$ 10 % with emission peaking at 721 nm. [91] Such value is above the theoretical upper limit of conventional fluorescent OLEDs, achieved there thanks to a high η_{PL} and TADF.

Following the seminal report of 2012, the field of TADF molecules has seen a vivid interest as the materials are purely organic and allow for some of the highest reported values. With visible light applications in mind, such as lighting and screens on various devices (*e.g.* TVs, smartphones, etc.), it is interesting to look at the best efficiencies reported for OLED devices for the three primary colours, red, green and blue that employ TADF compounds. Wu *et al.* from the Departments of Chemistry and Materials Science and Engineering of the National Tsing Hua University in Taiwan reported the synthesis of two diboron-based molecules that, when embedded in OLEDs have a green emission peaking at 528 nm and achieved an impressive $\eta_{EL} = 37.8$ %. [105] Lin *et al.* from the Departments of Electrical Engineering and Chemistry of the National Taiwan University reported the molecular architecture based on the spiroacridine-triazine hybrid that resulted in OLEDs with "sky blue" emission peaking at 480 nm and $\eta_{EL} = 36.7$ %. [106] Lastly, Li *et al.* from the University of Kyushu in Japan, the Materials Science and Engineering Commonwealth Scientific and Industrial Research Organisation (CSIRO) in Victoria, Australia and the Functional Materials Laboratory Nippon Steel and Sumikin Chemical Co. in Japan, reported an orange-red emitter peaking at 610 nm that achieved an impressive $\eta_{EL} = 17.5$ %. [107] Impressively, all three aforementioned record efficiencies are reported for simple, planar OLED structures that don't have any outcoupling enhancements, but do have optimised architectures with injecting and blocking layers to balance the injecting carriers and contain the recombination within the emissive layer. Most importantly, all three are fully organic compounds omitting the use of toxic and expensive heavy metals or rare-earth complexes. Further to small-molecule materials showing TADF, polymers can also be synthesised to exhibit TADF. [108]

Applications of near-infrared emitting organic light-emitting diodes

Further to the visible light applications, materials that absorb and emit in the NIR are of great interest for many different sectors. NIR absorbing materials can be utilised for the enhancement of the efficiencies of solar cells. As mentioned above, a tandem solar cell approach can yield very high efficiencies and still harvest solar energy at wavelengths $>700\,\text{nm}$, which accounts for almost 50 % of the energy that the Sun emits. [15, 109] Given the biocompatibility of organic materials, biological and biomedical applications remain very promising fields. Combining NIR absorbing and emitting compounds, blood oxymetry is one example that can utilise NIR OLEDs and photodetectors. [110, 111]

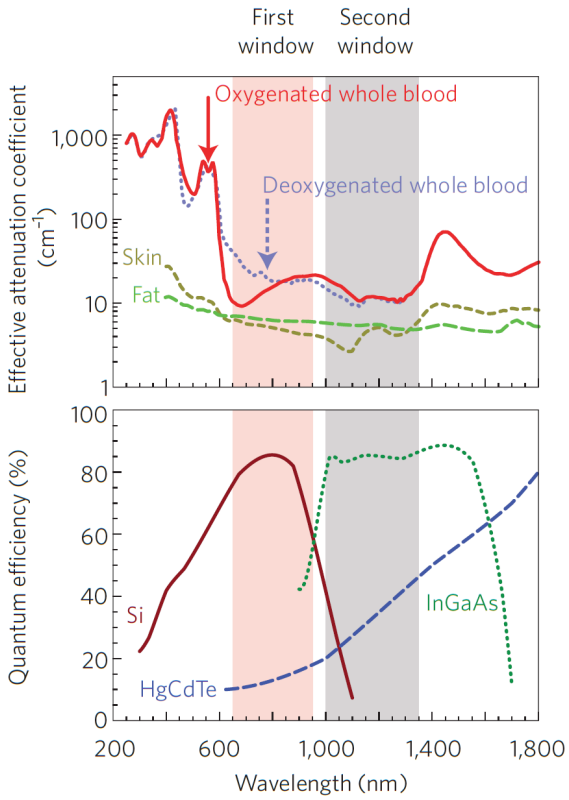

Figure 1.14 | Top: Absorption (effective attenuation coefficient) spectra of biological tissue. **Bottom:** Sensitivity curves of typical sensors used. The shaded red and grey areas represent two near-infrared (NIR) windows. Image reproduced from [112].

The interest of NIR devices in many bio-related applications is also driven by the fact that biological tissue (blood, fat tissue and skin) has a local minimum in the absorption of light, illustrated in Figure 1.14. [112] Combining the low tissue absorption and $>50\,\%$ silicon (CCD) detector efficiency, thus making the wavelength range $\lambda = 700 - 950\,\text{nm}$ an ideal potential for NIR OLEDs. [112] This fact makes NIR OLEDs good candidates for healthcare applications in

photodynamic therapy (PDT) and low level light therapy (LLLT) [113–115]. Further applications of NIR OLEDs are found in defence and security. [48, 116] Since the human eye is not sensitive to NIR light, NIR OLEDs are also candidates for applications in all-optical networking systems such as Light-Fidelity (Li-Fi) to substitute the existing Wi-Fi and overcome the bandwidth limitations. [49, 117, 118]

NIR emitting OLEDs fabricated, characterised and presented below yielded unprecedented η_{EL} values, with efficiencies up to $\sim 4\,\%$ and EL peaking at $> 850\,\text{nm}$. It is to the best of the author's knowledge that such values represent the highest values ever reported in the literature for heavy-metal-free (and in cases metal-free altogether) NIR emitters with a lifetime in the order of $\tau \sim$ ns, at the time of writing of this thesis, as it is also indicated in the Figure 1.13 when compared to the organic molecules.

2 | Experimental methods

"Cuncti adsint meritaeque
expectent praemia palmae"

UCL motto

In this chapter, a short description of the methods used to prepare samples, characterise them and analyse the data collected is given.

2.1 Solution Preparation

The solutions were prepared by weighting the materials in powder form, polymers and small oligomers. All dry materials were stored in a dry, N_2 filled glovebox, free from any solvent. Once the materials were weighted in their respective amber vials, the appropriate amount of solvent was added to arrive to a 10 mg/ml solution.

Blends of a host-guest approach, an approach that Chapter 3 utilises extensively, were made using appropriate volumes of each solution to arrive to the desired loading, *e.g.* add to 297 μl of 10 mg/ml F8BT solution, 3 μl of a 10 mg/ml porphyrin oligomer solution to make a F8BT:porphyrin 1.0 w/w % solution. In the case of the polymers in Chapter 4, pure polymers were prepared in 10 mg/ml solutions of anhydrous chlorobenzene.

All solutions were made in a second dry, N_2 filled glovebox using anhydrous solvents supplied from Sigma Aldrich.

2.2 Thin films preparation

In this thesis, thin films were prepared using spin-coating. Starting from the same solutions reported above, an appropriate volume was loaded to a pipette and was dropped on the substrate. Depending on the substrate that was used, either a glass spectrosil, a simple glass slide, the OLED ITO substrate (*vide supra*), the volume varied from $\sim$ 50 µl to $\sim$ 100 µl. The substrate was subsequently rotating at an appropriate speed to fabricate a required thickness film. The thickness of the films was verified using a Dektak profilometer and an atomic force microscope (AFM) if the resolution of the Dektak was not sufficient.

Typical thickness for the active layers were $\sim$ 100 nm. The thickness of the films was verified frequently with the profilometer to verify the repeatability of the experiments. It was also repeated every time a new batch of a commercial polymer was bought and used, or when a new material was introduced. The varying exhaust conditions of the spin coaters (both when spin coating in air and in the glovebox), resulting from fluxes of air, made the results reproducible with a $\sim 10 - 20$ % accuracy in the thickness of the resulting film, independently of the substrate, though smaller substrates tend to have a decreased reproducibility. It has been shown that the thickness of the active layer has a great influence in the resulting electroluminescence spectrum and electroluminescence external quantum efficiency (η_{EL}). [119, 120, 120] For the F8BT-based OLEDs that have

been extensively used in the present thesis has been shown that a $\sim 100\,\text{nm}$ active layer has the best results.

poly(3,4-ethylenedioxythiophene)-poly(styrenesulfonate) (PEDOT:PSS), being a water dispersed polymer, was spin coated outside the glovebox, in ambient conditions. All other spin coating was carried out inside an N_2 filled, dry glovebox.

2.3 Optical properties

Optical properties are primarely investigate by collecting UV-VIS-NIR steady-state absorption and emission spectra.

Steady-state absorption spectroscopy

Absorption spectra are collected either in solution or in thin-films. Solution absorption spectra are typically collected using a quartz cuvette with a 10 mm. The blank is collected with a cuvette filled with the solvent that is used to dilute the material.

Thin film absorption is usually collected from fused-silica spectrosil substrates, on top of which the material to be investigated is deposited. Typical deposition techniques are spray-coating, dip-coating, spin-coating, blade-coating, drop-casting, etc. In the frame of this thesis, spin-coating is used exclusively as the most appropriate way of thin-film forming for the applications concerned. The blank is taken using a clean spectrosil.

Steady-state emission spectroscopy

Emission spectra are collected using an ANDOR-Shamrock 163 spectrometer coupled with an ANDOR-Newton charge-coupled device (CCD) unit. The Andor is capable of providing a resolution of $\sim$ 0.3 nm and is cooled to $-50\,^{\circ}\text{C}$. The Andor has a window of *ca.* 500 nm which is rotatable using a micrometric screw. This allows the rotation of a diffraction grating as to adjust the viewing window from the near-UV to the near-IR ($\sim 300-950\,\text{nm}$). For correct calibration of the window, the 629 nm peak of the fluorescent lights in the room was used and was cross-calibrated using laser diodes with precisely known emission wavelengths.

The instrument allowed for the custom adjustment of the exposure time and the number of accumulations to improve the signal-to-noise ration. Typical

values for the results presented are 0.1 s exposure/integration time and 100 accumulations. However, in certain weak emitters in the near-IR, longer integration times were used to allow for improved signal-to-noise ratio. A final adjustment was the opening slit that allows for more light to enter the instrument at the cost of resolution.

The response of the Andor is corrected using calibration factors that were calculated for specific wavelength, as described in the Section 2.3 below. The spectra presented in this thesis were collected using the Andor spectrometer.

In order to collect emission spectra, solutions and thin-films were excited with various sources. Throughout the thesis, various laser sources were used to excite the molecules, according to the absorption spectra, in order to be resonant with an absorption peak. The excitation source is noted in the captions, however the sources used are continue wave laser diodes bought from Thorlabs emitting in 405, 445, 520 nm. Additional sources used are a 375 nm and a 450 nm picosecond pulsed laser diodes from Edinburgh Instruments, the same used for the TCSPC technique described below in Section 2.5 and a 325 nm He-Cd gas laser. Finally, during certain measurements, to perform comparative studies that is not presented below and during the calibration presented below, a Thorlabs laser diode emitting at 780 nm was also used.

Calibration and improvement of the η_{PL} measurements

The calibration of the response of our spectrometer so far was done using a calibrating lamp with a black body emission of a known temperature. The black body emission spectrum is given by:

$$R_s(\lambda, T) = \frac{2hc^2}{\lambda^5} \frac{1}{e^{hc/\lambda k_B T} - 1} \tag{2.1}$$

As for all the instruments, a response function correction factor was needed to correct the collected spectrum for the instrument's responsivity. A typical correction factor was collecting a spectrum of a black-body emitter, such as a calibration lamp, of a known temperature. This would allow to create a correction simply by comparing the theoretical spectrum to the collected one. This was proven to be correct and accurate for our instrument for a number of viewing windows. However, careful consideration and investigation of some values in the near-UV showed that there was a discrepancy between the expected and obtained values. This led to the in-depth investigation of the causes and the detailed calibration of the Andor.

To calibrate, three "viewing windows" were chosen, as to facilitate η_{PL} measurements:

- $315 - 790\,\text{nm}$ window for η_{PL} measurements using any source in the near-UV, such as the 325 nm He-Cd and the 375 nm picosecond lasers.
- $380 - 870\,\text{nm}$ window for η_{PL} measurements using the 405 and 450 nm laser diodes.
- $480 - 965\,\text{nm}$ window for η_{PL} measurements using primarily the 520 nm laser diode and any other in the red-near-IR. This was also the main window used for OLED measurements.

and the three corresponding correction factors were created. This allowed to standardise our measurements, with accurate calibration factors and wavelength ranges, but also to speed up the collection and analysis steps.

To carry out the calibration, a xenon lamp spectrum was collected using a calibrated photodiode (PD). The PD was calibrated directly by the manufacturer, Bentham. The spectrum was collected at 5 nm steps, for the range $300 - 950\,\text{nm}$. Since the spectrum responsivity (R) that was provided by Bentham was measured in $[R] \propto [\text{W}]^{-1}[\text{nm}]^{-1}$, a division with the wavelength was necessary to obtain the corrected PD spectrum in Watts. Following that, the same spectrum was collected every 5 nm using the Andor spectrometer, using the three ranges $315 - 790\,\text{nm}$, $380 - 870\,\text{nm}$ and $480 - 965\,\text{nm}$. Since the photodiode was collecting a signal from the complete 5 nm, each spectrum collected with the Andor was integrated. This led to the creation of the xenon lamp power spectrum using the Andor. The three calibration factors were obtain by simply dividing:

$$\text{correction factor} = \frac{I_{\text{Andor}}}{I_{\text{PD}}} \tag{2.2}$$

The resulting calibration factors can be seen in Figure 2.1 below comparing the results for three calibration ranges for both inside and outside the integrating sphere that was used for all the η_{PL} measurements reported in the present thesis.

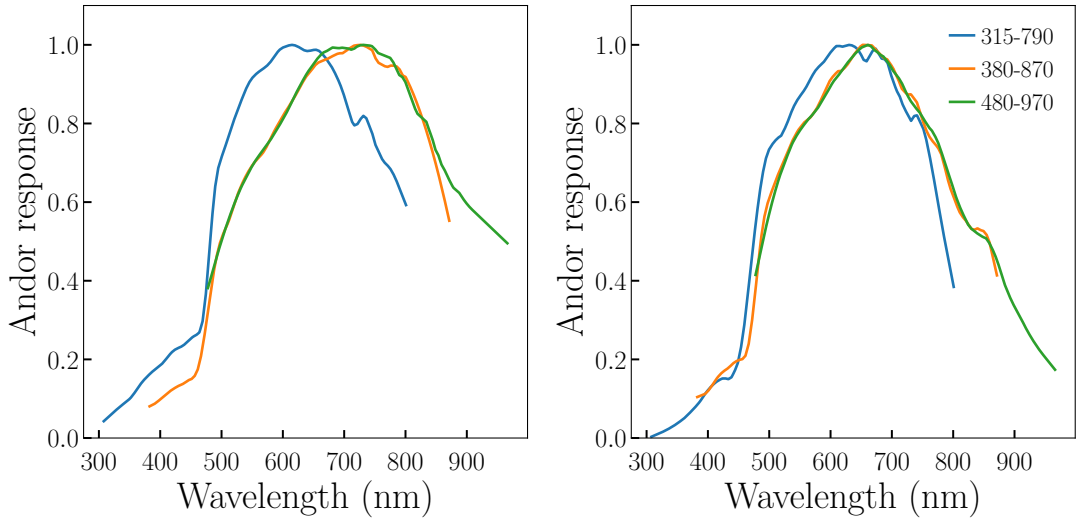

(a) Outside the sphere **(b)** Inside the sphere

Figure 2.1 | The resulting calibration factors for the three ranges for the response of the spectrometer for measurements (a) outside the integrating sphere and (b) inside the integrating sphere.

The same procedure was followed both for inside and outside the integrating sphere, as to compensate for the response function of the sphere. To correct a spectrum collected with the Andor, it suffices to divide the spectrum by the correction factor calculated. It is important, for the correct calculation of the measurements, that once a spectrum has been collected using the Andor spectrometer that is multiplied by the wavelengths as to convert the power (radiometric quantity) to photon flux (photometric quantity). Our calibrations were compared to literature values of calibrations standards against measurements in our labs. The calibration standards used and the methodology for the calculations can be found in [121] and the final results are presented in Table 2.1 below.

Table 2.1 | Table comparing the photoluminescence quantum efficiency (η_{PL}) values of calibration standards and the experimental results. η_{PL}^{lit} refers to the values found in [121], η_{PL}^{exp} refers to the experimental results obtained after measuring with the new calibration factors, η_{PL}^{BB} refers to the previous approach of using the black body approximation. λ_{exc} is the wavelength of excitation.

Range	Sample	λ_{exc} (nm)	η_{PL}^{lit} (%)	η_{PL}^{exp} (%)	η_{PL}^{BB} (%)
315 – 790	C102	405	76.0	68.60	98.9
315 – 790	C153	405	54.5	60.00	76.0
380 – 870	C153	405	54.5	69.00	85.0
380 – 870	C153	450	54.5	64.80	65.7
380 – 870	Rh101	520	91.3	87.50	93.0
480 – 965	Rh101	520	91.3	81.50	81.0
380 – 870	Ox170	520	57.9	43.00	43.0
480 – 965	Ox170	520	57.9	41.00	42.0
480 – 965	IR125	780	13.2	0.65	8.0
480 – 965	IR140	780	16.7	1.50	12.5

Results proved to be encouraging for the new calibration factors. However, before arguing the accuracy in the NIR, some discrepancies are to be expected when comparing to the literature values, as different suppliers were used, compared to those used by the authors in [121]. Also, exciting at 780 nm with emission well in the NIR and a detector that has reduced sensitivity in that spectral range, are both factors contributing to some less accurate results. It is worth noting that no results presented in this thesis were calculated using a 780 nm excitation.

Notably, all the measurements of Chapter 3 were carried out using these calibration factors, though the results of Chapter 4 are with the previous ones. However, the range of wavelengths that the materials of Chapter 4 were emitting prove to be the most accurate of the "black-body" method, with a negligible difference.

2.4 Photoluminescence quantum yield measurements

As photoluminescence quantum efficiency (η_{PL}) we define the ratio of the number of photons emitted by the number of the photons absorbed:

$$\eta_{PL} = \frac{photons\ \ emitted}{photons\ \ absorbed} \tag{2.3}$$

There are two main procedures to experimentally define the η_{PL}, a relative and an absolute. For the *relative method*, the determination of η_{PL} of a sample is based on the measurement of the spectrum and comparing it to a sample with a known η_{PL}, a *standard* by using the formula:

$$\eta_{PL}^{sample} = \frac{I_{sample}}{I_{ref}} \frac{A_{ref}(\lambda_{exc})}{A_{sample}(\lambda_{exc})} \eta_{PL}^{ref} \tag{2.4}$$

However, there is a second procedure to measure η_{PL}, an *absolute method*, that has been reported by de Mello *et al.* [122] and includes:

- An excitation source, typically a laser
- An integrating sphere with the inner surface coated with a diffusely reflecting material
- A detector

The experimental setup is illustrated in Figure 2.2 bellow. All values of η_{PL} presented in this thesis have been calculated using this method.

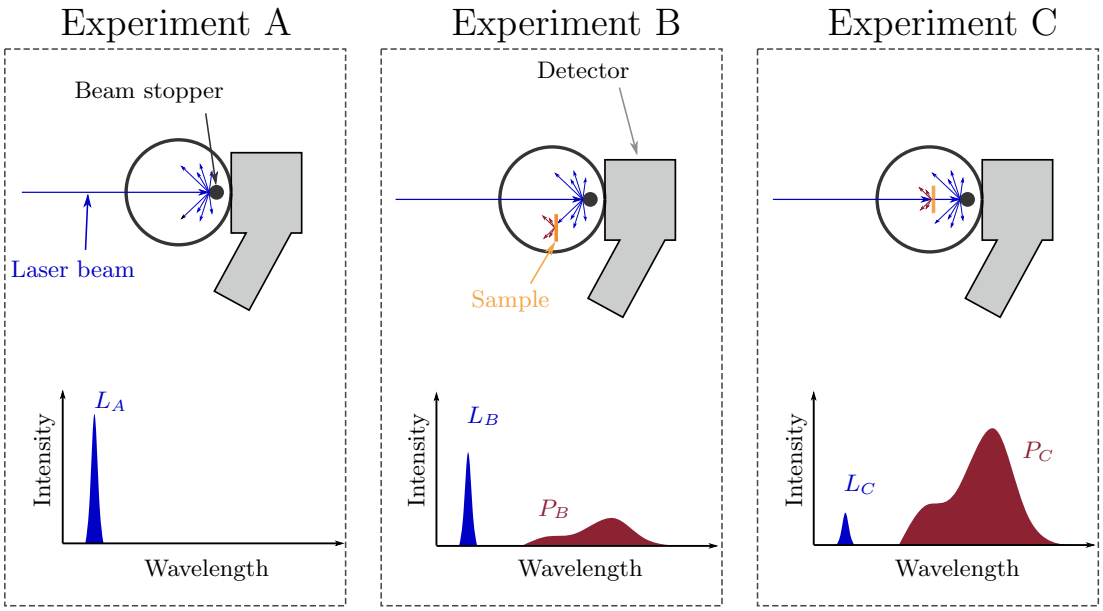

Figure 2.2 | Experimental photoluminescence quantum efficiency (η_{PL}) measurement setup where the integrating sphere is depicted as the black circle, the detector as the grey square, the laser light as the blue line and the sample as the red rectangle. The measurement includes three experiments: The integrating sphere **(A)** without the sample, **(B)** with the sample but not hit directly by the beam and **(C)** with the sample hit directly by the beam. Image adapted from [122].

For the calculation of the experimental η_{PL} there are three measurements that are required:

(a) A measurement with the integrate sphere empty, with only the excitation source directed inside, in our case a laser: Measurement A, where L_A is the laser light.
(b) A measurement where the sample is placed inside the integrating sphere but it is not hit directly by the laser light and the only source of excitation is reflected light: Measurement B where L_B is the laser light and P_B is the emission of the sample.
(c) A measurement where the sample is placed inside the integrating sphere and is hit directly by the laser light: Measurement C where L_C is the laser light and P_C is the emission of the sample.

The experimental procedure is summarised in an elegant formula:

$$\eta_{PL} = \frac{P_C - (1 - A)P_B}{L_A A} \tag{2.5}$$

where A is defined as $A = (1 - \frac{L_C}{L_B})$.

The laser light intensity is gradually quenched in favour of the emission of the material, whose emission in contrary is gradually increasing as depicted in Figure 2.2.

An additional way to define η_{PL} is in terms of the radiative and not-radiative rates:

$$\eta_{PL} = \frac{k_r}{k_r + k_{nr}} \tag{2.6}$$

where k_r is the *radiative rate* for the $S_1 \rightarrow S_o$ transition and k_{nr} is the *non-radiative decay*. By determining experimentally η_{PL} (Equation 2.4), the radiative an non-radiative constants can be calculated by combining Equation 2.6 and

$$\tau = \frac{1}{k_r + k_{nr}} \tag{2.7}$$

where τ is the *fluorescent lifetime*, the time a molecule "spends" in the excited state before relaxing to the S_0. τ is experimentally measured using time-correletated single photon counting (TCSPC).

In the frame of this thesis, all the η_{PL} results presented where calculated using the absolute method summarised in Figure 2.2. To account for any micro-variations in the laser intensity, each of the A, B and C experiments was repeated five times and then averaged over the results. The results presented below are in the form $\langle \eta_{PL} \rangle \pm \sigma$, where:

$\langle \eta_{PL} \rangle$ is the average η_{PL}, $\langle \eta_{PL} \rangle = \dfrac{\sum_{i=0}^{5} \eta_{PL_i}}{5}$
σ is the standard deviation of the five measurements

If a large σ was observed during the analysis of the results, the measurements were repeated with the sample.

2.5 Time-correlated single photon counting

Time-correletated single photon counting (TCSPC) is a technique that uses a pulsed laser and fast electronics to determine the fluorescence lifetime. A laser pulse from a pulsed laser with high repetition rate is exciting a sample. The laser pulse acts also as a trigger signal for the electronics to "expect" the arrival of a photon. The detector's electronics and software are designed so only one photon will be counted after each trigger.

By measuring the time between trigger and photon arrival the photons that are detected are correlated to the excitation pulse and a histogram of the PL intensity vs time is created. The resulting plots are then fitted with an exponential function, like:

$$R(t) = A_0 + \sum_{i=1}^{n} A_i e^{(-\frac{t}{t_i})} \tag{2.8}$$

where A_0 is a constant that takes into account the background, A_i is the weight of the exponential and t_i is the lifetime.

To calculate the average lifetime $t_{\oslash}$, the Equation 2.9 is used:

$$t_{\oslash} = \begin{cases} \dfrac{\sum_{i=1}^{n} A_i t_i}{\sum_{i=1}^{n} A_i}, & \text{if } \sum_{i=1}^{n} A_i = 1 \\ \sum_{i=1}^{n} \frac{A_i ti}{A_i}, & \text{if } \sum_{i=1}^{n} A_i \neq 1 \end{cases} \tag{2.9}$$

All the decays that are presented in this thesis are bi-exponential decays fitted with a bi-exponential function. The resulting two lifetimes are averaged using the respective weights.

The minimum measurable time by the instrument is referred to as the instrument response function (IRF). To collect the IRF, a scattering sample,

in this case some soap provided by the manufacturer dissolved in deionised water was used, is irradiated by the same laser used for the measurements. The window of the collection is moved close to the maximum of the laser peak. The laser used throughout the thesis for the TCSPC measurements was emitting at $\lambda = 450\,\text{nm}$. The window of the collection for the IRF was placed at $\sim 460\,\text{nm}$ to increase the signal.

For all the fits that are presented, the decays were fitted with a tail fit. This is due to the long collection times (900 s) for each sample, meaning that for each of the decays presented below, it took 900 s to collect each spectrum. This increased the average noise (dark counts) and as a result, when the IRF was collected, the average noise was considerably lower and/or the maximum counts were significantly higher, depending on the measurement conditions, thus forcing the fitting software to overestimate/underestimate the fits.

However, in one occasion, a reconvolution fit (taking into consideration the IRF) is presented below (notably in Figure 3.33). The instrument has a characteristic shoulder when measuring the decay, that in very short decays it becomes evident. The IRF of the TCSPC system is shown in Figure 2.3 below.

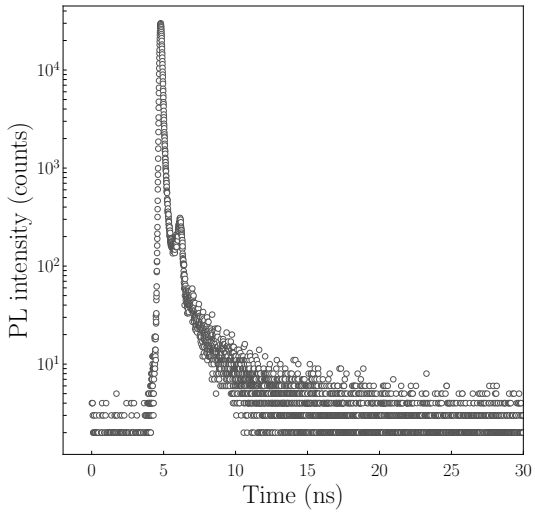

Figure 2.3 | Instrument response function (IRF) for the TCSPC system used to measure the time decays presented in this thesis.

2.6 Devices fabrication

Further characterisation of the materials includes the incorporation into organic light-emitting diodes (OLEDs) as emissive layers. The fabrication of OLEDs is a multi-step process that starts from a thorough cleaning of the substrates, spin

coating of the different layers, thermal evaporation of the cathode metals and concludes with encapsulating the devices to protect from oxidation, specifically of the cathode metals.

The fabrication process begins by cleaning the glass indium tin oxide (ITO) substrates; they are placed in an acetone and isopropanol bath and are sonicated for 15 min each step. The samples are then dried under a N_2 flux and are then treated with O_2 plasma at 10.2 W for 15 min. The O_2 plasma modifies the work function of the ITO from $\sim$ 4.6eV to $\sim$ 4.8eV, as well as modifying it morphologically. [69, 70, 123]

The following step is the spin coating of the hole injector poly(3,4-ethylenedioxythiophene)-poly(styrenesulfonate) (PEDOT:PSS) from a 3.8 % water dispersion. The spin rate of 5000 rpm results into a uniform layer of $\sim$ 50 nm thickness. This step doesn't influence the modification of the work function. [70] The samples are then transferred in a N_2 filled dry glovebox (GB) and are thermally annealed at 150 °C for 10 min. This annealing process removes any remaining water from the PEDOT:PSS layer.

From this part onwards, the samples are only handled within the inert atmosphere of the GB. On top of the PEDOT:PSS layer is spin coated the emissive layer. The emissive layer's thickness is kept at $\sim$ 100 nm. To verify the thickness, prior to spin coating on the ITO substrate, fused silica substrates are used and the thickness is measured using a Dektak profilometer.

Once the spin coating is complete, the samples are loaded into a thermal evaporator. At that point the cathode metals, calcium (Ca) and aluminium (Al), are thermally evaporated on the emissive layer at $\sim 10^{-6}$ mbar. 30 nm of Ca are first evaporated at a rate of 0.4 Å/s follow by 200 nm of Al at a rate of 2 Å/s. During the thermal evaporation of the metal, the substrates are cooled to circa 6 °C to prevent crystallisation of the organic layers. [124] The combination the patterned ITO and the evaporated contacts results in each device having 6 pixels of $\sim 4.5\,mm^2$ surface on each substrate.

Once the evaporation is complete, a small drop of encapsulating epoxy is dropped on the metals and a small glass slide placed on top of the epoxy. This serves as a protection of the pixels from the atmospheric oxygen and water. The insertion of the electrical legs for the contacts completes the fabrication process. An exploded view of a typical device is illustrated in Figure 2.4 below.

In the frame of this thesis, and for the needs of initial tests of materials in OLED devices, a second type of substrate was used that doesn't contain patterned ITO, supplied by Colorado Concept Coatings LLC, but the pixels are defined by an evaporation shadow mask that results in 8 pixels of $3.5\,mm^2$ that are

not encapsulatable. To avoid oxidation of the Ca layer, this type devices are transported under a nitrogen atmosphere to a vacuum chamber and measured under a $\sim 10^{-2}$ mbar pressure. However, results from this type of devices are omitted from this thesis to remain consistent and report comparable results.

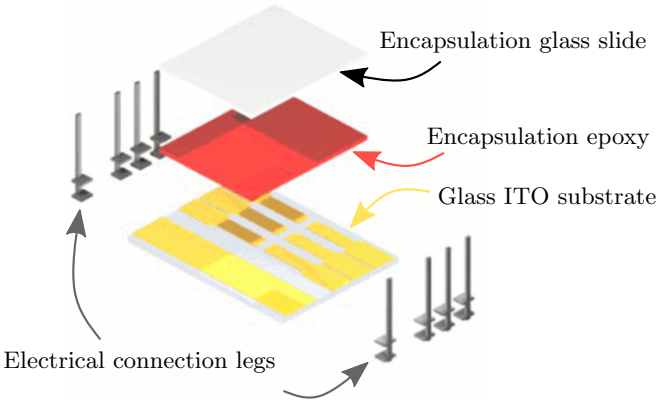

Figure 2.4 | Exploded view of the pre-patterned glass indium tin oxide (ITO) substrates (ITO shown in yellow), encapsulating epoxy (red), glass slide and electrical connection legs. Image adapted from ossila.com.

A fully fabricated and encapsulated device is shown in Figure 1.10.

2.7 Electrical properties

The current was measured by a Keithley 2400 source meter, which also supplied the voltage. The luminous output was measured from a 100 mm^2 calibrated silicon photodiode by a Keithley 2000 multimeter. The EL spectra were collected with the same Andor spectrometer that was used for the PL experiments presented above.

The different characteristic extracted and presented in this thesis from the current density - voltage - radiance (JVR) curves include the electroluminescence external quantum efficiency (η_{EL}), radiance, current density, and turn on voltage (V_{ON}).

The efficiency of the device is summarised by the expression of η_{EL}:

$$\eta_{EL} = \eta_{PL} * r_{st} * \gamma_{cap} * \eta_{out} \tag{2.10}$$

According to Varo et al., a unified model was proposed in 2014 to discuss the JV curves in a space charge limited regime. [125] According to the authors, at low voltages there is an Ohmic regime, described by Ohm's law. At higher

voltages, Child's law is used to interpret the quadratic-fitted curve. Lastly, the last part of the curve is fitted with higher than quadratic model. The mobility depends on temperature, electric field applied and carrier concentration. As already mentioned, charge injection commences at the flat band condition and any current measured below that voltage is due to leakages and short-circuits due to imperfections of the polymer layers.

In this thesis, materials studied are either partly or entirely emitting in at $\lambda > 700\,\text{nm}$, *i.e.* in the near-infrared (NIR). For this reason, radiance (R) is reported rather than luminance.

In the frame of this thesis, the turn-on voltage of an OLED is arbitrarily defined as the voltage at which the radiance is:

$$\text{V}_{\text{ON}} = \text{V}(R = 3.5 \times 10^{-5}\,\text{mW/cm}^2) \tag{2.11}$$

where it is well above the detection threshold of the photodiode, $\sim$ 3-5 times the average noise.

The software used for controlling the Keithley that supplied and measured the current and the voltage of the OLED, as well as reading of the Keithley from the photodiode is shown in Figure 2.5.

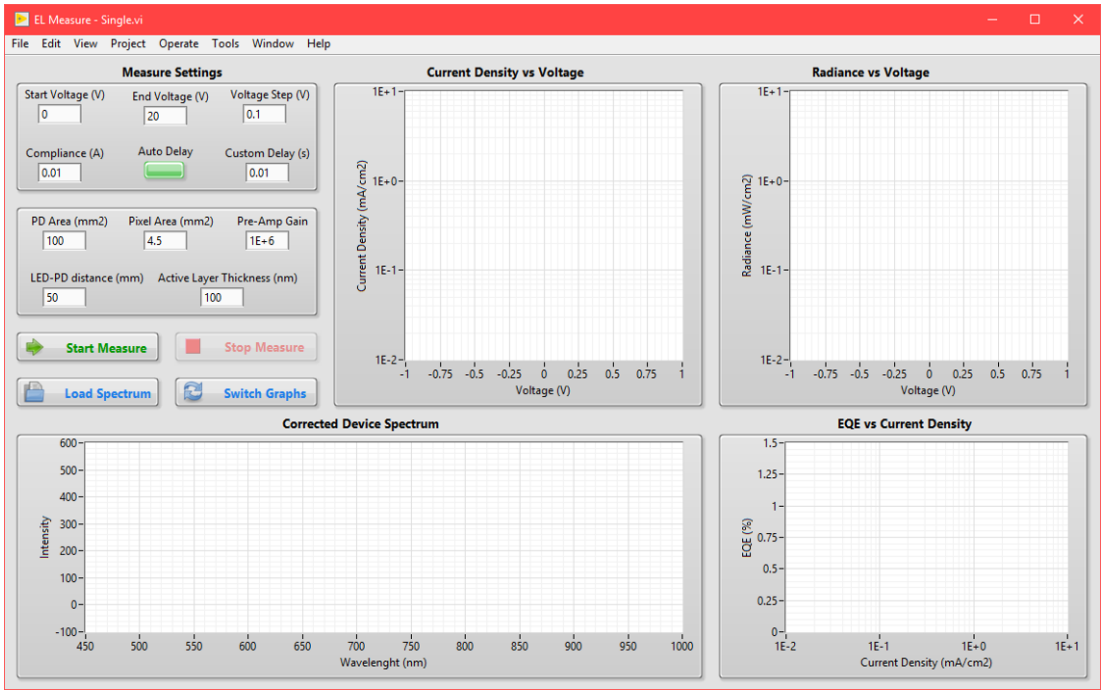

Figure 2.5 | LabVIEW software screenshot for the measuring of the OLEDs.

Another LabVIEW software was developed, based on the one presented

in Figure 2.5 that allowed for a constant applied current density or voltage to measure the lifetime. Depending on the mode selected, the voltage or current density respectively was recorded, along with the light output that would subsequently allow the evolution of η_{EL} over time. A screenshot of this software is shown in Figure 2.6.

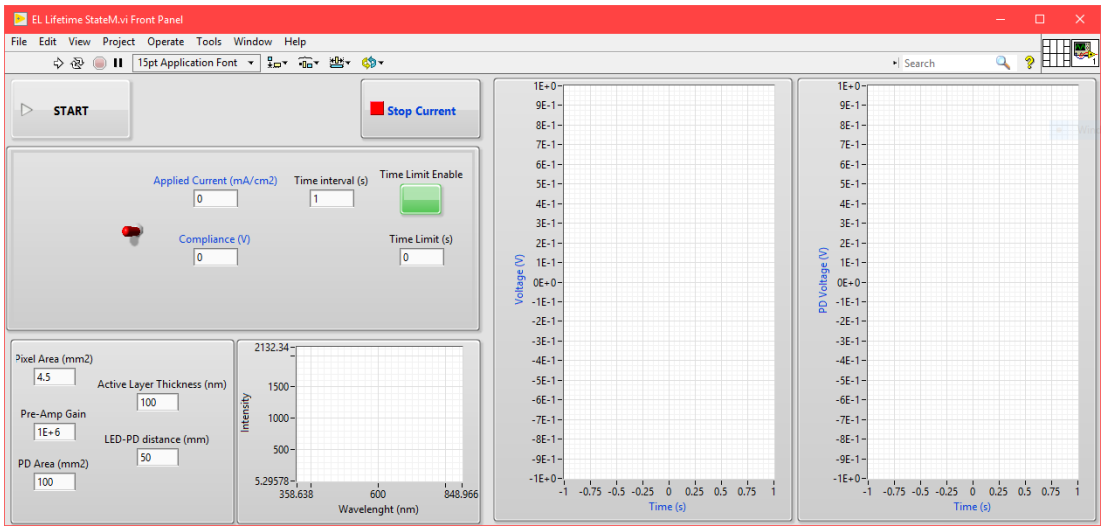

Figure 2.6 | LabVIEW software screenshot for the measuring of the OLEDs lifetime.

The red switch in the middle controls the strategy, either applied voltage or applied current density (illustrated). There is also the choice of carrying out the experiment for a predefined amount of time, as well as the time interval between measurements. In the unfortunate case of the diode breaking, the software has a safety feature that will terminate the measurement to avoid any further risks.

2.8 Near-infrared emission calculation

This is thesis is focused around near-infrared (NIR) emitting materials, so it is the author's view that the NIR emission of the materials is worth mentioning. In the tables and plots of Chapter 3 below, the "NIR PL and EL %" refer to the percentage of the emission of the sample that falls at $\lambda > 700\,\text{nm}$, that has been conventionally defined as the lower limit of NIR light.

2.9 Analysis

The analysis of the data collected was carried out using a variety of tools available. Initial analysis was done with LabVIEW, the same software that collected the

data and was used for the Keithley controls. η_{PL} calculations were initially performed with a combination of OriginPro and Microsoft Excel. Some LabVIEW routines were developed that allowed the automation of the calculation. A screenshot of the η_{PL} calculation software is shown in Figure 2.7.

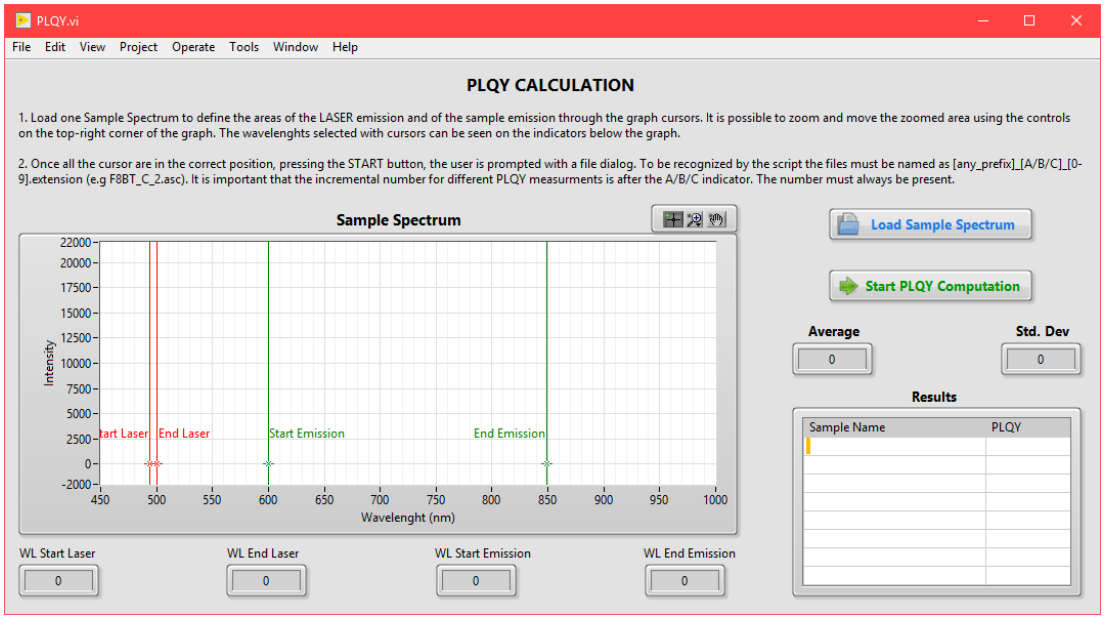

Figure 2.7 | LabVIEW software screenshot for the calculation of η_{PL}.

It is worth noting that the software of Figure 2.5 exported directly the data corrected for the response of the photodiode.

Further analysis was carried out using custom routines developed by the author in python 3.6 and above using a number of libraries (*e.g.* pandas 0.22, matplotlib 2.1.2, numpy 1.14) that resulted in full automation of numerous processes. All the Figures depicting data were plotted using python and matplotlib.

Some of the spectra presented in this thesis were noisy due to a low emission (both PL and EL, *e.g.* when collecting the OLED spectra at the V_{ON} or a low η_{PL}). Another issue that has been observed is some interference fringes at low energies ($\lambda > \sim 850\,\text{nm}$). To avoid such phenomena in the plots, a Savitzky–Golay filter was applied to the spectra using a 3rd degree polynomial and 51 points as parameters from the scipy library in python. [126]

3 | Porphyrin oligomers as highly efficient near-infrared emitters

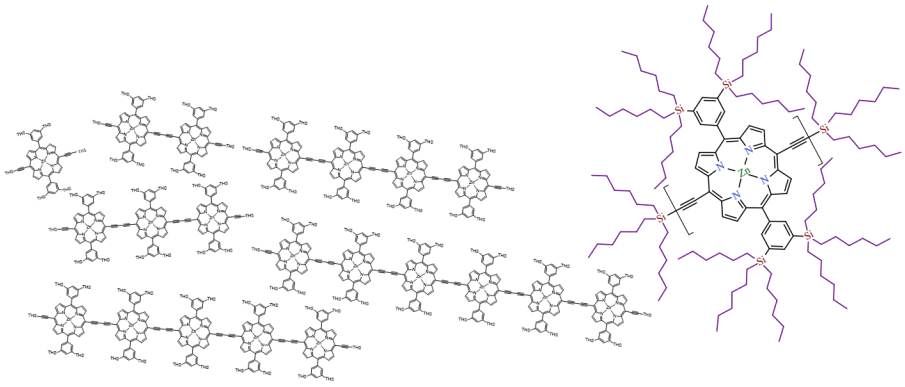

A collection of highly efficient, near-infrared emitting porphyrin oligomers employing novel, bulky sidechains were studied. Varying the length, coordinating metal or connecting bonds altered their emissive properties and embedding them in OLEDs resulted in unprecedented performance of external quantum efficiency.

3.1 Overview of the chapter

During the time of this research, the author carried out various experiments at different times. To better organise this chapter, the results presented below are organised in a better "story-telling" way, rather than chronological or significance order.

A series of zinc porphyrin oligomers with bulky sidechains, ranging from a monomer *l*-P1 to a long oligomer/polymer *l*-PN, are presented below. Among the oligomers tested is *l*-P6, a hexamer where special focus was given, as at the time of the first measurements in *ca* November 2015, in the beginning of the author's research, it gave the highest and most promising results. It also served as a direct comparison to a study that was previously published by our groups regarding a similar hexamer.

Another parallel study was about five different hexamers, whose difference is the coordinating metal at the centre of each porphyrin unit, a metal-free hexamer, two light metals - magnesium and zinc - and two heavy metals - platinum and palladium.

Lastly, a new pentamer was synthesised that had modified links between each unit, resulting in a shorter oligomer but with significantly red-shifted emission compared to the other oligomers, and very good performance.

All the porphyrin oligomers were synthesised in the laboratories of Prof. Harry L. Anderson, FRS in the Chemical Research Laboratory of the University of Oxford. The zinc oligomers and the five hexamers were synthesised by Dr. Ibrahim Bulut, although the hexamers were purified by Dr. Michel Rickhaus. The pentamer was synthesised by Dr. Lara Tejerina. The author attended training during a secondment placement in Oxford University that included the synthesis of the monomers incorporating the heavy metals, later to be polymerised and formed the hexamers characterised.

Porphyrins in this chapter were used in a donor-acceptor architecture (*vide infra*), with polymers being the donors and the porphyrins the acceptors. While a maximum effort was made to have completely comparable and consistent results in this chapter, certain factors were beyond the author's control. Such a factor was one polymer host material, F8BT, that was supplied by American Dye Source Inc (ADS). In this thesis, three different batches of F8BT from ADS where used as host, and unfortunately one of them, the one used in the majority of the experiments, was under-performing compared to the one used for the initial hexamer and novel pentamer experiments. While this does not seem to affect the efficiencies in either η_{PL} or η_{EL}, it is noted for clarity and for explanation of some

of the results presented below.[7] Furthermore, a second host used, PIDT-2TPD, was a polymer synthesised by Dr. Petri Murto in the laboratories of Prof. M. Anderson in Chalmers University, and given its "custom" nature, supply was not sufficient to cover all the experiments.

To sum up, the chronological order that took place for the experiments is the following:

1. Zinc hexamer characterisation (including photoluminescence quantum efficiency (η_{PL}) in solution of all the zinc oligomers) in blends with F8BT with good performance [8]
2. Zinc oligomer series (repeating experiments with the same hexamer as above) in blends with under-performing F8BT
3. Five hexamers with different coordinating metals in blends with under-performing F8BT
4. Acetylene-linked pentamer in blends with both F8BT batches and with PIDT-2TPD

While in the context of the present thesis the results are organised as:

1. Zinc oligomer series, including all the results of the hexamer characterisation in Section 3.3
2. Five hexamers with different coordinating metals in Section 3.4
3. Acetylene-linked pentamer in Section 3.5

The purity and authenticity of the synthesised compounds was verified by the synthetic chemistry group in Oxford prior to all the physical characterisation that was carried out in UCL. The characterisation included ^{1}H NMR spectroscopy, Maldi-ToF Mass spectroscopy, and also by recycling Gel Permeation Chromatography (GPC) by checking the retention times, and UV-VIS and PL spectroscopy. This process assesses the presence of shorter/longer oligomers. The final product has $>98\,\%$ purity as a result from the measurements from the aforementioned techniques. These data are typically included in the supporting information of publications (*vide supra*).

Further to the characterisation that was carried out in Oxford, another measure to verify the authenticity of the materials was to compare it with the

[7] After a long exchange of communication with ADS and a thorough attempt to identify the problem, this was impossible in the course of this thesis. A study on the η_{PL} and η_{EL} of the different batches was carried out under the exact same conditions and it was clear that the "good batch" was outperforming the "bad" by a factor of ~ 2 as pure material.

[8] *N.B.* Though all the η_{PL} measurements were later repeated before the rest of the zinc series characterisation.

existing literature for the same or similar compounds with measured purities and experimentally verified structure. Prof. H. L. Anderson and his group have a deep expertise in porphyrin synthesis and a few of the materials presented in this paper have also been characterised with other methods by other groups. By repeating similar measurements, *e.g.* absorption and photoluminescence experiments in dilute solution, similar spectra were observed for the dimer, tetramer and hexamer. [127, 128] Notably, the hexamer optical characteristics are similar to the ones obtained by another hexamer, albeit with different sidechains, in 2011 by our group. [87] Further to the optical properties, the oligomers also showed good agreement with [129] in terms of oscillator strength.

Details about the synthesis of the porphyrins have been extensively published by the group of Prof. H. L. Anderson in the past. The synthesis of the zinc porphyrin oligomers presented in Section 3.3 has been reported in [130, 131]. The synthesis of the oligomers studied in [127], that are similar to the ones studied in this thesis, has been published in [131–133] The synthesis of the platinum porphyrin hexamer in Section 3.4 can be found in [134], with further synthetic details to be published in the near future as the manuscript, including the data of the Section 3.4 is in preparation. The pentamer presented in Section 3.5 has been published in [135–137].

While it is important to have a good understanding of the synthetic processes, the characterisation and verification of the materials that are studied is beyond the scope and expertise of the author to reproduce and interpret NMR and mass spectroscopy results. The curious reader is kindly redirected to the cited papers above, and the references therein, in regards to the synthetic routes and methods followed to prepare the porphyrin oligomers of this chapter.

3.2 Porphyrins and their applications

The word porphyrin originates from the Greek word *πορφυρό* (*porphyró*) meaning purple / dark red. *Nomen est omen*, porphyrins display purple / dark red colours and red to near-infrared (NIR) emission, *i.e.* $\lambda > 700\,\text{nm}$. Porphyrin derivatives are met in Nature to harvest sunlight (chlorophyll) and mimic enzymes. [138–140] Furthermore, iron-coordinated porphyrins, called hemes but more commonly recognised as being part of the compound hemogoblin that is the red pigment in blood. Hemes are also responsible for the delivery of oxygen to various tissues. The chemical structure of Heme B is presented in Figure 3.1 below.

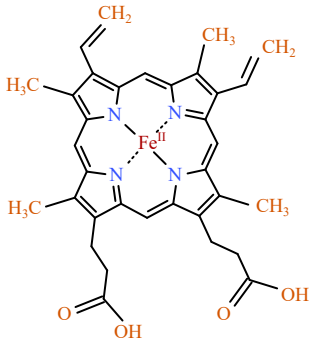

Figure 3.1 | Chemical structure of Heme B, a porphyrin found in the hemoglobin protein that transports oxygen to tissues.

Further to their presence in human biology and other applications in Nature, they are also a very interesting class of conjugated materials that shows remarkable optoelectronic properties, with applications for *in-vivo* photodynamic therapy [141, 142] and exhibit promising non-linear optical properties. [143] Porphyrins have also been used in dye-sensitised solar cells [24, 144–146] and as two-photon dyes. [147] Studies have also shown that porphyrin compounds can be used for NIR-to-vis up-conversion, a process that can prove useful in photovoltaics technology giving the possibility to capture the elusive NIR photons from traditional solid-state devices. [148] Nevertheless, the porphyrins are more commonly met in light-emitting applications, such as organic light-emitting diodes (OLEDs) (*vide infra*). Porphyrins also show an ease in the chemical synthesis allowing for some extraordinary structures to be created. Such approaches for the molecular design include ladder-type molecules [131, 149] to porphyrin 6-, 12-, 24-, 30- and up to 40- units (!) nanorings, giving rise to some astounding scanning tunnelling microscopy images (STM) such as the one in Figure 3.2. [87, 133, 150–154]

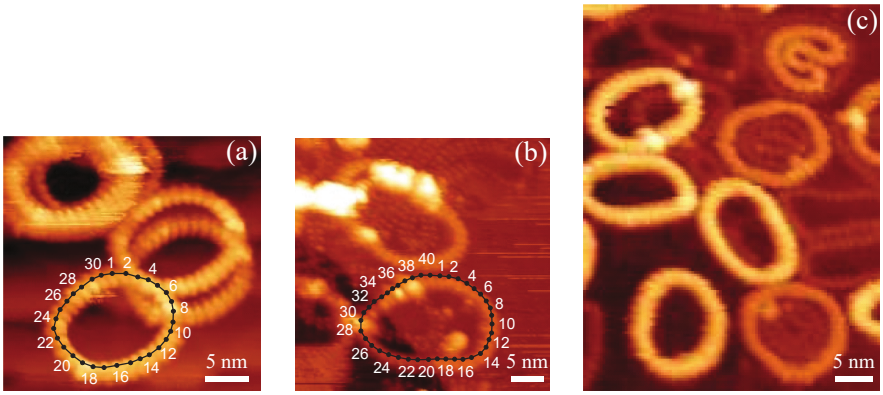

Figure 3.2 | Scanning tunnelling microscopy images of nanorings deposited on gold surfaces. (a) Shows a 30-unit nanoring with numbered the individual porphyrin units. (b) Shows a 40-unit nanoring with numbered the individual porphyrin units. (c) Shows some nested 30-unit nanorings. In all three the scale bars are 5 nm. Image reproduced and adapted from [152].

Their emission can be tuned from red to NIR and shows strong absorption bands in the visible (notably the Soret or B band) at *ca.* 400 − 550 nm. A series of lower energy bands spread to the NIR (notably the Q bands, Q_x and Q_y) starting from *ca.* 550 nm for the monomer and shifting to lower energies and increasing in strength with increasing length of the repeating unit. [129, 155] The B band originates from the $S_0 \rightarrow S_2$ transition, while the Q bands originate from the $S_0 \rightarrow S_1$ transition.

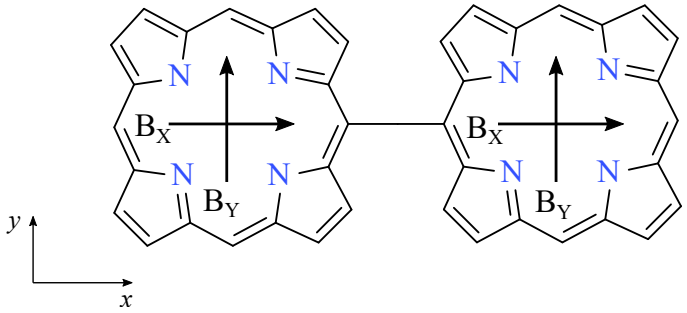

Figure 3.3 | Soret or B band transitions in a porphyrin depicting the B_x and B_y transition components. Image reproduced from [149].

The Soret band originates from two perpendicular components of the transition dipole moment, B_X and B_Y, as shown in Figure 3.3. If x is considered as the axis of the oligomer, the axis along which the porphyrins are joined, B_y transitions are parallel and face-to-face while B_x are head-to-tail. Transition dipoles of each type couple and as a result the excited state is split, where the B_x component, that is along the porphyrin chain, is the low-energy component and the B_y, that is in the same plane but perpendicular to the chain, is the high-energy. The B_x band is unaffected by the torsional orientation in the solid state

and stills gives rise the Soret band. [149] Similarly to the Soret band, the Q band is split into two components at $n > 1$, where n is the number of porphyrin units in the chain. The lower-energy is parallel to the axis of the porphyrin Q_x and the high-energy is perpendicular to the chain Q_y.

Porphyrins are highly luminescent molecules, with various reports declaring very high efficiencies. [92, 101, 133, 155, 156] Typical applications in light-emission are OLEDs, and given the porphyrins tunability in the emission, their electroluminescence (EL) peaks in the range starting $\sim 650\,\text{nm}$ up to $> 900\,\text{nm}$. [87, 92, 93, 101, 102, 155, 157, 158]

The zinc porphyrin oligomers presented in this thesis were also highly fluorescent, exhibiting some of the highest values of photoluminescence quantum efficiency (η_{PL}) in solution reported. When embedded in OLEDs as NIR emitting guests, the oligomers exhibited the highest reported electroluminescence external quantum efficiency (η_{EL}) to date[9], in the respective spectral range, for a "heavy-metal-free" compound. Their peaks of emission spanned for the monomer from $\sim 650\,\text{nm}$ and showed bathochromic shift with increasing length of the oligomers, up to $> 800\,\text{nm}$ for the longest oligomers studied.

The *meso*-butadiyne linked-, zinc-, linear- porphyrin oligomers (l-Pn), along with the five different hexamers and the novel pentamer that were studied and are presented in this thesis, were synthesised by the group of Prof. H. L. Anderson FRS at the Chemistry Research Laboratory of the University of Oxford. [130, 131] During the synthesis of the platinum and palladium compounds, the author was present as part of a secondment placement at the University of Oxford to be trained in chemical synthesis.

[9] From the first measurement in early 2016 up to the time of the writing, late 2018-early 2019, the results presented in this thesis are the "record" efficiencies for heavy-metal-free, fluorescent, NIR emitters.

3.3 Zinc porphyrin oligomers

3.3.1 Solution photoluminescence of zinc porphyrin oligomers

Aggregation prevention in the oligomers studied previously was based in the metal-coordinating additive pyridine. [87] Differently from the porphyrin oligomer studied by our groups in 2011 [87], the oligomers were modified by adding bulky trihexylsilyl (THS) chains to the aryl groups that offer a large steric hindrance to prevent aggregation and its chemical structure is shown in Figure 3.4.

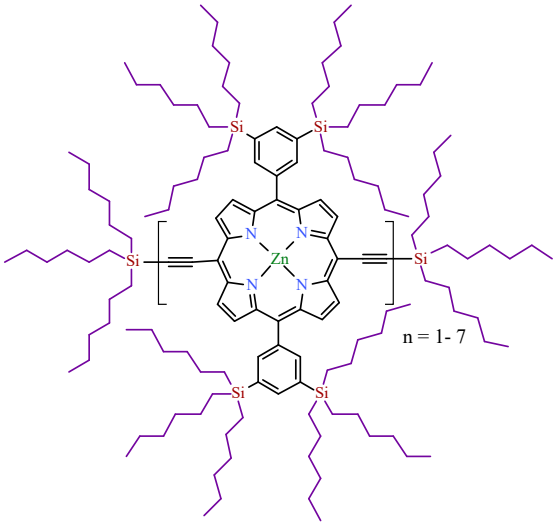

Figure 3.4 | Chemical structure of the porphyrin used in this thesis with the bulky THS side chains highlighted in purple.

The main spectral component of the absorption spectra are the B and Q bands (*vide infra*). The B band spread in the blue-green part of the spectrum for all porphyrin oligomers, increasing in width but shows little spectral shift among the oligomers. It spanned between $400 - 550\,\text{nm}$ and is created by the transition $S_0 \rightarrow S_2$. The Q_x band is experiencing some more dramatic changes with a strong bathochromic shift and an increase of the oscillator strength, as expected. [159] The alignment of the corresponding dipole moment and the extended conjugation are the main reasons for these phenomena. [128] It also showed an overall broadening because of the freedom of the porphyrin units in the chains to rotate around the *meso*-butadiyne links. [128, 132] The spectra of the novel series of linear porphyrin oligomers in toluene solution are shown in Figure 3.5.

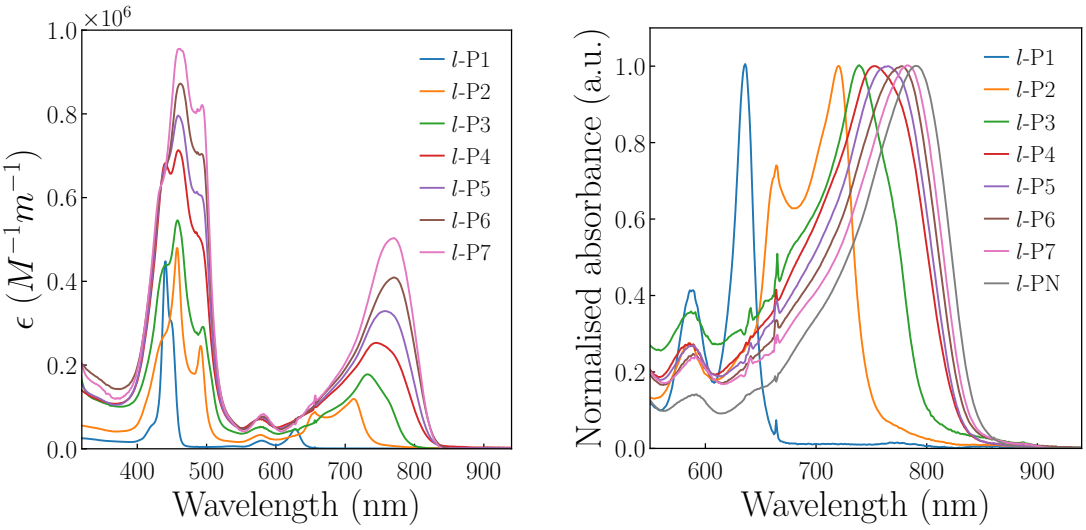

(a) Extinction coefficient (ϵ) **(b)** Normalised absorbance

Figure 3.5 | (a) Extinction coefficient and **(b)** normalised absorbance of the zinc porphyrin oligomers focused in the Q bands, in dilute anhydrous toluene solution ($\sim$ µg/ml). Note the gradual increase in intensity and red-shift of the Q_x band from the monomer to the heptamer. The extinction coefficient of *l*-PN is missing, as it is a polymeric oligomer with not a precisely fixed length, calculating its molecular weight is difficult, as it is tracing back to the synthesis batch of this specific compound. The ϵ data were supplied by Dr. I. Bulut from the University of Oxford.

It is visible from Figure 3.5a that the oscillator strength (f) increased with increasing number of porphyrin units in both absorption Soret (or B) and Q bands. This is thanks to the alignment of the dipole moment along the x axis of the oligomer and the extend conjugation. [155] To further enhance this claim, the oscillator strength for the Q_x transition was calculated and is plot in Figure 3.6 below.

The oscillator strength, f, is a measure for the strength of an optical transition and can has been defined as:

$$f = \frac{mc}{\pi e^2 n} \int \sigma'(\nu) d\nu \tag{3.1}$$

where σ' is the absorption cross section and $\sigma' = 3.82 \times 10^{-21} \epsilon$, where ϵ is the extinction coefficient.

The oscillator strength can therefore be calculated using the experimentally defined measurements, *i.e.* the extinction coefficient and wavenumbers as:

$$f = \frac{4.39 \times 10^{-9}}{n} \int \epsilon(\nu) d\nu \tag{3.2}$$

For the calculation of f, the integration considers only the specific transition, Q_x, by deconvolving the spectrum.

The oscillator strength (f) showed a linear increase with increasing oligomer length and is in agreement with previous studies that calculated (f) for similar oligomers. [129] The (f/N) is also plotted to show the evolution of f per number of units, which interestingly showed the same increase from monomer to dimer as in ref. [129].

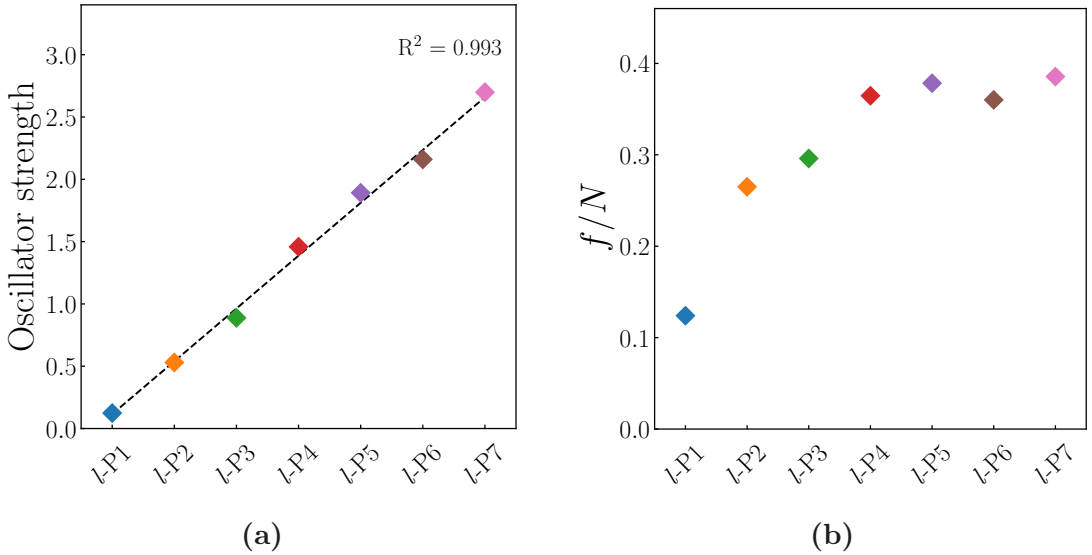

Figure 3.6 | **(a)** Oscillator strength for the Q_x band of the porphyrin oligomers and **(b)** oscillator strength per porphyrin unit. The l-PN value is missing as the extinction coefficient was also missing that was needed for the calculations. The R^2 value of the linear fit is also plotted to show the linear increase of the oscillator strength with increasing number of units.

The spectral position of the high-energy Soret band was practically stable in the region $400-550$ nm, while the low energy Q_x band red-shifts with increasing length of the oligomer from 630 nm for the monomer l-P1 to $\sim$ 800 nm for l-PN, as highlighted in Figure 3.5b thanks to the extended conjugation along the oligomer. [155] The observed broadening of the Q_x is attributed to a torsional heterogeneity of the units that are free to rotate. [128, 132] Contrarily, Q_y seemed spectrally stable at $\sim$ 580 nm and "saturates" in intensity at the tetramer and above.

Following with the emissive properties of these compounds, the emission of the zinc porphyrins studied is originating from the S_1, as internal conversion from $S_2 \rightarrow S_1$ is very fast. [129] Twisted conformers that are excited to S_1, planarise before the emission within a $\sim$ 100 ps timescale. [128, 132, 160] Consequently, fluorescence spectra in solution, presented in Figure 3.7a, displayed a narrow high-energy peak that red-shifts with increasing oligomer length from *ca.* 630 nm for l-P1 to $>$ 800 nm for l-PN.

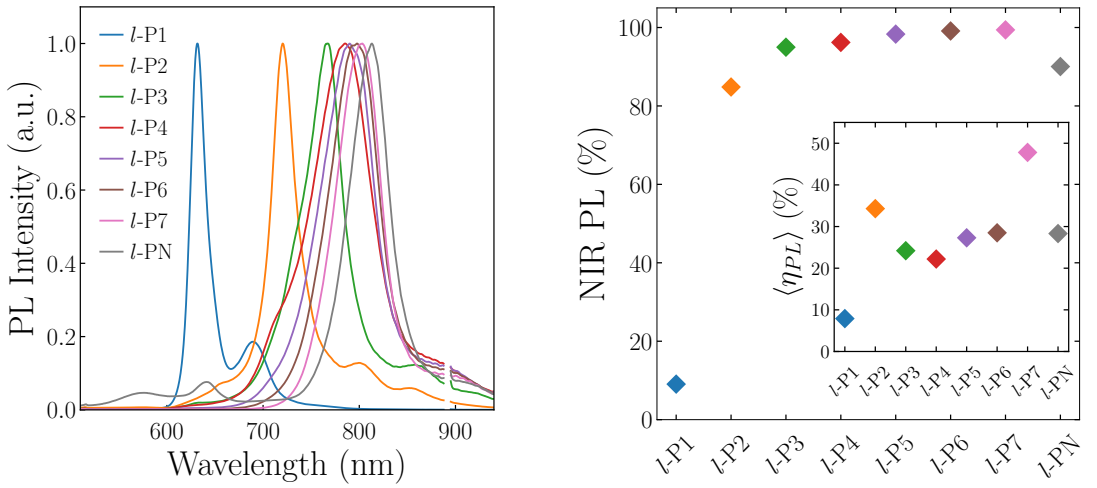

(a) Normalised photoluminescence **(b)** NIR emission and η_{PL}

Figure 3.7 | (a) Normalised photoluminescence spectra of the zinc oligomers. **(b)** % of the photons emitted at $\lambda > 700\,\text{nm}$. **(b) inset** Absolute photoluminescence quantum efficiency (η_{PL}) results measured as described in Section 2.4 above and according to [122]. The spectra, NIR PL calculations and η_{PL} measurements were carried out following excitation at 450 nm at room temperature in dilute toluene solution ($\sim$ µg/ml). The missing part in (a) of the spectrum at 890 nm is to remove the second order of diffraction of the excitation laser in our spectrometer.

Since these molecules are termed "NIR emitters", it is noteworthy that for $n > 2$, the oligomers emitted $> 96\,\%$ of the photons in the NIR and practically $100\,\%$ for the *l*-P6 and *l*-P7, as shown in Figure 3.7b. The zinc monomer *l*-P1 had only $\sim 10\,\%$ in the NIR, while the dimer exhibited $> 80\,\%$ NIR emission. Interestingly, *l*-PN showed some increased emission in the green-red, attributed to possible degradation of the material, or decomposition of the longer chains to shorter oligomers, or simply given its nature of polymeric, to some shorter oligomers that "escaped" purification and are within the polydispersity. Those peaks are shown in Figure 3.7a and highlighted at the drop of the NIR emission to $\sim 90\,\%$ in Figure 3.7b. In all oligomers, a secondary vibronic peak was displayed in the low-energy part of the peak.

In the inset of Figure 3.7b are presented the photoluminescence quantum efficiency (η_{PL}) results. The oligomers were measured in dilute toluene solution ($\sim$ µg/ml), in air and at room temperature according to the procedure reported in [122] and described in Section 2.3. *l*-P2 and *l*-P7 showed impressive results with $\langle\eta_{PL}\rangle = 34.3 \pm 0.7\,\%$ and $\langle\eta_{PL}\rangle = 47.8 \pm 0.6\,\%$ respectively. The monomer was surprisingly low at only $\langle\eta_{PL}\rangle = 7.9 \pm 0.2\,\%$. *l*-P6 that was of special interest due to the direct comparison with a previous study, yielded $\langle\eta_{PL}\rangle = 28.5 \pm 1.5\,\%$. As it is visible from the plot in Figure 3.7b, the oligomers "saturate" at $\langle\eta_{PL}\rangle \sim 24\,\%$ excluding *l*-P7 being somewhat of an outlier compared to the rest of the series,

with *l*-P7 increasing the average to $\langle \eta_{PL} \rangle \sim 27\,\%$. Notably, all oligomers outperformed the monomer by ≥ 3 times on average. Interpreted differently, an increase of η_{PL} with decreasing energy gap (E_G) is observed, a direct contradiction with the E_G law. The E_G law predicts that chemically similar materials are expected to show an exponential increase of the non-radiative rate due to an increased overlap of the vibrational manifolds of the ground and excited states. [81] The values presented can be found in Table 3.1, and a more detailed view in Table A.1.

It is worthy to note that a sample of the same P6 linear hexamer that was published by Fenwick et al. [87], with 3,5-bis(octyloxy)phenyl (OCT) sidechains instead of THS, was tested alongside the rest of the zinc oligomers. Not surprisingly, by avoiding the metal coordinating pyridine, the P6(OCT) yielded a $\langle \eta_{PL} \rangle = 6.7 \pm 0.6\,\%$ in dilute toluene solution. This showed the beneficial role of the bulky THS sidechains in minimising aggregation by the large steric hindrance they afforded.

To test further the claim of the beneficial role of the THS sidechains, pure porphyrin zinc pentamer and hexamer were spin coated on spectrosil substrate to form thin films. The porphyrins were not luminescent enough in pure films to have a measurable η_{PL}, however, it was possible to collect a spectrum and to compare it to a 4-benzylpyridine (BP) containing. Using a 4 % loading of BP in the solution, no noticeable increase in the luminescence of the films was observed as to be measurable for η_{PL} experiments. What was interesting, however, was the stark difference in the spectra of the two oligomers, with and without the BP, as noted in Figure 3.8. It is evident that the addition of BP alters the film formation, causing a significant bathochromic shift of the emission, but more importantly an intense peak in the red at $\sim 640\,\text{nm}$, in agreement with the peak of the emission of the monomer, *l*-P1. [10]

Following these results, BP was discounted from being used further in the experiments and pure film PL was not investigated, owing also partially to the limited quantity that was synthesised.

[10] These tests were carried out at the very beginning of the study, immediately prior to the commencement of the author's appointment at UCL, by Dr. Alessandro Minotto. The purpose was to have an immediate comparison between the pure film PL performance since a good performance was expected from the addition of the THS sidechains. Unfortunately, the films were not luminescent enough to have a measurable η_{PL}, so following the previous study strategy, BP was used to assess the possible advantages.

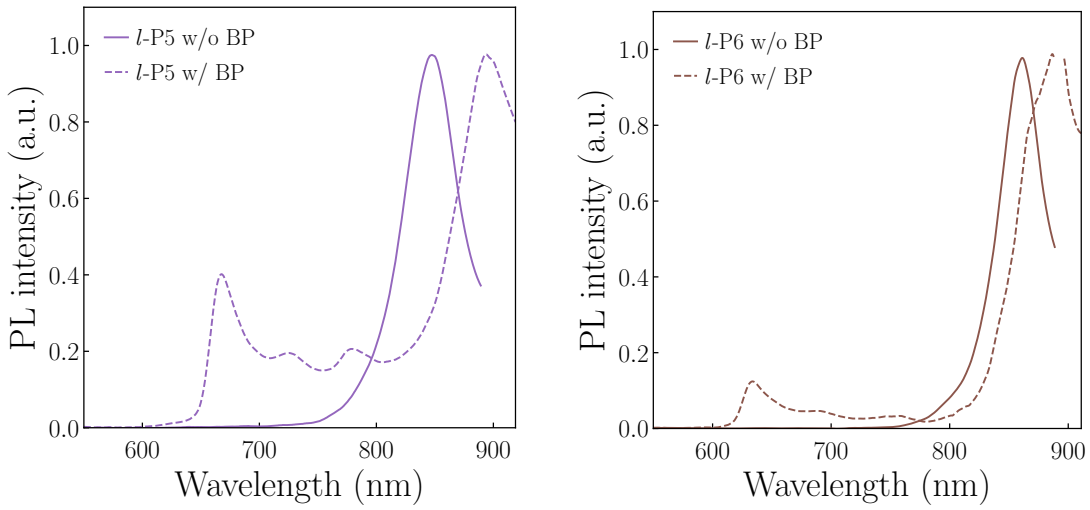

(a) *l*-P5 w/ and w/o BP **(b)** *l*-P6 w/ and w/o BP

Figure 3.8 | Photoluminescence spectra of **(a)** *l*-P5 and **(b)** *l*-P6 spin coated in thin films with and without the use of the metal coordinating additive 4-benzylpyridine (BP). Solid lines refer to the spectra without the use of BP, dotted lines refer to the spectra with the addition of BP.

One can gain further insights on the radiative processes by collecting time-resolved photoluminescence spectra using time-correletated single photon counting (TCSPC). In Figure 3.9 are presented the time-resolved PL spectra in a 2-D contour plot. The decays at the respective maxima of each emission are plotted, the bi-exponential tail fits and the residuals are plotted in Figure 3.10. The experimental setup allowed for the option to choose between a time limit or a maximum number of counts before stopping collecting data. In the interest of having quantitatively comparable data, all the maps were collected using a time window of 900 s and every 10 nm. This way, one can plot the emission spectrum at different time delays.

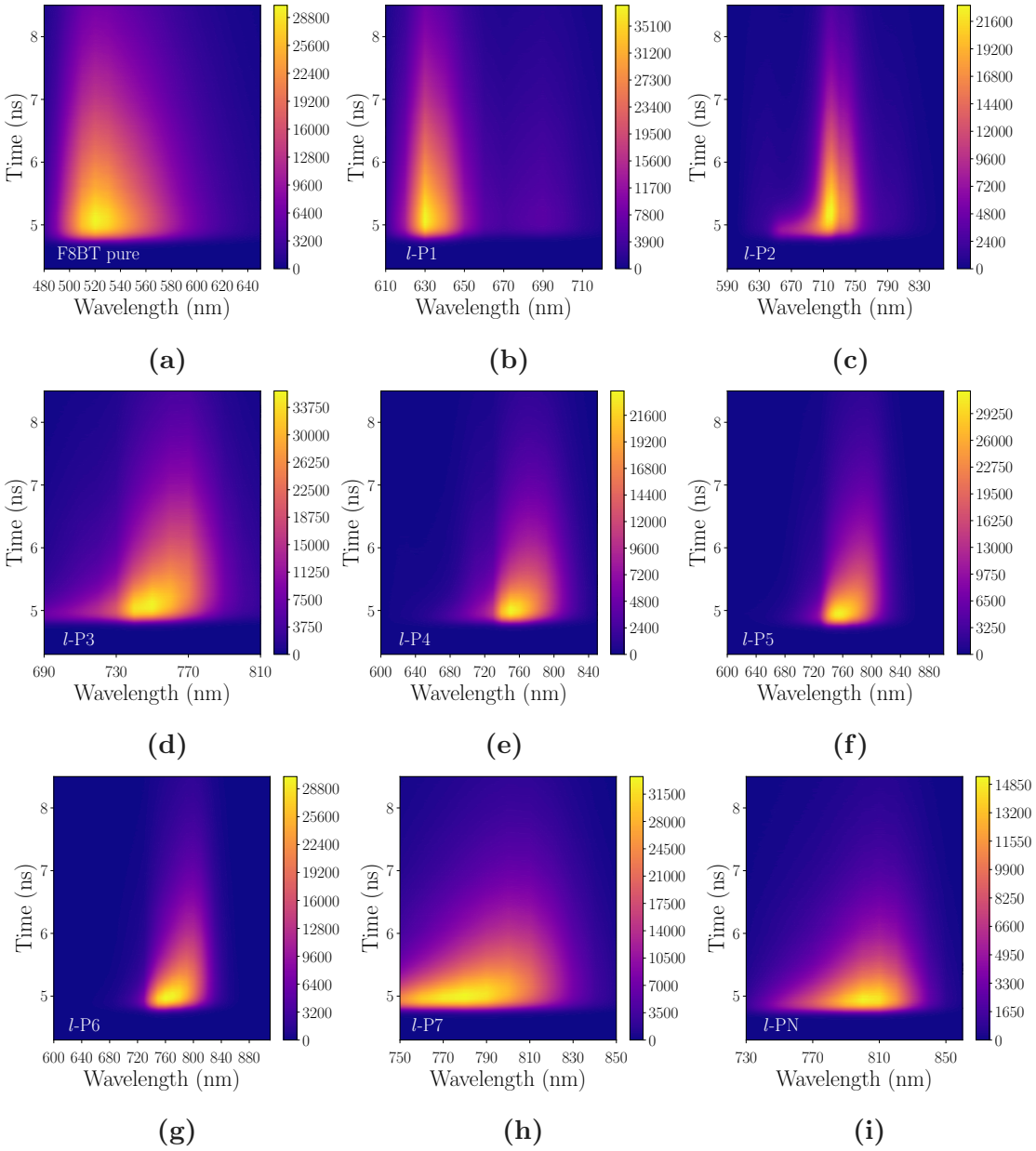

Figure 3.9 | TCSPC time decay contour plots of the oligomers in dilute toluene solution ($\sim$ µg/ml). The time scale all the spectra is from 4.3 ns to 8.5 ns confirming the fluorescence emission of the oligomers. The colour scales are counts. The spectra were collected integrating for 900 s for each wavelength. The $\Delta\lambda$ of the collection was set to 10 nm and the time decays were collected every 10 nm, with a repetition rate of the 450 nm picosecond laser allowing a time window of 50 ns.

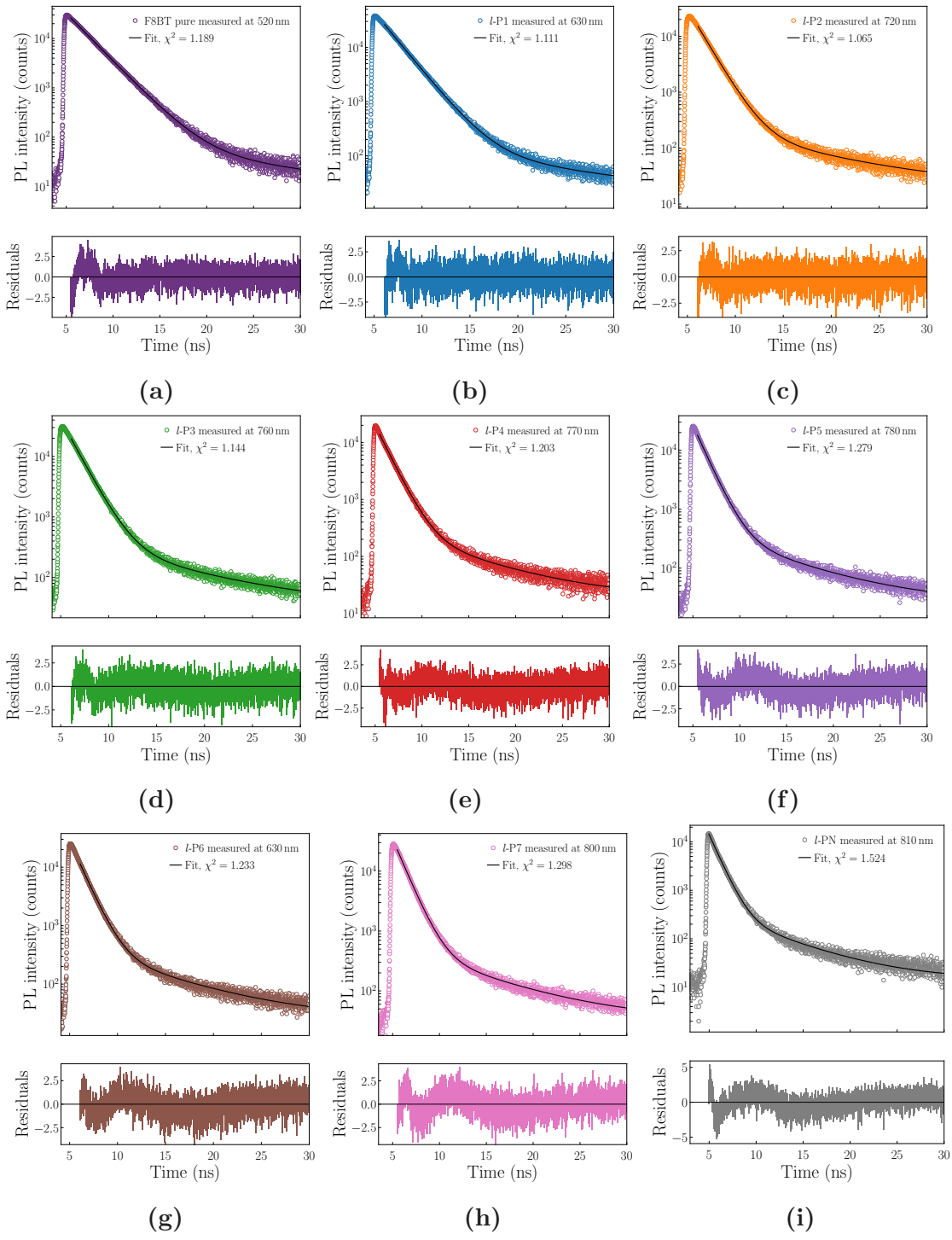

Figure 3.10 | TCSPC time decay plots of the oligomers in dilute toluene solution ($\sim$ µg/ml). Each decay was measured at the respective maximum of the emission. For each decay, the respective tail fit is shown with black solid line and the corresponding goodness of the fit (χ^2) is noted. Below each plot are the weighted residuals of the fit. The time scale all the spectra is from 5 ns to 30 ns. The spectra were collected integrating for 900 s for each sample.

All the figures of Figure 3.9 confirmed a singlet emission since all were in

the $\sim$ ns time regime *i.e.* fluorescence emission. By fitting the PL decay at the relative maxima of emission, one can extract the lifetime, a procedure described in 2.5. All the decays were fitted with a bi-exponential decay, as presented in Figure 3.10, and the respective residuals are shown below each decay.. In Figure 3.11 are presented the calculated lifetimes and the radiative and non-radiative rates for each oligomer. As it is noticeable in Figure 3.11a, the lifetime decreased from $\sim$ 2 ns for the monomer to *circa* half, 1 ns, for the longest oligomer, as a results of the increase of both radiative (k_r) and non-radiative (k_{nr}) rates (*vide infra*).

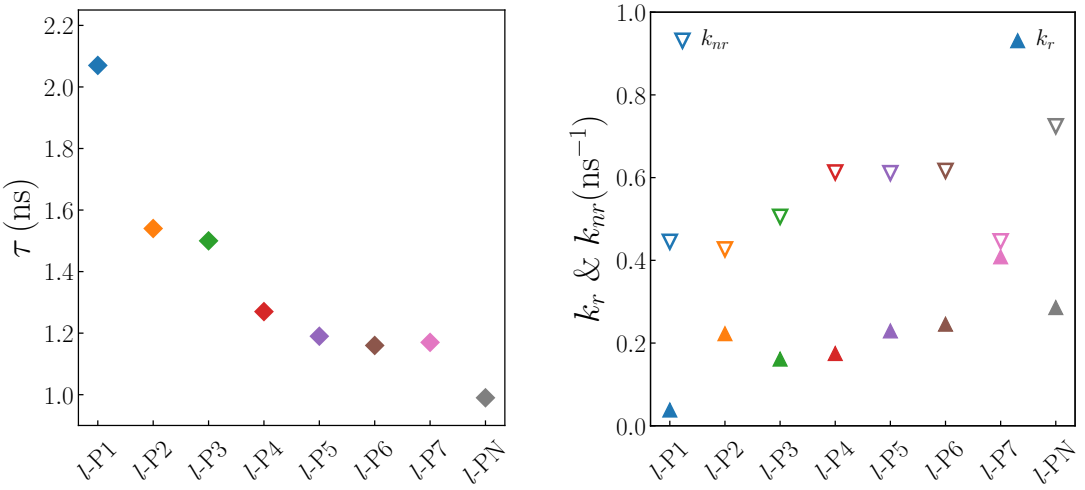

(a) PL lifetime **(b)** Radiative and non-radiative rates

Figure 3.11 | (a) Calculated photoluminescence lifetime (τ) for the zinc oligomers. **(b)** Calculated radiative and non-radiative rates (k_r and k_{nr} respectively) for the zinc oligomers. The lifetime measurements were carried out following excitation at 450 nm at room temperature in dilute toluene solution ($\sim$ µg/ml), using the same solutions as for the η_{PL} measurements reported above.

By considering the η_{PL} values that are presented in Figure 3.7b, the values for k_r and k_{nr} can be calculated and are presented in 3.11b. These values served as direct contradiction to what is expected by the energy gap (E_G) law (*vide infra*). The E_G law predicts an increasing k_{nr}, from an efficient internal conversion (IC) $S_1 \rightarrow S_0$, with a decreasing energy gap, *i.e.* red-shift of the emission. This would result in a decrease of the η_{PL} that was not experimentally confirmed.

By changing the oligomer lengths, the chemical properties are significantly impacted, with an increase of both the oscillator strength and the spatial delocalisation of the first singlet excited state (S_1). Therefore, the increasing trend of the k_{nr}, presented in 3.11b, is attributed to a concomitant suppression of intersystem crossing (ISC). It is expected that ISC is suppressed with increase

oligomer length as a result of the increasing spatial difference between singlet and triplet excited states. [53, 155, 161]

Further corroborating the argument of these oligomers being a good-performing NIR emitter, there is an increase of k_r with increasing oligomer length, resulting in more efficient NIR emitters as the oligomers elongate. Overall, both increasing η_{PL} and the singlet nature of the oligomers emission result in promising materials to be further studied, and contribute to achieving the highest reported electroluminescence external quantum efficiency (η_{EL}) when incorporated in OLEDs, as presented below.

3.3.2 Solid-state photoluminescence of zinc porphyrin oligomers

Prior to fabricating and characterising OLEDs, solid-state photoluminescence performance of the oligomers is needed. Despite the bulky THS sidechains, the oligomers were poor emitters in the solid state as pure materials, with spin-coated films showing large aggregates, even by naked eye. Photoluminescence experiments showed that their emission was below the detection threshold of our detector, *i.e.* their emission was almost entirely quenched due to concentration quenching.

It was, therefore, necessary to identify a suitable material to be used as host, with good charge transport and optical properties, allowing for a good spectral overlap and efficient Förster resonant energy transfer (FRET) from the polymer host to the oligomer guest, a usual strategy to avoid concentration quenching. [162] From the different commercial polymers available in our laboratories, poly[(9,9-dioctylfluorenyl-2,7-diyl)-*alt*-(4,4'-(N-(p-butylphenyl))diphenylamine) (TFB) and poly[(9,9-di-n-octylfluorenyl-2,7-diyl)-*alt*-(benzo[2,1,3]thiadiazol-4,8-diyl)] (F8BT) where chosen as the ones with the best spectral overlap, as illustrated in Figure 3.12a below, where the emission of F8BT and TFB in thin films is presented, and the absorption spectrum of *l*-P6. The chemical structures of both polymers is also illustrated in Figure 3.12b. As mentioned above, the B band showed little spectral shifting with varying oligomer length, while only Q_x showed the pronounced bathochromic shift. Therefore, both polymers were the best options for their respective emission spectra. TFB was chosen for its significant PL overlap with the oligomers B band, while F8BT due to its spectral overlap with the Q bands manifold, mainly the Q_y. The F8BT had the twofold advantage of being the polymer host in some previous works from our group, thus providing some valuable expertise in the characterisation, and as it is shown below in Figure 3.19, a better HOMO-LUMO alignment with the NIR emitters resulting in a type-I or quasi type-I heterojunction. [95, 163]

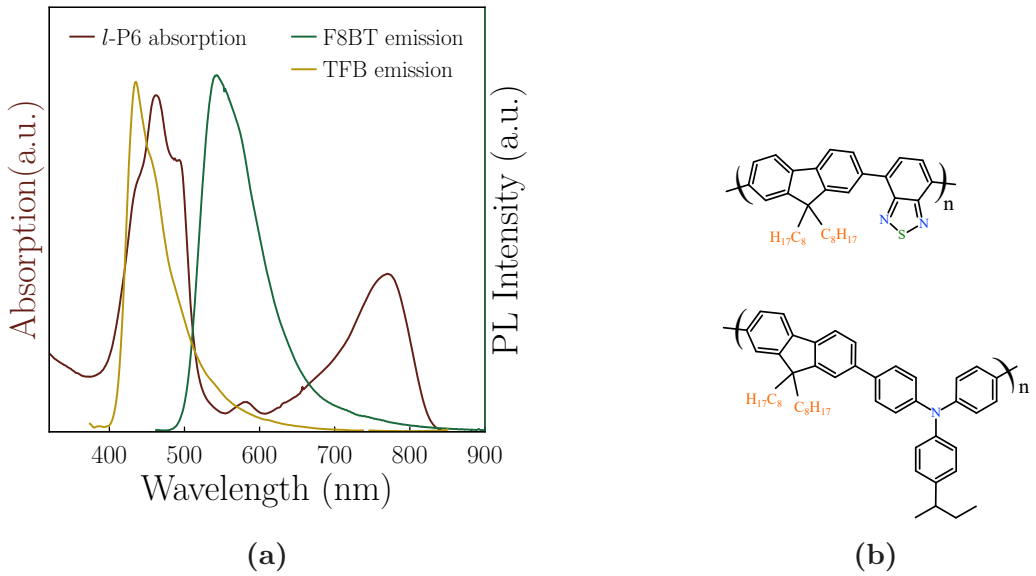

(a) **(b)**

Figure 3.12 | **(a)** *l*-P6 absorption (red) in dilute toluene solution and the two polymer hosts photoluminescence, F8BT (green) and TFB (yellow) in thin films. It is evident the good spectral overlap between the hosts emission and the guest absorption. **(b) top:** poly[(9,9-di-n-octylfluorenyl-2,7-diyl)-*alt*-(benzo[2,1,3]thiadiazol-4,8-diyl)] (F8BT) and **bottom:** poly[(9,9-dioctylfluorenyl-2,7-diyl)-*alt*-(4,4'-(N-(p-butylphenyl))diphenylamine) (TFB) chemical structures structures.

F8BT is a green emitter, a polyfluorene derivative with high $\langle \eta_{PL} \rangle$ values in solid state, with values of *circa* 60 % and 100 % in solution (*vide infra*). First reported by Janietz *et al.* in 1998, polyfluorene and its copolymers quickly became popular for light-emission applications. [164, 165] It is one of the most widely studied polymers in light-emitting devices, with good electron and transport properties exhibiting hole and electron mobilities on the order of $10^{-3}\,\mathrm{cm^2\,V^{-1}\,s^{-1}}$ and $10^{-4}\,\mathrm{cm^2\,V^{-1}\,s^{-1}}$ respectively, and a low-lying lowest unccupied molecular orbit (LUMO) at $\sim 3.3 - 3.5\,\mathrm{eV}$ below vacuum. [166–169] On the other hand, TFB, another polyfluorene derivative, has its emission higher than F8BT, at the blue region and has been extensively studied as an interlayer, rather than a host material. [38, 163, 170–173] There are, however, studies that have used TFB as a host material, but are not that common. [174] It has a $\langle \eta_{PL} \rangle$ value at $\sim 25\,\%$ in thin films, about half that of F8BT.

Knowing the effects of high concentration to the photoluminescence of the oligomers, the loading of the oligomers in the two hosts (F8BT and TFB) was kept low, allowing for efficient light emission, but high enough to quench the host photoluminescence and obtain significant NIR emission. The blends investigated were *host*:*l*-Pn 1.0, 2.5 and 5.0 $w/w\,\%$, *i.e.* 99 parts of host polymer, 1 part of guest oligomer was blended for the $1.0\,w/w\,\%$, *etc.* The blends are all weighted and made by adding the required volume of 10 mg/ml solution of oligomers, to

the required volume of equally 10 mg/ml solution of polymer host. The process of solution preparation is explained in Chapter 2. The blended solutions were subsequently spin coated to form thin films of $\sim$ 100 nm thick. It is noteworthy that, given the chronological order of the experiments carried out and the special attention given to the hexamer, both lower and higher concentration of the F8BT:*l*-P6 blends were explored, but the results obtained were not satisfactory and are therefore omitted from this thesis, to maintain a uniformity between all the oligomers. [11]

The absorption spectra of F8BT:*l*-P6 and TFB:*l*-P6 are presented in Figure 3.13 below. Since the spectra were dominated by the absorption of the polymer host in both F8BT and TFB matrices, only the *l*-P6 spectra are presented to maintain some simplicity. Also, as already mentioned, *l*-P6 was investigated further in OLEDs.

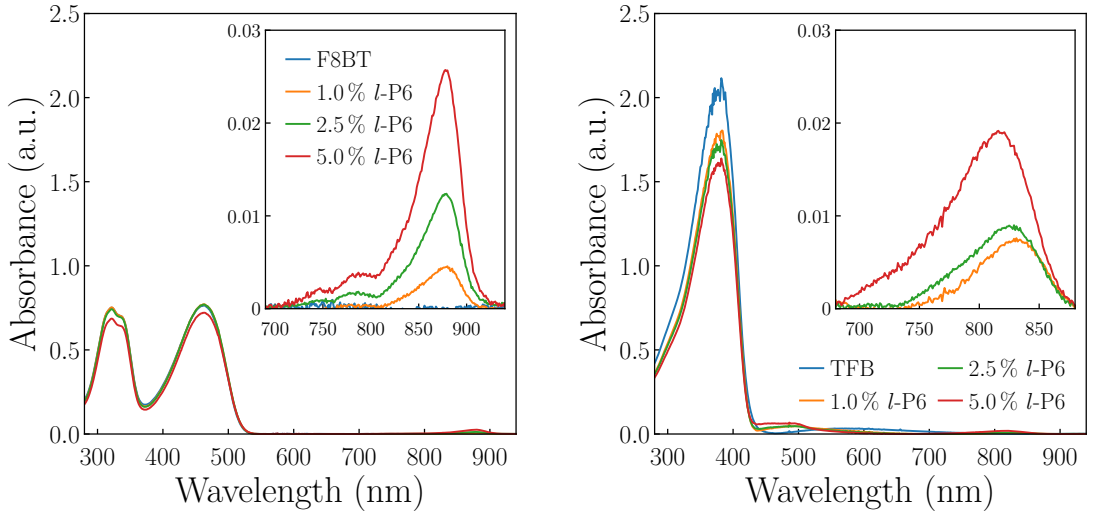

(a) F8BT:*l*-P6 absorption

(b) TFB:*l*-P6 absorption

Figure 3.13 | (a) F8BT:*l*-P6 and **(b)** TFB:*l*-P6 absorption spectra. The insets in both are a "zoomed" view of the Q_x absorption band of the oligomers in the 700 − 900 nm region.

In the F8BT:*l*-P6 absorption (Figure 3.13a), the two distinctive F8BT components are present at 325 nm and 450 nm, whereas the Q_x components of the oligomer were at 800 − 900 nm region. Compared to the solution absorption (Figure 3.5), a $\sim$ 100 nm red shift is observed, attributed to a more planar conformation of the oligomer in the polymer matrix. Also, the higher energy

[11] However, in the interest of reporting them, the lowest loading of F8BT:*l*-P6 0.5 % exhibited a higher $\langle \eta_{PL} \rangle = 32 \pm 3$ % than the rest of the loadings but with a significantly lower NIR emission (35 %) given the low loading, and F8BT:*l*-P6 10 % exhibited a noticeably reduced $\langle \eta_{PL} \rangle = 3 \pm 1$ % but higher NIR emission (85 %). Also, when explored in OLEDs, the results were not comparable to the rest of the blends, as presented and explained below.

peaks, present only in the solid state, are attributed to a reduced torsional heterogeneity compared to the solution. When the oligomers are in solution, they are free to rotate around the butadiyne links. [128] In a previous study, it was found that oligomers that have their torsional degrees of freedom restricted (*e.g.* in a high viscosity solvent) tend to show distinct absorption features in the Q band, something observed in the spectra of the F8BT:*l*-P6 blends that the oligomer was blended with a polymer and spin coated. [132]

TFB:*l*-P6 spectra (Figure 3.13b) showed a similar behaviour, dominated by the single absorption feature of TFB at $\sim$ 370 nm. However, *l*-P6 Q_x band was slightly blue shifted compared to the F8BT ones, attributed to the different planarisation of the oligomer in the solid solution. Not surprisingly, though, in both F8BT and TFB blends, an increasing loading of the oligomer resulted in increasing intensity of the Q_x band.

Moving to the photoluminescence of the blends, the spectra showed more interest than the absorption, with more pronounced differences between oligomers. The F8BT:*l*-Pn blends spectra are presented in the panel of Figure 3.14 below. All the spectra have been normalised for the emission of the porphyrin. This highlights the effect of increasing loading of the oligomers in the polymer matrix in all but F8BT:*l*-PN in Figure 3.14h. It is therefore confirmed that there is efficient FRET from the polymer host to the oligomers, and while it is not perfect, F8BT emission is gradually quenched.

However, in the case of F8BT:*l*-P7 (Figure 3.14g), and more pronounced in the case of F8BT:*l*-PN (3.14h), the effect of increasing concentration doesn't quench significantly F8BT PL. This fact is attributed to the increased length of the oligomers, especially for *l*-PN, that increases the average distance between chromophores resulting in reduced efficiency of FRET.

It is important to note that the oligomers showed an $\sim$ 80 nm red-shifted emission compared to the PL in solution (Figure 3.7a). This is attributed partially to an increased planarity that resulted in increase of the conjugation length and to signs of aggregations. It is also noteworthy that the oligomers showed a minimal Stokes' shift that is a sign of rigidity of the oligomers in the polymer, something observed in porphyrin oligomers and ladder-like polymers but, also, to a dipole coupling in a J-Aggregate-like formation. [160, 175, 176]

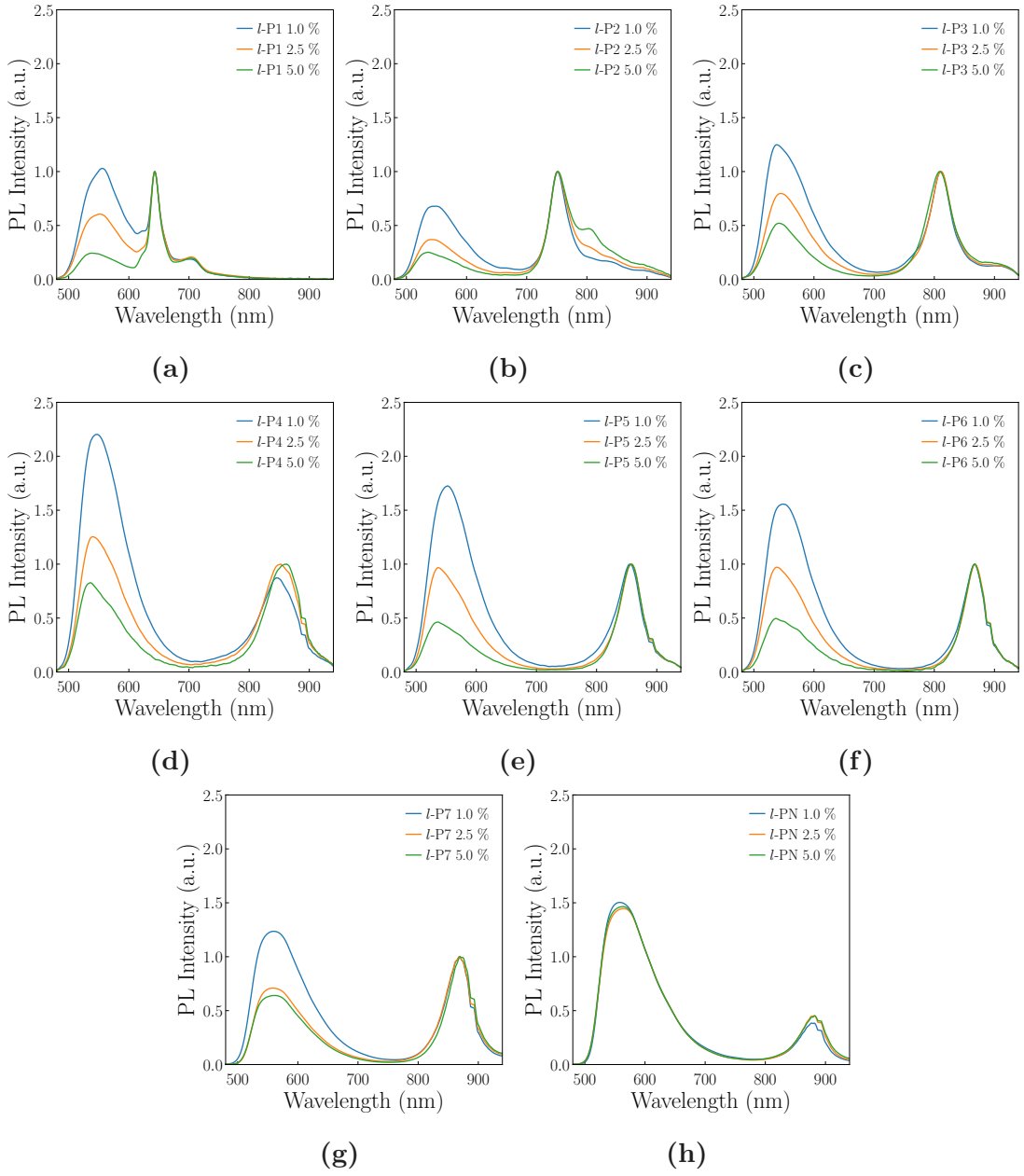

Figure 3.14 | (a) - (h) Photoluminescence spectra of the oligomers in blends with F8BT spin coated on glass spectrosils ($\sim$ 100 nm thick) collected outside the integrating sphere using a 445 nm diode laser. All the spectra have been normalised for the oligomers emission to highlight the gradual quenching of the F8BT host in favour of the guest emission. blue represent the F8BT:*l*-Pn 1.0 % loading, yellow the 2.5 % and green the 5.0 %. Both x and y scales are the same in all plots to facilitate comparisons. The small "bump" in some plots ((d) through (h)) at $\sim$ 890 nm is the second order of diffraction of the excitation laser (445 nm).

Another important factor considered when studying PL of blends is both the η_{PL} and the % of photons emitted in the NIR that are presented in Figure 3.15 below. It is immediately visible that across all oligomers, increasing loading resulted in lowering the η_{PL}, an effect attributed to concentration quenching.

Contrarily, increasing the loading of the oligomers in the polymer matrix resulted in increasing the percentage of photons emitted in the NIR. However, comparing the values with the pure oligomers in solution, a drop is observed in NIR PL due to residual emission of the polymer host, that also boosted slightly η_{PL} values for the lower loading of 1.0 %, but dropped with the higher loadings when the effects of concentration quenching were more pronounced.

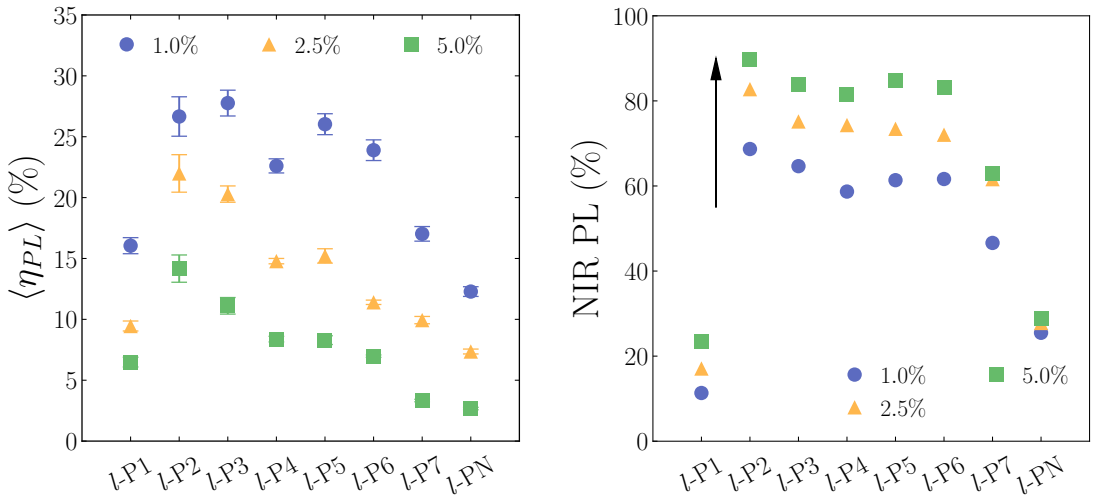

(a) η_{PL} **(b)** % of NIR PL

Figure 3.15 | (a) photoluminescence quantum efficiency (η_{PL}) **(b)** near-infrared (NIR) photoluminescence (PL) of the F8BT:*l*-Pn blends. The arrow in (b) emphasises the increase of the % of the photons emitted at $\lambda > 700$ nm. With blue is the 1.0 %, yellow is the 2.5 % and green is the 5.0 % loading.

Impressively, an $\langle\eta_{PL}\rangle$ value ~ 30 % in the solid-state was achieved without the use of additives, such as 4-benzylpyridine (BP) to minimise aggregation. [87] This corroborated further the positive effect of the THS sidechains, and a significant improvement when compared to similar oligomers without THS sidechains that require the metal coordinating BP to show η_{PL} values > 1 %. [87] To further prove the effect, the η_{PL} of the THS-free porphyrin used by Fenwick *et al.* was measured again. An F8BT:P6 10 w/w % blend was prepared and found to have $\langle\eta_{PL}\rangle \sim 1$ %.

One might notice that comparing the absorption spectra of F8BT (Figure 3.13a) and that of the oligomers (Figure 3.5a), there is a significant overlap of the second characteristic absorption band of F8BT with the main absorption peak of the oligomers, the *B* band. Knowing that the excitation laser is a 445 nm diode laser, one can claim that the emission of the porphyrins is not thanks to FRET, but rather directly exciting the porphyrins. To test this claim, the same samples of F8BT:*l*-P6 that were tested for η_{PL} and whose spectra are presented in Figure

3.14f, where tested for PL intensity by collecting the spectra following selective excitation of only the F8BT. To achieve that, a 325 nm He-Cd gas laser was used, resonant with the high energy absorption peak of F8BT. The results, presented in Figure 3.16 confirm that the relative intensities of F8BT-*l*-P6 remain almost the same, corroborating the claim of efficient FRET.

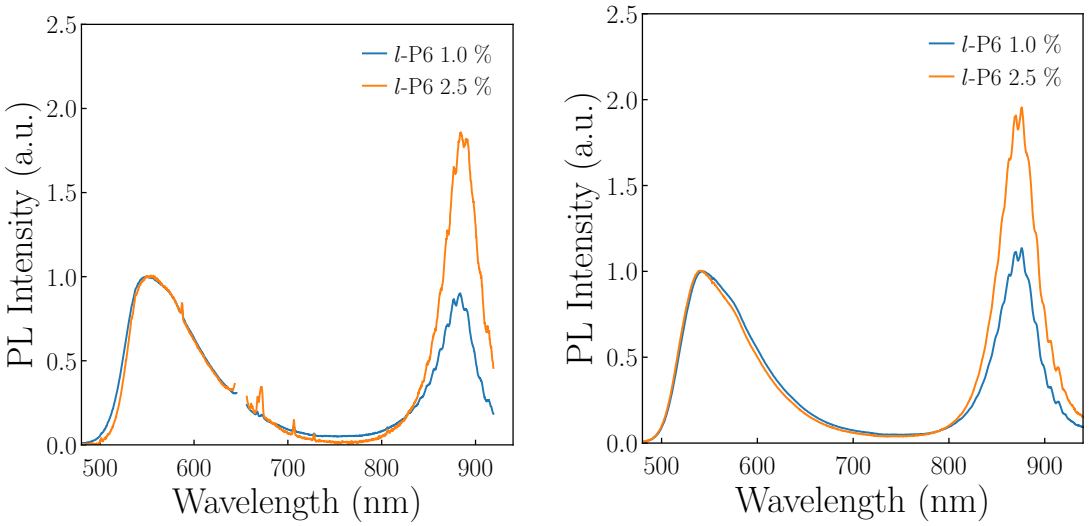

(a) $\lambda_{exc} = 325\,\text{nm}$ **(b)** $\lambda_{exc} = 450\,\text{nm}$

Figure 3.16 | Comparison of the F8BT:*l*-P6 photoluminescence (PL) following excitation with two different laser sources: **(a)** 325 nm **(b)** 445 nm. The relative intensities remain almost the same, corroborating the claim of efficient Förster resonant energy transfer (FRET). The missing part at $\sim 650\,\text{nm}$ is the second order of diffraction of the excitation laser.

Before proceeding with the OLED characterisation, it is worth noting that the results presented above refer to the F8BT:*l*-Pn blends, omitting the TFB blends so far. As mentioned above, the TFB did not perform well compared to the F8BT one, and therefore only the hexamer was tested, just as presented in the absorption spectra. However, FRET was efficient as expected by the better spectral overlap, resulting in higher values for η_{PL} and similar for NIR PL, making TFB:*l*-P6 a very promising candidate for efficient NIR OLEDs. The PL spectra of the TFB:*l*-P6 blends are presented in Figure 3.17 below. Nevertheless, as it is shown below, TFB blends did not perform well in OLEDs. Since the characterisation of the hexamer preceded the rest of the oligomers, it was deemed unnecessary to utilise the little material that was available in a study that didn't show much potential compared to F8BT.

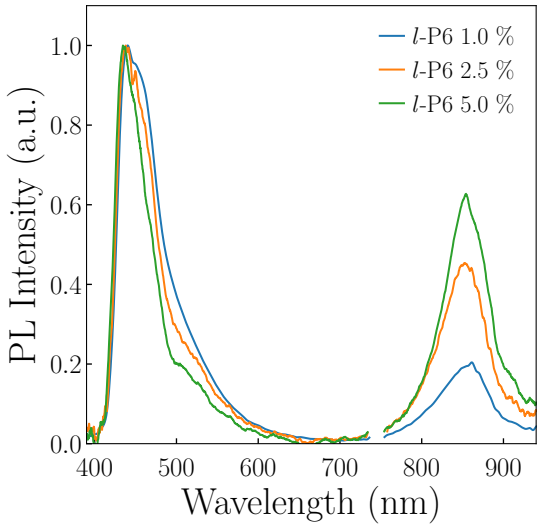

Figure 3.17 | TFB:*l*-P6 photoluminescence (PL) spectra following excitation at 371 nm.

The significant values presented above (such as η_{PL} and % of NIR PL) are summarised in Table 3.1 below. However, all the values from both solution and thin film photoluminescence characterisation are noted in the detailed Table A.1 at the end of the present thesis.

As it has been previously mentioned, the hexamer being of special value thanks to the previous study of cyclic and linear zinc hexamers of Fenwick *et al.* [87], the same P6(OCT) was tested in blends with F8BT. The same F8BT:P6(OCT) 10.0 % that was published, afforded a $\langle\eta_{PL}\rangle < 1\,\%$ without the metal coordinating 4-benzylpyridine (BP), increased to $\sim 12\,\%$ by adding a $3\,w/w\,\%$ BP. The same blends were also tested alongside the *l*-P6(THS) and achieved a $\langle\eta_{PL}\rangle = 1\,\%$, corroborating the previous results of Fenwick et al. Comparatively, a lower concentration of F8BT:*l*-P6(OCT) 2.5 % was also tested, that is not reported in the 2011 study, and achieved a $\langle\eta_{PL}\rangle = 8\,\%$.

All the blends presented above were used as active layer in the final step of the characterisation, i.e. incorporation into OLEDs. The results described so far represent some of the highest values reported for NIR emitters. The high values of η_{PL} are the basis for achieving good η_{EL} performance, as it was explained in Equation 1.27.

Table 3.1 | Summary of the major optical properties of the zinc porphyrin oligomers in solutions and thin films, including photoluminescence quantum efficiency (η_{PL}) and near-infrared (NIR) photoluminescence (PL).

Sample	$\langle\eta_{PL}\rangle^{sol}$ (%)	NIR PL $_{sol}$ (%)	$\langle\eta_{PL}\rangle^{film}$ (%)	NIR PL $_{film}$ (%)
F8BT pure			59.9 ± 2.5	3.0
l-P1 1.0 %			16.1 ± 0.7	11.3
l-P1 2.5 %	7.9 ± 0.2	9.1	9.5 ± 0.41	17.1
l-P1 5.0 %			6.5 ± 0.4	23.5
l-P2 1.0 %			26.6 ± 1.6	68.7
l-P2 2.5 %	34.3 ± 0.7	84.8	21.9 ± 1.5	82.8
l-P2 5.0 %			14.2 ± 1.1	89.6
l-P3 1.0 %			27.8 ± 1.1	64.6
l-P3 2.5 %	24.2 ± 0.7	94.9	20.3 ± 0.7	75.1
l-P3 5.0 %			11.1 ± 0.7	83.9
l-P4 1.0 %			22.6 ± 0.6	58.7
l-P4 2.5 %	22.2 ± 0.5	96.2	14.8 ± 0.2	74.3
l-P4 5.0 %			8.4 ± 0.2	81.6
l-P5 1.0 %			26.1 ± 0.9	61.3
l-P5 2.5 %	27.3 ± 0.4	98.3	15.2 ± 0.6	73.4
l-P5 5.0 %			8.3 ± 0.4	84.7
l-P6 1.0 %			23.9 ± 0.9	61.6
l-P6 2.5 %	28.5 ± 1.5	99.1	11.4 ± 0.2	72.1
l-P6 5.0 %			6.9 ± 0.1	83.1
l-P7 1.0 %			17.1 ± 0.6	46.7
l-P7 2.5 %	47.8 ± 0.6	99.4	9.9 ± 0.3	61.6
l-P7 5.0 %			2.7 ± 0.1	62.9
l-PN 1.0 %			12.3 ± 0.4	25.5
l-PN 2.5 %	28.3 ± 0.7	90.1	7.4 ± 0.2	27.8
l-PN 5.0 %			2.7 ± 0.1	28.8
TFB pure			26	0.0
l-P6 1.0 %			30	60.0
l-P6 2.5 %	28.5 ± 1.5		31	64.0
l-P6 5.0 %			24	71.0

3.3.3 Zinc porphyrin oligomers OLEDs

With the very good results achieved in the photoluminescence (PL) characterisation described in Sections 3.3.1 and 3.3.2 above, organic light-emitting diodes (OLEDs) were fabricated, using the same blends and loading as presented above as the emissive layers. The detailed procedure for the fabrication process is described above in Section 2.6. The OLEDs fabricated have the typical multilayer structure using indium tin oxide (ITO) as the transparent anode and poly(3,4-ethylenedioxythiophene)-poly(styrenesulfonate) (PEDOT:PSS) as a hole transporting layer, but also a polymer layer that will increase the spatial difference of the active layer from the metal anode. PEDOT:PSS will also move the recombination region further away from the metal electrode, as recombinations tend to take place closer to the electrode that injects the lower mobility carriers, i.e. holes in these devices. [177] On top of PEDOT:PSS is spin coated the active layer, using the same loadings as described above. Finally, the metal cathodes are thermally evaporated including a layer of calcium and a protective layer of aluminium. The resulting architecture, illustrated in Figure 3.18, is ITO/PEDOT:PSS/active layer/calcium/aluminium that has afforded very good results in the past and our group has an extensive expertise in optimising the deposition processes. The resulting architecture is illustrated in Figure 3.18 below.

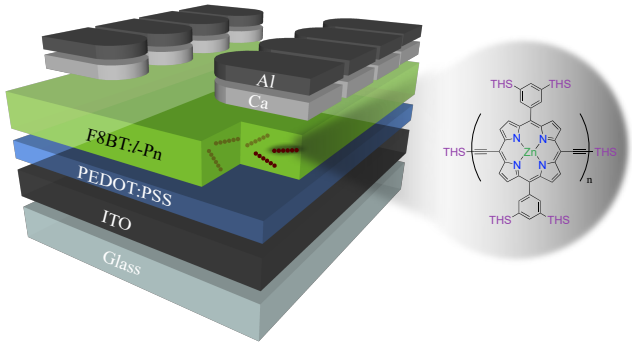

Figure 3.18 | Illustration of the architecture of the organic light-emitting diodes (OLEDs) fabricated. The architecture is ITO/PEDOT:PSS/active layer/calcium/aluminium, where as emissive layer with green is the F8BT:*l*-Pn blends. The chemical structure of the porphyrin oligomers is shown to the right and illustrated as dark-red chains in the emissive layer.

Due to the volume of available plots to describe the rich insights deducted from the OLEDs characterisation and include the most possible metrics available, the results plotted may seem overwhelming, and possibly complicated to understand. However, the results are grouped in a comprehensive way and have been colour-coded for easier understanding. The major curves are presented in the panels

3.20 and 3.21 below.

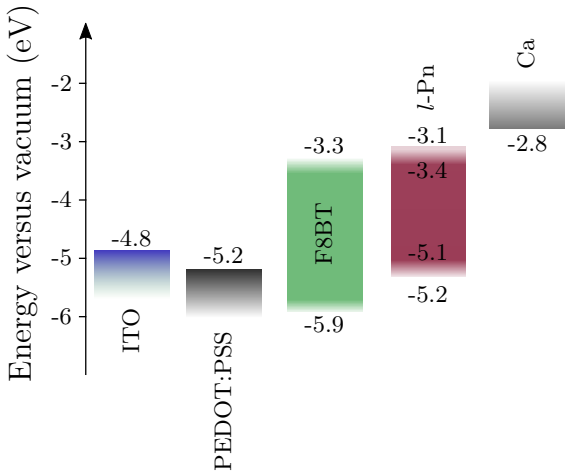

Figure 3.19 | Energy level diagram of the materials used for the organic light-emitting diodes (OLEDs) fabrication. The values for the HOMO-LUMO levels of the zinc oligomers are taken from [87, 127]. The values for the F8BT energy levels are taken from [87, 178].

The electroluminescence (EL) spectra are on the first column (left), the current density - voltage - radiance (JVR) curves in the second (middle) and the electroluminescence external quantum efficiency (η_{EL}) versus current density on the third (right) for each of the F8BT:*l*-Pn blends. Blue lines and symbols represent the F8BT:*l*-Pn 1.0 %, yellow for the 2.5 % and green the 5.0 % loading. In the JVR curves, solid lines refer to the current density versus voltage measured in mA/cm^2, while dashed lines to the radiance versus voltage, measured in mW/cm^2. Radiance was chosen, rather than luminance for the light emission of the devices since the largest part of the EL is in the NIR.

Starting from the EL spectra, oligomers showed a slight shift compared to the photoluminescence (PL) presented in Figure 3.14 of the same blends, since charges have more opportunities to find lower energy sites to recombine. [94] What is evident immediately is the significantly increased quenching of the host emission in favour of the guest near-infrared (NIR) emitter. A synergistic result of a good spectral overlap and a good energy level alignment, but also thanks to the aforementioned excellent charge transport properties of F8BT, all contributing in the radiative recombination of the excitons in the low-energy sites of the oligomers. [179] As a result, EL is spectrally pure with >90 % of emission at $\lambda > 700$ nm for oligomers with $n > 2$, while the mainly red emitting *l*-P1 showed 17 % NIR emission with emission peaking at $\sim$ 650 nm. While these results refer to 5.0 % loading, 2.5 % blends had very similar performance in the % of photons emitted in the NIR. As depicted also in the Figures 3.20a through 3.20j and 3.21a through 3.21j, 1.0 % loading had some enhanced host emission, still

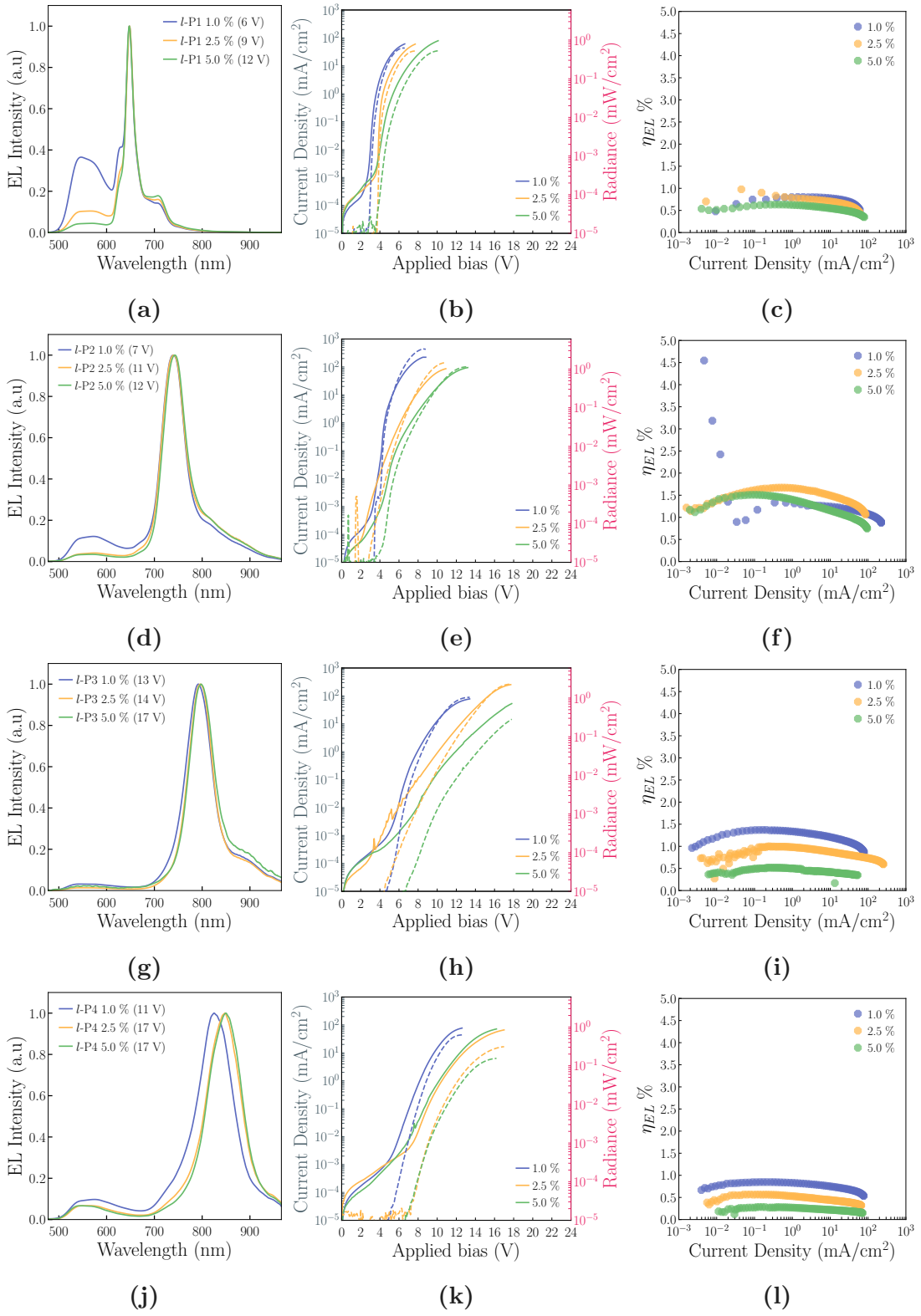

Figure 3.20 | First panel with the optoelectronic properties of the oligomers. Blue lines and symbols represent the F8BT:*l*-Pn 1.0 %, yellow for the 2.5 % and green the 5.0 % loading, for n = 1 − 4. **(a, d, g, j)** (left column) depict the electroluminescence (EL) spectra, **(b, e, h, k)** (central column) the current density - voltage - radiance (JVR) and **(c, f, i, l)** (right column) the electroluminescence external quantum efficiency (η_{EL}) of the OLEDs. The legends in **(a, d, g, j)** refer to the voltage at which the spectra where collected.

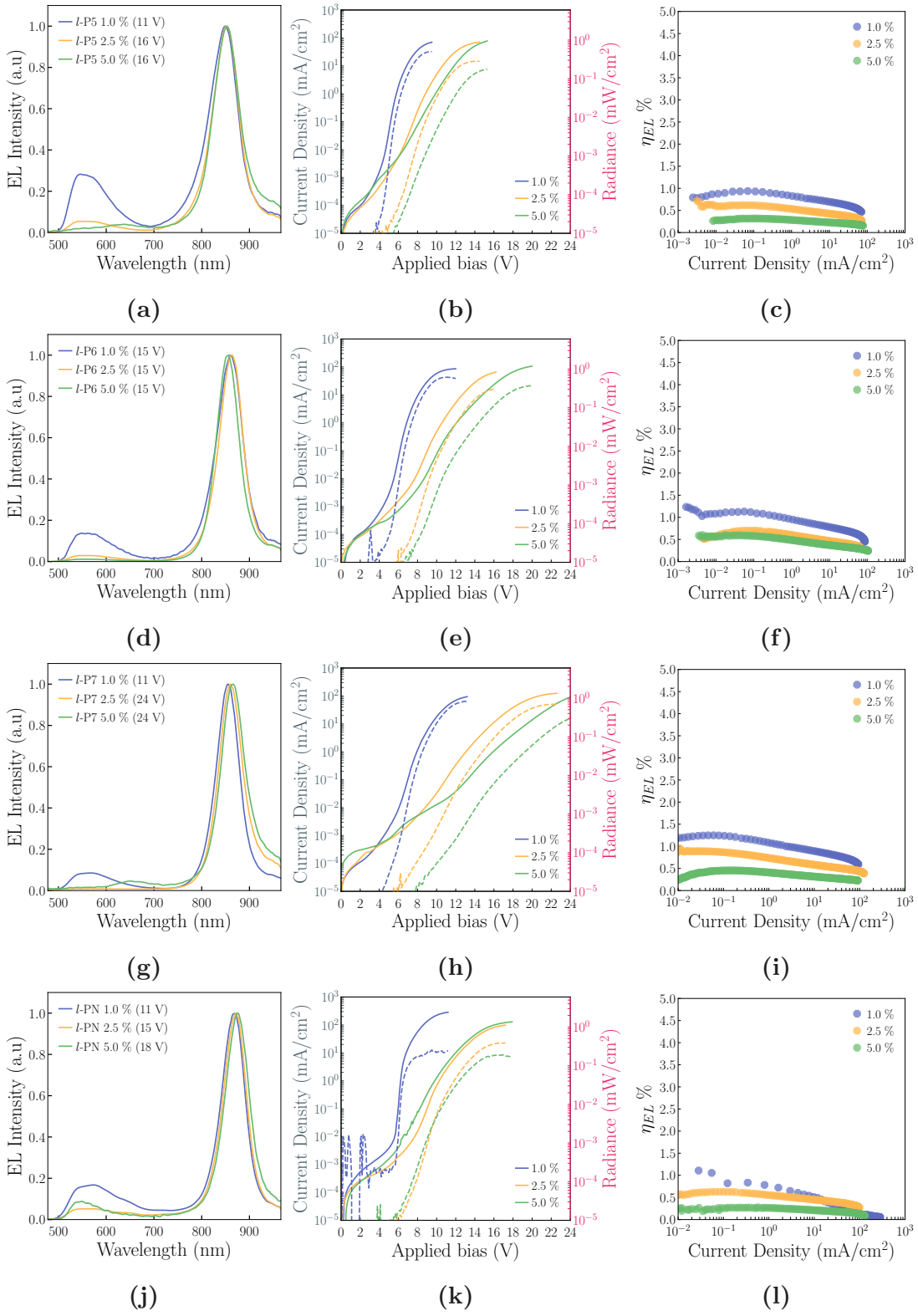

Figure 3.21 | Second panel with the optoelectronic properties of the oligomers. Blue lines and symbols represent the F8BT:*l*-Pn 1.0 %, yellow for the 2.5 % and green the 5.0 % loading, for n = 5 − 7 & N. **(a, d, g, j)** (left column) depict the electroluminescence (EL) spectra, **(b, e, h, k)** (central column) the current density - voltage - radiance (JVR) and **(c, f, i, l)** (right column) the electroluminescence external quantum efficiency (η_{EL}) of the OLEDs. The legends in **(a, d, g, j)** refer to the voltage at which the spectra where collected.

however achieving a remarkable $>80\,\%$ NIR emission for oligomers with $n>2$, with the exception of F8BT:*l*-P5 1.0 % that emitted 75 % of photons in the NIR. These results are summarised in Figure 3.22.

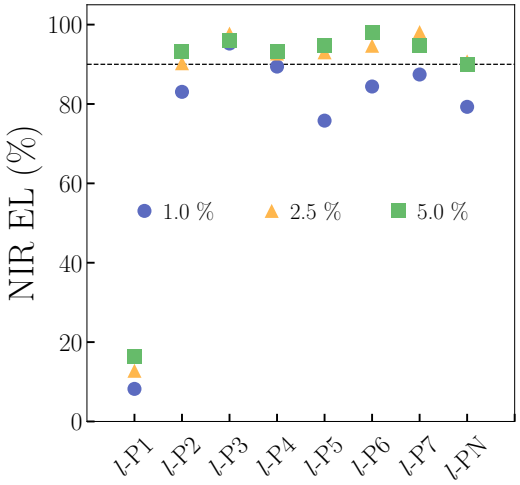

Figure 3.22 | Percentage of photons emitted in the near-infrared (NIR) for the zinc oligomers. Blue symbols represent the F8BT:*l*-Pn 1.0 %, yellow for the 2.5 % and green the 5.0 % loading. The results were calculated from spectra collected at the saturation voltage, the voltage at which light emission (radiance) is maximum. The dashed line is highlighting the 90 % point.

As per the PL results (Figure 3.15b), EL of *l*-PN showed some enhanced emission at $\lambda<700\,\text{nm}$, attributed to some shorter oligomers, possible due to degradation of the samples, but also to the increased distance between chromophores making FRET less efficient. This resulted in the longest oligomer being the least efficient NIR emitter.

In Figure 3.23a below are presented the maxima of η_{EL} for each sample. In Figure 3.23b are presented the average maxima among the different fabricated OLEDs. It is evident that the lower concentration achieved higher maximum η_{EL} for all the oligomers, except the monomer, with a "champion" device of the F8BT:*l*-P2 1.0 % achieving a record $\eta_{EL} = 4.3\,\%$. Notably, the record value was measured at a current density of $J\sim10^{-2}\,\text{mA/cm}^2$, at a radiance of $R>10^{-3}\,\text{mW/cm}^2$, well above the detection limit of our detector, and as it is visible from Figure 3.26d, the emission is mainly attributed to the NIR emitter.

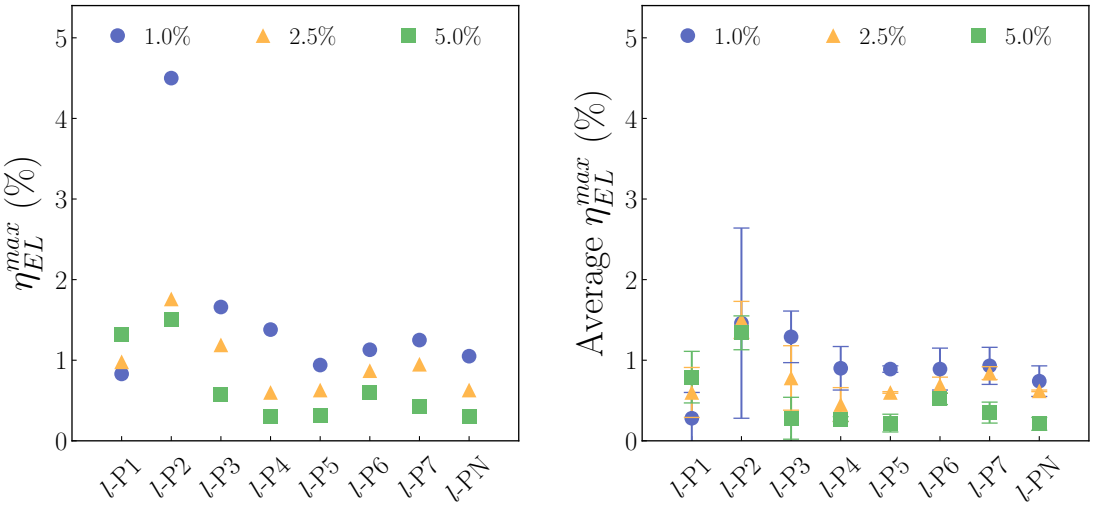

(a) Maximum η_{EL} **(b)** Average maximum η_{EL}

Figure 3.23 | (a) Maximum electroluminescence external quantum efficiency (η_{EL}) and **(b)** average maximum electroluminescence external quantum efficiency (η_{EL}) for the zinc porphyrin oligomers OLEDs.

With the exception of this very high value of the dimer, all the oligomers showed stable performance across the fabricated devices. All the dimer devices showed better performance than the rest of the oligomers, in terms of maximum η_{EL}, and had $\eta_{EL}^{max} > 1.0\,\%$ and all at reasonable current densities. However, the dimer, as the rest of the oligomers, showed some roll-off with increasing applied bias (and therefore increasing current density). This is typical of OLEDs and can be attributed to a variety of exciton quenching processes. Such processes could be triplet-triplet annihilation (TTA), unbalanced charge carriers resulting in a preferential build-up of one type of charge that can serve as a quenching site for the excitons, but also charge trapping in the low energy sites. [180–183] However, the somewhat less pronounced roll-off in the case of the highest concentration, *i.e.* the presence of more dopants, can be attributed to the reduced self-quenching, where the roll-off is determined by the charge pair dissociation rather than triplet-triplet annihilation. [92] It also noticeable from both subfigures of Figure 3.23 that increasing the concentration of the dopant results in reduced η_{EL}, an effect attributed to concentration quenching. [184] Finally, by looking at the η_{EL} of the pure F8BT OLEDs in Figure B.2c, the dopant increased the maximum efficiency of the devices in all cases. Plots with all the η_{EL} versus applied bias curves can be found in Figures C.1 through C.8.

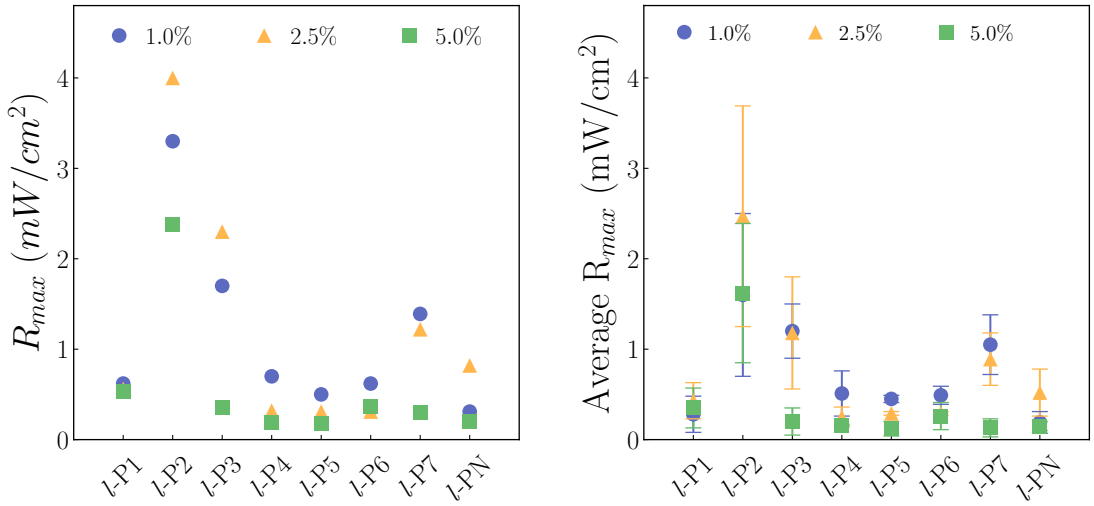

(a) Maximum radiance **(b)** Average maximum radiance

Figure 3.24 | **(a)** Maximum radiance and **(b)** average maximum radiance for the zinc porphyrin oligomers OLEDs.

Figures 3.24a and 3.24b show the maximum and average maximum radiance measured for the various devices, respectively. Also in in terms of light emission, *l*-P2 was the best performer in all three concentrations showing maximum values of $R > 2\,\mathrm{mW/cm^2}$. Furthermore, just as the results of η_{EL}, lower concentrations afforded higher values, corroborating the argument of aggregation quenching.

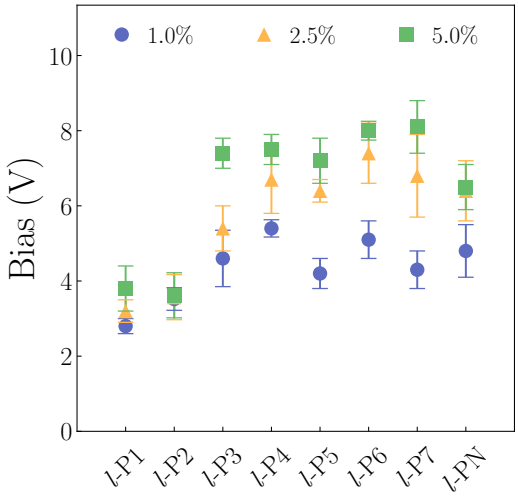

Figure 3.25 | Average turn-on voltage of the zinc porphyrin oligomers OLEDs. As turn-on voltage is defined the voltage at which light emission (radiance) goes above $3.5 \times 10^{-5}\,\mathrm{mW/cm^2}$.

Interestingly, *l*-P2 blends showed coherently low turn-on voltages (V_{ON}) of $\sim 3.5\,\mathrm{V}$. As mentioned above in Section 2.7, V_{ON} is defined in this thesis as the voltage at which the light emission (radiance) goes above $3.5 \times 10^{-5}\,\mathrm{mW/cm^2}$.

Again, higher concentrations resulted in higher V_{ON} biases, a typical behaviour of host-guest OLEDs. [184, 185] This observation of increased V_{ON} with higher concentrations could corroborate a previous argument of the porphyrins acting as charge traps that results in increased applied biases, reduced η_{EL}, but also extended ohmic regime that can be observed from the JVR plots of Figures 3.20 and 3.21. [179] In all JVR plots, the higher concentrations exhibited this extended ohmic regime.

By looking at the η_{EL} versus J curves in Figures 3.20 and 3.21 above, it could be argued that, since the η_{EL}^{max} is measured at relatively low current densities, it was not the oligomers emitting, but rather the polymer host, however unlikely given the larger E_G that the host has. In order to explore how the blends behaved at low voltages, the spectra at the very minimum applied bias that our detector could detect a signal were collected. In order to explore how the different blends emitted depending on the applied bias, the spectra at various biases until the saturation voltage were subsequently collected and are presented in Figures 3.26 and 3.27 below. The voltage-resolved spectra have been normalised for the maximum of the emission to emphasise the ratio between F8BT and *l*-Pn emission. The pure F8BT OLEDs showed very stable voltage-resolved spectra and from the very first photons collected to the saturation voltage, the spectrum is identical to the one presented in Figure B.2a, and is therefore omitted from this chapter for simplicity. The spectra can be found in the appendix in Figure B.3.

As in Figures 3.20 and 3.21, the increase quenching of the emission of F8BT in the two higher concentrations is noticeable . The spectra showed remarkable stability and in all devices the first photons emitted that were detectable by our spectrometer, originated from the NIR emitters. In all of the oligomers, the 1.0 % blend exhibited an enhanced host emission at higher voltages. This effect is attributed to a combination of two factors; the saturation of the low energy emissive sites at increasing injected charge carries, therefore the excitons are recombining at the polymer host, rather than the NIR emitters and the ease of injecting carriers in the HOMO and LUMO of the host. This phenomenon is significantly suppressed at the 2.5 % and 5.0 % loadings due to the existence of more traps where the excitons can recombine rather than being emitted from the host. There was also some subtle broadening of the NIR peak in the high-energy tail, attributed to an increase temperature due to the increased carrier injection and the higher applied biases. [186]

All the EL results presented in the Figures above are summarised in the Table 3.2 below. Further details and direct comparisons with the PL data can be made using the Tables A.2 and A.1 in the appendix.

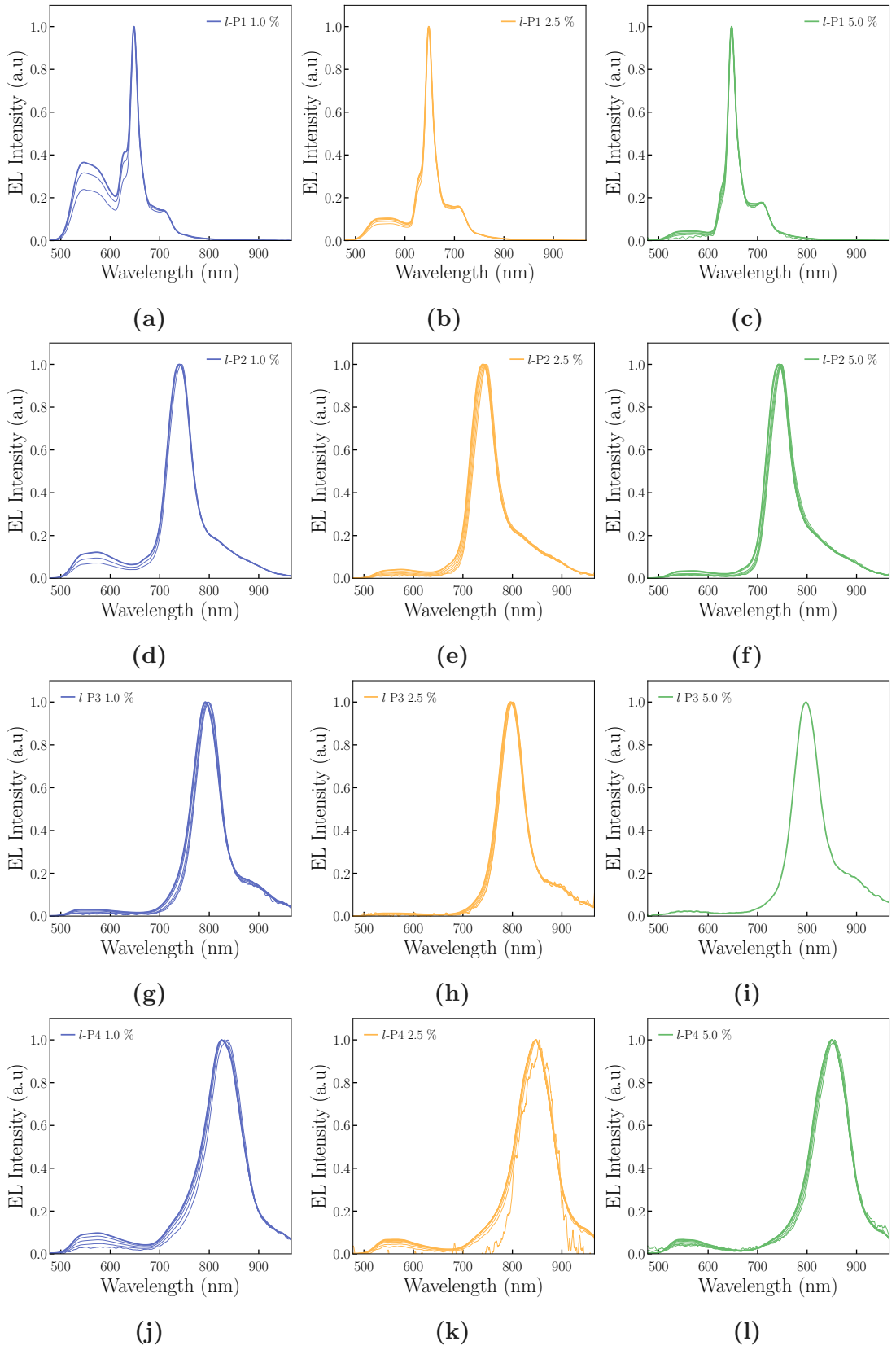

Figure 3.26 | Voltage-resolved spectra for the zinc porphyrin oligomers OLEDs. Blue lines represent the F8BT:*l*-Pn 1.0 %, yellow for the 2.5 % and green the 5.0 % loading. The spectra collection started at the minimum voltage that was above the detection threshold and the last was the saturation voltage and were collected in steps of 1 V.

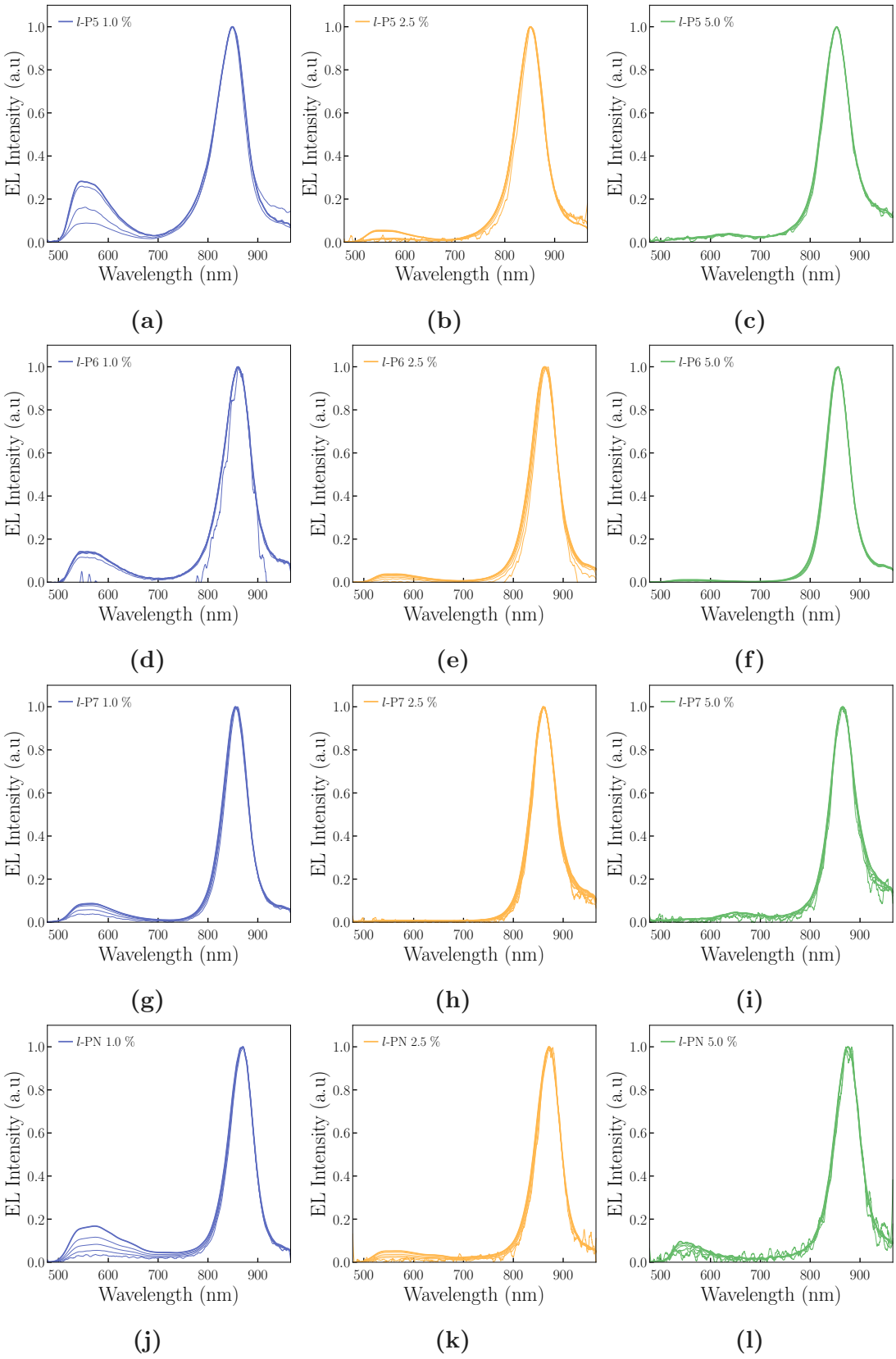

Figure 3.27 | Voltage-resolved spectra for the zinc porphyrin oligomers OLEDs. Blue lines represent the F8BT:*l*-Pn 1.0 %, yellow for the 2.5 % and green the 5.0 % loading. The spectra collection started at the minimum voltage that was above the detection threshold and the last was the saturation voltage and were collected in steps of 1 V.

Table 3.2 | Summary of the EL properties of the zinc oligomers OLEDs.

Sample	η_{EL}^{max} (%)	$\langle\eta_{EL}^{max}\rangle$ (%)	R_{max} (mW/cm^2)	$\langle R_{max}\rangle$ (mW/cm^2)	V_{ON} (V)
F8BT pure	0.3	0.3 ± 0.04	0.9	0.4 ± 0.19	3.7 ± 0.46
l-P1 1.0 %	0.8	0.3 ± 0.3	0.6	0.3 ± 0.2	2.8 ± 0.2
l-P1 2.5 %	0.9	0.6 ± 0.3	0.6	0.4 ± 0.2	3.2 ± 0.3
l-P1 5.0 %	1.3	0.8 ± 0.3	0.5	0.4 ± 0.2	3.8 ± 0.6
l-P2 1.0 %	4.5	1.5 ± 1.2	3.3	1.6 ± 0.9	3.5 ± 0.3
l-P2 2.5 %	1.7	1.5 ± 0.2	4.0	2.5 ± 1.2	3.6 ± 0.6
l-P2 5.0 %	1.5	1.3 ± 0.2	2.4	1.6 ± 0.8	3.6 ± 0.6
l-P3 1.0 %	1.6	1.3 ± 0.3	1.7	1.2 ± 0.3	5 ± 0.75
l-P3 2.5 %	1.2	0.8 ± 0.4	2.3	1.2 ± 0.6	5 ± 0.6
l-P3 5.0 %	0.6	0.3 ± 0.3	0.4	0.2 ± 0.2	7 ± 0.4
l-P4 1.0 %	1.4	0.9 ± 0.3	0.7	0.5 ± 0.2	5 ± 0.23
l-P4 2.5 %	0.6	0.5 ± 0.2	0.3	0.3 ± 0.1	6.7 ± 0.9
l-P4 5.0 %	0.3	0.3 ± 0.03	0.2	0.2 ± 0.01	7.5 ± 0.4
l-P5 1.0 %	0.9	0.9 ± 0.04	0.5	0.5 ± 0.04	4.2 ± 0.4
l-P5 2.5 %	0.6	0.6 ± 0.01	0.3	0.3 ± 0.02	6.4 ± 0.3
l-P5 5.0 %	0.3	0.2 ± 0.1	0.2	0.1 ± 0.08	7.2 ± 0.6
l-P6 1.0 %	1.1	0.9 ± 0.3	0.6	0.5 ± 0.1	5.1 ± 0.5
l-P6 2.5 %	0.9	0.7 ± 0.1	0.3	0.3 ± 0.02	7.4 ± 0.8
l-P6 5.0 %	0.6	0.5 ± 0.07	0.4	0.3 ± 0.1	8 ± 0.25
l-P7 1.0 %	1.3	0.9 ± 0.2	1.4	1.1 ± 0.3	4.3 ± 0.5
l-P7 2.5 %	0.9	0.8 ± 0.08	1.2	0.9 ± 0.3	6.8 ± 1.1
l-P7 5.0 %	0.4	0.4 ± 0.1	0.3	0.1 ± 0.1	8.1 ± 0.7
l-PN 1.0 %	1.1	0.7 ± 0.2	0.3	0.2 ± 0.1	4.8 ± 0.7
l-PN 2.5 %	0.6	0.6 ± 0.01	0.8	0.5 ± 0.3	6.4 ± 0.8
l-PN 5.0 %	0.3	0.2 ± 0.1	0.2	0.2 ± 0.05	6.5 ± 0.6

Just as mentioned previously, *l*-P6 was also tested in blends with a polymer emitting at higher energies than F8BT, which also had better spectral overlap (Figure 3.12). In order to examine how this spectral overlap is beneficial when in devices, the same TFB:*l*-P6 blends reported in Figure 3.17 where used as emissive layer in OLEDs, with the exception of the 5.0 % blend. The results are presented in Figure 3.28 below.

It is immediately visible that TFB blends had a much lower η_{EL} values, with both blends having a $\eta_{EL}^{max} \sim 0.13\,\%$, the lowest among the blends tested. It is also noticeable the second peak observed in the $600 - 700$ nm observed in the blends, that was not present in the pure TFB OLEDs. By considering the HOMO-LUMO levels of TFB and *l*-P6, this peak can be attributed to an intermolecular transition, as its energy (1.8−2.0 eV) corresponds to the energy difference between $\mathrm{HOMO_{TFB}}$ - $\mathrm{LUMO_{\textit{l}\text{-P6}}}$, corroborated by the fact that this band is absent in the PL spectra (Figure 3.17) and from the pure TFB OLEDs (Figure 3.28a). However,

a second possible interpretation is that of the "keto" defects, originating from oxidative degradation of the TFB layer that form trap states for charges and excitons. [187, 188]

Furthermore, the EL is peaked at 812 and 822 nm for the 1.0 % and 2.5 % respectively, a $\sim$ 50 and $\sim$ 40 nm blue shift compared to the F8BT:*l*-P6 blends, showing that the hexamer has a different conformation in the two different matrices. The surprisingly low η_{EL} values achieved are, therefore, attributed to these two interpretations of intermolecular transitions and "keto" defects, together with the energetic barrier for electron injection by the LUMO of TFB.

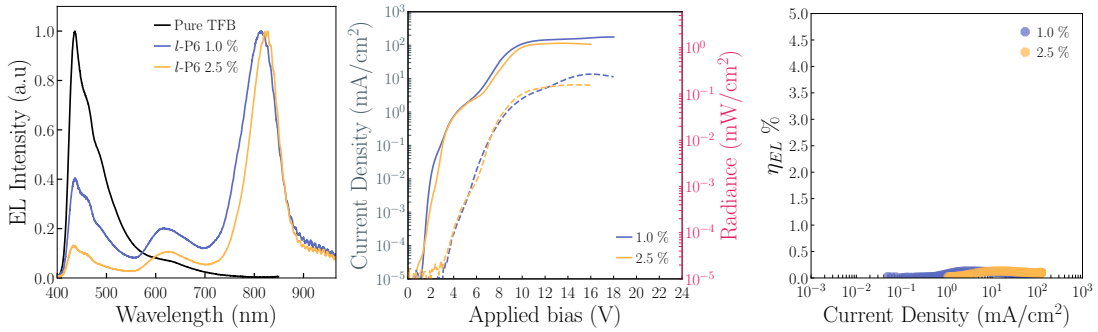

(a) **(b)** **(c)**

Figure 3.28 | Pure TFB and TFB:*l*-P6 OLED properties. **(a)** (left) depicts the electroluminescence (EL) spectra, **(b)** (centre) the current density - voltage - radiance (JVR) and **(c)** (right) the electroluminescence external quantum efficiency (η_{EL}) of the OLEDs.

Further to the rest of the zinc oligomers presented above, it is noteworthy to report the results afforded by the P6(OCT) hexamer that was tested by Fenwick *et al.* [87] In that study, it was reported that non 4-benzylpyridine (BP) F8BT:P6(OCT) blends achieved a $\eta_{EL} \sim 0.01$ %, increased by a factor of ten to $\eta_{EL} \sim 0.1$ % with the addition of 3.0 w/w % BP. Testing the same P6(OCT) against the *l*-P6(THS), but in a lower concentration of 2.5 %, instead of the reported in the study 10.0 %, achieved a $\eta_{EL}^{max} \sim 0.3$ %, 1/3 of the value achieved by the *l*-P6(THS), with the same 1/3 worse performance for the light emitted (radiance), but with a similarly good NIR emission of >90 % of the photons at $\lambda > 700$ nm.

3.3.4 Conclusions

In this section, the full optical and electro-optical characterisation of 8 zinc porphyrin oligomers was reported. Starting from the monomer and increasing the oligomers length up to the heptamer, and an eighth long oligomer, termed "polymer" were tested starting from dilute solution measurements up to organic light-emitting diodes (OLEDs) fabrication. The porphyrin oligomers incorporated novel bulky trihexylsilyl (THS) chains that offered a large steric hindrance and prevented aggregation efficiently. This claim was tested against a THS-free hexamer and was proven valid. Despite the long and bulky sidechains, pure porphyrin films were not emissive enough, so a host-guest strategy was utilised, with the hosts being two widely studied, commercially available polymers, namely poly[(9,9-di-n-octylfluorenyl-2,7-diyl)-*alt*-(benzo[2,1,3]thiadiazol-4,8-diyl)] (F8BT) and poly[(9,9-dioctylfluorenyl-2,7-diyl)-*alt*-
(4,4'-(N-(p-butylphenyl))diphenylamine) (TFB). With TFB photoluminescence (PL) having an important spectral overlap with the porphyrin high-energy Soret band and F8BT PL overlapping with the Q bands of the oligomers, thin films were characterised. The characterisation included photoluminescence quantum efficiency both in solution, and in thin films, PL intensity and absorption spectra. The near-infrared (NIR) PL was calculated for all the oligomers in solution and thin films. intersystem crossing (ISC) was reduced thanks to the increasing spatial extent between triplets and singlets mitigating the increase of the non-radiate rates, while concomitantly increasing the oscillator strength and the radiative rate, and the aggregation prevention afforded by the THS sidechains resulted in efficient emission at $\lambda > 700\,\text{nm}$, with η_{PL} values up to 47 % and 100 % NIR emission.

By incorporating the blends as active layer in OLEDs, very high electroluminescence external quantum efficiency (η_{EL}) up to 4.3 % was achieved with NIR emission remaining well above 90 % for many oligomers. These results proved to be a challenge to the energy gap law and pave the way for the fabrication of NIR emitting OLEDs with heavy-metal-free material.

A rule of thumb states that higher carrier mobilities result in lower operating voltages, but it has also been suggested that lower mobilities result in higher η_{EL}, at the expense of reducing the response time of an OLED. [177, 189] With this in mind, the relatively low V_{ON}, the significantly high η_{EL} and radiance, the F8BT:*l*-P2 2.5 % can be considered as the best trade-off of an efficient NIR emitter from the zinc porphyrin oligomers presented above. It was also visible from the THS vs OCT comparison that the bulkier sidechains do have a profound

effect on the η_{EL} and η_{PL} values achieved, but also to the light output of the OLEDs. Finally, the TFB:*l*-P6 blends proved that a favourable spectral overlap does not translate to efficient OLEDs and the dominant process for light emission in OLEDs is charge trapping in the low energy emitter, making HOMO-LUMO alignment more important that spectral overlap.

3.4 Porphyrin hexamers

Given the promising results achieved by the porphyrin oligomers using as coordinating metal zinc, that were presented in Section 3.3 above, the same bulky trihexylsilyl (THS) chains architecture was used, but changing the coordinating metal. A range of hexamers was synthesised by Dr. Ibrahim Bulut in at the Chemistry Research Laboratory of the University of Oxford in the group of Prof. Harry L. Anderson, FRS using magnesium, palladium, platinum and a metal-free hexamer were synthesised to investigate the results of heavier or lighter metals and if the elusive triplets could be harvested. The chemical structure of the oligomers is illustrated in Figure 3.29.

It is, therefore, expected to have the same excellent aggregation preventing properties of the THS sidechains, but with the heavier metals to obtain phosphorescence and, subsequently, increase of the efficiencies. As it has been mentioned above, the zinc hexamer was of special attention given the promising previous study of our groups, and so only hexamers were characterised with the different coordinating metals. [87] Previously, the oligomers were referred to as *l*-Pn, with n=1-7 and N for the polymer. To maintain the homogeneity in this thesis, the different hexamers are referred to as *l*-P6 X, where X is the element at the centre of each unit, *e.g.* H_2 for the metal-free or Pd for the palladium.

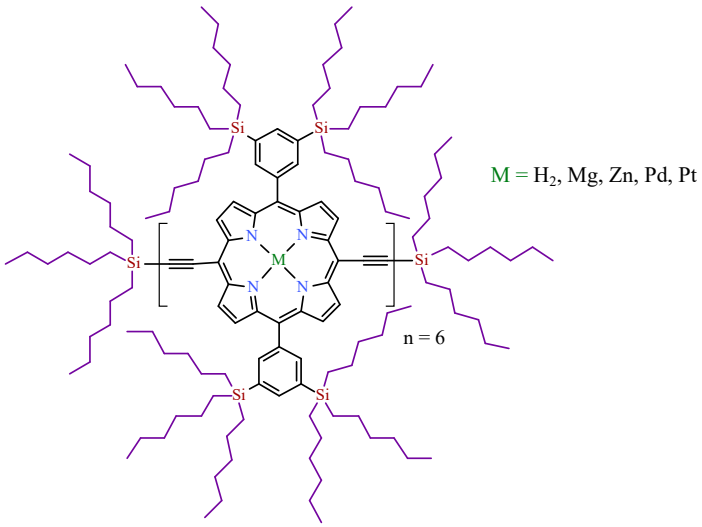

Figure 3.29 | Chemical structure of the porphyrin with the bulky THS side chains highlighted in purple. With M is noted the different elements in the centre of each porphyrin unit: free-base (metal free), magnesium, zinc, palladium and platinum.

3.4.1 Solution photoluminescence of porphyrin hexamers

In Figure 3.30a are presented the absorption spectra of the five hexamers in dilute anhydrous toluene solution ($\sim$ µg/ml). It is surprising the spectral scattering of the Q_x band among the five hexamers, spanning from $\sim$ 680 nm for the *l*-P6 Pt, and red-shifting with decreasing atomic number of the element at the centre of each porphyrin unit. Notably, *l*-P6 Pd was peaked at $\sim$ 700 nm, *l*-P6 Zn at $\sim$ 780 nm. *l*-P6 H_2 broke the pattern peaking at $\sim$ 790 nm and *l*-P6 Mg the most red-shifted peaking at $\sim$ 830 nm. Similar to the the zinc oligomers above, the Soret band remained spectrally stable in the $\sim 400 - 500$ nm region.

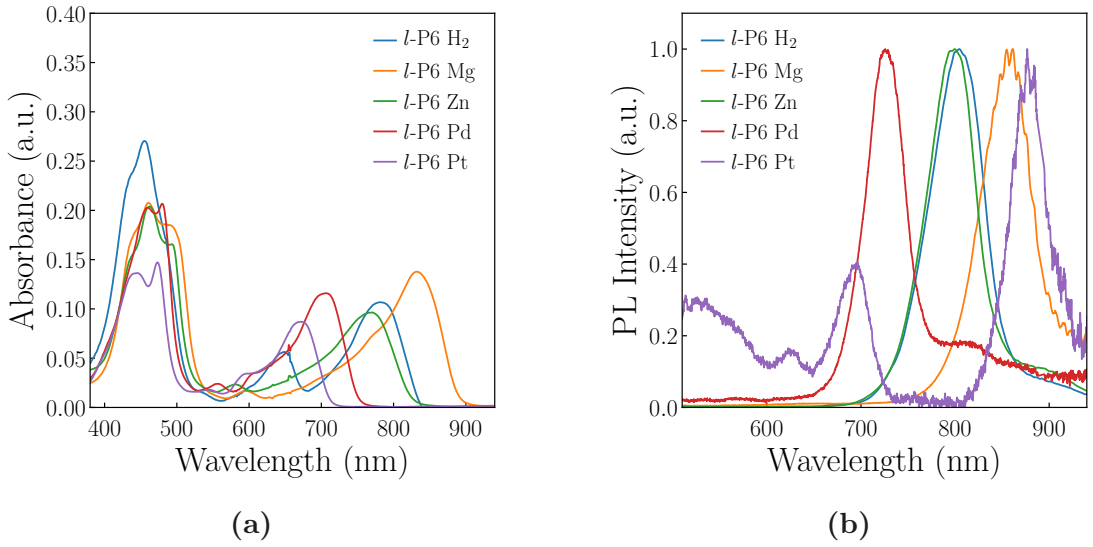

(a) **(b)**

Figure 3.30 | (a) Absorbance and **(b)** normalised photoluminescence (PL) of the hexamers, in dilute anhydrous toluene solution ($\sim$ µg/ml). The PL spectra were collected following excitation at 450 nm from a laser diode.

In the presence of the two heavy metals, platinum and palladium, one would expect to see an importantly red-shifted emission originating from the triplet states. As discussed above, the triplet states lie lower, in energy, than singlets (Figure 1.6), so phosphorescence would be red-shifted compared to fluorescence. However, the palladium hexamer showed no signs of triplet emission, while the platinum had very weak emission, however showing some phosphorescence. The photoluminescence (PL) spectra of the oligomers in dilute anhydrous toluene solution ($\sim$ µg/ml) are presented in Figure 3.30b. The same trend of decreasing of the emitted photons with increasing atomic weight was observed, save for the magnesium hexamer. However, *l*-P6 Pt exhibited an intense secondary emission peak in the $\sim$ 900 nm region and a weaker at $\sim$ 700 nm. The former is attributed to the $S_1 \rightarrow S_0$ transition while the latter to the $T_1 \rightarrow T_0$. The other four oligomers, including the palladium, did not display any secondary peaks. *l*-P6

Pt had its fluorescence peaked at $\sim 720\,\text{nm}$, *l*-P6 Zn and H_2 almost coincidental at $\sim 800\,\text{nm}$ and *l*-P6 Mg at $\sim 840\,\text{nm}$. Another surprising spectral feature of the *l*-P6 Pt was a strange band observed in the higher energies, $\sim 500 - 650\,\text{nm}$ that was more intense by exciting the molecule with a 520 nm emitting laser, rather than the 450 nm used for these spectra. Cross-contamination (*e.g.* from another polymer or oligomer during the experiments) was ruled out since the peak intensified with excitation at lower energies during a discussion of the data with the synthetic group, however it is difficult to speculate how it originated. A different source of this emission could be a chemical residue from the synthesis or purification steps, but further investigation is required.

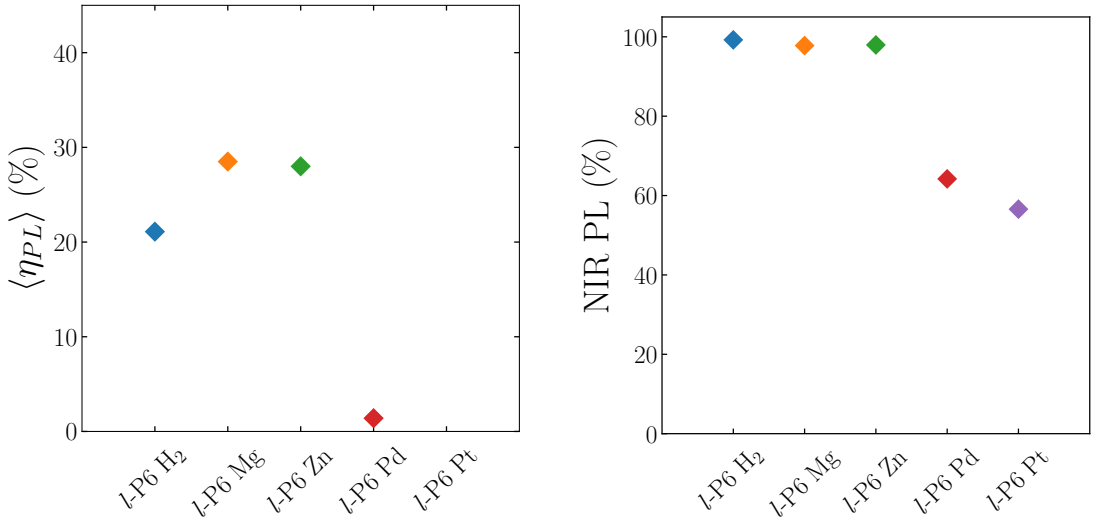

(a) η_{PL} **(b)** NIR emission

Figure 3.31 | (a) Absolute photoluminescence quantum efficiency (η_{PL}) results measured as described in Section 2.4 above and according to [122]. **(b)** % of the photons emitted at $\lambda > 700\,\text{nm}$. The spectra, NIR PL calculations and η_{PL} measurements were carried out following excitation at 450 nm at room temperature in dilute toluene solution ($\sim$ µg/ml).

As it can be deducted from the noisy spectrum in Figure 3.30b, *l*-P6 Pt was not very emissive. This was corroborated when trying to measure the η_{PL}, depicted in Figure 3.31a. Unfortunately, the *l*-P6 Pt PL was below our detection threshold for η_{PL} measurements. *l*-P6 Pd showed some measurable PL, achieving a $\langle \eta_{PL} \rangle \sim 1\,\%$. However, the three heavy-metal-free hexamers has much higher η_{PL} values, with *l*-P6 H_2 yielding $\sim 20\,\%$, *l*-P6 Mg $\sim 30\,\%$ and *l*-P6 Zn, already reported (*vide supra*) $\sim 28\,\%$.

The near-infrared (NIR) PL results were not promising for the heavy-metal-containing materials either. In Figure 3.31b are presented the percentage of photons at $\lambda > 700\,\text{nm}$. The heavy-metal-containing *l*-P6 Pd and Pt and their significantly blue-shifted emission, compared to the three other hexamers,

afforded $\sim 60\,\%$ of NIR emission. It is worth noting that the *l*-P6 Pt NIR PL was further hindered by the band in the $\sim 500 - 650\,\text{nm}$ region. Contrarily, the *l*-P6 H_2, Mg and Zn showed $\sim 100\,\%$ of NIR emission.

To investigate further the nature of the PL of the five hexamers, time-correletated single photon counting (TCSPC) was utilised to quantify the radiative (k_r) and non-radiative k_{nr} rates and the lifetime of the PL. Similar to the zinc oligomers presented in Figure 3.9, 2-D contour plots were measured for the hexamers. While TCSPC is not the most optimised method for measuring phosphorescence, the pulsed lasers used have the option of modifying the repetition rate. Thus, a short repetition rate of 50 MHz was used for the *l*-P6 H_2, Mg, Zn and Pd that did not show any signs of phosphorescence. *l*-P6 Pt was used a much lower repetition rate allowing an observation window of 500 ns, enough to see any long-living species and quantify the lifetime, and if needed explore further with more appropriate equipment.

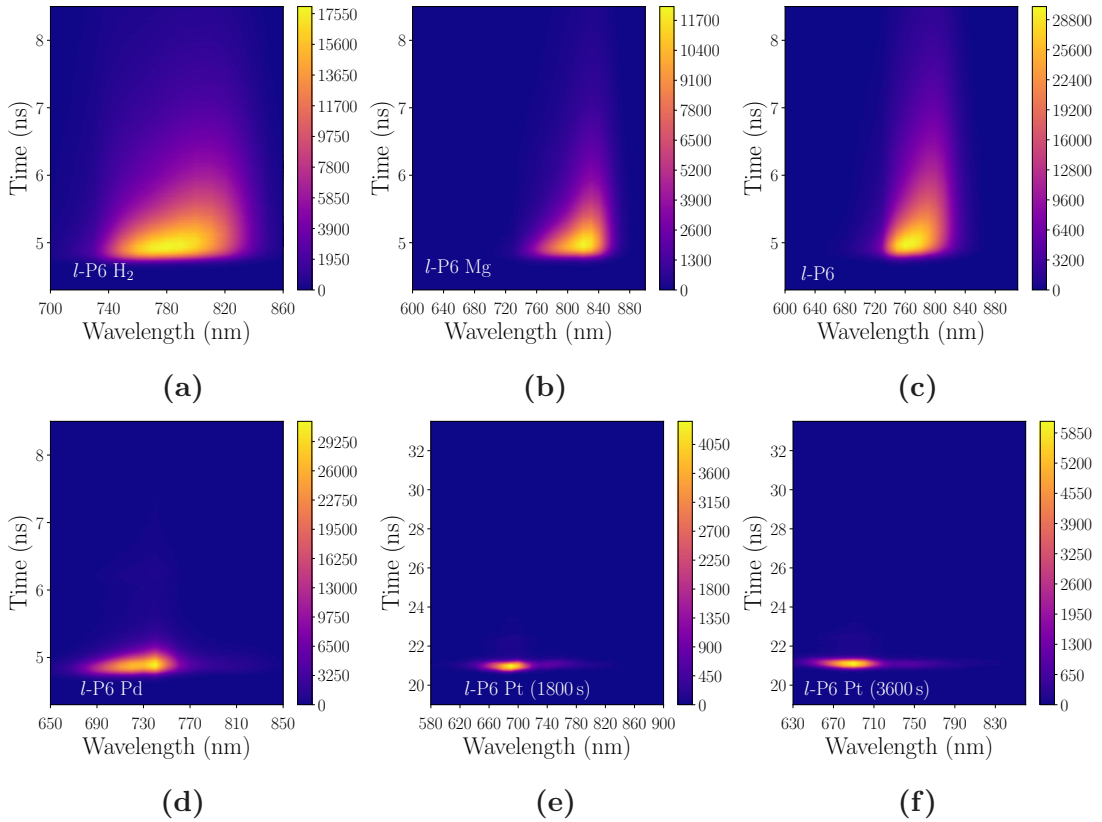

Figure 3.32 | TCSPC time decay contour plots of the hexamers in dilute toluene solution ($\sim$ µg/ml). The time scale for (**a, b, c, d**) is from 4.3 ns to 8.5 ns confirming the fluorescence emission of the oligomers. The time scale for (**e, f**) is 19 ns to 33.5 ns. The colour scales are counts. The spectra were collected integrating for 900 s for each wavelength, while the *l*-P6 Pt was collected for **(e)** 1800 s and **(f)** 3600 s to compensate for low η_{PL} and increase the signal-to-noise ratio. The $\Delta\lambda$ of the collection was set to 10 nm and the time decays were collected every 10 nm, with a repetition rate of the 450 nm picosecond laser at 50 MHz.

The reduced repetition rate resulted in a lower average power, that combined with the low emission from *l*-P6 Pt required to increase the collection time from 900 s to 1800 s and 3600 s.

Further to the 2D maps presented in Figure 3.32 above, the time decays at the respective maxima of the emission are presented in Figure 3.33. It is noteworthy that, while all samples presented are tail fits for the reasons outlined in Section 2.5, *l*-P6 Pd decay was fitted with a reconvolution fit to explain the secondary shoulder of the emission. This shoulder is due to the instrument response function (IRF), shown in Figure 2.3.

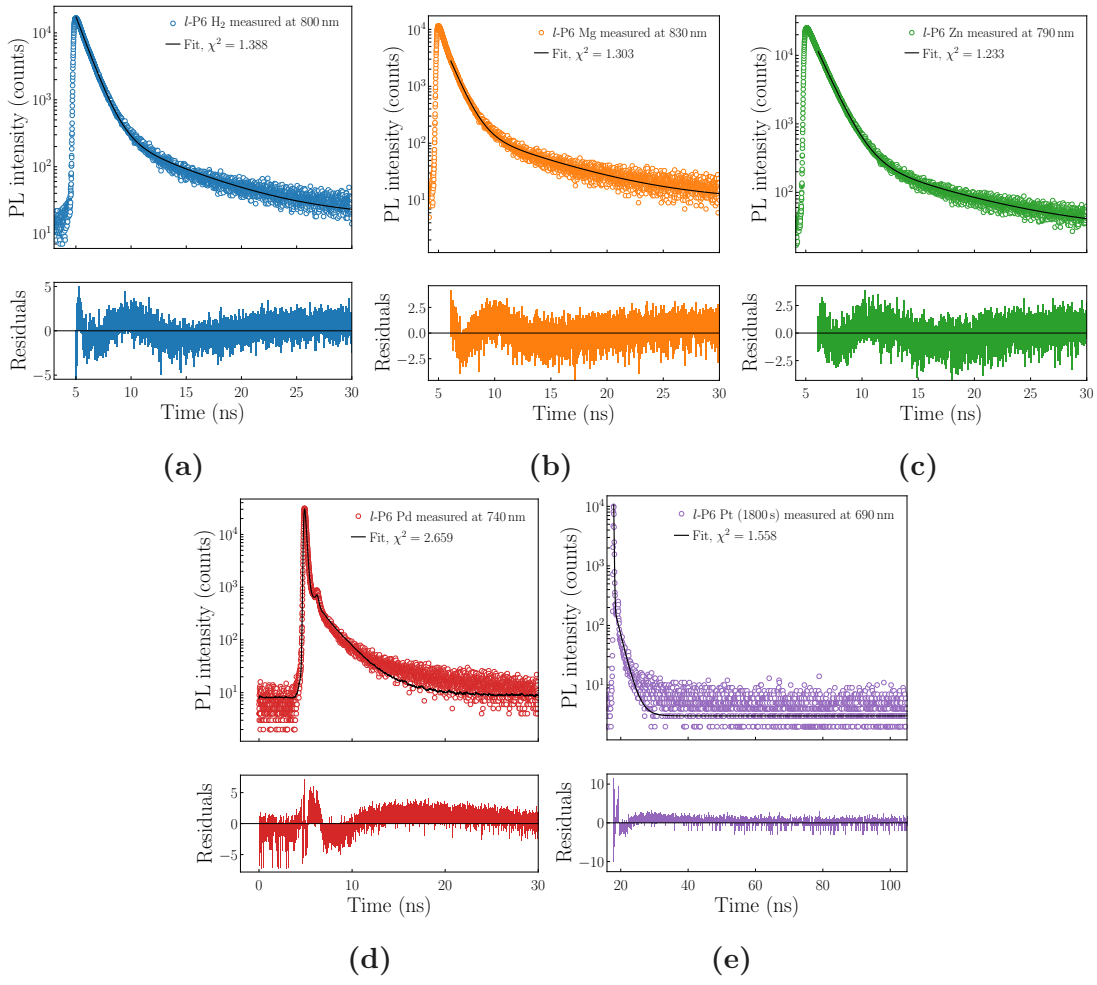

Figure 3.33 | TCSPC time decay plots of the hexamers in dilute toluene solution (∼ µg/ml). Each decay was measured at the respective maximum of the emission. For each decay, the respective fit is shown with black solid line and the corresponding goodness of the fit (χ^2) is noted. Below each plot are the weighted residuals of the fit. The time scale for the spectra in **(a,b,c)** is from 5 ns to 30 ns, in **(d)** is 0 ns to 30 ns and for (e) is 5 ns to 105 ns. For *l*-P6 Pd in **(d)**, the decay was fitted with a reconvolution fit due to the very short decay and to take into consideration the characteristic second shoulder, a feature from the instrument. The spectra in **(a-d)** were collected integrating for 900 s for each sample, while the spectrum in **(e)** was integrated for 1800 s.

As it is immediately visible, *l*-P6 Pt showed no signs of long-lived species despite using double and quadruple integrating time than the rest of the oligomers. This could be due to the very low η_{PL} that resulted in lower signals for the TCSPC, and with the repetition rate lowered to allow for the longer time window, this meant a much lower average power output of the laser. But even in measurements of longer times with no upper limit (measuring times of many hours), no long living species could be observed. Surprisingly, the PL lifetime (τ) of *l*-P6 Pd and Pt were significantly shorter than the the other three oligomers, visible from the Figure 3.32 and 3.34a, where the calculated lifetimes are presented. This is representative of a faster decay path that, according to Equation 2.7, could be attributed to either increasing k_r or k_{nr}. Combining with Equation 2.6 the values of the radiative and non-radiative rates can be calculated, and are presented in Figure 3.34b.

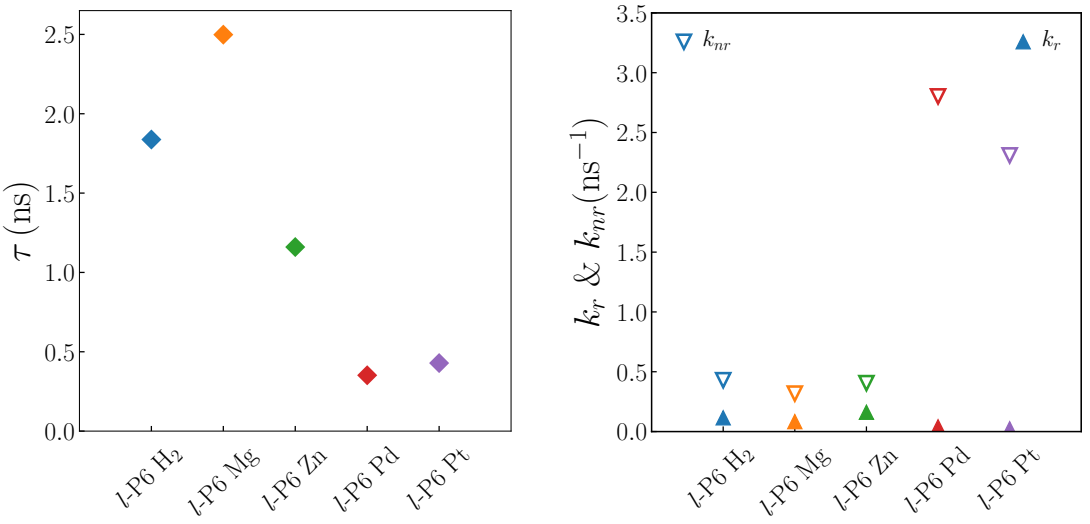

(a) PL lifetime **(b)** Radiative and non-radiative rates

Figure 3.34 | (a) Calculated photoluminescence lifetime for the hexamers. **(b)** Calculated radiative and non-radiative rates (k_r and k_{nr} respectively) for the hexamers. The lifetime measurements were carried out following excitation at 450 nm at room temperature in dilute toluene solution ($\sim$ µg/ml), using the same solutions as for the η_{PL} measurements reported above.

Not surprisingly, a significant increase of k_{nr} is observed, explaining the low η_{PL} and very fast τ. Magnesium metal-free hexamers are in the same trend as the zinc hexamer, and not outliers compared to the rest of the zinc oligomers (Figure 3.11b). It is worth noting that all oligomers showed a bi-exponential decay and the lifetimes presented are the average lifetime as calculated from Equation 2.9. All the results presented in this section are summarised in detail in Table A.3 and the major optical properties in Table 3.3.

However low the η_{PL} values obtained, in the prospect of having efficient near-infrared (NIR) emitting OLEDs, the hexamers were tested in the solid-state to investigate their optical properties.

3.4.2 Solid-state photoluminescence of porphyrin hexamers

Same as per the zinc oligomers, the hexamers were not tested as pure films. Instead, the same polymer, poly[(9,9-di-n-octylfluorenyl-2,7-diyl)-*alt*-(benzo[2,1,3]thiadiazol-4,8-diyl)] (F8BT), was used as a host and the hexamers as near-infrared (NIR) emitting dopants in the same three low loadings of 1.0, 2.5 and 5.0 w/w %. As it was shown, F8BT was an excellent host for NIR emission, despite a rather poor spectral overlap with the oligomers. The fact of forming a type-I heterojunction and the excellent electrical properties have afforded some impressive results so far.

In Figure 3.35 below are presented the photoluminescence (PL) spectra of the hexamers in blends with F8BT.

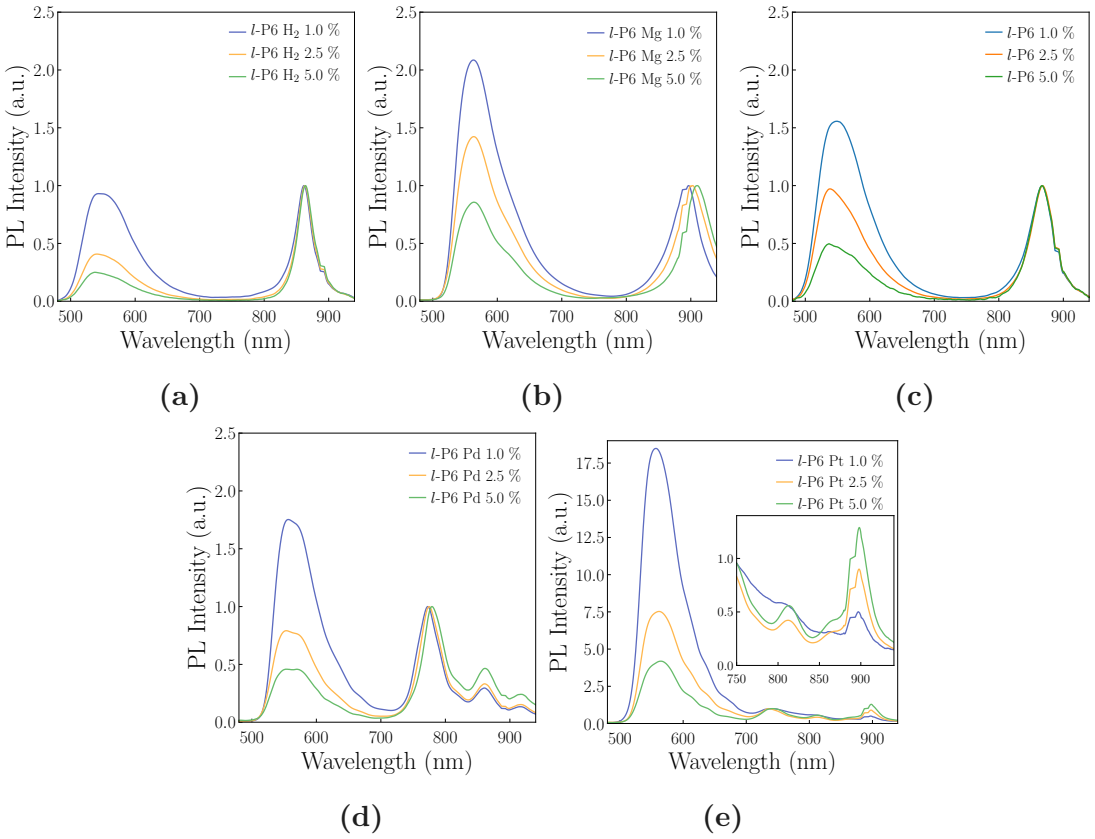

Figure 3.35 | (a) - (e) Photoluminescence spectra of the hexamers in blends with F8BT spin coated on glass spectrosils ($\sim$ 100 nm thick) collected outside the integrating sphere using a 445 nm diode laser. All the spectra have been normalised for the oligomers emission to highlight the gradual quenching of the F8BT host. Blue represents the 1.0 % loading, orange the 2.5 % and green the 5.0 %. Both x and y scales are the same in all plots to facilitate comparisons.

Not surprisingly, *l*-P6 Pt showed a very weak PL, however with the second,

attributed to triplet emission, lower energy peak visible. *l*-P6 Pd showed a more structured PL spectrum with a more pronounced secondary peak at $\sim 850\,\text{nm}$ compared to the solution spectrum. All hexamers displayed a red-shift of $\sim 40\,\text{nm}$ compared to the solution PL, progressively red-shifting further with increasing loading, indicating concentration aggregation. Also in the hexamers case, a more planar geometry afforded a more extended conjugation that resulted in this red-shift compared to the solution measurements. Impressively, while *l*-P6 H_2 and Zn had almost identical PL in solution, there is a stark difference in the solid-state with the metal-free hexamer having a much narrower PL of full width at half maximum (FWHM) of $\sim 30\,\text{nm}$ compared to $\sim 40\,\text{nm}$ for the zinc one. This is indicative of a more uniform distribution of planar hexamers, that lacking a metal centre, could have less interactions with the sulphur or nitrogen atoms of F8BT, as it has been utilised in the case of the metal-coordinating 4-benzylpyridine (BP) the interaction between the zinc atom of the porphyrin with a nitrogen atom of BP. [87]

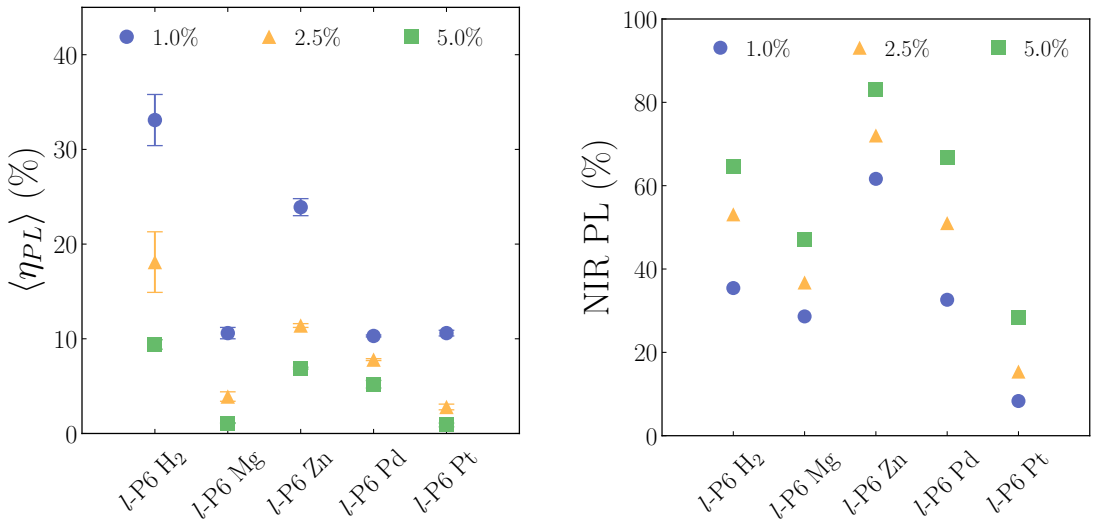

(a) η_{PL} **(b)** NIR emission

Figure 3.36 | (a) photoluminescence quantum efficiency (η_{PL}) **(b)** near-infrared (NIR) photoluminescence (PL) of the F8BT:*l*-P6 *X* blends. With blue is the 1.0 %, yellow is the 2.5 % and green is the 5.0 % loading.

In Figure 3.36a are presented the η_{PL} values of the hexamers in solution and in Figure 3.36b the percentage of photons emitted at $\lambda > 700\,\text{nm}$. As it is visible from Figure 3.36a, if the results of the magnesium hexamer are considered as an outlier, there is a clear trend of decreasing $\langle \eta_{PL} \rangle$ with increasing atomic number of the element in the centre. *l*-P6 H_2 1.0 % had the highest value of $\langle \eta_{PL} \rangle \sim 32\,\%$ for the 1.0 % loading, followed by the zinc for the same concentration of $\langle \eta_{PL} \rangle \sim 25\,\%$. *l*-P6 H_2 2.5 % showed an $\langle \eta_{PL} \rangle$ of $\sim 18\,\%$ with the rest of the loadings in the

$\sim 10\,\%$ or below region. *l*-P6 Pd and Pt showed low values, expected from the bad results in solutions, surprisingly though, with *l*-P6 Mg performing similarly, with only the 1.0 % loading in all three compounds being close to 10 %. However, all hexamers showed the same trend of the zinc oligomers, of decreasing $\langle \eta_{PL} \rangle$ with increasing loading, corroborating the argument of concentration quenching.

The same "anarchy" in the results was observed in the NIR PL (Figure 3.36b). *l*-P6 Pt, with its very low PL from the hexamer, was limited to $\sim 20\,\%$ or less emitted in the NIR. *l*-P6 Zn showed the highest NIR PL, with $> 60\,\%$ of the photons emitted in the NIR for all three loadings. Surprisingly again, *l*-P6 Mg remained below the 50 % mark for all loadings, while *l*-P6 Pd 2.5 and 5.0 % showed more than half their emission in the NIR. Lastly, *l*-P6 H_2 1.0 % also showed a value below 50 %, but the higher loadings emitted $> 50\,\%$ in the NIR. Similarly to the zinc oligomers presented above, the poor spectral overlap of the host F8BT and the hexamers played an important role of keeping Förster resonant energy transfer (FRET) low. However, spectral overlap is not the main factor affecting the energy transfer mechanism in OLEDs, and higher NIR emission values are expected thanks to charge trapping in the lower-energy sites.

All the results presented are summarised in detail in Table A.3, including solution and solid-state results to facilitate comparisons, with the major optical properties in Table 3.3 below.

Table 3.3 | Summary of the major optical properties of the zinc porphyrin oligomers in solutions and thin films, including photoluminescence quantum efficiency (η_{PL}) and near-infrared (NIR) photoluminescence (PL).

Sample	$\langle\eta_{PL}\rangle^{sol}$ (%)	NIR PL $_{sol}$ (%)	$\langle\eta_{PL}\rangle^{film}$ (%)	NIR PL $_{film}$ (%)
F8BT pure	~ 100	1.0	59.9 ± 2.5	5.70
l-P6 H2 1.0 %			33.1 ± 2.7	35.43
l-P6 H2 2.5 %	21.1 ± 0.6	99.5	18.1 ± 3.2	53.10
l-P6 H2 5.0 %			9.4 ± 0.5	64.50
l-P6 Mg 1.0 %			10.6 ± 0.6	28.60
l-P6 Mg 2.5 %	20.7 ± 3.5	97.8	3.9 ± 0.5	36.80
l-P6 Mg 5.0 %			1.1 ± 0.04	47.10
l-P6 Zn 1.0 %			23.9 ± 0.9	61.60
l-P6 Zn 2.5 %	28.5 ± 1.5	99.1	11.4 ± 0.2	72.10
l-P6 Zn 5.0 %			6.9 ± 0.1	83.10
l-P6 Pd 1.0 %			10.3 ± 0.1	32.60
l-P6 Pd 2.5 %	1.4 ± 0.5	64.2	7.8 ± 0.1	51.10
l-P6 Pd 5.0 %			5.2 ± 0.4	66.90
l-P6 Pt 1.0 %			10.6 ± 0.3	8.40
l-P6 Pt 2.5 %	-	56.6	2.8 ± 0.3	15.40
l-P6 Pt 5.0 %			0.9 ± 0.2	28.40

3.4.3 Porphyrin hexamers OLEDs

Given the very interesting results achieved in the photoluminescence (PL) characterisation described in Sections 3.4.1 and 3.4.2 above, organic light-emitting diodes (OLEDs) were fabricated, using the same blends and loadings, as presented above, as the emissive layers. The detailed procedure for the fabrication process is described in Section 2.6. The OLEDs fabricated have a multilayer structure, depicted in Figure 3.37 below, using indium tin oxide (ITO) as the transparent anode and poly(3,4-ethylenedioxythiophene)-poly(styrenesulfonate) (PEDOT:PSS) as a hole transporting layer. On top of PEDOT:PSS is spin coated the active layer, and finally the metal cathodes are thermally evaporated including a layer of calcium and a protective layer of aluminium. The resulting architecture is ITO/PEDOT:PSS/active layer/calcium/aluminium.

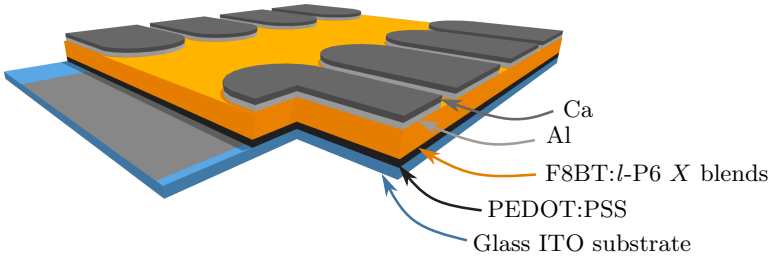

Figure 3.37 | Illustration of the architecture of the organic light-emitting diodes (OLEDs) fabricated. The architecture is ITO/PEDOT:PSS/active layer/calcium/aluminium, where as emissive layer with orange is the F8BT:*l*-P6 *X* blends.

Starting from the electroluminescence (EL) spectra, presented in the first column (left) of Figures 3.38 and 3.39, similarly to the zinc oligomers, the hexamers showed an expected slight red-shift compared to the PL measurements. However, as per the EL spectra of the zinc oligomers, a more severe quenching of the emission of the F8BT was observed in all oligomers, significantly improving the near-infrared (NIR) emission (*vide supra*). *l*-P6 H_2 showed a very narrow emission for all three loadings of $\sim$ 35 nm ($\sim$ 60 meV) FWHM, peaking at $\sim$ 864 nm with an unexpected increase of the red-tail of the 1.0 % loading (Figure 3.38a, blue line). Surprisingly, *l*-P6 Mg showed almost complete quenching of the F8BT host in all three concentration, an effect the other hexamers showed only for the 2.5 and 5.0 % and had the EL peaking at $\sim$ 890 nm. Concerning the heavy-metal containing hexamers, *l*-P6 Pd didn't show any sign of phosphorescence while *l*-P6 Pt showed an enhanced emission of the triplet state with the phosphorescence peak being significantly intensified, however co-existing with the fluorescence, giving rise to potential applications as oxygen sensor since oxygen is known to quench the triplet emission. [190] The phosphorescence

emission also showed increasing intensity with increasing loading. *l*-P6 Pd EL spectrum maintained the same structure and secondary lower energy peak seen previously in the film PL spectrum (Figure 3.35d), with EL peaking at $\sim 765\,\text{nm}$. All the hexamers showed a slight bathochromic shift with increasing loading, attributed to intermolecular interactions.

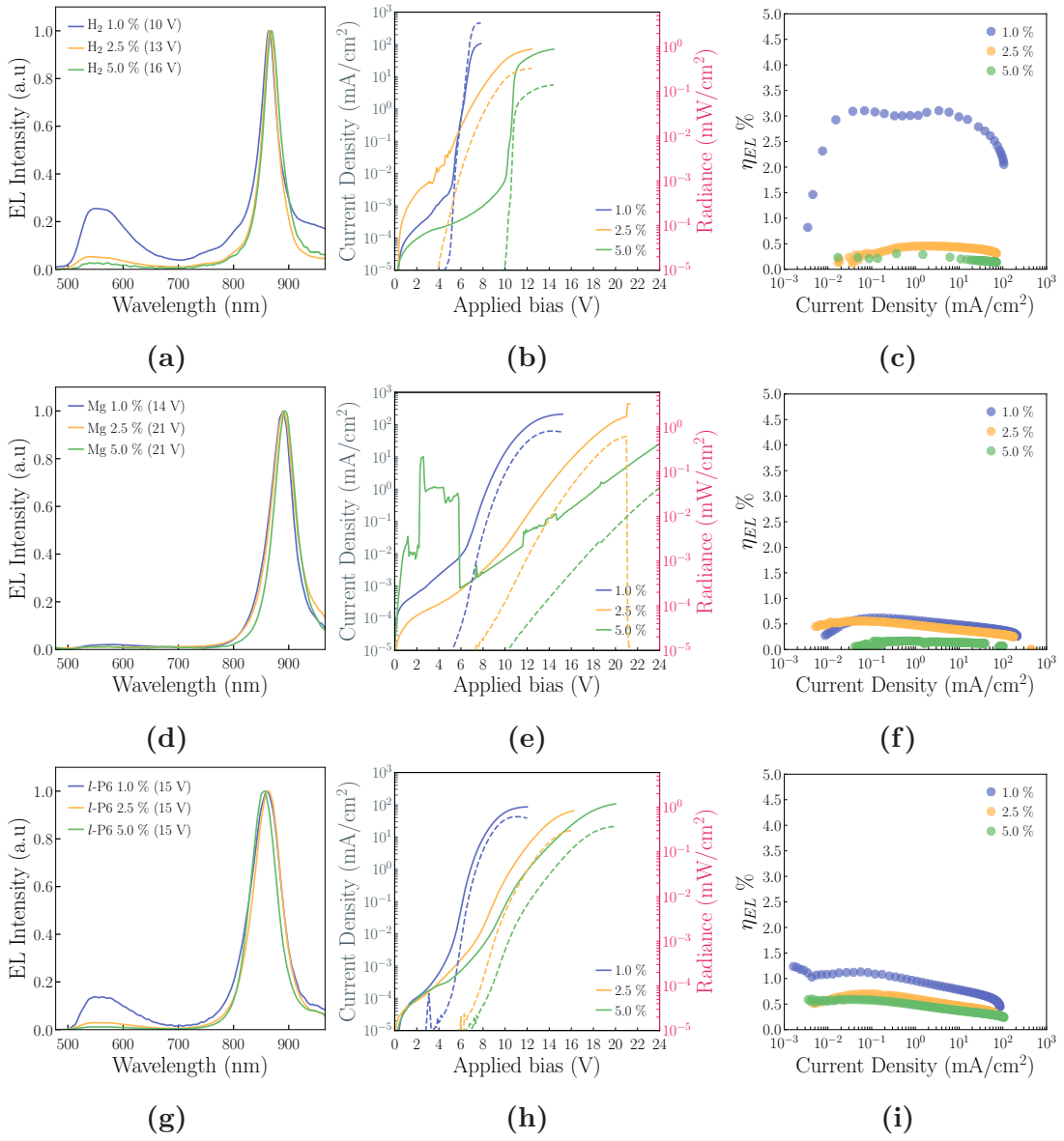

Figure 3.38 | First panel with the optoelectronic properties of the hexamers. Blue lines and symbols represent the F8BT:*l*-P6 *X* 1.0 %, yellow for the 2.5 % and green the 5.0 % loading. **(a, d, g)** (left column) depict the electroluminescence (EL) spectra, **(b, e, h)** (central column) the current density - voltage - radiance (JVR) and **(c, f, i)** (right column) the electroluminescence external quantum efficiency (η_{EL}) of the OLEDs. The legends in **(a, d, g)** refer to the voltage at which the spectra where collected.

Looking at the η_{EL} versus current density curves, the hexamers performed

similarly to the rest of the oligomers, with η_{EL} remaining relatively stable in low to average current densities, exhibiting a roll-off when moving towards higher ones. But with the stark difference of the *l*-P6 H_2 1.0 % that had a remarkably high η_{EL}, that increased with increasing current density, passing to an impressive $\eta_{EL} \sim 3\,\%$ and remaining high until higher current densities of $\sim 1-2\,\mathrm{mA/cm^2}$. The curves presented in Figure 3.38c, similarly to all the other η_{EL} vs J curves above and below, depict the highest value achieved, with several devices maxima being outliers, something that is visible from the average η_{EL}^{max} plots and the high standard deviation. However, *l*-P6 H_2 1.0 % showed a remarkable stability of all devices tested, evident from the low standard deviation in the average maximum η_{EL} reported in Table 3.4, showing this same behaviour. The higher loadings all showed lower values, but still remain impressive considering the spectral range, with EL peaking at $\sim$ 864 nm. Not surprisingly, given the moderate results from the PL characterisation, *l*-P6 Pt exhibited some very low η_{EL} values for all loadings. Plots with all the η_{EL} versus applied bias curves can be found in Figures C.1 through C.8.

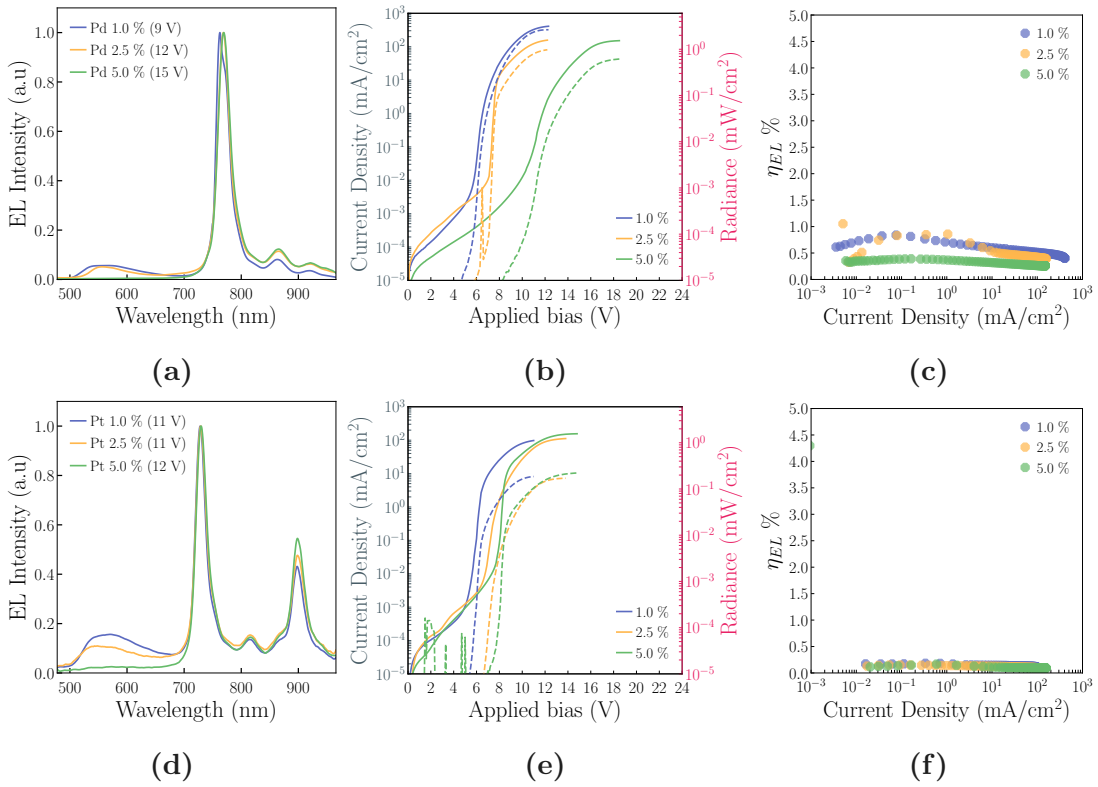

Figure 3.39 | Second panel with the optoelectronic properties of the hexamers. Blue lines and symbols represent the F8BT:*l*-P6 *X* 1.0 %, yellow for the 2.5 % and green the 5.0 % loading. **(a, d, g)** (left column) depict the electroluminescence (EL) spectra, **(b, e, h)** (central column) the current density - voltage - radiance (JVR) and **(c, f, i)** (right column) the electroluminescence external quantum efficiency (η_{EL}) of the OLEDs. The legends in **(a, d, g)** refer to the voltage at which the spectra where collected.

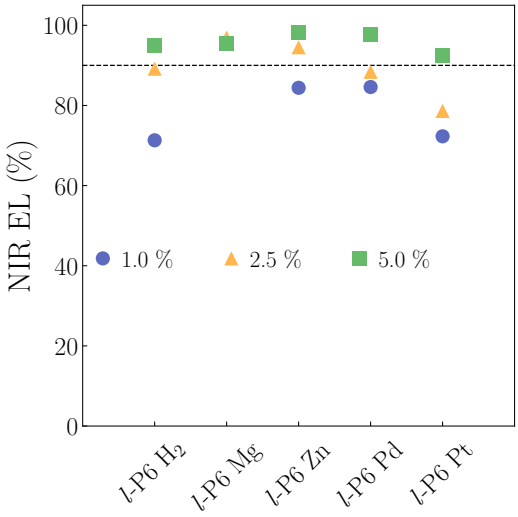

Figure 3.40 | Percentage of photons emitted in the near-infrared (NIR) for the hexamers. Blue symbols represent the 1.0 % blends, yellow the 2.5 % and green the 5.0 % loading. The results were calculated from spectra collected at the saturation voltage, *i.e.* the voltage at which light emission (radiance) is maximum. The dashed line is highlighting the 90 % point.

Regarding the NIR emission, depicted in Figure 3.40, the hexamers showed significant improvement compared to the PL spectra, as expected, with NIR EL being at $> 90\,\%$ for all the hexamers with the 5.0 % loading. 2.5 % loading showed some enhanced host emission, but still was $> 80\,\%$ except the platinum hexamer that had the most blue-shifted singlet EL, peaking at ~ 730 nm, but still showed $> 70\%$ EL for all three loadings. As mentioned above, *l*-P6 Mg had almost completely quenched the F8BT emission resulting in $\sim 100\,\%$ NIR emission

In Figure 3.41 are depicted the η_{EL} results, with η_{EL}^{max} in Figure 3.41a and the average maximum η_{EL} ($\langle \eta_{EL}^{max} \rangle$) in 3.41b. As already discussed, *l*-P6 H_2 1.0 % was crowned "champion" with a $\eta_{EL}^{max} \sim 3.2\,\%$, followed by *l*-P6 Zn 1.0 % achieving a $\eta_{EL}^{max} \sim 1.2\,\%$. Surprisingly, the heavy-metal containing *l*-P6 Pd had $\eta_{EL}^{max} \sim 1\,\%$ for both 1.0 and 2.5 %.

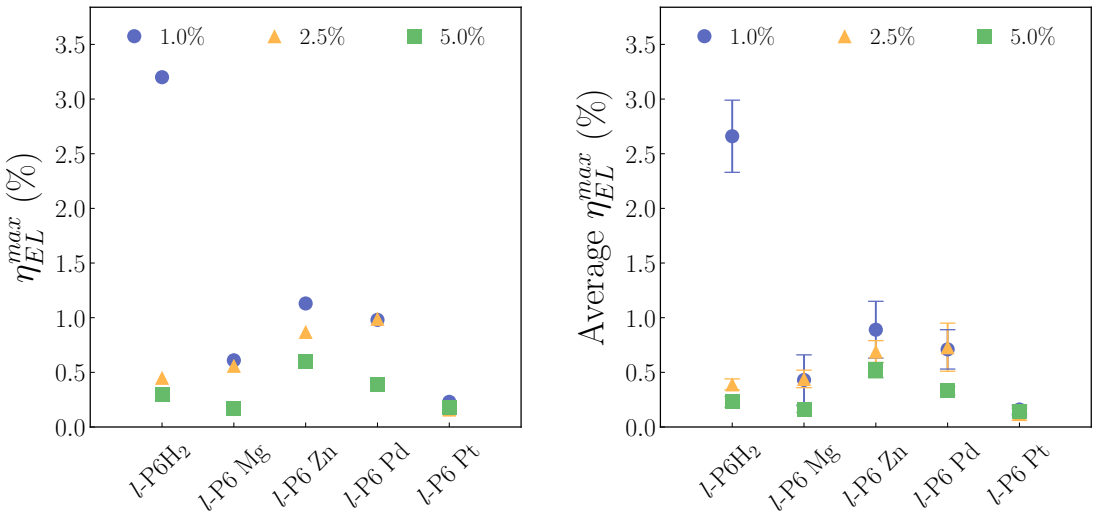

(a) Maximum η_{EL} **(b)** Average maximum η_{EL}

Figure 3.41 | (a) Maximum electroluminescence external quantum efficiency (η_{EL}) and **(b)** average maximum electroluminescence external quantum efficiency (η_{EL}) for the hexamer OLEDs.

Interestingly, the η_{EL}^{max} values achieved were consistent across the different devices tested, as shown in 3.41b by the small standard deviation (errorbar). Notably, *l*-P2 1.0 % from the zinc oligomer series of Section 3.3 yielded a remarkable $\eta_{EL}^{max} \sim 4.3\,\%$ (Figure 3.23a). However, the $\langle \eta_{EL}^{max} \rangle$ of the same sample was at $\sim 1.5\,\%$, with a high standard deviation implying an outlier for the best performing device. Contrarily, *l*-P6 H_2 had a very consistent performance that afforded a substantial $\langle \eta_{EL}^{max} \rangle \sim 2.6\,\%$. Both heavy metal containing *l*-P6 Pd and Pt had $\langle \eta_{EL}^{max} \rangle < 1\,\%$.

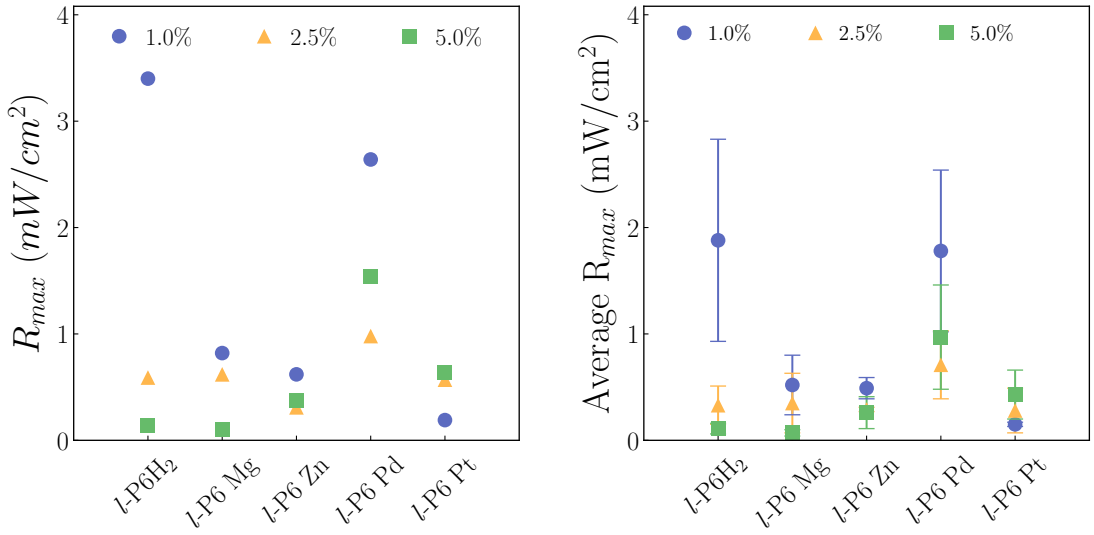

(a) Maximum radiance **(b)** Average maximum radiance

Figure 3.42 | (a) Maximum radiance (R_{max}) and **(b)** average maximum radiance for the hexamer OLEDs.

The same consistency cannot be said for the light output (R) performance of the OLEDs, with the average R_{max} of *l*-P6 H_2 and Pd showing an important errobar, however with impressive maximum values of $\sim$ 3.2 mW/cm^2 and $\sim$ 2.5 mW/cm^2 for the H_2 and Pd respectively. Again, *l*-P6 Pt was termed the worst performer amongst the hexamers, surprisingly though with its highest loading of 5.0 % displaying the highest R amongst the three loadings. *l*-P6 Mg and Zn showed a rather low light output, with values below $\sim$ 1 mW/cm^2, with Mg 5.0 % having an average $R_{max} < 0.1$ mW/cm^2. It was also noteworthy that *l*-P6 Mg 5.0 % was the blend with the worst JVR plots (Figure 3.38e), showing an extended ohmic behaviour and very "rough" JV curves.

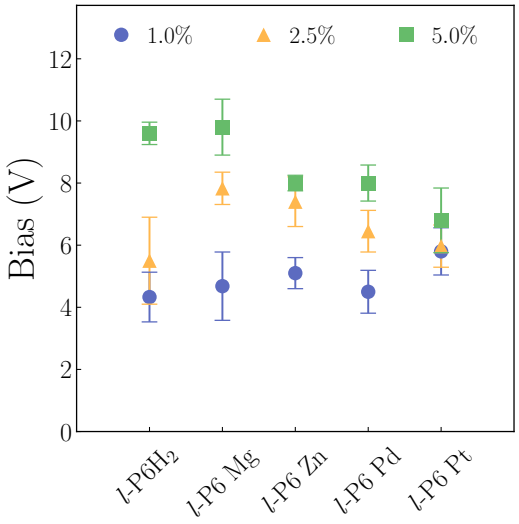

Figure 3.43 | Average turn-on voltage of hexamer OLEDs. As turn-on voltage is defined the voltage at which light emission (radiance) goes above $3.5 \times 10^{-5}\,\mathrm{mW/cm^2}$.

Another impressive characteristic of the hexamers was the trend of decreasing turn on voltage (V_{ON}) with increasing atomic weight of the ligand for the 5.0 %, while for the 1.0 % there was a flat-slightly increasing trend. *l*-P6 H_2 1.0 %, as the best performing so far, had the lowest V_{ON} of $\sim 4\,V$. *l*-P6 Pt was surprisingly consistent across all three loadings, with $V_{ON} \sim 6\,V$. *l*-P6 H_2 and Mg 5.0 % exhibited the highest V_{ON} of the hexamers of $\sim 9.7\,V$. The 2.5 % loading V_{ON} was scattered amongst the hexamers with values ranging from 5.5 and 6 V for H_2 and Pt to 6.5 and $\sim 7.6\,V$ for Pd and Mg and Zn respectively.

All the EL characterisation results presented in the Figures above are summarised in the Table 3.4 below. Further details and direct comparisons with the PL data can be made using the Tables A.4 and A.3 in the appendix.

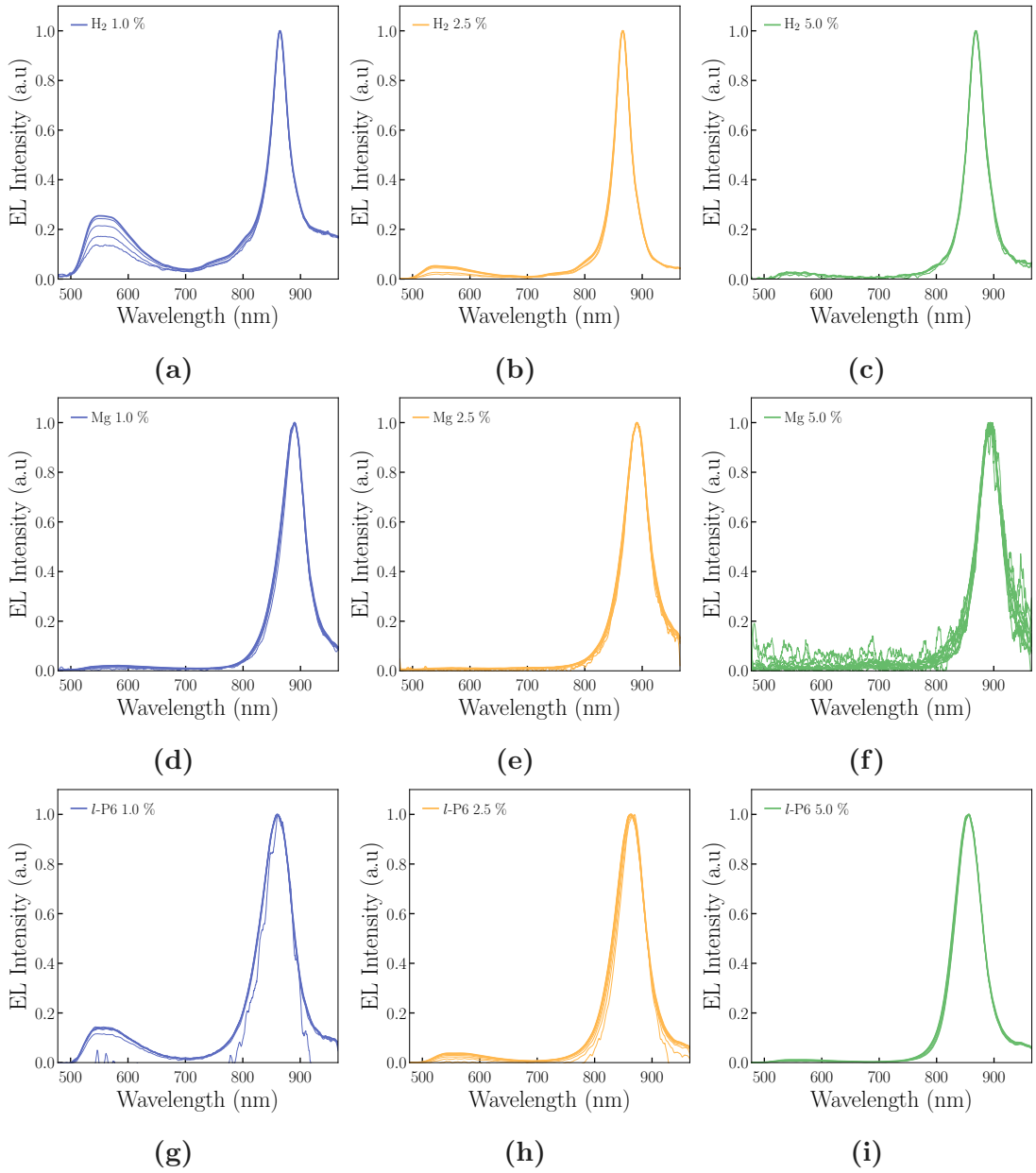

Figure 3.44 | Voltage-resolved spectra for the hexamer OLEDs. Blue lines represent the F8BT:*l*-P6 *X* 1.0 %, yellow for the 2.5 % and green the 5.0 % loading. The spectra collection started at the minimum voltage that was above the detection threshold of our spectrometer and the last (thick lines) was the saturation voltage, the voltage at which radiance was maximum. The spectra were collected in steps of 1 V.

Lastly, in Figures 3.44 and 3.45 are reported the voltage-resolved spectra of the hexamers. Similarly to the zinc oligomer presented in Figures 3.26 and 3.27, the spectra show that at the very V_{ON} it is the hexamers emitting rather than the polymer host, a logical conclusion given that the charges injected with get trapped in the low-energy emitters and recombine there. Increasing the applied bias resulted in an increase of the polymer host emission, more importantly for

the 1.0 % loading.

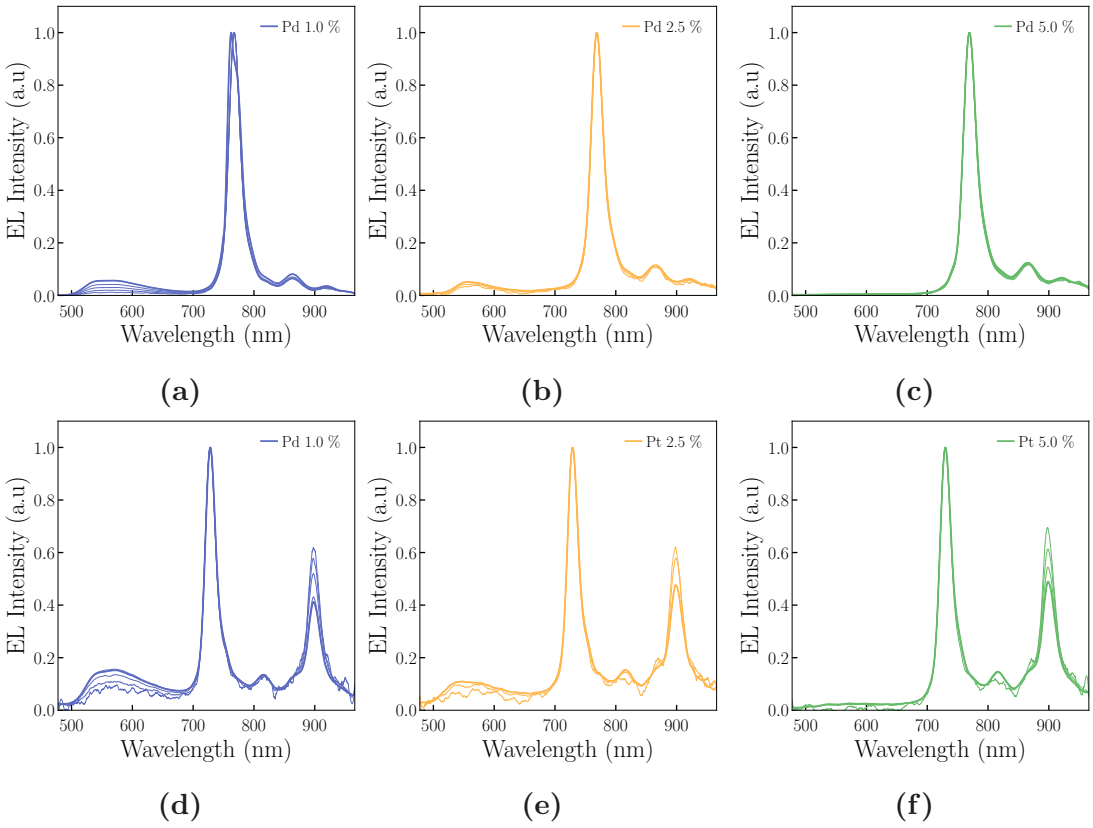

Figure 3.45 | Voltage-resolved spectra for the hexamer OLEDs. Blue lines represent the F8BT:*l*-P6 *X* 1.0 %, yellow for the 2.5 % and green the 5.0 % loading. The spectra collection started at the minimum voltage that was above the detection threshold of our spectrometer and the last (thick lines) was the saturation voltage, the voltage at which radiance was maximum. The spectra were collected in steps of 1 V.

What is impressive, however, with the voltage resolved spectra presented were the ones of *l*-P6 Pt. In all three loadings there is a clear decrease of the intensity of the phosphorescence peak, an observation that is in line with the interpretation of triplet-triplet annihilation (TTA). With the term TTA, a special case of energy transfer is referred to, via electron exchange interactions. TTA occurs when two triplets interact to produce an excited singlet state and a ground singlet state.

The interpretation of TTA in the case of *l*-P6 Pt is evidenced by the increased applied bias, and therefore current density, when more carriers are injected into the emitting layer and TTA becomes the dominant triplet decay process in operating devices. [75, 191] TTA has been observed in F8BT-based OLEDs [192] and the role of the host material is important when TTA is considered. [75] Finally, it is expected to observe an increasing TTA trend with increased current density (a result of the increasing applied bias) as more triplets are formed and

the average distance between triplets is decreased, given that TTA can occur only if two triplet excitons are in close proximity. [183]

F8BT-based OLEDs have been recently demonstrated to exhibit a behaviour of triplet-assisted emission, increasing the efficiency of OLEDs above the singlet allowed threshold. [193] This further increases the complexity of the processes taking place in these devices, allowing for further investigation, *e.g.* in transient EL measurements.

Table 3.4 | Summary of the EL properties of the hexamer OLEDs.

Sample	η_{EL}^{max} (%)	$\langle\eta_{EL}^{max}\rangle$ (%)	R_{max} mW/cm^2	$\langle R_{max}\rangle$ mW/cm^2	V_{ON} (V)
F8BT pure	0.32	0.28 ± 0.04	0.88	0.4 ± 0.19	3.7 ± 0.46
l-P6 H2 1.0 %	3.20	2.66 ± 0.33	3.40	1.88 ± 0.95	4.33 ± 0.8
l-P6 H2 2.5 %	0.50	0.39 ± 0.05	0.60	0.33 ± 0.18	5.5 ± 1.4
l-P6 H2 5.0 %	0.30	0.23 ± 0.05	0.10	0.11 ± 0.05	9.6 ± 0.36
l-P6 Mg 1.0 %	0.60	0.43 ± 0.23	0.80	0.52 ± 0.28	4.68 ± 1.1
l-P6 Mg 2.5 %	0.60	0.44 ± 0.08	0.60	0.35 ± 0.28	7.83 ± 0.52
l-P6 Mg 5.0 %	0.20	0.163 ± 0.03	0.10	0.07 ± 0.03	9.8 ± 0.9
l-P6 Zn 1.0 %	1.10	0.89 ± 0.26	0.60	0.49 ± 0.1	5.1 ± 0.5
l-P6 Zn 2.5 %	0.90	0.69 ± 0.1	0.30	0.29 ± 0.02	7.4 ± 0.8
l-P6 Zn 5.0 %	0.60	0.52 ± 0.07	0.40	0.26 ± 0.15	8 ± 0.25
l-P6 Pd 1.0 %	1.00	0.71 ± 0.18	2.60	1.78 ± 0.76	4.5 ± 0.69
l-P6 Pd 2.5 %	1.00	0.73 ± 0.22	1.00	0.71 ± 0.32	6.45 ± 0.67
l-P6 Pd 5.0 %	0.40	0.33 ± 0.04	1.50	0.97 ± 0.49	8 ± 0.58
l-P6 Pt 1.0 %	0.20	0.16 ± 0.04	0.20	0.15 ± 0.02	5.8 ± 0.76
l-P6 Pt 2.5 %	0.20	0.12 ± 0.06	0.60	0.28 ± 0.21	5.97 ± 0.68
l-P6 Pt 5.0 %	0.20	0.14 ± 0.03	0.60	0.43 ± 0.23	6.8 ± 1.04

3.4.4 Conclusions

In this chapter, the characterisation of six novel linear porphyrin hexamers with different elements coordinating the centre of each porphyrin cavity was reported. Starting from a metal-free porphyrin hexamer to a heavy-metal containing phosphorescent platinum hexamer, they were characterised in dilute solution by means of absorption and emission spectroscopy. The absolute photoluminescence quantum efficiency (η_{PL}) was measured using an integrating sphere and the near-infrared (NIR) was calculated from the photoluminescence (PL) intensity spectra.

The oligomers showed an impressive circa 100 % NIR emission for the metal-free and light metals. The expected phosphorescence from the heavy metals was only present in the case of the platinum hexamer, however with a reduced NIR emission. The palladium hexamer didn't show any signs of phosphorescence, which combined with a very blue-shifted emission compared to the other hexamers, resulted in poor NIR emission performance; both heavy metals containing hexamers had NIR emission in the order of ~ 60 %. In terms of η_{PL}, *l*-P6 Pt showed PL below our detection threshold for photoluminescence efficiency measurements, while *l*-P6 Pd was marginally detectable and yielded a $\langle\eta_{PL}\rangle \sim 1$ %. However, the other three hexamers achieved values in the same order of the rest of the zinc oligomers, with *l*-P6 H_2 having $\langle\eta_{PL}\rangle$ of ~ 20 %, *l*-P6 Mg of $\langle\eta_{PL}\rangle$ of ~ 30 % which was the highest amongst the hexamers, and *l*-P6 Zn having $\langle\eta_{PL}\rangle$ of ~ 28 % too. Furthermore, by using time-correletated single photon counting (TCSPC), the lifetime of the excited states of the hexamers was investigated and found to be very fast, in the $\sim$ ns range, including the palladium and platinum containing ones.

To characterise the hexamers in the solid state, the well-known and well-studied commercial polymer poly[(9,9-di-n-octylfluorenyl-2,7-diyl)-*alt*-(benzo[2,1,3]thiadiazol-4,8-diyl)] (F8BT) was used as host, with the hexamers acting as NIR emitting traps. η_{PL} was high for the *l*-P6 H_2 having $\langle\eta_{PL}\rangle > 10$ % for all loadings, peaking at ~ 32 % for the 1.0 %. *l*-P6 Mg had severely lowered $\langle\eta_{PL}\rangle$ of ~ 10 % for the 1.0 % and lower for the higher concentrations, similar to the *l*-P6 Pd and Pt, while *l*-P6 Zn achieved a reasonable ~ 23 % for the 1.0 %, lowering with increasing loading however. In terms of NIR emission, the blends showed scattered performance, with the magnesium hexamer showing the larger proportion of photons emitted in the $\lambda > 700$ nm and the platinum being the worse.

By incorporating the blends as active layer in organic light-emitting diodes (OLEDs), very high electroluminescence external quantum efficiency (η_{EL}) up to 3.2 % was achieved with NIR emission remaining well above 90 % for many

oligomers. These results proved to be a challenge to the energy gap law and pave the way for the fabrication of NIR emitting OLEDs with heavy-metal-free material. With a scope of having biocompatible NIR emitting high η_{EL} OLEDs, *l*-P6 H_2 proved to be an ideal candidate. Despite the heavy metal platinum, *l*-P6 Pt didn't prove as efficient as other phosphorescent platinum porphyrins reported in the literature, however verified that porphyrin oligomers with their high spatial difference between the signlet and triplet excited states are efficient intersystem crossing (ISC) suppressors.

3.5 Novel zinc porphyrin pentamer

Continuing the study of porphyrin oligomers, a new pentamer was synthesised and characterised. As mentioned above, the synthesis was carried out by Dr. Lara Tejerina at the group of Prof. Harry L. Anderson, FRS at the Chemistry Research Laboratory of the University of Oxford. The characterisation was carried out during the secondment placement of Dr. Tejerina in UCL.

Contrary to the zinc porphyrin pentamer part of the study presented in Section 3.3, this pentamer has shorter, π-conjugated single acetylene bonds between adjacent units. This results in a shorter oligomer with extended conjugation along the whole molecule, which translates in red-shifted emission compared to the butadiyne-linked oligomers described above. Similarly to the *l*-Pn oligomers, zinc was the coordinating metal at the centre of each unit in this pentamer too.

The chemical structure of the porphyrin is depicted in Figure 3.46 below. The oligomer has the same trihexylsilyl (THS) sidechains as the porphyrin oligomers studied in Section 3.3 above and shown in Figure 3.4. However, this pentamer had different ending units in place of THS, namely 3-cyanopropyldiisopropylsilyl (CPDIPS). In the frame of this Section, this pentamer is referred to as CP-*l*-P5 to distinguish it from the *l*-P5 described above.

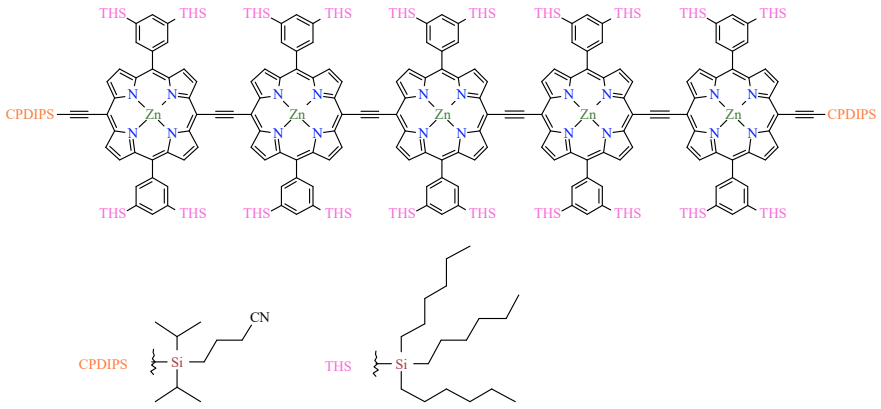

Figure 3.46 | Chemical structure of the novel single acetylene linked pentamer. The new CP-*l*-P5 pentamer has the same THS sidechains as previously reported, with new CPDIPS ending groups and zinc as the coordinating metal at the centre of each porphyrin unit.

3.5.1 Solution photoluminescence of the zinc porphyrin pentamer

The absorption and photoluminescence (PL) spectra are illustrated in Figure 3.47a, while the contour plot of the PL decay is shown in Figure 3.47b.

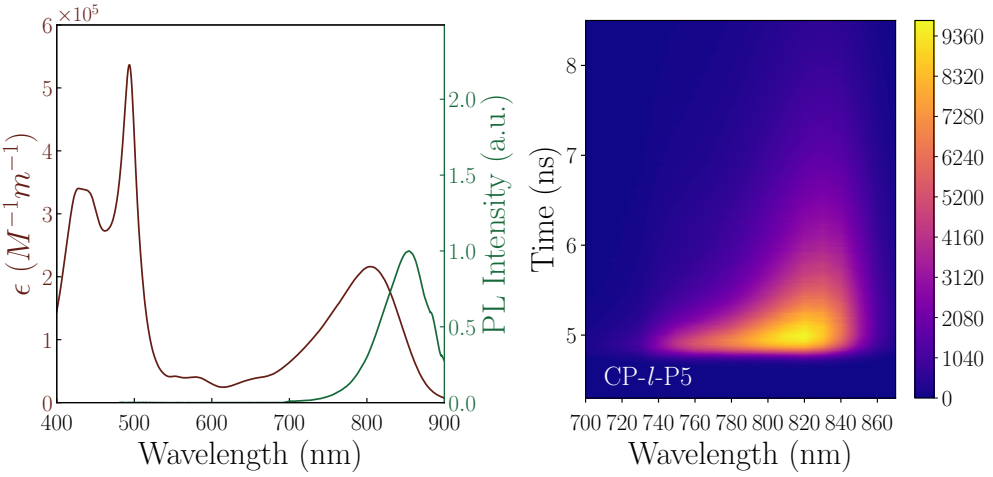

Figure 3.47 | (a) Extinction coefficient in red and photoluminescence (PL) in green of the novel CP-*l*-P5 pentamer in dilute anhydrous toluene solution (∼ µg/ml). **(b)** TCSPC time decay contour plot of the oligomer in dilute toluene solution (∼ µg/ml). The time scale is 4.3 ns to 8.5 ns confirming the fluorescence emission of the oligomers. The colour scale is counts. The spectrum was collected integrating for 900 s for each wavelength. The $\Delta\lambda$ of the collection was set to 10 nm and the time decay was collected every 10 nm, with a repetition rate of the 450 nm picosecond laser at 50 MHz.

As already mentioned, this oligomer has significantly red-shifted emission with the Q_x band peaking at 805 nm, a ∼ 25 nm red-shift compared to *l*-PN, the zinc oligomer with the most red-shifted Q_x band (Figure 3.5 and Table A.1). Not surprisingly, the Soret band remained in the same region as the butadiyne-linked oligomers, ∼ 400 − 550 nm. This oligomer showed an important Stokes' shift of ∼ 50 nm, more than double compared to the second from the butadiyne-linked (Table A.1). CP-*l*-P5 also showed the further near-infrared (NIR) emission, with its PL peaking at ∼ 853 nm and an impressive spectral purity of > 99.9 % of photons at $\lambda > 700$ nm. CP-*l*-P5 achieved a photoluminescence quantum efficiency (η_{PL}) in solution of ∼ 30 %-in line with the other oligomers (see Figure 3.7).

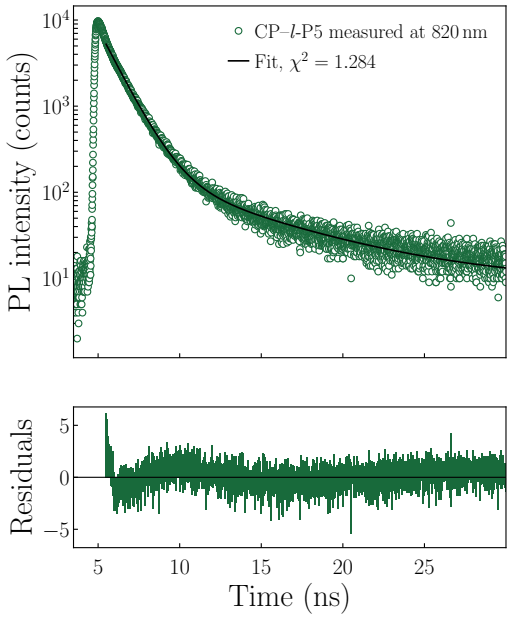

Figure 3.48 | TCSPC time decay plot of the oligomer in dilute toluene solution ($\sim$ µg/ml), the respective tail fit is shown with black solid line and the corresponding goodness of the fit (χ^2) is noted. Below each plot are the weighted residuals of the fit. The time scale is 5 ns to 30 ns and the spectrum was collected integrating for 900 s.

The effectiveness of these oligomers to suppress intersystem crossing (ISC) has been demonstrated with the heavy metal containing hexamers above, and this pentamer has a fluorescence emission, as demonstrated in Figures 3.47b and 3.48, where the TCSPC decay spectra are shown and the respective fit. [12] Notably, when fitted with the bi-exponential decay, the pentamer had a $\tau \sim 2$ ns decay lifetime. By using the η_{PL} and τ values, the radiative and non-radiative rates can be calculated and were $k_r \sim 0.15\,\text{ns}^{-1}$ and $k_{nr} \sim 0.34\,\text{ns}^{-1}$.

All these characteristics add up to a very promising material in this unexplored field of NIR emitters, and it was further characterised in the solid state. The same polymer used in this study, *i.e.* poly[(9,9-di-n-octylfluorenyl-2,7-diyl)-*alt*-(benzo[2,1,3]thiadiazol-4,8-diyl)] (F8BT) was chosen as its host, since the impressive results yielded so far. The chemical structure of F8BT is shown in Figure 3.49c. However, a second polymer was also used to explore the difference when using hosts with different energy gaps.

A previous work by Minotto et al. had shown that a novel red emitting polymer, Poly[4,4,9,9-tetrakis(4-hexylphenyl)-4,9-dihydro-s-indaceno[1,2-b:5,6-b']dithiophene2,7-diyl-*alt*-5,5'-bis(2-octyldodecyl)-4H,4'H-[1,1'-bithieno[3,4-

[12] *N.B.* The TCSPC spectrum has the same time scale as the plots of Figure 3.9, and was collected from similar concentration and conditions to facilitate the comparisons.

c]pyrrole]- 4,4',6,6'(5H,5'H)-tetrone-3,3'-diyl] (PIDT-2TPD), combined with a NIR emitting guest has yielded impressive results. [90] To examine the prospects of CP-*l*-P5, PIDT-2TPD was also used as a host polymer. The chemical structure of PIDT-2TPD is illustrated in Figure 3.49 below.

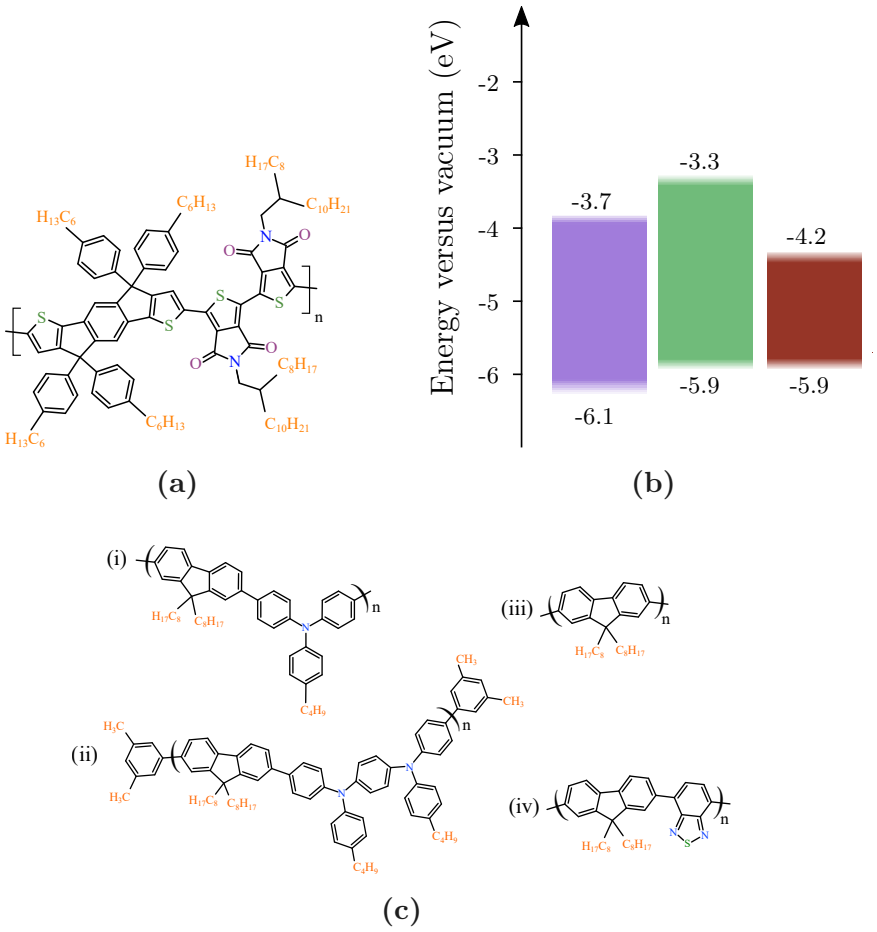

Figure 3.49 | **(a)** Chemical structure of the novel red-emitting polymer, PIDT-2TPD, abbreviated here as PIDT-2TPD. **(b)** Energy levels (highest occupied molecular orbit (HOMO) and lowest unccupied molecular orbit (LUMO)) of the PIDT-2TPD (purple) and F8BT (green). For PIDT-2TPD (-3.7 and -6.1 eV) and CP-*l*-P5 (-4.2 and -5.9 eV) correspond to the cyclic voltammetry measurements [90]. **(c)** Chemical structures of the four polymer hosts used with CP-*l*-P5. **(i)** poly[(9,9-dioctylfluorenyl-2,7-diyl)-*alt*-(4,4'-(N-(p-butylphenyl))diphenylamine) (TFB) and the three polyfluorene derivatives: **(ii)** poly[(9,9-dioctylfluorenyl-2,7-diyl)-*co*-(N,N'-diphenyl)-N,N'-di(pbutylphenyl)-1,4-diamino-benzene)] (PFB), **(iii)** polyfluorene (PFO) and **(iv)** poly[(9,9-di-n-octylfluorenyl-2,7-diyl)-*alt*-(benzo[2,1,3]thiadiazol-4,8-diyl)] (F8BT). The values of F8BT are taken from [87, 178].

In addition to F8BT, three more blue emitting polymers were used as hosts. Like the *l*-P6 experiments discussed above, to investigate

the energy transfer processes with hosts that emit at higher energies, three blue emitting polyfluorene derivatives were used with CP-*l*-P5 in 1.0 % loading. Notably, the three polymers, depicted in Figure 3.49c, are polyfluorene (F8), poly[(9,9-dioctylfluorenyl-2,7-diyl)-*alt*-(4,4'-(N-(p-butylphenyl))diphenylamine) (TFB) and poly[(9,9-dioctylfluorenyl-2,7-diyl)-*co*-(N,N'-diphenyl)-N,N'-di(pbutylphenyl)-1,4-diamino-benzene)] (PFB).

Similarly to what the TFB:*l*-P6 experiments showed (*vide infra*), the η_{PL} and overall device behaviour, in terms of turn-on voltage, light output and electroluminescence external quantum efficiency (η_{EL}), with these blends were not comparable to those achieved by F8BT and PIDT-2TPD. In favour of brevity, the results are omitted from this Section, but are noted in Table A.5.

3.5.2 Solid-state photoluminescence of zinc porphyrin pentamer

To maintain consistency throughout the experiments, and facilitate the comparisons, the same three loadings were made, from the same three guest:host concentrations were characterised, *i.e.* 1.0, 2.5 and 5.0 w/w %. The process of preparing the solutions is detailed in Chapter 2.

The PL spectra of the pure polymers and of the blends are shown in Figure 3.50 below. The absorption spectra are omitted for simplicity since are dominated by the hosts absorption. However, similar to the observations noted above of using a different host for *l*-P6 (Figure 3.13), the pentamer has a different conformation when diluted in the two polymers resulting in the Q_x band peaking at $\sim$ 880 nm for the F8BT blends and $\sim$ 830 nm for the PIDT-2TPD blends.

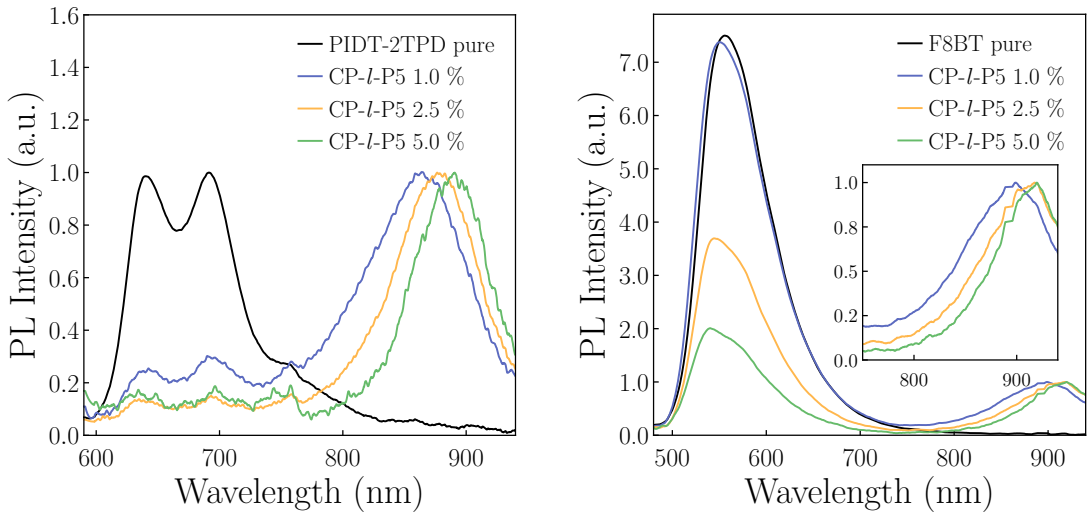

(a) PIDT-2TPD blends **(b)** F8BT blends

Figure 3.50 | Photoluminescence spectra of the novel CP-*l*-P5 pentamer in blends with **(a)** F8BT and **(b)** PIDT-2TPD, spin coated on glass spectrosils ($\sim$ 100 nm thick), collected inside the integrating sphere using a 445 nm diode laser for the F8BT blends and 520 nm diode laser for the PIDT-2TPD blends. All the spectra have been normalised for the oligomers emission to highlight the gradual quenching of the hosts in favour of the guest emission. Blue represent the 1.0 % loading, yellow the 2.5 % and green the 5.0 %, while with black are the pure polymers. The inset in (b) highlights the red-shifting of the CP-*l*-P5 emission.

Similarly, the PL was significantly red-shifted compared to the solution, but also showed different emission peaks in the two different hosts. The F8BT blends had a red-shifted emission peaked at 894 nm for the F8BT:CP-*l*-P5 1.0 %, while 2.5 and 5.0 % peaked at 917 nm (inset of Figure 3.50b), a small variation already observed in the electroluminescence (EL) emission of the butadiyne-linked

zinc oligomers (notably Figures 3.20j and 3.21g), but also of the *l*-P6 in the TFB blends (Figure 3.28). The same phenomenon is observed in the PIDT-2TPD:CP-*l*-P5 blends, with a progressive red-shift from 861 nm for the 1.0 %, to 876 nm for the 2.5 %, to 891 nm for the 5.0 % (Figure 3.50a). This slight red-shift with increasing CP-*l*-P5 concentration is consistent with aggregation, also corroborated by the reduced photoluminescence quantum efficiency (η_{PL}) (Figure 3.51a).

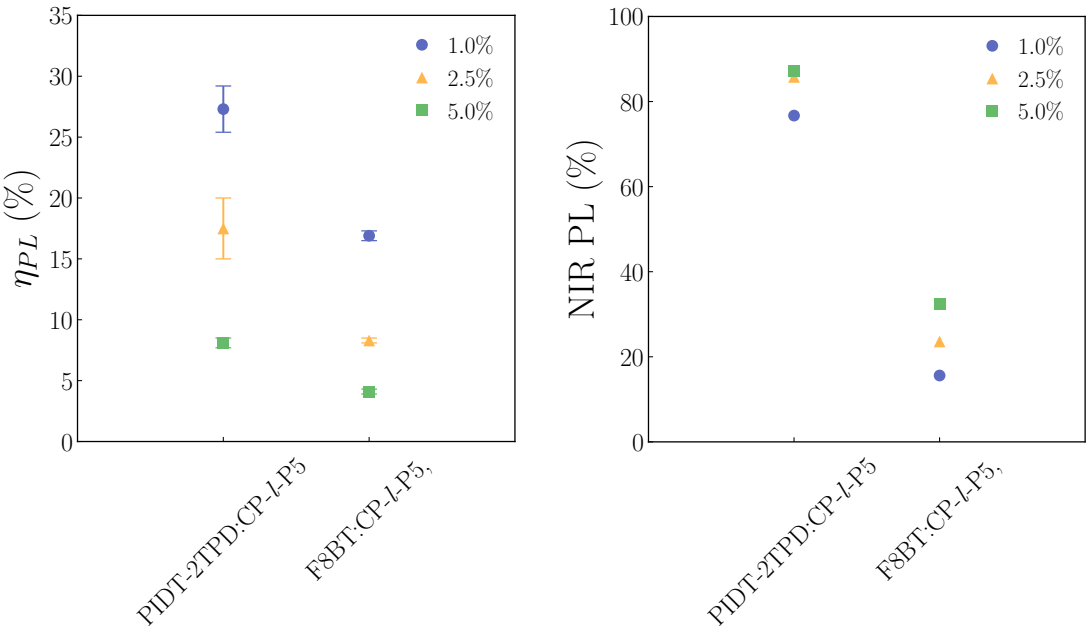

(a) η_{PL} **(b)** % of NIR PL

Figure 3.51 | (a) photoluminescence quantum efficiency (η_{PL}) **(b)** near-infrared (NIR) photoluminescence (PL) of the PIDT-2TPD: and F8BT: CP-*l*-P5 blends. With blue is the 1.0 %, yellow is the 2.5 % and green is the 5.0 % loading.

This batch of F8BT used for the pentamer experiments had an $\langle\eta_{PL}\rangle \sim 50\,\%$. When CP-*l*-P5 is blended, F8BT blends showed a progressively reducing $\langle\eta_{PL}\rangle$ from $\sim 17\,\%$ for 1.0 %, to $\sim 8\,\%$ for 2.5 % and $\sim 4\,\%$ for 5.0 %. Contrarily, and as expected, increasing the loading gradually quenched the host emission, achieving a 15 % NIR PL for 1.0 %, 23 % for 2.5 % and 32 % for 5.0 %.

Pure PIDT-2TPD in the solid state yielded an $\langle\eta_{PL}\rangle \sim 30\,\%$, slightly lower than the commercial F8BT. Interestingly, PIDT-2TPD blends achieved higher $\langle\eta_{PL}\rangle$ values, even though decreasing with increasing CP-*l*-P5 loading. Notably, 1.0 % showed an $\langle\eta_{PL}\rangle$ of $\sim 27\,\%$, 2.5 % showed $\sim 17\,\%$ and 5.0 % showed $\sim 8\,\%$. The higher values of NIR PL of 77 % for 1.0 %, 86 % for 2.5 % and 87 % for 5.0 % indicated a more efficient Förster resonant energy transfer (FRET) from the red-emitting PIDT-2TPD rather than F8BT.

All the results presented above are summarised in the detailed Table A.1 and presented in the same table as the other zinc porphyrin oligomers to facilitate comparisons.

Both results from these blends in the solid state, along with the excellent results from the F8BT blends and the butadiyne-linked oligomers of Section 3.3 above and the impressive performance in Minotto *et al.* in [90], all lead to the expectation of efficient organic light-emitting diodes (OLEDs), that were fabricated and characterised, and are presented below.

3.5.3 Zinc porphyrin pentamer OLEDs

Given the comparatively good results achieved in the photoluminescence (PL) characterisation described in Sections 3.5.1 and 3.5.2 above, OLEDs were fabricated, using the same blends and loading as presented above as the emissive layers. The detailed procedure for the fabrication process is described above in Section 2.6. The OLEDs have the typical multilayer structure using indium tin oxide (ITO) as the transparent anode and poly(3,4-ethylenedioxythiophene)-poly(styrenesulfonate) (PEDOT:PSS) as a hole transporting layer. The active layer is spin coated on top of PEDOT:PSS, and finally the metal cathodes are thermally evaporated including a layer of calcium and a protective layer of aluminium. The resulting architecture is ITO/PEDOT:PSS/Active layer/calcium/aluminium, illustrated in Figure 3.52, that has afforded very good results in the past and our group has an extensive expertise in optimising the deposition processes.

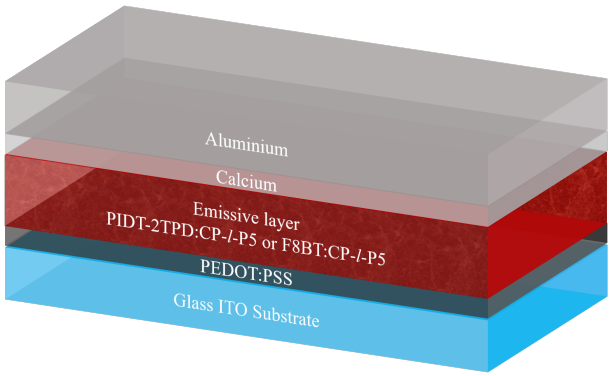

Figure 3.52 | Illustration of the architecture of the organic light-emitting diodes (OLEDs) fabricated. The architecture is ITO/PEDOT:PSS/Emissive layer/calcium/aluminium, where as emissive layer with red is illustrated the PIDT-2TPD:CP-*l*-P5 blends and with yellow the F8BT:CP-*l*-P5.

Similar to the results presented above, the electroluminescence (EL) spectra are on the first column (left), the current density - voltage - radiance (JVR) curves in the second (middle) and the electroluminescence external quantum efficiency (η_{EL}) versus current density on the third (right) for each of the F8BT:*l*-Pn blends. Blue lines and symbols represent the F8BT:*l*-Pn 1.0 %, yellow for the 2.5 % and green the 5.0 % loading. In the JVR curves, solid lines refer to the current density versus voltage measured in mA/cm^2, whereas dashed lines to the radiance versus voltage, measured in mW/cm^2. Radiance was chosen, rather than luminance for the light emission of the devices since the largest part of the EL is in the NIR.

Starting from the EL spectra, both blends performed remarkably well in terms of host quenching and % of NIR emission. Following the previous trends,

increasing the guest loading progressively quenched the emission of the host polymer. Similar to some of the previous EL spectra, a small red-shift is observed with increasing concentration of the pentamer in the polymer matrix, notable in the CP-*l*-P5 blends from $\sim$ 840 nm for the 1.0 % loading, to $\sim$ 845 nm for the 2.5 %, to $\sim$ 860 nm for the 5.0 %. For the F8BT:CP-*l*-P5 blends a smaller shift was observed from $\sim$ 880 nm for the 1.0 % to $\sim$ 896 nm for the higher loadings. Similar behaviour of progressively red-shifting emission with increasing concentration of a dopant in host-guest architectures has also been reported in the literature. [91] However, just as the PL results (Figure 3.50), EL is peaked at lower energies for the F8BT blends, indicating a different, more planar, conformation of the oligomer. It is worth noting that this red-shift could also be interpreted as signs of aggregation.

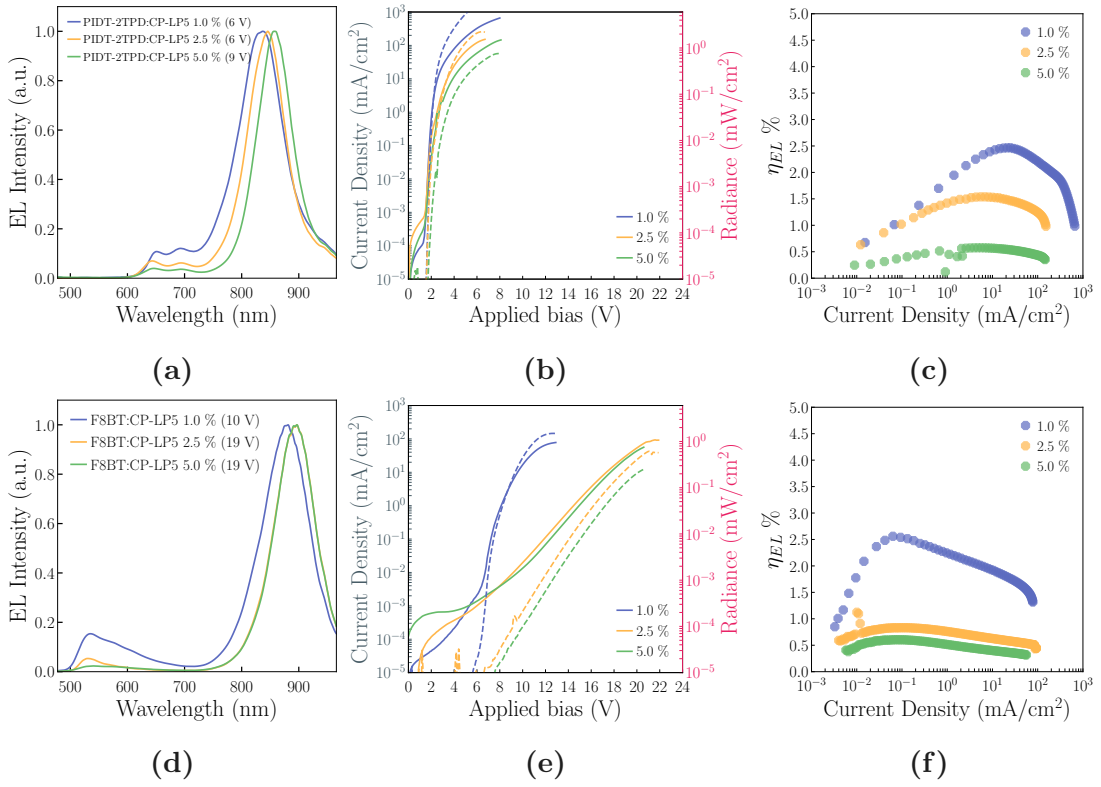

Figure 3.53 | Panel with the optoelectronic properties of the novel pentamer. Blue lines and symbols represent the F8BT:*l*-P6 *X* 1.0 %, yellow for the 2.5 % and green the 5.0 % loading. **(a, d, g)** (left column) depict the electroluminescence (EL) spectra, **(b, e, h)** (central column) the current density - voltage - radiance (JVR) and **(c, f, i)** (right column) the electroluminescence external quantum efficiency (η_{EL}) of the OLEDs. The legends in **(a, d, g)** refer to the voltage at which the spectra where collected.

It is evident from the EL spectra in Figures 3.53a and 3.53d that the emission is predominantly at $\lambda > 700$ nm. Notably, PIDT-2TPD:CP-*l*-P5 blends outperformed the F8BT blends in terms of NIR emission with $>$ 93 % of the

photons in the NIR for the 1.0 % peaking at > 99 % for the 5.0 %, while the 2.5 % had > 96 % in the NIR. F8BT:CP-*l*-P5 blends performed equally well for the higher concentrations with > 96 and > 97 % for the 2.5 and 5.0 % loadings respectively. The 1.0 %, as it is also visible from the EL spectrum, showed a more important host emission showing, nevertheless, >84 % of photos at $\lambda > 700$ nm. These results are summarised in Figure 3.54. It is interesting to compare the EL NIR emission to the PL one (Figures 3.54 and 3.51b respectively). The more strongly quenched polymer hosts in both cases suggest that in the OLEDs, the radiative mechanism is direct recombination in the low-energy sites of the porphyrin. Similar results were observed in all previous OLED experiments using F8BT as host (Figures 3.22 and 3.40 for the zinc oligomer series and the hexamers respectively).

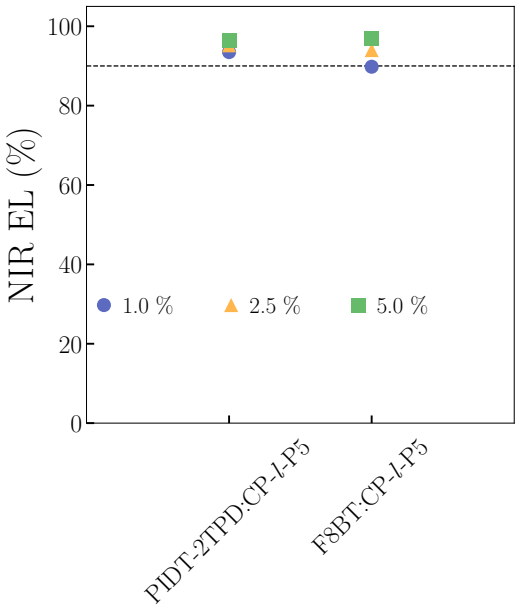

Figure 3.54 | Percentage of photons emitted in the near-infrared (NIR) for the zinc pentamer. Blue symbols represent the 1.0 % blends, yellow the 2.5 % and green the 5.0 % loading. The results were calculated from spectra collected at the saturation voltage, *i.e.* the voltage at which light emission (radiance) is maximum. The dashed line is highlighting the 90 % point.

In Figure 3.55a are presented the maximum values of electroluminescence external quantum efficiency (η_{EL}) for each of the different blends and in Figure 3.55b are depicted the values of the average of the η_{EL} achieved for each device. As mentioned in Chapter 2, each device comprises from 6 pixels. For the CP-*l*-P5 experiments, 2 devices (*i.e.* 12 pixels) were fabricated with F8BT and PIDT-2TPD for each loading of 1.0 and 2.5 %, and one device for the higher 5.0 % loading, expecting a lower performance from the higher loading. While the F8BT blends achieved a slightly higher η_{EL}^{max} of $\sim$ 2.5 %, PIDT-2TPD blends showed a

more consistent operation with the maximum values showing a lower standard deviation with a higher average maximum value of $\sim 1.96\,\%$ for the $1.0\,\%$ blends. In both blends, as per the other zinc oligomers, increasing the loading of the porphyrin resulted in reduced η_{EL}, a sign of concentration aggregation. Therefore, higher concentrations exhibited a progressively reducing η_{EL}^{max}, however with more consistent values for both blends. Plots with all the η_{EL} versus applied bias curves can be found in Figures C.1 through C.8.

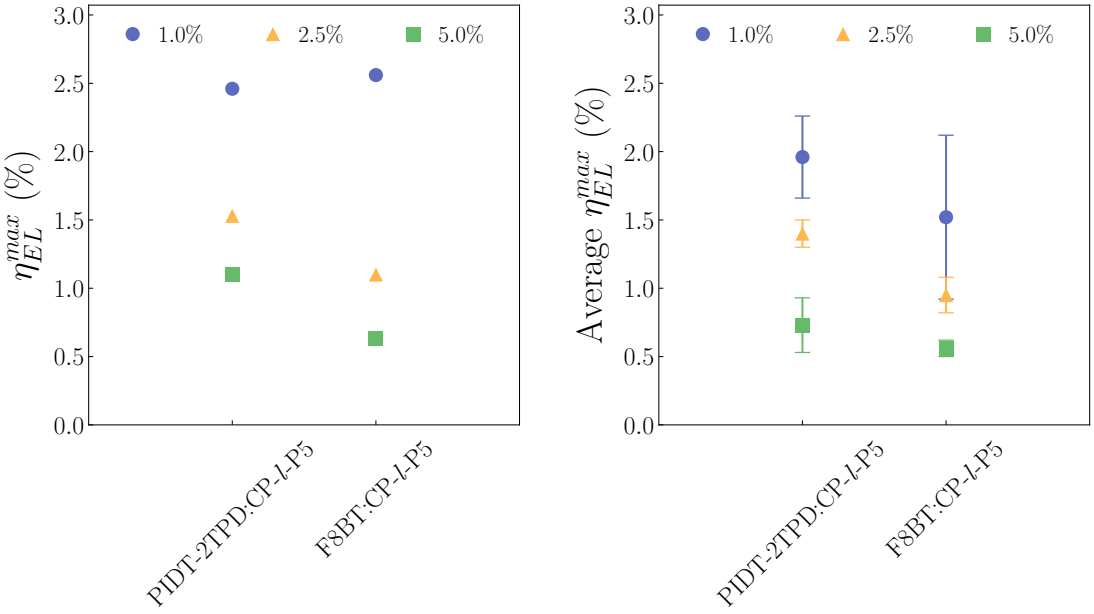

(a) Maximum η_{EL} **(b)** Average maximum η_{EL}

Figure 3.55 | (a) Maximum electroluminescence external quantum efficiency (η_{EL}) and **(b)** average maximum electroluminescence external quantum efficiency (η_{EL}) for the CP-*l*-P5 OLEDs.

Interestingly, despite the similar performance in terms of η_{EL}, the two blends had very different behaviour in light emission, with the PIDT-2TPD blends showing higher radiance (R) values of $\sim 3.5\,\mathrm{mW/cm^2}$, in the same order of magnitude of the *l*-P2 and *l*-P3 (Figure 3.24a), but with lower standard deviation, indicating, again, a more consistent good performance from the CP-*l*-P5. This can be explained by the higher current densities that flowed through the PIDT-2TPD devices, compared to the F8BT ones, resulting in more recombination and therefore higher light output (Figures 3.53b and 3.53e).

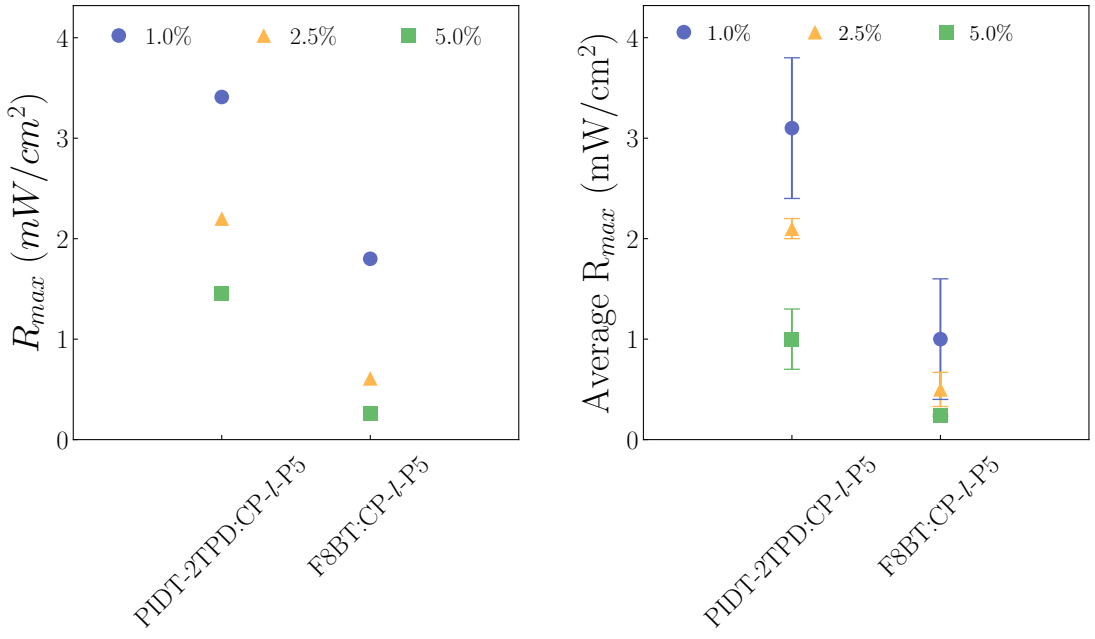

(a) Maximum radiance **(b)** Average maximum radiance

Figure 3.56 | (a) Maximum radiance and **(b)** average maximum radiance for the zinc pentamer OLEDs.

Another significant difference in the performance of the two blends was that the turn-on voltage (V_{ON}) for the PIDT-2TPD blends was almost stable across all the devices and blends at 1.6 V with very steep JVR curves that saturate at $\sim$ 6 V, while the F8BT:CP-i-P5 1.0 % has a V_{ON} $\sim$ 5 V, with the two higher concentration at $>$ 8 V, similar to the rest of the oligomers (Figure 3.25), however a property that is mostly attributed to the polymer host, rather than the porphyrin guest. It is noteworthy, though, that the guests in all cases had an important effect on the turn on voltage by modifying the energetic barrier for bipolar charge injection. Looking at the shape of the pre-V_{ON} JV curve, the expected quadratic dependency was not observed indicating a trap-mediated charge transport.

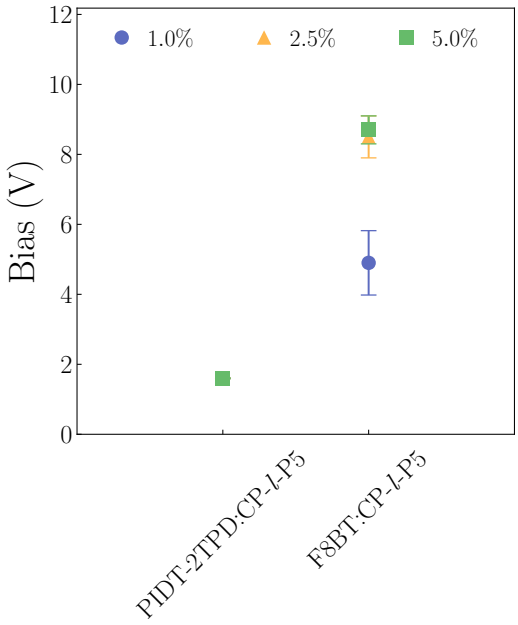

Figure 3.57 | Average turn-on voltage of the pentamer OLEDs. As turn-on voltage is defined the voltage at which light emission (radiance) goes above 3.5×10^{-5} mW/cm^2.

Lastly, as per the blends in all the previous oligomers presented in this Chapter, the very first photons emitted from the OLEDs are photons emitted from the guest. This is visible from the voltage-resolved spectra in Figure 3.58 below. Again, similarly to the other zinc oligomers, the 1.0 % blend devices showed emission spectra that were unstable in regards of host/guest ratios, especially for the F8BT blends. Notably, they showed a progressively increasing emission of the polymer host with the increase of the applied bias, *i.e.* the number of injected charge carriers, attributed to the saturation of emission sites. However, the absence of such behaviour from the PIDT-2TPD blends could be an indication of some long-lived processes, such as thermally-activated delayed fluorescence or triplet-triplet annihilation.

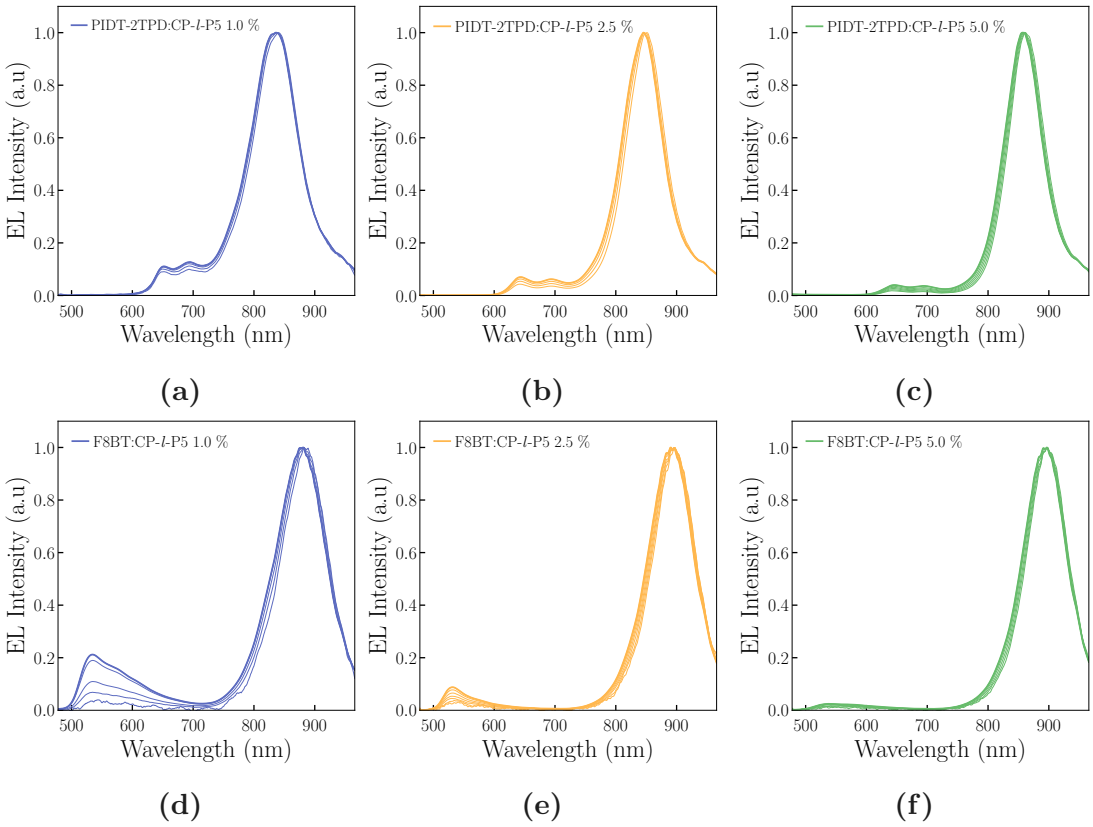

Figure 3.58 | Voltage-resolved spectra for the pentamer OLEDs. Blue lines represent the polymer:CP-*l*-P5 1.0 %, yellow for the 2.5 % and green the 5.0 % loading. The spectra collection started at the minimum voltage that was above the detection threshold of our spectrometer and the last (thick lines) was the saturation voltage, the voltage at which radiance was maximum. The spectra were collected in steps of 1 V.

It is worth mentioning that in all metrics captured and presented so far, the butadiyne-linked *l*-P5 was significantly outperformed by CP-*l*-P5, same as all the other zinc, butadiyne linked oligomers emitting in the same spectral region. This makes CP-*l*-P5 as a very good candidate for NIR emitting, heavy-metal free, efficient OLEDs. When these results are compared to the efficiencies reported in literature in the Zampetti *et al.*, they are found to outperform many of the reports. [79]

All the aforementioned results are summarised in Table 3.5. A more extensive comparison of the results can be found in the appendix, in Table A.5.

Table 3.5 | Summary of the EL properties of the CP-*l*-P5 OLEDs.

Sample	η_{EL}^{max} (%)	$\langle\eta_{EL}^{max}\rangle$ (%)	R_{max} (mW/cm^2)	$\langle R_{max}\rangle$ (mW/cm^2)	V_{ON} (V)
PIDT-2TPD pure		1.55 ± 0.1		2.3 ± 0.5	1.7 ± 0.01
PIDT-2TPD 1.0 %	2.46	1.96 ± 0.3	3.41	3.1 ± 0.7	1.6 ± 0.01
PIDT-2TPD 2.5 %	1.53	1.4 ± 0.1	2.20	2.1 ± 0.1	1.6 ± 0.01
PIDT-2TPD 5.0 %	1.10	0.73 ± 0.2	1.45	1 ± 0.3	1.6 ± 0.01
F8BT pure	0.95	0.77 ± 0.3	3.60	2.8 ± 0.8	3.3 ± 0.3
F8BT 1.0 %	2.56	1.52 ± 0.6	1.80	1 ± 0.6	4.9 ± 0.92
F8BT 2.5 %	1.10	0.95 ± 0.13	0.61	0.5 ± 0.17	8.5 ± 0.6
F8BT 5.0 %	0.63	0.56 ± 0.06	0.26	0.24 ± 0.01	8.7 ± 0.4

Further to PIDT-2TPD and F8BT, three more polymers were investigated as polymer hosts, similarly to the hexamer *l*-P6 presented above (Figure 3.28). The three polymers are poly[(9,9-dioctylfluorenyl-2,7-diyl)-*alt*-(4,4'-(N-(p-butylphenyl))diphenylamine) (TFB), poly[(9,9-dioctylfluorenyl-2,7-diyl)-*co*-(N,N'-diphenyl)-N,N'-di(pbutylphenyl)-1,4-diamino-benzene)] (PFB) and polyfluorene (PFO). The chemical structures of these polymers are presented in Figure 3.49c. However, the results obtained were not comparable to the ones afforded by F8BT and PIDT-2TPD and are omitted for simplicity and brevity, they are presented, however, in the Table A.5 for comparison.

3.5.4 Zinc porphyrin pentamer OLEDs lifetime

Since the very short time that passed between the synthesis of the CP-*l*-P5 and the characterisation reported above, and the creation of some custom LabVIEW routines (Chapter 2), it was possible to carry out lifetime measurements on the fabricated OLEDs. With the flexibility to choose between constantly applied bias and current density, *i.e.* a steady flow of charges, the time before the light emission fell below a threshold could be monitored. Such measurements are not often reported in the literature, or the results of the present thesis below and above, a realistic, applications-orientated study was able to be carried out, similar to the one in Cacialli *et al.* [194] Given the capturing of all metrics of the devices, it was possible to monitor the evolution of radiance or η_{EL}, or any other characteristic, over the period of time.

The lifetime results are presented in Figure 3.59, while in Figure 3.59a are presented the results of the evolution of η_{EL} over time for the best performing, in terms of η_{EL}, F8BT:CP-*l*-P5 and PIDT-2TPD:CP-*l*-P5 OLEDs. For both blends, the 1.0 % loading was tested. Figure 3.59b depicts the evolution of light emission (radiance) over time for the same device.

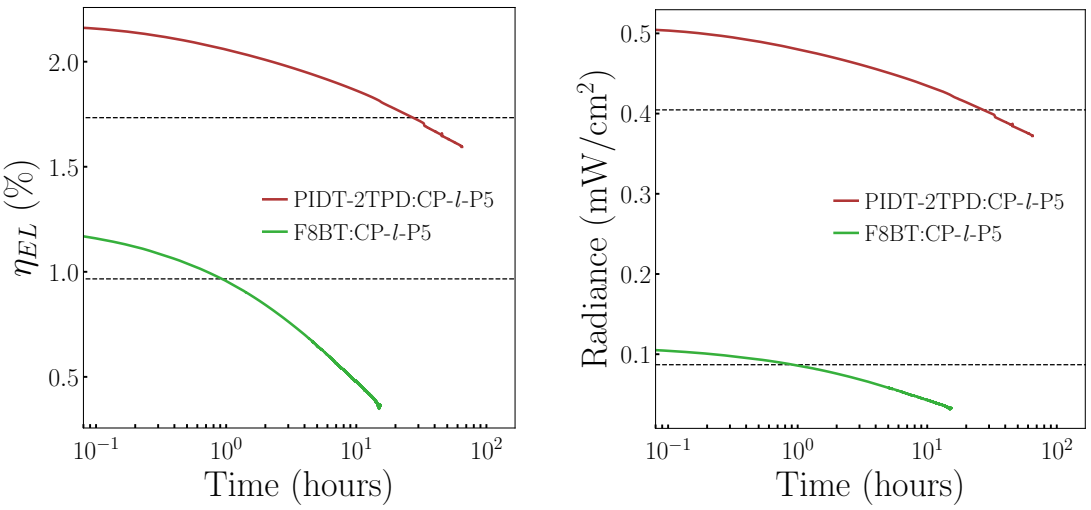

(a) η_{EL} versus time

(b) R_{max} versus time

Figure 3.59 | Pentamer OLEDs lifetime measurements for **(a)** electroluminescence external quantum efficiency (η_{EL}) over time and **(b)** radiance (R) over time. The horizontal dashed lines represent the 80 % of the initial (maximum) value.

For these experiments, a constant applied current density was chosen. This ensured a stable charge injection, that saw an increasing applied bias over time. On the contrary, a steady applied bias would lead to a decreasing current density, and the, expected, reduction of the η_{EL} would be difficult to be attributed to

device degradation or simply to a reduced charge injection, which in turn also indicates a degrading device. Also, it would not be comparable to chose the same applied current density for both devices, since the PIDT-2TPD devices exhibited higher currents than the F8BT devices (Figures 3.53b and 3.53e). For the PIDT-2TPD:CP-*l*-P5 1.0 % device, 15.6 mA/cm^2 was applied, corresponding to 3.1 V applied bias and the peak of the $\eta_{EL} \sim 2.1$ %. Given the different shape of the η_{EL} versus current density curves of the two blends (Figure 3.53), for the F8BT:CP-*l*-P5 1.0 % device, 6.2 mA/cm^2 was applied. This value corresponds to 10 V initial applied bias, however it is a point on the JV curve after the peak of the η_{EL} in the η_{EL} vs J curve, but $\sim$ halfway before the saturation voltage. At that point, the device exhibited $\eta_{EL} \sim 1.1$ %.

It is immediately visible that the F8BT devices had lost $\sim$ 80 % of the initial performance within $\sim$ 1 h of the beginning, while the same loading in the PIDT-2TPD withstood $\sim$ 32 h of constant operation before dropping below the 80 % mark. [13] More interesting, however, is the fact that the F8BT devices showed almost 100 % identical spectra before and after the measurements, while PIDT-2TPD showed an enhanced red tail of the oligomer emission, as shown in Figure 3.60. Similar observations have been reported, where broadening and spectral red-shift is attributed to a pushing of the recombination zone closer to the ITO electrode. [195]

Due to material degradation and possible crystallisation of the organic layer on the ITO side [196], defects are formed that act as hole traps, being closer to the anode electrode, effectively moving the recombination zone. [195] It has been demonstrated that moving the recombination zone away from the electrodes contributes to the increase of the lifetime of the devices. [197] It has also been reported that degradation of the organic layer occurs at the interface of the organic layer with the metallic layers of the electrodes, both cathode and anode. [198] Another degradation mechanism in OLEDs is the increase of the temperature of the device during operation, increasing non-radiative losses. [196, 199] Furthermore, in small-molecule phosphorescent OLEDs, chemical reactions within the emissive layer have been reported. [200]

[13] It is noteworthy that the 80 % mark was arbitrary set, partially because the PIDT-2TPD blends never reached the 50 % in the timeframe of the experiments, and a combination of lack of time and conflicts of blocking the lab for the measurements, restricted further experiments to reach lower values.

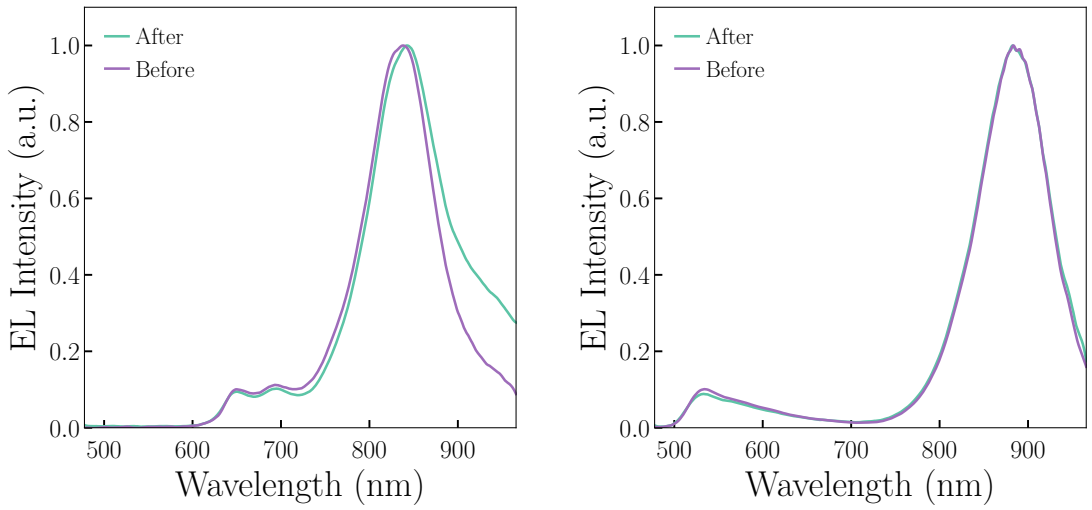

(a) PIDT-2TPD:CP-*l*-P5 1.0 % **(b)** F8BT:CP-*l*-P5 1.0 %

Figure 3.60 | Pentamer OLEDs spectra before and after the lifetime measurements for **(a)** PIDT-2TPD:CP-*l*-P5 and **(b)** F8BT:CP-*l*-P5 based OLEDs.

A possible method for improving the lifetime of the device is to reduce the energy barrier for electron injection. This can be done using alkaline metals and their salts, such as LiF. [196, 201] The addition of a heat dissipating layer, or cooling method other than the environmental heat sink, could also benefit the device lifetime and operating voltages.

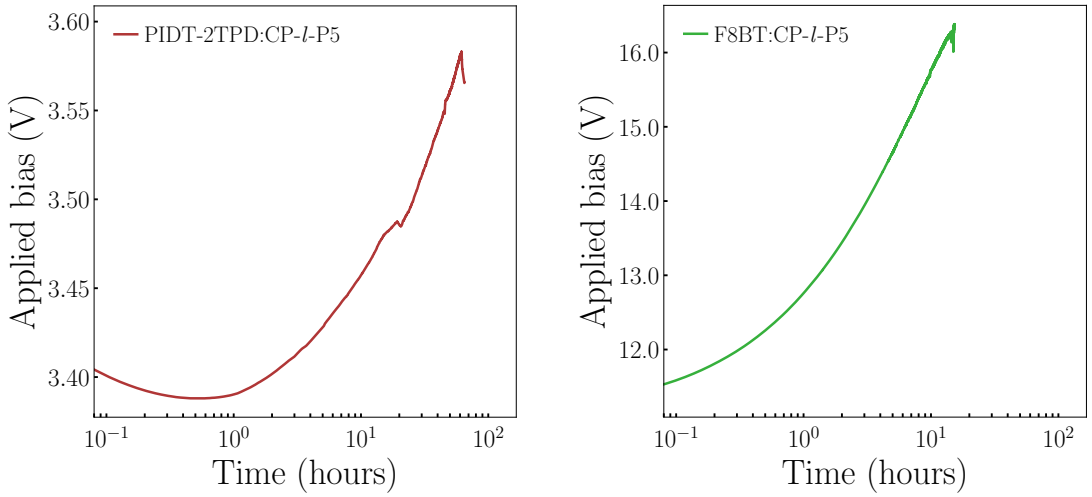

(a) PIDT-2TPD:CP-*l*-P5 1.0 % **(b)** F8BT:CP-*l*-P5 1.0 %

Figure 3.61 | Evolution of the applied bias in the **(a)** PIDT-2TPD:CP-*l*-P5 and **(b)** F8BT:CP-*l*-P5 based OLEDs.

Another interesting parameter to compare is the evolution of the applied bias for the devices during the test. As it can be expected, keeping the J

constant, the applied bias required to maintain the J constant increased in a nearly linear manner, as it is shown in Figure 3.61. This increase over time of the increasing applied bias to keep the J constant can be attributed to the degradation of the organic layers. It could either be a consequence of the loss of conjugation in the active layer or phase separation of PEDOT and PSS [123], but also to defects generation that limit the effective carrier mobility and th charge transport properties, resulting in the observed voltage increase and the luminescence decrease. [165, 195, 200]

All these results, the fact that PIDT-2TPD:CP-*l*-P5 showed higher η_{EL}, higher percentage of NIR emission, higher radiances, lower turn-on voltages and longer lifetimes corroborate the fact that amongst all the zinc porphyrin oligomers, the CP-*l*-P5 blended in PIDT-2PD are ideal candidates for NIR emitting OLEDs.

3.5.5 Conclusions

To conclude, in this section, the full optical and electro-optical characterisation of the novel linear, π-conjugated, single acetylene linked, zinc porphyrin pentamer oligomer, CP-*l*-P5. This pentamer is shorter than the butadiyne linked counterpart, resulting in an extended conjugation along the oligomer backbone. Consequently, the emission of the oligomer in solution is red-shifted, compared to the butadiyne-linked counterparts, with emission in dilute toluene solution peaking at $\sim$ 850 nm. It showed impressive performance in terms of photoluminescence quantum efficiency (η_{PL}) of $\sim$ 30 % and spectral purity, with its emission $\sim$ 100 % at $\lambda > 700$ nm.

Similarly to the previous excellent results, poly[(9,9-di-n-octylfluorenyl-2,7-diyl)-*alt*-(benzo[2,1,3]thiadiazol-4,8-diyl)] (F8BT) was chosen as a polymer host to investigate the properties of the oligomer in solid-state emission. Further to F8BT, a novel red-emitting polymer was also utilised, PIDT-2TPD. Both blends had very good performance in terms of η_{PL}, achieving a maximum of >25 % for the PIDT-2TPD blends and >15 % for the F8BT blends. Interestingly, the PIDT-2TPD blends had impressive performance of near-infrared (NIR) emission of $\sim$ 80 % and higher, while F8BT remained at a surprisingly low $\sim$ 20 %.

By incorporating the blends as active layers in organic light-emitting diodes (OLEDs), impressively high electroluminescence external quantum efficiency (η_{EL}) was achieved and high spectral purity. η_{EL} values peaked at $\sim$ 2.5 % for both F8BT and PIDT-2TPD blends, while the PIDT-2TPD blends exhibited >97 % emission at $\lambda > 700$ nm at a very low turn-on voltage of $\sim$ 1.6 V. Nevertheless, F8BT blends showed equally impressive NIR emission of >90 % for all the different loadings. Furthermore, the PIDT-2TPD OLEDs also had extremely impressive light output (radiance) values of >1.5 mW/cm^2 for all loadings, while F8BT had similar values for the lower loading.

All conclusions point towards PIDT-2TPD:CP-*l*-P5 as the champion devices. This is corroborated by the durability tests of the devices. PIDT-2TPD based OLEDs demonstrated a $\sim$ 32 h lifetime of constant operation before their performance drops below 80 % of the initial values. F8BT-based devices only lasted $\sim$ 1 h for the same test.

This proves that efficient and long-lasting near-infrared emitting organic light-emitting diodes can be envisaged using the combination of two novel materials, a red-emitting polymer host and a near-infrared emitting oligomer guest, that do not incorporate toxic or expensive heavy metals.

3.6 Summary & statistics on the porphyrin oligomers

This Chapter was focused on the extensive characterisation of various porphyrin oligomers and their potential in being used as efficient near-infrared emitting organic light-emitting diodes. From the variety of oligomers studied, three managed to stand out giving substantial emission at $\lambda > 700\,\text{nm}$. Notably, F8BT:*l*-P2 from the zinc porphyrin oligomer series of Section 3.3, F8BT:*l*-P6 H_2 from the five different hexamers of Section 3.4 and PIDT-2TPD:CP-*l*-P5 from the novel pentamer charactesiation of Section 3.5.

The nature of this study, being explorative of the optoelectronic properties of these materials, necessitated a number of devices being fabricated. An insight on the statistics of the samples studied was presented, by showing in all cases both maximum values, but also the average maximum as a metric of the dispersity of the efficiencies. It is the author's view that a further insight on this would be of interest to the reader, and therefore a histogram of the efficiencies achieved versus the number of devices that achieved the efficiency, per concentration as well as total, is presented in Figures 3.62 and 3.63 below. Furthermore, a histogram and a boxplot of the same statistics are presented in Figure 3.63 to summarise the distributions.

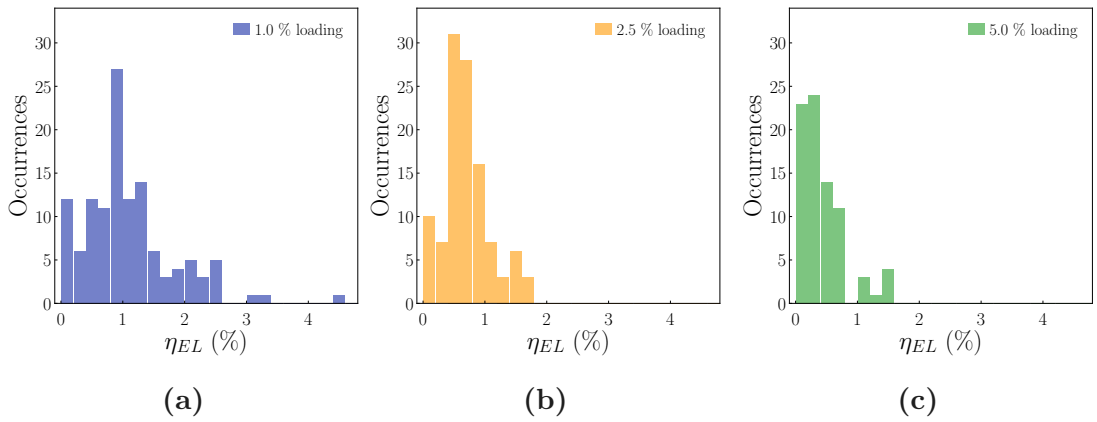

Figure 3.62 | Statistics on the devices fabricated presented in this thesis. These figures depict the distribution of the electroluminescence external quantum efficiency (η_{EL}) per loading (1.0, 2.5 and 5.0 %).

It is evident from Figure 3.62 above that 1.0 % has the advantage in terms of efficiencies, with more devices achieving $\eta_{EL} > 1\,\%$, also the loading with the champion devices. Increasing the loading of the oligomer in the polymer host resulted in significantly decreasing the η_{EL}, as demonstrated by the η_{EL}

distribution that was skewed towards lower values in Figure 3.62 and 3.63b.

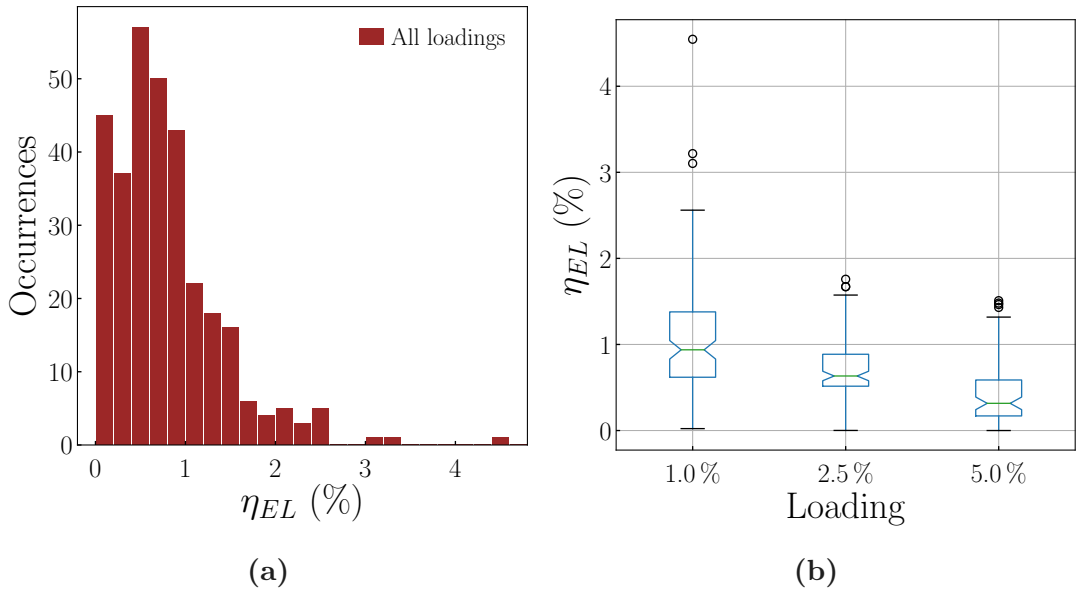

Figure 3.63 | Distribution of the electroluminescence external quantum efficiency (η_{EL}) across all concentrations.

Figure 3.63a summarises the efficiencies achieved independently of the loading. As per Figure 3.62, a large number of devices had efficiencies of $\eta_{EL} \sim 1\,\%$. From the box plot of the Figure 3.63b, there is a 95 % confidence interval from the devices presented of the 1.0 % loading for $\eta_{EL} \sim 1\,\%$. It is also noticeable the progressive decrease of the η_{EL}, while, as already mentioned, there were a few outliers in the $\eta_{EL} > 3\,\%$ for the 1.0 %, which were the "champion" devices.

The plots of Figure 3.63 do prove that high efficiencies are achievable through careful synthesis and choice of materials, despite the devices not being optimised for the highest efficiency. It also corroborates a "packing effects" interpretation of the higher loadings, since the 1.0 % had the most devices with higher efficiencies.

As already mentioned above, the results of the porphyrin oligomers presented in this Chapter "break" the record of the highest value reported for purely organic, fluorescent NIR emitters. Despite testing some oligomers that contained heavy metals, it was the heavy-metal-free oligomers that yielded very high efficiencies. Re-adapting Figure 1.13 to exclude the inorganic and quantum dot NIR OLEDs, Figure 3.64 below shows how the results presented above compare to organic compounds efficiencies reported in the literature. In the sake of clarity, only the results with efficiencies $\eta_{EL} > 1.5\,\%$ are reported in the plot.

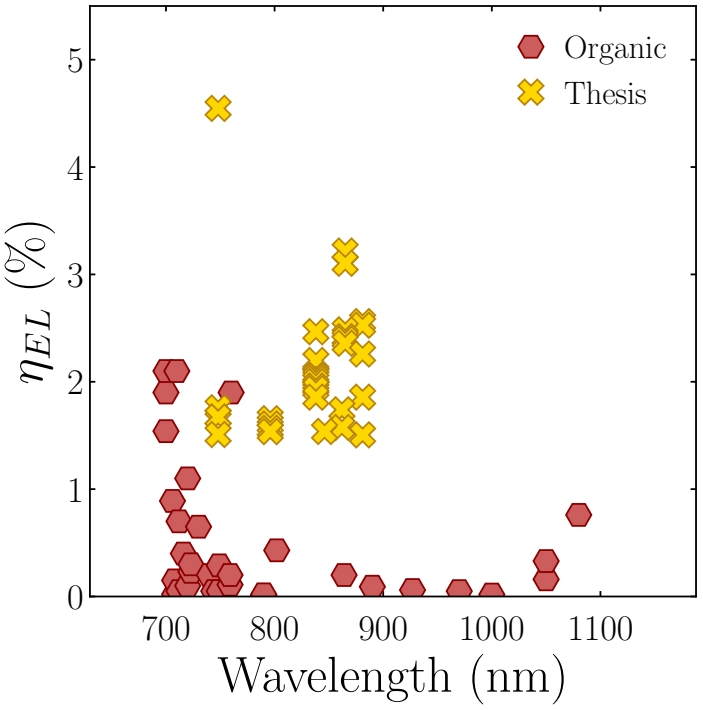

Figure 3.64 | Electroluminescence external quantum efficiency (η_{EL}) as a function of emission wavelength for organic near-infrared (NIR) organic light-emitting diodes (OLEDs) published to date and the results presented in this thesis. [96]

Since the best efficiencies reported can be argued to be outliers, and as shown in Figure 3.63b the confidence interval is at $\sim$ 1.0 %, considering the average maximum η_{EL} that the devices achieved, still remains higher than the majority of the results reported and still hold the record. Namely, F8BT:*l*-P6 H_2 1.0 % achieved an average maximum η_{EL} of 2.66 %, and PIDT-2TPD:CP-*l*-P5 1.0 % yielded an average maximum η_{EL} of 1.96 %, slightly below the best reported in Figure 3.64.

All three categories of porphyrin oligomers presented in this chapter serve as a proof of concept that efficient NIR OLEDs, using purely fluorescent materials that do not require heavy, toxic and expensive elements such as platinum or lead, are feasible. With proper engineering of the energy levels and an optimised device architecture, an even more prolonged device lifetime and efficiency can be achieved, allowing for daily, real world use.

4 | Highly luminescent encapsulated polymers based on diketopyrrolopyrrole

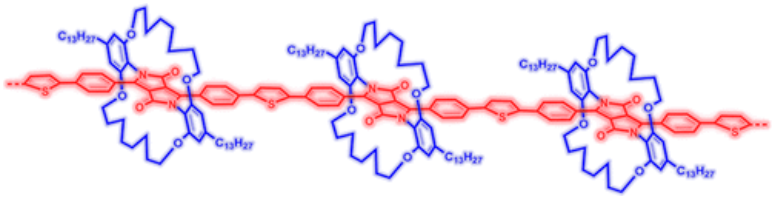

The research and part of the data presented in this chapter are published in Leventis *et al.*, JACS 2018. [85]

Three compounds of diketopyrrolopyrrole polymers were synthesised by A. Leventis in Dr. Bronstein's research group at University College London Department of Chemistry, and characterised. The full extend of the aggregation minimisation is examined when the three compounds are compared to their non-encapsulated counterparts.

4.1 Diketopyrrolopyrrole-based polymers

A class of molecularly engineered materials to prevent aggregation are materials with a *rotaxinated* architecture; in this particular case it is a conjugated core protected by a macrocycle. [83, 202] *Rotaxanes* can have conjugated polymer cores consisting from polymers such as poly(p-phenylene vinylene) (PPV), polyfluorenes (PFO) and poly(para-phenylene) (PPP, benzene polymer). These polymer cores are threaded through α- or β- cyclodextrin macrocycles fitted with bulky endgroups to prevent the macrocycle from slipping off the conjugated polymer chain during processing. The chemical structure of rotaxanes is shown in Figure 4.1. [203] The protection of the core results in blue-shift of the photoluminescence (PL) when compared to the un-protected cores. Rotaxanes find applications in OLEDs [84], exhibit lasing [204] and can be water soluble. [83] [15]

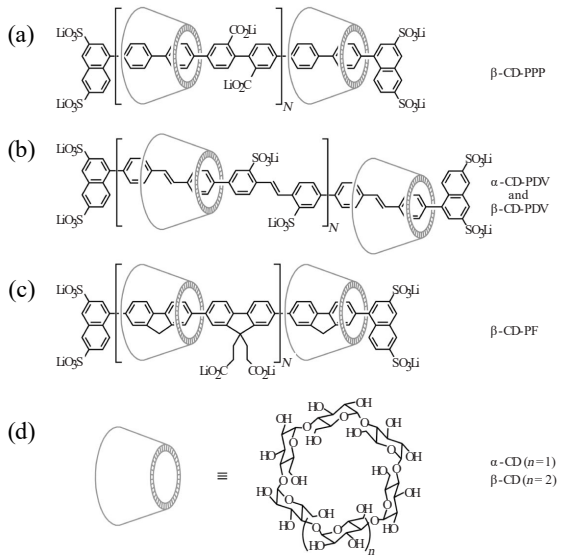

Figure 4.1 | Chemical structure of cyclodextrin-threaded conjugated rotaxanes incorporating as core **(a)** poly(para-phenylene) (PPP), **(b)** poly(p-phenylene vinylene) (PPV) and **(c)** polyfluorenes (PFO). **(d)** Chemical structure of the cyclodextrin with 6-membered macrocycle (α-CD) and 7-membered macrocycle (β-CD). Image reproduced from ref. [84].

A similar approach was followed by Sugiyasu *et al.* in 2010 to sheathe a polythiophene core within its covalently linked cyclic sidechains. [205] In this way, planar polymers can maintain their π-conjugation length which results in

The introduction figure in the previous page is reproduced from [85] in JACS.

[15] While H. L. Anderson is known to the reader from the significant contributions to the synthesis, physical and chemical characterisation on the porphyrins, some of which are presented in the Chapter 3 of the present thesis, he has also researched the synthesis of rotaxanes and our research groups have an extensive history of characterisation of such structures.

high carrier mobilities. X-ray analysis reveals that the bithiophene backbone is nearly planar and with a diameter of 1.2 nm one can envisage applications in Organic Integrated Circuits. [205] In 2013, Pan *et al.* successfully synthesised a red-emitting insulated molecular wire with a remarkable $\langle \eta_{PL} \rangle \sim 13\,\%$. [206] To the extent of the author's knowledge, Sugiyasu [205] and Pan [206] are the only demonstrations of red-emitting encapsulated insulated molecular wires. Examples in the blue have been demonstrated by some groups. [203, 207–211]

Our groups followed a similar strategy by designing and synthesising a new class of sterically hindered encapsulated diketopyrrolopyrrole (DPP)-based polymers, whose chemical structure is shown in Figure 4.2. DPP is one of the most widely used structures in conjugated polymers. It exhibits chemical stability and ease in modifying, resulting in various applications, from dyes in automotive industry (namely *Rosso corsa*, nicknamed "Ferrari red" [163]) to various optoelectronic devices. It shows high photoluminescence quantum efficiency (η_{PL}) in solution, giving rise to applications as a fluorescent dye but exhibits a high tendency to π-π stack and therefore minimising applications in the solid state.

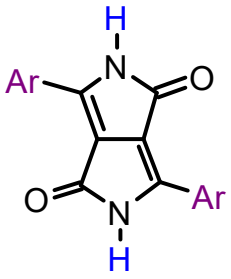

Figure 4.2 | Chemical structure of diketopyrrolopyrrole.

To prevent this effect, an encapsulating approach was followed, resulting in DPP-based insulated molecular wires that showed very high $\langle \eta_{PL} \rangle$ in solution ($> 90\,\%$), and also prevented the severe PL quenching in the solid state by sheathing the DPP core using its own side chains to minimise the efficient π-π stacking. The packing effect is more pronounced in the red and NIR emitting materials, as an increased planarity is required to reduce sufficiently the energy gap and obtain emission to lower energies. This allowed the first demonstration of highly-efficient red emitters in the solid-state.

Applications for DPP-based polymers have been reported as efficient organic photovoltaics, thin-film transistors, [212–214] OLEDs, [215–218] and red-dye pigments [219, 220]. DPP favours π-π stacking and is not considered as a candidate for solid-state emissive applications (*vide supra*). By modifying and encapsulating the DPP backbone and copolymerising it with polyfluorene

(compound DPP:F), thiophene (compound DPP:T) and phenylene (compound DPP:P) the π-π stacking, and therefore aggregation quenching, can be prevented, allowing efficient emission even in the solid-state. This strategy is illustrated in Figure 4.3 bellow.

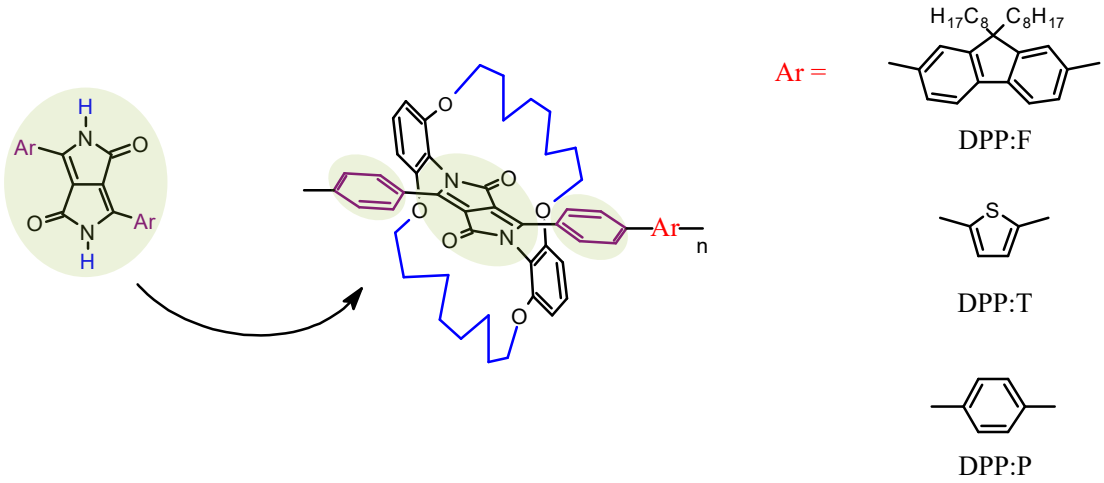

Figure 4.3 | Representation of the encapsulation strategy of the DPP core (green shade) is encapsulated and copolymerised with polyfluorene (compound DPP:F), thiophene (compound DPP:T) and phenylene (compound DPP:P).

However, DPP polymers have not been considered as efficient solid-state emitters due to their tendency to π-π stack and form dark aggregates. A preferred approach to cope with this issue is the co-polymerisation with a wider gap host in the polymer chain. [163, 215–221] Unlike similar studies that PFO derivatives, like F8BT, were blended with DPP:F8BT copolymers in very small loadings to minimise aggregation effects, [163] or DPP derivatives in blends with F8BT [88].

Our approach was to encapsulate the DPP units and co-polymerise with PFO in a 1:1 ratio. A similar strategy was followed by Cao *et al.* where they copolymerised PFO with DPP, obtaining however, lower η_{PL} values than the ones presented below. [221] To evaluate, understand and quantify the extent of the success of our encapsulation strategy, the non-encapsulated, denoted as naked herein, polymers were synthesised and characterised. The experimental results presented below contain both encapsulated polymers abbreviated as E-DPP:Ar and their naked counterparts, abbreviated as N-DPP:Ar, where Ar is "F" for polyfluorene, "P" for phenylene or "T" thiophene, respectively for the three compounds, as shown in Figure 4.3.

The DPP derivatives studied and presented in this thesis were synthesised by the group of Dr. H. Bronstein in the Department of Chemistry at University College London. [16] Details regarding the synthesis can be found in ref. [85].

[16] However, at the time of the writing, Dr. H. Bronstein is at the University of Cambridge.

4.2 Solution photoluminescence of diketopyrrolopyrrole polymers

Starting from the E-DPP:F compound which is a DPP:PFO copolymer, whose chemical structures are illustrated in Figure 4.4a, it showed clear spectra in dilute chlorobenzene (CB) solution ($\sim$ 4 µg/ml) with a high-energy absorption band at $\sim$ 350 nm and second lower-energy but higher intensity at $\sim$ 520 nm while the emission of the 0-0 transition is peaking at 570 nm (the emission peak of PFO is at 420 nm [222]), exhibiting a $\sim$ 50 nm Stokes' shift. The spectra of DPP:F are shown in Figure 4.4d.

The molecular weight of the polymer was measured and found to be $M_W \sim 65.8$ kDa. Interestingly, E-DPP:F exhibited a remarkable $\langle \eta_{PL} \rangle$ of almost unity, 94.8 $\pm$ 1.0 %. It is noted that η_{PL} measurements were carried out in air, in room temperature. The excitation wavelength was with a ThorLabs diode laser emitting at 520 nm and measured according to the protocol reported in Section 2.4 and reference [122].

The DPP:Thiophene compound, whose chemical structure are illustrated in Figure 4.4c, E-DPP:T, showed a completely different behaviour, with the high-energy absorption band exhibiting a lower intensity compared to DPP:F and 10 nm red-shift of the low-energy peaking at 580 nm. The PL of E-DPP:T in dilute CB solution is peaked at 620 nm for the 0-0 transition. E-DPP:T showed lower $\langle \eta_{PL} \rangle$ than E-DPP:F, but remained high comparing to other DPP polymers in the literature, at 73.6 $\pm$ 1.2 % and a molecular weight of $M_W \sim 23.8$ kDa. The enhanced shoulder on the red-tail of the emission implied a rigid framework. The optical properties are summarised in Figure 4.4f.

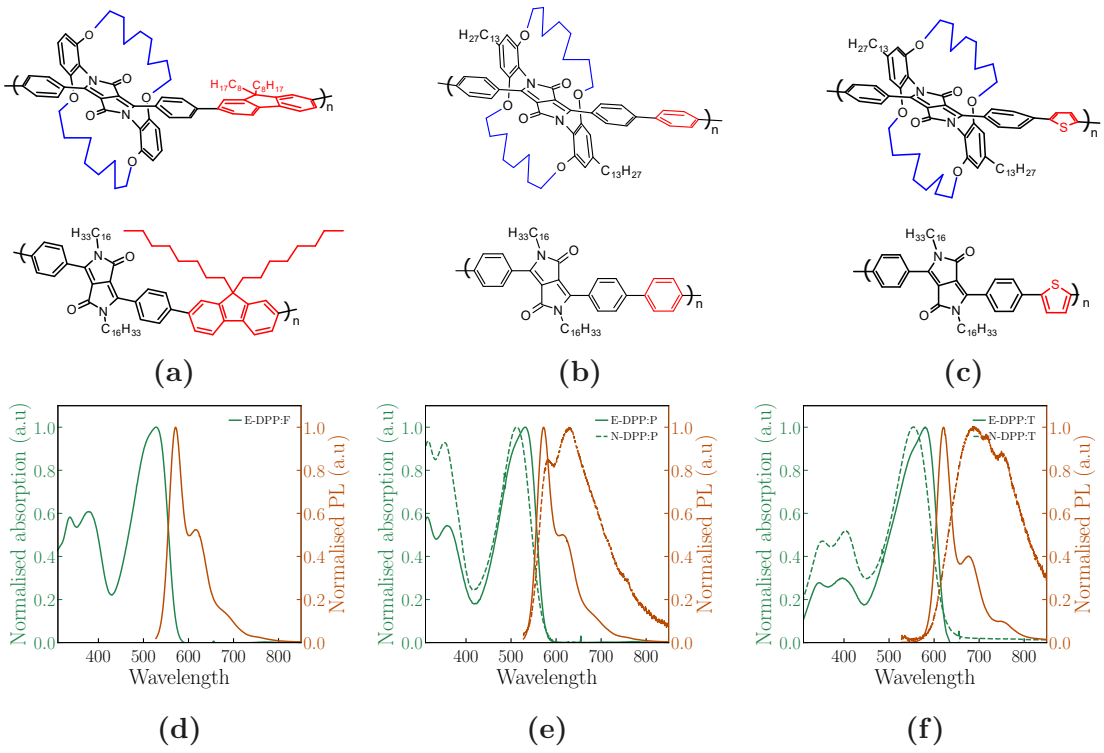

Figure 4.4 | The upper part of the figure shows the chemical structures of the encapsulated alternating co-polymers (top) and their naked counterparts (bottom) of **(a)** DPP:F, **(b)** DPP:P and **(c)** DPP:T. The lower part shows the absorption (green lines) and photoluminescence (PL) (orange lines) spectra of the encapsulated (solid lines) and naked (dashed lines) of **(d)** DPP:F, **(e)** DPP:P and **(f)** DPP:T respectively (in dilute CB solution ($\sim$ µg/ml)).

The third encapsulated compound, DPP:P, a DPP:Phenylene copolymer whose chemical structure is illustrated in Figure 4.4b, showed spectra that resemble those of DPP:F, both in absorption and emission with similar Stokes' Shift and peaks of the emission, as shown in Figure 4.4e. However, the $M_W \sim 26.7\,\text{kDa}$ was lower and showed a lower $\langle \eta_{PL} \rangle$ of $74 \pm 1.2\,\%$, similar values to DPP:T. Such a Stokes' shift is thought to occur due to torsions along the backbone, but is advantageous for minimising self-absorption effects. [206]

As mentioned above, to further prove the beneficial role of the encapsulating architecture of the materials, the polymers were tested against the performance of their unprotected counterparts. With the exception of DPP:F that the test was not conclusive due to a monomeric behaviour and problematic synthesis, N-DPP:P and N-DPP:T (where N stands for *naked*) showed significantly lower $\langle \eta_{PL} \rangle$, unstructured and broad spectra, and deep red-shifts. The optical properties of this series of polymers is summarised in Table 4.1. N-DPP:F was not investigated further in the study and no experimental data are presented

Table 4.1 | Summary of optical properties of the encapsulated and non-encapsulated DPP polymers in dilute chlorobenzene solution, in air and room temperature, with the photoluminescence quantum efficiency (η_{PL}) and maxima of emission and absorption respectively, for the three encapsulated polymers and their naked counterparts.

Sample	$\langle\eta_{PL}\rangle$(%)	λ_{max}^{em} (nm)	λ_{max}^{abs} (nm)
E-DPP:F	94.8 ± 1.0	572	527
N-DPP:F	- [a]	-	-
E-DPP:P	74.0 ± 1.2	573	528
N-DPP:P	19.0 ± 3.3	628	512
E-DPP:T	73.6 ± 1.2	620	581
N-DPP:T	18.2 ± 1.3	688	553

[a] : N-DPP:F was not investigated further in the study.

In the panel depicted in Figure 4.4, all the spectra are illustrated and encapsulated-non-encapsulated are grouped for comparison. It is visible that all the spectra exhibited a broadening and red-shifted emission, signs of aggregation, observation confirmed by the decreased η_{PL} of the naked counterparts.

4.3 Solid-state photoluminescence of diketopyrrolopyrrole polymers

To further characterise the material and test the effects of encapsulation in the challenging solid-state, the polymers were spin-coated on quartz spectrosil substrates from a 10 mg/ml CB solution. It is notable that the polymers were soluble in CB without the need of increased temperature or spinning. The substrates were cleaned with acetone and IPA in ultrasonic baths, and the polymers were subsequently spin-coated inside a N_2 glovebox at 1500 rpm, as explained in detail in Chapter 2, to obtain a $\sim$ 100 nm thick film. Any further characterisation was carried out in air, in room temperature. The spectra of the polymers are presented in the Figure 4.5.

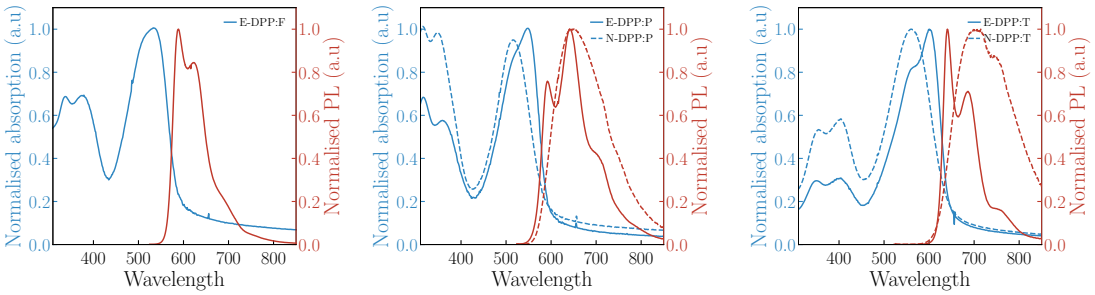

Figure 4.5 | Absorption (blue lines) and photoluminescence (PL) (red lines) spectra of the Encapsulated (solid lines) and naked (dashed lines) of **(a)** DPP:F, **(b)** DPP:P and **(c)** DPP:T respectively in thin films ($\sim$ 100 nm).

All spectra exhibited the common feature of enhancement of the red-tail 0-1 transition shoulder in PL, when compared to the solution ones. The differences in the absorption spectra, however, were more subtle, with a small red-shift of the absorption maximum by 20 nm in case of DPP:T and DPP:P. In PL, all three experienced a red-shift, $\sim$ 20 nm for DPP:F and DPP:T and a surprising $\sim$ 70 nm for DPP:P, but this can be attributed to the increase of the red-tail shoulder. The second, higher energy 0-0 transition shoulder is at $\sim$ 590 nm, $\sim$ 20 nm red-shifted compared to the solution measurement. This could also be an artefact during the collection of the spectra, the angle between sample-laser-detector and the enhancement of the 0-1 transition peak that would result in more consistent results amongst the three E-DPP polymers. The red shift of the emission compared to the solution measurements can be attributed to an increased planarity, rising from the more ordered phase of the solid-state compared to the solution one.

The broadening and red-shifting of the emission is a sign of considerable aggregation that the naked counterparts showed, which has been suppressed from the encapsulation in the E:DPP polymers. The key-factor that supported this claim of an efficient protection of the emissive properties, however, was the $\langle\eta_{PL}\rangle$. Already noticeable from the solution measurements and becoming evident in the solid-state, in the case of the encapsulated polymers was remarkably high, yielding for E-DPP:F = 19.8 %, E-DPP:T = 27.8 % and E-DPP:P = 22.6 % when the naked polymers N-DPP:T = 5.6 % and N-DPP:P = 8 %. As mentioned above, N-DPP:F is not measured. The optical properties of the DPP polymers are summarised in Table 4.2.

Table 4.2 | Summary of optical properties of the encapsulated and non-encapsulated DPP polymers in thin films ($\sim$ 100 nm), with the photoluminescence quantum efficiency (η_{PL}) and maxima of emission and absorption respectively, for the three encapsulated polymers and their non-encapsulated counterparts.

Sample	$\langle\eta_{PL}\rangle$(%)	$\lambda^{em}_{max}\,(nm)$	$\lambda^{abs}_{max}\,(nm)$
E-DDP:F	19.8 ± 1.1	589	531
N-DPP:F	- [a]	-	-
E-DPP:P	22.6 ± 1.1	640 [b]	548
N-DPP:P	8.0 ± 0.3	648	514
E-DPP:T	27.8 ± 1.3	640	601
N-DPP:T	5.6 ± 0.5	704	560

[a] : N-DPP:F was not investigated further in the study. [b] : This represents the maximum value of the emission. However a higher energy shoulder peaked at $\sim$ 590 nm would be more in trend with the other polymers and could be an artefact of the measurement and the angle of the collection of the spectra.

It is noteworthy that the $\langle\eta_{PL}\rangle$ of 27.8 % in the case of E-DPP:T is one of the highest values reported for a solid-state η_{PL} red-emitting conjugated polymer. The $\langle\eta_{PL}\rangle$ values reported for the E-DPP compounds confirm a very effective encapsulation strategy and the first demonstration of highly-fluorescent DPP polymers in the solid state. As this paves the way for applications in devices such as OLEDs, OLEDs were fabricated using the DPP polymers as emissive layer.

4.4 Diketopyrrolopyrrole polymers OLEDs

As discussed, the DPP polymers exhibit a fantastic potential for optoelectronic applications. To prove this claim, OLEDs were fabricated and characterised incorporating the DPP polymers, both encapsulated and naked, as the active layer. Following the procedure described above in Section 2.6, DPP-incorporating OLEDs were fabricated and characterised, allowing to examine the effects of the encapsulation strategy in devices. The electroluminescence (EL) spectra, JVL curves and electroluminescence external quantum efficiency (η_{EL}) are presented in Figure 4.6 below.

These powerfully confirm a wealth of advantages afforded by the encapsulation, in terms of radiance, efficiency, and of spectral purity of the emission.

From the EL spectra (Figures 4.6d and 4.6g) it is evident that the naked compounds featured significantly wider, red-shifted and essentially featureless electroluminescence, which fully corroborated the interpretation that their emission is aggregation-dominated. More specifically, N-DPP:P showed a $\sim$ 70 nm bathochromic shift from 583 nm for E-DPP:P to 650 nm for N-DPP:P. The spectral width (full width at half maximum, FWHM) was increased from $\sim$ 80 nm to 131 nm for N-DPP:P and even more for DPP:T (FWHM $\sim$ 32 nm for E-DPP:T compared to $\sim$ 170 nm for N-DPP:T), and a red-shift of $\sim$ 50 nm.

By looking at the current density - voltage - radiance (JVR) characteristics [17] (Figures 4.6b, 4.6e and 4.6h), it is noticeable that the encapsulation did not cause hindering of charge injection and transport compared to the naked compounds, as the onsets were comparable for the two classes of materials, if not lower for the minority carriers for the E:DPP compounds (*vide infra*). Majority carriers (unipolar) injection began immediately for applied biasses $>0\,V$, with the further minority carrier injection, and the associated light emission, initiated at applied biasses as low as $\sim$ 2.7 V for E-DPP:F, $\sim$ 2.5 V for E-DPP:P and $\sim$ 1.9 V for E-DPP:T. Contrarily, EL for the naked compounds started at applied biasses $\sim$ 5 V higher for N-DPP:P and $\sim$ 1 V higher for N-DPP:T. Interestingly, Figures 4.6e and 4.6h also indicate that whereas the current onset of luminescence was comparable for all devices incorporating encapsulated polymers, at $\sim 0.02\,mA/cm^2$, the EL current onset for the naked polymers is significantly higher, *i.e.* $\sim 0.2\,mA/cm^2$ for N-DPP:P and $\sim 5\,mA/cm^2$ for N-DPP:T.

These differences of quenching the electro-generated excited states are

[17] Radiance rather than luminance is reported as a significant part of the spectrum is in the near infrared ($\lambda > 700$ nm), as mentioned in Chapter 2.

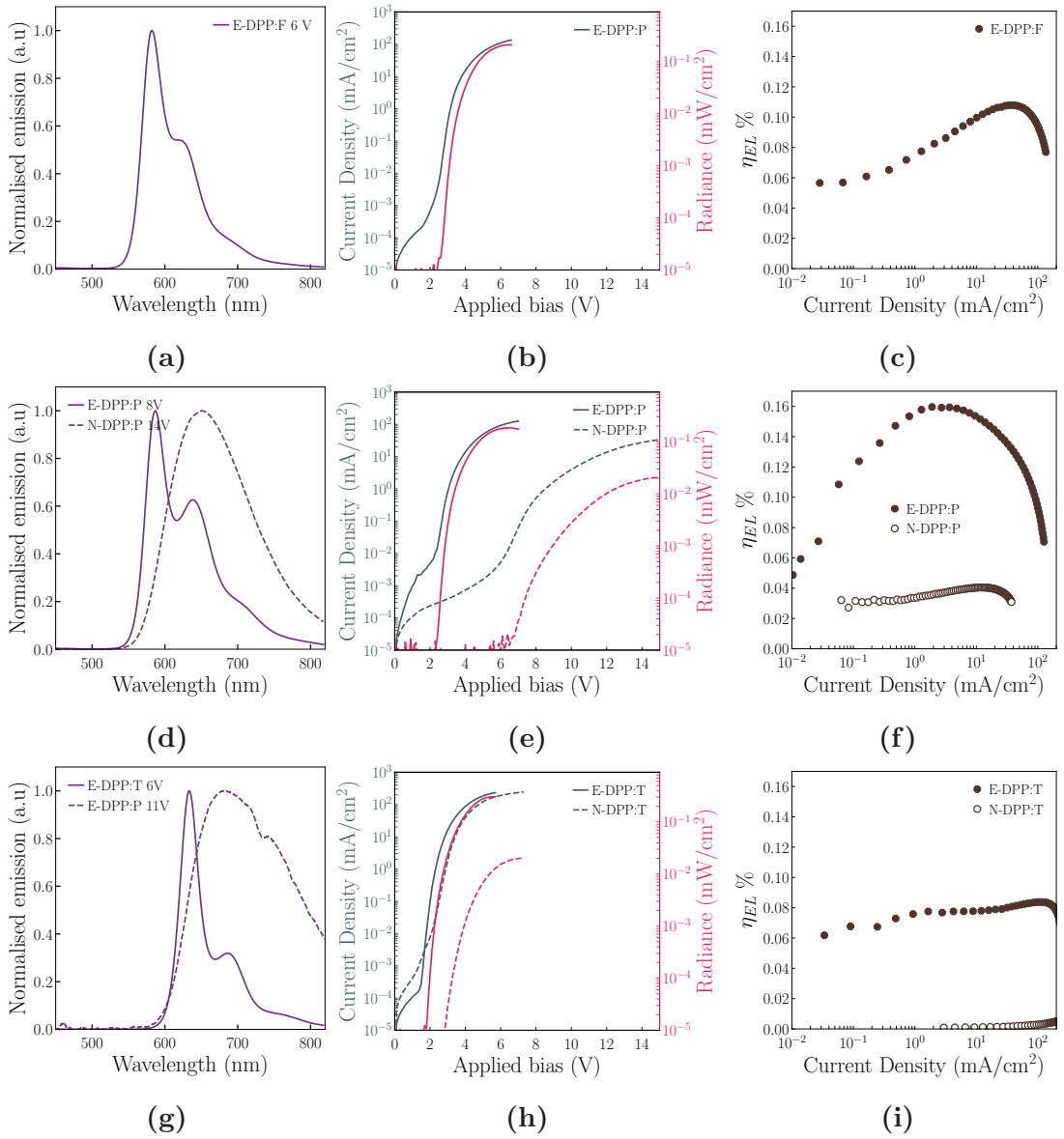

Figure 4.6 | Panel with the optoelectronic properties of the DPP based organic light-emitting diodes (OLEDs). Dashed lines and empty symbols refer to the naked polymers while solid lines and filled symbols refer to encapsulated. **(a, d, g)** Electroluminescence spectra (purple lines), **(b, e, h)** current density - voltage - radiance (JVR) curves (grey lines for current density and pink lines for radiance), **(c, f, i)** external quantum efficiency versus current density (brown symbols) curves for **(a, b, c)** DPP:F, **(d, e, f)** DPP:P and **(g, h, i)** DPP:T. The legends in **(a, d, g)** refer to the voltage at which the spectra where collected. Due to its unsuitably low molecular weight and problematic synthesis, the N-DPP:F was not investigated further in the study.

attributed to the naked compounds' aggregation effects, so that light emission only exceeded the limit for detection for higher current densities and biasses. The higher η_{EL} for the E-DPP compounds, 0.16 % for E-DPP:P, 4 times higher than the 0.04 % of N-DPP:P and 0.08 % for E-DPP:T, 16 times higher than the 0.005 % of N-DPP:T also afforded significantly higher radiances at the respective saturation biasses, impressively more than an order of magnitude, *i.e.* from $\sim$ 0.2 mW/cm^2 for the E-DPP polymers to $\sim$ 0.02 mW/cm^2 for the naked counterparts. It was further observed that amongst the encapsulated compounds, the maximum η_{EL} was obtained by E-DPP:P (η_{EL} = 0.16 %), but exhibited an important η_{EL} roll-off with increasing current density, whereas E-DPP:T had essentially stable η_{EL} for significant current densities ($\eta_{EL} \sim 0.07$ %), in the order of $\sim$ 100 mA/cm^2. Finally, E-DPP:F η_{EL} (Figure 4.6c) exhibited a behaviour between the two other E-DPP, reduced η_{EL} roll-off, but still present, however with peak η_{EL} = 0.1 %, slightly higher than E-DPP:T, but still lower than E-DPP:P, nevertheless at higher current densities ($\sim$ 40 mA/cm^2).

All the optoelectronic properties of the fabricated and characterised OLEDs are summarised in the Table 4.3, where the advantages of the encapsulation can be quantified. Plots with all the η_{EL} versus applied bias curves can be found in Figures C.1 through C.8.

Table 4.3 | Summary of the optoelectronic properties of the organic light-emitting diodes (OLEDs) incorporating the DPP polymers.

Sample	V_{ON} (V) [a]	$\langle R_{max}$ mW/cm$^2\rangle$ [b]	η_{EL}^{max} [c]	$\langle \eta_{EL}^{max} \rangle$ [d]	λ_{max}^{EL} (nm) [e]
E-DPP:F	2.7 ± 0.05	0.23 ± 0.05	0.11	0.1 ± 0.02	582
N-DPP:F	- [f]	-	-	-	-
E-DPP:P	2.5 ± 0.07	0.24 ± 0.09	0.16	0.14 ± 0.02	583
N-DPP:P	7.3 ± 0.25	0.02 ± 0.002	0.04	0.04 ± 0.0002	650
E-DPP:T	1.9 ± 0.05	0.29 ± 0.01	0.084	0.072 ± 0.009	630
N-DPP:T	3.1 ± 0.11	0.02 ± 0.001	0.005	0.005 ± 0.0004	679

[a] : Voltage at which radiance $> 3 \times 10^{-5}$mW/cm^2. [b] : Average maximum radiance. [c] : Maximum electroluminescence external quantum efficiency. [d] : Average maximum external quantum efficiency. [e] : Maximum of the emission. [f] : N-DPP:F was not investigated further study.

4.5 Conclusions

In the Table 4.4 is shown a summary of the major optical and optoelectronic properties of the DPP polymers characterised.

In view of the larger intensity of the 0-0 compared to 0-1 transition in the EL spectra (Figure 4.6g), usually taken as an indication for suppression of aggregation effects [223], the sharp onset of EL at the lowest voltage within this set of materials (ca. 1.9 V), and the stable efficiency up to $\sim 100\,\mathrm{mA/cm^2}$, E-DPP:T can be considered as the most promising compound for OLEDs.

Table 4.4 | Summary of the major characteristics of DPP polymers, including solution and thin-film photoluminescence quantum efficiency (η_{PL}), absorption and photoluminescence maxima and organic light-emitting diode (OLED) characteristics, including electroluminescence external quantum efficiency (η_{EL}), average turn-on voltages and electroluminescence maxima.

	Solution			Thin Films			OLEDs		
Sample	$\langle\eta_{PL}\rangle$(%)	λ^{em}_{max} (nm)	λ^{abs}_{max} (nm)	$\langle\eta_{PL}\rangle$(%)	λ^{em}_{max} (nm)	λ^{abs}_{max} (nm)	η^{max}_{EL} (%)	V_{ON} (V)[a]	λ^{em}_{max} (nm)
E-DPP:F	94.8 ± 1.0	572	527	19.8 ± 1.1	589	531	0.11	2.7 ± 0.05	582
N-DPP:F	-[b]	-	-	-	-	-	-	-	-
E-DPP:P	74.0 ± 1.2	573	528	22.6 ± 1.1	640 [c]	548	0.16	2.5 ± 0.07	583
N-DPP:P	19.0 ± 3.3	628	512	8.0 ± 0.3	650	514	0.04	7.3 ± 0.25	650
E-DPP:T	73.6 ± 1.2	620	581	27.8 ± 1.3	640	601	0.084	1.9 ± 0.05	630
N-DPP:T	18.2 ± 1.3	688	553	5.6 ± 0.5	704	560	0.005	3.1 ± 0.11	679

[a]: V_{ON} is defined when radiance is $> 3 \times 10^{-5}\,\mathrm{mW/cm^2}$.
[b] : N-DPP:F was not investigated further in the study due to problematic synthesis and monomeric behaviour.[c] : This represents the maximum value of the emission. However a higher energy shoulder peaked at $\sim 590\,\mathrm{nm}$ would be more in trend with the other polymers and could be an artefact of the measurement and the angle of the collection of the spectra.

From the results presented, it is visible that the encapsulating nature of E-DPP:F, E-DPP:P and E-DPP:T was beneficial and improved the characteristics and efficiencies of the devices. The unexpected low η_{EL} exhibited, though, could show further improvement by optimising the device architecture and active layer thickness.

To conclude, three diketopyrrolopyrrole-based encapsulated polymers were synthesised and characterised optically by means of solution and thin film absorption and photoluminescence spectroscopy and photoluminescence quantum efficiency (η_{PL}), as well as optoelectronically by means of fabrication and characterisation of organic light-emitting diodes (OLEDs) incorporating the three encapsulated polymers as emissive layers. The three compounds displayed impressively high solution η_{PL} up to almost unity, with significantly high values also in the solid state, allowing the diketopyrrolopyrrole polymers to be

used in optoelectronic devices such as OLEDs. The sheathed conjugated core prevents aggregation quenching, promoting an enhanced backbone colinearity, a claim corroborated by scanning tunnelling microscopy that showed linear, conformationally defect-free polymer domains.

5 | Conclusions and Outlook

"This is the way the world ends
This is the way the world ends
This is the way the world ends
Not with a bang but with a whimper"
– The Hollow Men

T. S. Eliot

This thesis provided an outlook on aspects of general interest in the vast field of organic optoelectronics, with a special focus on organic light-emitting diodes (OLEDs). In Chapter 1, a general overview organic semiconductors (OS) was given, with a historic review of major achievements. A special focus to a rather new class of materials was reported, perovskites, and how the "sister" field of organic photovoltaic (OPV) devices has pushed organics. Following this, what is the main topic of this thesis was discussed, the optical and electronics properties of OS, as well as OLEDs.

Chapter 2 presented the experimental methods used throughout the research forming this thesis. From solution preparation, to photoluminescence quantum efficiency (η_{PL}) measurements and time-correletated single photon counting (TCSPC) characterisation, to OLED devices fabrication and measuring tools, various details that explain how the results were calculated and presented.

5.1 Challenges

This thesis dealt with narrow-band organic emitters, with photoluminescence (PL) peaked in the red and near-infrared (NIR). Addressing and achieving efficient emission in this spectral region is challenging for two main reasons. First, there is a tendency of the non-radiative rate (k_{nr}) to increase exponentially when the energy gap is decreasing, necessary to achieve NIR emission. This is summarised by the so-called "energy-gap law" that was first formalised in 1970.

A second challenge is the tendency the materials show towards π-π stacking. To sufficiently reduce the energy gap for red and NIR emission, a more extended conjugation is needed. This results in more planar molecules that in turn tend to facilitate π-π stacking.

In the course of this thesis, both limitations were addressed by employing two different approaches. By means of molecular design and material properties, porphyrin oligomers and encapsulated polymers achieved high efficiencies in solution, while also showing efficient electroluminescence external quantum efficiency (η_{EL}) when incorporated in OLEDs.

5.2 Porphyrin oligomers as near-infrared emitters

By means of photophysical and optoelectronic investigations, a family of porphyrin oligomers, π-conjugated organic semiconductors, were described and characterised. These semiconductors are emissive molecules, tackling the challenging part of the lower energies of the spectrum, given the increased planarity required to lower the emission energy of a molecule, that concomitantly causes unwanted π-π stacking and aggregation quenching and the "energy-gap law" limiting the efficiency. To prevent the effects of those limiting factors, two strategies were reported: the use of bulky side chains with a large steric hindrance as a mean of aggregation prevention and the increase of the length of the molecule chain as a mean of "energy-gap law" limitation.

A series of very efficient porphyrin oligomers with emission peaking at $\lambda > 700\,\text{nm}$ were presented. The oligomers presented in Chapter 3 proved that spectrally pure and very efficient NIR emitting OLEDs are feasible, and while omitting the use of heavy metals that are toxic, these oligomers remain bio-compatible.

5.3 Diketopyrrolopyrrole polymers

By employing a second approach of aggregation prevention, *i.e.* an encapsulation architecture that sheaths the conjugated core, a series of very efficient, novel diketopyrrolopyrrole (DPP) based red emitting polymers were discussed in Chapter 4. With only a few previous reports in the literature of benefiting from this architecture, these polymers maintained the π-conjugation length. By comparing the encapsulated polymers performance with their naked counterparts, it was possible to prove the beneficial role the encapsulation played from dilute solution measurements to incorporation into OLEDs.

5.4 Contribution of this work

With the results outlined in Chapters 3 and 4, this work showed that the hurdles low energy-gap materials face can be addressed. The so-called "energy-gap law" can be overcome with a twofold approach the porphyrin oligomers utilise. Firstly, the increase of the oligomer length suppresses intersystem crossing (ISC) as a result of the increased mismatch of singlet and triplet spatial extent. Secondly, increasing the oscillator strength results in the increase of the radiative rate, k_r. It was also demonstrated that another hurdle the NIR emitting materials face, the π-π stacking and the concomitant aggregation quenching due to the increased planarity needed for sufficiently extended conjugation, is suppressed by utilising molecular design methods, *i.e.* bulky sidechains.

Both approaches resulted in the demonstration of the highest η_{EL} reported, to date and to the best of the author's knowledge, for heavy-metal-free and metal-free altogether OLEDs, emitting in this spectral region with a fluorescence lifetime of $\sim$ ns. A metal-free hexamer-based OLED showed almost pure NIR electroluminescence (EL) with η_{EL} up to $\sim 3.2\,\%$, an unprecedented value for metal-free materials not leveraging reverse ISC or phosphorescence. Notably, a novel pentamer with slightly modified chemical structure incorporating zinc, achieved a somewhat lower $\eta_{EL} \sim 2.5\,\%$, still above the reported values for similar emitters, however showed remarkable stability over continuous operation, with $> 80\,\%$ of the initial η_{EL} maintained over 32 h. This is an impressive value considering that the diodes fabricated where not optimised for stability during continuous operation.

Further to the bulky chains, another approach to preventing π-π stacking was demonstrated when the, known for its strong propensity to π-π stack and aggregate, diketopyrrolopyrrole (DPP) was co-polymerised and encapsulated

using its own sidechains. The encapsulation was demonstrated when both encapsulated and naked polymers where compared under the same conditions to prove the benefits of this strategy, even when considering η_{PL} measurements in dilute solution, where the aggregation effects would be minimised. η_{PL} values of the encapsulated polymers where > 3 times higher than the naked counterparts in dilute solution, increasing up to ~ 5 times in the solid state. This proved the polymers to remain highly efficient in the solid state, where DPP was limited. Notably, the encapsulated polymers achieved η_{EL} values of up to 16 times higher than the naked analogue, demonstrating huge potential for further investigation.

This work has highlighted the possibilities that host-guest strategies, such as the polymer-porphyrin approach, or co-polymerisation and encapsulation, allow to overcome the traditional hurdles of the so-called "energy-gap law" and the detrimental π-π stacking of low-energy emission in the solid state.

5.5 Future research

DPP-based polymers showed exceptionally high fluorescence efficiency values in solution and some of the highest ever reported in the solid-state for their respective spectral range, however with lower-than-expected external quantum efficiencies when embedded in OLEDs. The prospects they showed could fuel further research towards exploring different OLED architectures and measuring the HOMO-LUMO levels as to find more appropriate materials for interlayers or electrodes. Given the good results the novel red-emitting polymer (PIDT-2TPD), presented in Section 3.5, showed in terms of OLED stability, and the fact that DPP is widely used in many optoelectronic and dye-related applications, the DPP-based encapsulated polymers could prove a great alternative in efficient red OLEDs for solution processed applications.

Drawing further inspiration from good results of PIDT-2TPD based OLEDs in blends with the porphyrin oligomers, the DPP-polymers could be employed in a similar host-guest strategy with some of the best NIR emitting porphyrin oligomers to form even more efficient NIR OLEDs.

Porphyrin oligomers also showed an impressive potential as efficient NIR OLEDs, using both zinc and metal-free novel oligomers as emitters. Chemical design allowed for an easy tuning of the emission wavelength, by varying both the chemical elements in the centre of each porphyrin unit and the length of the oligomer, thus providing flexibility for future applications where fine tuning of the emission peak is needed. The η_{EL} afforded was unprecedented for a heavy-metal-free, and metal-free altogether, for this spectral range, and with unoptimised devices showing long device lifetimes under continuous operation, the studies presented above pave the way for efficient NIR emitting OLEDs that are no longer emissive or using expensive rare-earth, precious or toxic metals.

Finally, trying to force phosphorescent emission from a platinum-containing porphyrin hexamer showed how efficiently ISC is suppressed in these oligomers, resulting, however, in poor emissive properties of the platinum oligomer based OLEDs. Interestingly, a distinctive two-peaked EL spectrum was observed, owing to the recombination of both singlet and triplet excitons. One could envisage an application where similar OLEDs are employed to monitor oxygen levels. Oxygen is known to have detrimental properties in triplet excitons, so observing an intensity increase of the phosphorescence peak of the OLED could signify a drop of the oxygen levels in a room, e.g. with odourless noble or inert gases, such as a nitrogen filled glovebox or a low-temperature cooling with liquid helium set-up, such as an MRI.

A | Summarising tables

Below are some summary tables with all the detailed data presented.

Table A.1 | Detailed table with the zinc porphyrin photoluminescence (PL) data in dilute solution and thin films.

Sample	$\langle\eta_{PL}\rangle^{sol}$ (%)	NIR PL $_{sol}$ (%)	Abs λ^{sol}_{max} (nm)	PL λ^{sol}_{max} (nm)	τ (ns)	k_r (ns^{-1})	k_{nr} (ns^{-1})	$\langle\eta_{PL}\rangle^{film}$ (%)	NIR PL $_{film}$ (%)	PL λ^{film}_{max} (nm)	Red shift (nm)
F8BT pure	$\sim$ 100	1	-	534	2.4	0.41	0.004	59.9 ± 2.5	3.0	555.0	21
l-P1 1.0 %								16.1 ± 0.7	11.3		
l-P1 2.5 %	7.9 ± 0.2	9.1	628	632	2.07	0.04	0.45	9.5 ± 0.41	17.1	642.0	10
l-P1 5.0 %								6.5 ± 0.4	23.5		
l-P2 1.0 %								26.6 ± 1.6	68.7		
l-P2 2.5 %	34.3 ± 0.7	84.8	712	720	1.54	0.22	0.43	21.9 ± 1.5	82.8	750.0	30
l-P2 5.0 %								14.2 ± 1.1	89.6		
l-P3 1.0 %								27.8 ± 1.1	64.6		
l-P3 2.5 %	24.2 ± 0.7	94.9	730	767	1.5	0.16	0.51	20.3 ± 0.7	75.1	811.0	44
l-P3 5.0 %								11.1 ± 0.7	83.9		
l-P4 1.0 %								22.6 ± 0.6	58.7		
l-P4 2.5 %	22.2 ± 0.5	96.2	745	781	1.27	0.17	0.62	14.8 ± 0.2	74.3	855.0	74
l-P4 5.0 %								8.4 ± 0.2	81.6		
l-P5 1.0 %								26.1 ± 0.9	61.3		
l-P5 2.5 %	27.3 ± 0.4	98.3	757	787	1.19	0.23	0.62	15.2 ± 0.6	73.4	858.0	71
l-P5 5.0 %								8.3 ± 0.4	84.7		
l-P6 1.0 %								23.9 ± 0.9	61.6		
l-P6 2.5 %	28.5 ± 1.5	99.1	769	793	1.16	0.25	0.62	11.4 ± 0.2	72.1	867.0	74
l-P6 5.0 %								6.9 ± 0.1	83.1		
l-P7 1.0 %								17.1 ± 0.6	46.7		
l-P7 2.5 %	47.8 ± 0.6	99.4	772	798	1.17	0.41	0.44	9.9 ± 0.3	61.6	869.0	71
l-P7 5.0 %								2.7 ± 0.1	62.9		
l-PN 1.0 %								12.3 ± 0.4	25.5		
l-PN 2.5 %	28.3 ± 0.7	90.1	782	810	0.99	0.29	0.72	7.4 ± 0.2	27.8	879.0	69
l-PN 5.0 %								2.7 ± 0.1	28.8		
TFB pure	-	-	-	-	-	-	-	26	0.0	430.0	-
l-P6 1.0 %								30	60.0		
l-P6 2.5 %								31	64.0	860.0	-
l-P6 5.0 %	28.5 ± 1.5	99.1	769	793	1.16	0.25	0.62	24	71.0		
PIDT-2TPD pure	-	-	-	-	-	-	-	28.8 ± 1.9	17.9	638.0	-
CP-*l*-P5 1.0 %								27.3 ± 1.9	76.7	861.0	8
CP-*l*-P5 2.5 %	30 ± 1.4	99.9	805	853	2.04	0.15	0.34	17.5 ± 2.5	85.8	876.0	23
CP-*l*-P5 5.0 %								8.1 ± 0.4	87.1	891.0	38
F8BT pure	$\sim$ 100	1	-	534	-	-	-	50.2 ± 0.4	50.0	556.0	22
CP-*l*-P5 1.0 %								16.9 ± 0.4	15.6	894.0	41
CP-*l*-P5 2.5 %	30 ± 1.4	99.9	805	853	2.04	0.15	0.34	8.3 ± 0. 2	23.6	917.0	64
CP-*l*-P5 5.0 %								4.1 ± 0.2	32.3	917.0	64

Table A.2 | Detailed table with the zinc porphyrin organic light-emitting diodes (OLEDs) data.

Sample	η_{EL}^{max} (%)	$\langle\eta_{EL}^{max}\rangle$ (%)	R_{max} mW/cm^2	$\langle R_{max}\rangle$ mW/cm^2	V_{ON} (V)	λ_{max}^{EL} (nm)	NIR EL (%)
F8BT pure	0.32	0.28 ± 0.04	0.88	0.4 ± 0.19	3.7 ± 0.46	560.0	
l-P1 1.0 %	0.83	0.28 ± 0.32	0.62	0.28 ± 0.2	2.8 ± 0.2		8.2
l-P1 2.5 %	0.98	0.6 ± 0.31	0.56	0.43 ± 0.2	3.2 ± 0.3	648.0	12.8
l-P1 5.0 %	1.32	0.79 ± 0.32	0.53	0.35 ± 0.22	3.8 ± 0.6		16.3
l-P2 1.0 %	4.50	1.46 ± 1.18	3.30	1.6 ± 0.9	3.52 ± 0.3		83.1
l-P2 2.5 %	1.76	1.5 ± 0.23	4.00	2.47 ± 1.22	3.57 ± 0.6	748.0	90.3
l-P2 5.0 %	1.51	1.34 ± 0.21	2.38	1.62 ± 0.77	3.62 ± 0.6		93.3
l-P3 1.0 %	1.66	1.29 ± 0.32	1.70	1.2 ± 0.3	4.6 ± 0.75		95.2
l-P3 2.5 %	1.19	0.78 ± 0.4	2.30	1.18 ± 0.62	5.4 ± 0.6	796.0	97.7
l-P3 5.0 %	0.58	0.28 ± 0.26	0.36	0.2 ± 0.15	7.4 ± 0.4		96.1
l-P4 1.0 %	1.38	0.9 ± 0.27	0.70	0.51 ± 0.25	5.4 ± 0.23		89.4
l-P4 2.5 %	0.60	0.45 ± 0.21	0.32	0.25 ± 0.11	6.7 ± 0.9	845.0	92.7
l-P4 5.0 %	0.30	0.27 ± 0.03	0.19	0.16 ± 0.01	7.5 ± 0.4		93.3
l-P5 1.0 %	0.94	0.89 ± 0.04	0.50	0.45 ± 0.04	4.2 ± 0.4		75.8
l-P5 2.5 %	0.63	0.6 ± 0.01	0.31	0.29 ± 0.02	6.4 ± 0.3	852.0	93.1
l-P5 5.0 %	0.32	0.22 ± 0.11	0.18	0.12 ± 0.08	7.2 ± 0.6		94.8
l-P6 1.0 %	1.13	0.89 ± 0.26	0.62	0.49 ± 0.1	5.1 ± 0.5		84.4
l-P6 2.5 %	0.87	0.69 ± 0.1	0.31	0.29 ± 0.02	7.4 ± 0.8	862.0	94.7
l-P6 5.0 %	0.60	0.52 ± 0.07	0.37	0.26 ± 0.15	8 ± 0.25		98.1
l-P7 1.0 %	1.25	0.93 ± 0.23	1.39	1.05 ± 0.33	4.3 ± 0.5		87.4
l-P7 2.5 %	0.95	0.84 ± 0.08	1.22	0.89 ± 0.29	6.8 ± 1.1	860.0	98.1
l-P7 5.0 %	0.43	0.35 ± 0.13	0.30	0.13 ± 0.1	8.1 ± 0.7		94.6
l-PN 1.0 %	1.05	0.74 ± 0.19	0.31	0.19 ± 0.12	4.8 ± 0.7		79.3
l-PN 2.5 %	0.63	0.62 ± 0.01	0.82	0.52 ± 0.26	6.4 ± 0.8	871.0	90.7
l-PN 5.0 %	0.30	0.21 ± 0.08	0.20	0.15 ± 0.05	6.5 ± 0.6		90.1
TFB:*l*-P6 1.0 %	0.13	0.11 ± 0.02	0.20	0.2 ± 0.06	4.3 ± 0.6	811.0	76.0
TFB:*l*-P6 2.5 %	1.13	0.09 ± 0.02	0.20	0.2 ± 0.04	4.3 ± 0.4	822.0	87.0

Table A.3 | Detailed table with the porphyrin hexamers photoluminescence (PL) data in dilute solution and thin films.

Sample	$\langle\eta_{PL}\rangle^{sol}$ (%)	NIR PL $_{sol}$ (%)	Abs λ^{sol}_{max} (nm)	PL λ^{sol}_{max} (nm)	τ (ns)	k_r (ns^{-1})	k_{nr} (ns^{-1})	$\langle\eta_{PL}\rangle^{film}$ (%)	NIR PL $_{film}$ (%)	PL λ^{film}_{max} (nm)	Red shift (nm)
F8BT pure	$\sim$ 100	1.0	-	534	2.40	0.410	0.004	59.9 $\pm$ 2.5	5.70	555	21
l-P6 H2 1.0 %								33.1 $\pm$ 2.7	35.43	863	-
l-P6 H2 2.5 %	21.1 $\pm$ 0.6	99.5	783	804	1.84	0.120	0.430	18.1 $\pm$ 3.2	53.10	863	59
l-P6 H2 5.0 %								9.4 $\pm$ 0.5	64.50	863	-
l-P6 Mg 1.0 %								10.6 $\pm$ 0.6	28.60	894	39
l-P6 Mg 2.5 %	20.7 $\pm$ 3.5	97.8	833	855	2.50	0.083	0.320	3.9 $\pm$ 0.5	36.80	900	45
l-P6 Mg 5.0 %								1.1 $\pm$ 0.04	47.10	907	52
l-P6 Zn 1.0 %								23.9 $\pm$ 0.9	61.60	-	-
l-P6 Zn 2.5 %	28.5 $\pm$ 1.5	99.1	769	795	1.16	0.250	0.620	11.4 $\pm$ 0.2	72.10	867	72
l-P6 Zn 5.0 %								6.9 $\pm$ 0.1	83.10	-	-
l-P6 Pd 1.0 %								10.3 $\pm$ 0.1	32.60	774	47
l-P6 Pd 2.5 %	1.4 $\pm$ 0.5	64.2	706	727	0.35	0.040	2.800	7.8 $\pm$ 0.1	51.10	774	47
l-P6 Pd 5.0 %								5.2 $\pm$ 0.4	66.90	779	52
l-P6 Pt 1.0 %								10.6 $\pm$ 0.3	8.40	739 & 895	44 & 19
l-P6 Pt 2.5 %	-	56.6	671	695 & 876	0.43	0.020	2.310	2.8 $\pm$ 0.3	15.40	740 & 895	45 & 19
l-P6 Pt 5.0 %								0.9 $\pm$ 0.2	28.40	741 & 895	46 & 19

Table A.4 | Detailed table with the porphyrin hexamers organic light-emitting diodes (OLEDs) data.

Sample	η_{EL}^{max} (%)	$\langle\eta_{EL}^{max}\rangle$ (%)	R_{max} mW/cm^2	$\langle R_{max}\rangle$ mW/cm^2	V_{ON} (V)	λ_{max}^{EL} (nm)	NIR EL (%)
F8BT pure	0.32	0.28 ± 0.04	0.88	0.4 ± 0.19	3.7 ± 0.46	560.0	
l-P6 H2 1.0 %	3.20	2.66 ± 0.33	3.40	1.88 ± 0.95	4.33 ± 0.8	864.0	71.3
l-P6 H2 2.5 %	0.50	0.39 ± 0.05	0.60	0.33 ± 0.18	5.5 ± 1.4	866.0	89.2
l-P6 H2 5.0 %	0.30	0.23 ± 0.05	0.10	0.11 ± 0.05	9.6 ± 0.36	869.0	95.1
l-P6 Mg 1.0 %	0.60	0.43 ± 0.23	0.80	0.52 ± 0.28	4.68 ± 1.1	890.0	95.5
l-P6 Mg 2.5 %	0.60	0.44 ± 0.08	0.60	0.35 ± 0.28	7.83 ± 0.52	891.0	96.9
l-P6 Mg 5.0 %	0.20	0.163 ± 0.03	0.10	0.07 ± 0.03	9.8 ± 0.9	894.0	95.5
l-P6 Zn 1.0 %	1.10	0.89 ± 0.26	0.60	0.49 ± 0.1	5.1 ± 0.5	860.0	84.4
l-P6 Zn 2.5 %	0.90	0.69 ± 0.1	0.30	0.29 ± 0.02	7.4 ± 0.8	863.0	94.5
l-P6 Zn 5.0 %	0.60	0.52 ± 0.07	0.40	0.26 ± 0.15	8 ± 0.25	856.0	98.3
l-P6 Pd 1.0 %	1.00	0.71 ± 0.18	2.60	1.78 ± 0.76	4.5 ± 0.69	763.0	84.6
l-P6 Pd 2.5 %	1.00	0.73 ± 0.22	1.00	0.71 ± 0.32	6.45 ± 0.67	769.0	88.4
l-P6 Pd 5.0 %	0.40	0.33 ± 0.04	1.50	0.97 ± 0.49	8 ± 0.58	769.0	97.8
l-P6 Pt 1.0 %	0.20	0.16 ± 0.04	0.20	0.15 ± 0.02	5.8 ± 0.76	728.0	72.3
l-P6 Pt 2.5 %	0.20	0.12 ± 0.06	0.60	0.28 ± 0.21	5.97 ± 0.68	729.0	78.6
l-P6 Pt 5.0 %	0.20	0.14 ± 0.03	0.60	0.43 ± 0.23	6.8 ± 1.04	730.0	92.5

Table A.5 | Detailed table with the CP-*l*-P5 organic light-emitting diodes (OLEDs) data.

Sample	η_{EL}^{max} (%)	$\langle\eta_{EL}^{max}\rangle$ (%)	R_{max} mW/cm^2	$\langle R_{max}\rangle$ mW/cm^2	V_{ON} (V)	λ_{max}^{EL} (nm)	NIR EL (%)
F8BT pure	0.95	0.77 ± 0.3	3.60	2.8 ± 0.8	3.3 ± 0.3	560.0	
F8BT(2) pure	0.13	0.13 ± 0.03	0.38	0.20 ± 0.14		560.0	
PIDT-2TPD pure		1.55 ± 0.1		2.3 ± 0.5	1.7 ± 0.01	640.0	46.0
PIDT-2TPD:CP-*l*-P5 1.0 %	2.46	1.96 ± 0.3	3.41	3.1 ± 0.7	1.6 ± 0.01	838.0	93.0
PIDT-2TPD:CP-*l*-P5 2.5 %	1.53	1.4 ± 0.1	2.20	2.1 ± 0.1	1.6 ± 0.01	846.0	96.0
PIDT-2TPD:CP-*l*-P5 5.0 %	1.10	0.73 ± 0.2	1.45	1 ± 0.3	1.6 ± 0.01	861.0	99.0
F8BT:CP-*l*-P5 1.0 %	2.56	1.52 ± 0.6	1.80	1 ± 0.6	4.9 ± 0.92	881.0	84.0
F8BT:CP-*l*-P5 2.5 %	1.10	0.95 ± 0.13	0.61	0.5 ± 0.17	8.5 ± 0.6	896.0	96.0
F8BT:CP-*l*-P5 5.0 %	0.63	0.56 ± 0.06	0.26	0.24 ± 0.01	8.7 ± 0.4	896.0	97.0
F8 pure	0.36	0.21 ± 0.12	0.37	0.36 ± 0.01	3.95 ± 0.5	510.0	
TFB pure	0.05	0.04 ± 0.01	0.70	0.68 ± 0.17	3.6 ± 0.2	436.0	
PFB pure	0.03	0.03 ± 0.01	0.62	0.63 ± 0.01	3.9 ± 0.01	487.0	
F8:CP-*l*-P5 1.0 %	0.35	0.29 ± 0.06	0.87	0.5 ± 0.36	5.9 ± 1	880.0	84.0
TFB:CP-*l*-P5 1.0 %	0.06	0.04 ± 0.01	0.78	0.51 ± 0.24	3 ± 0.01	835.0	68.0
PFB:CP-*l*-P5 1.0 %	0.03	0.02 ± 0.01	0.58	0.35 ± 0.24	3.01 ± 0.01	834.0	53.0

B | Pure polymers figures

This appendix includes the figures of the pure polymers used in the experiments of Chapter 3.

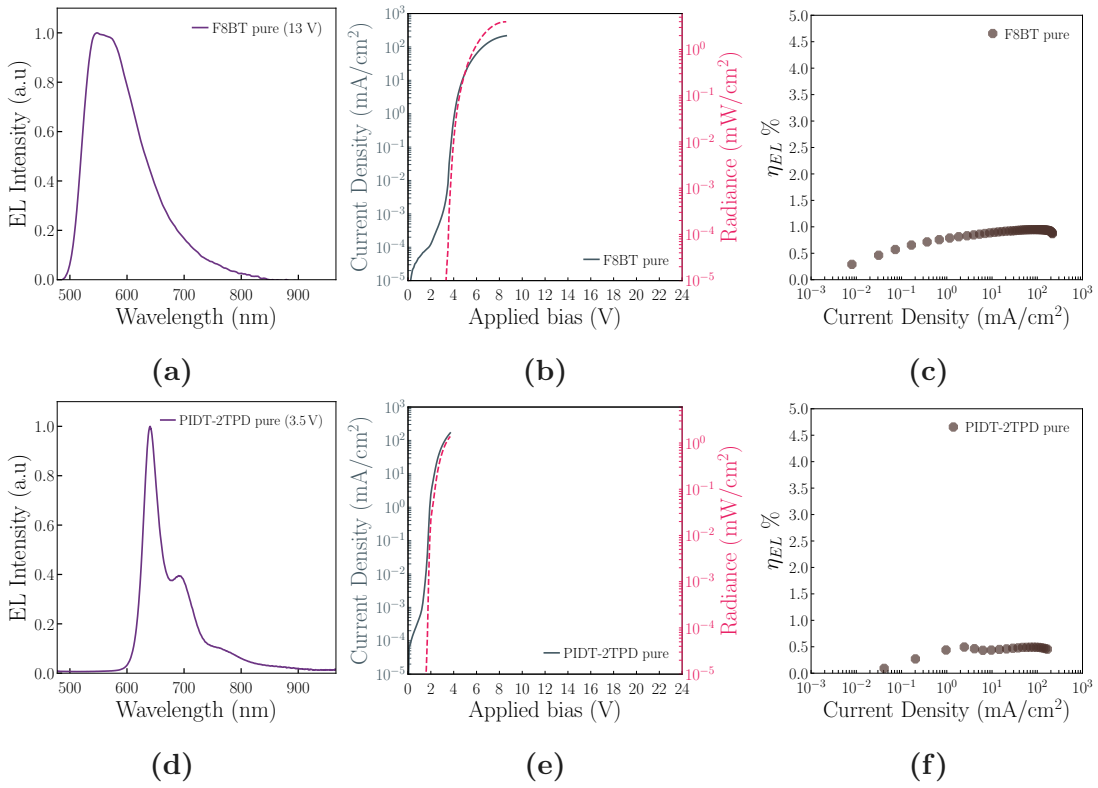

Figure B.1 | Pure F8BT (good batch) and pure PIDT-2TPD OLED properties. **(a, d)** (left) depicts the electroluminescence (EL) spectra, **(b, e)** (centre) the current density - voltage - radiance (JVR) curves and **(c, f)** (right) the electroluminescence external quantum efficiency (η_{EL}) versus current density of the OLEDs. The legends in **(a, d)** refer to the voltage at which the spectra where collected.

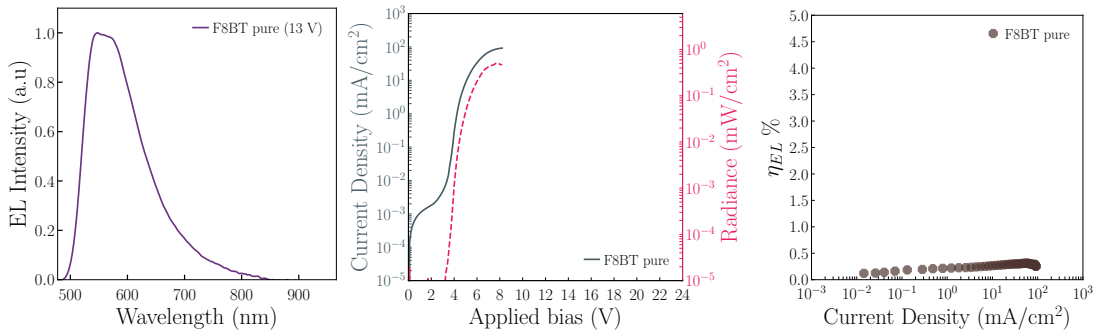

(a) **(b)** **(c)**

Figure B.2 | Pure F8BT (bad batch) OLED properties. **(a)** (left) depicts the electroluminescence (EL) spectra, **(b)** (centre) the current density - voltage - radiance (JVR) and **(c)** (right) the electroluminescence external quantum efficiency (η_{EL}) of the OLEDs. The legend in **(a)** refers to the voltage at which the spectra where collected.

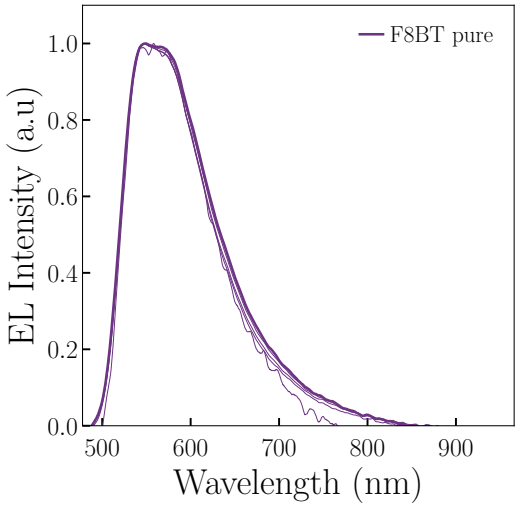

Figure B.3 | Voltage-resolved spectra for the pure F8BT organic light-emitting diodes (OLEDs).

C | η_{EL} versus Applied bias curves for OLEDs

In the Figures below are presented the electroluminescence external quantum efficiency (η_{EL}) versus applied bias curves for all the diodes that are presented in this thesis, in a grid format. This can facilitate comparisons.

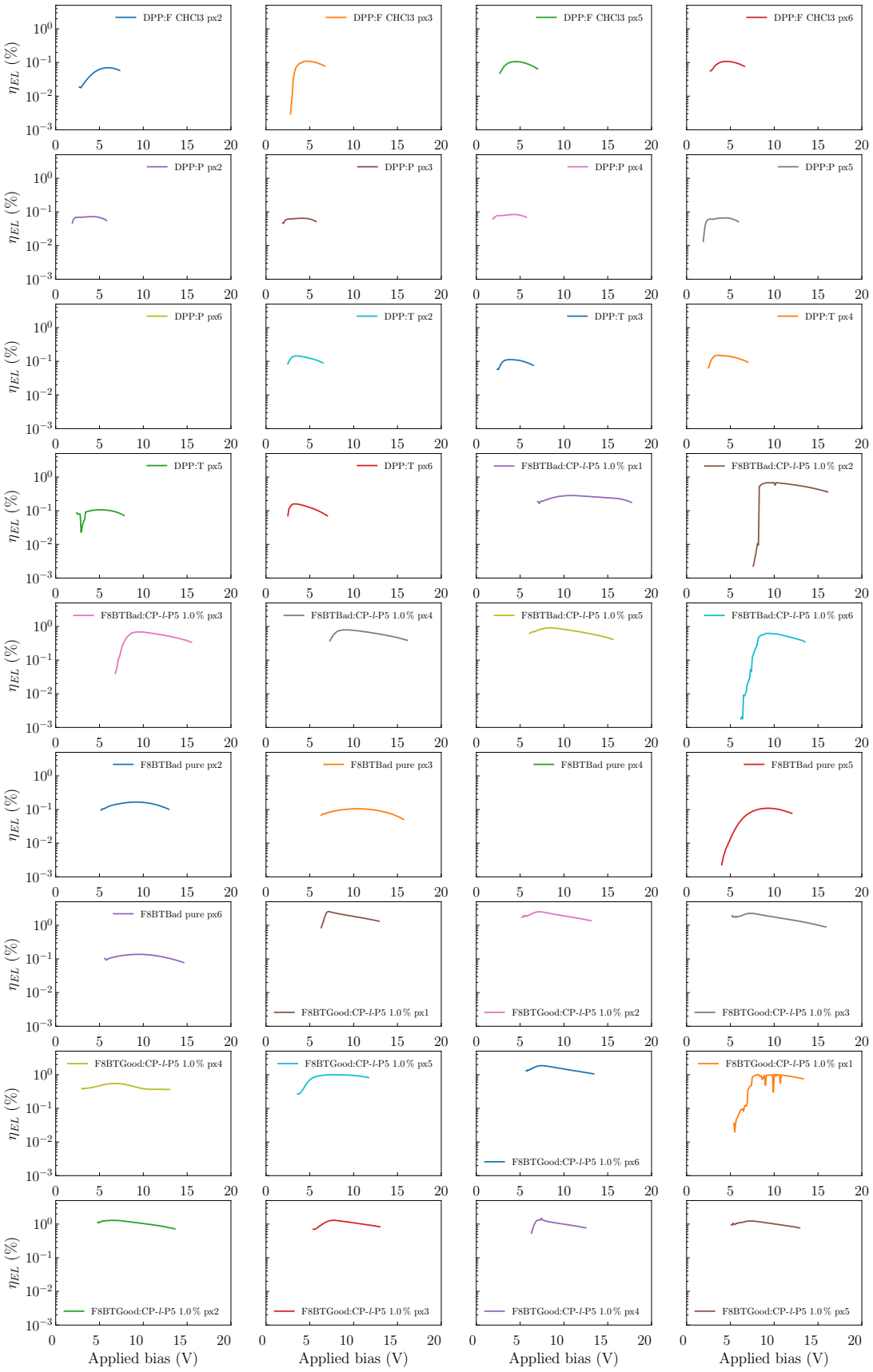

Figure C.1 | η_{EL} versus Applied bias curves for OLEDs (1).

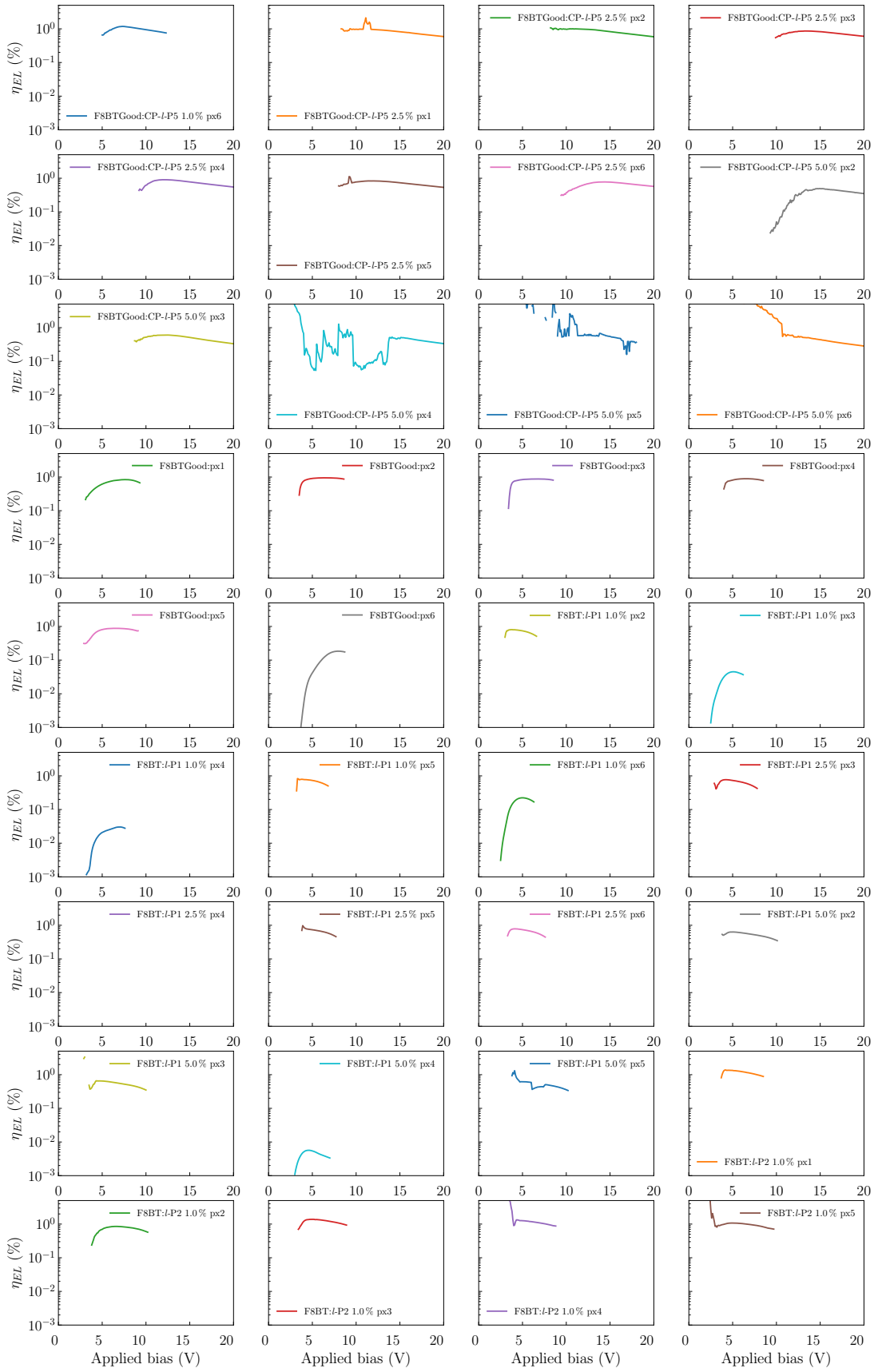

Figure C.2 | η_{EL} versus Applied bias curves for OLEDs (2).

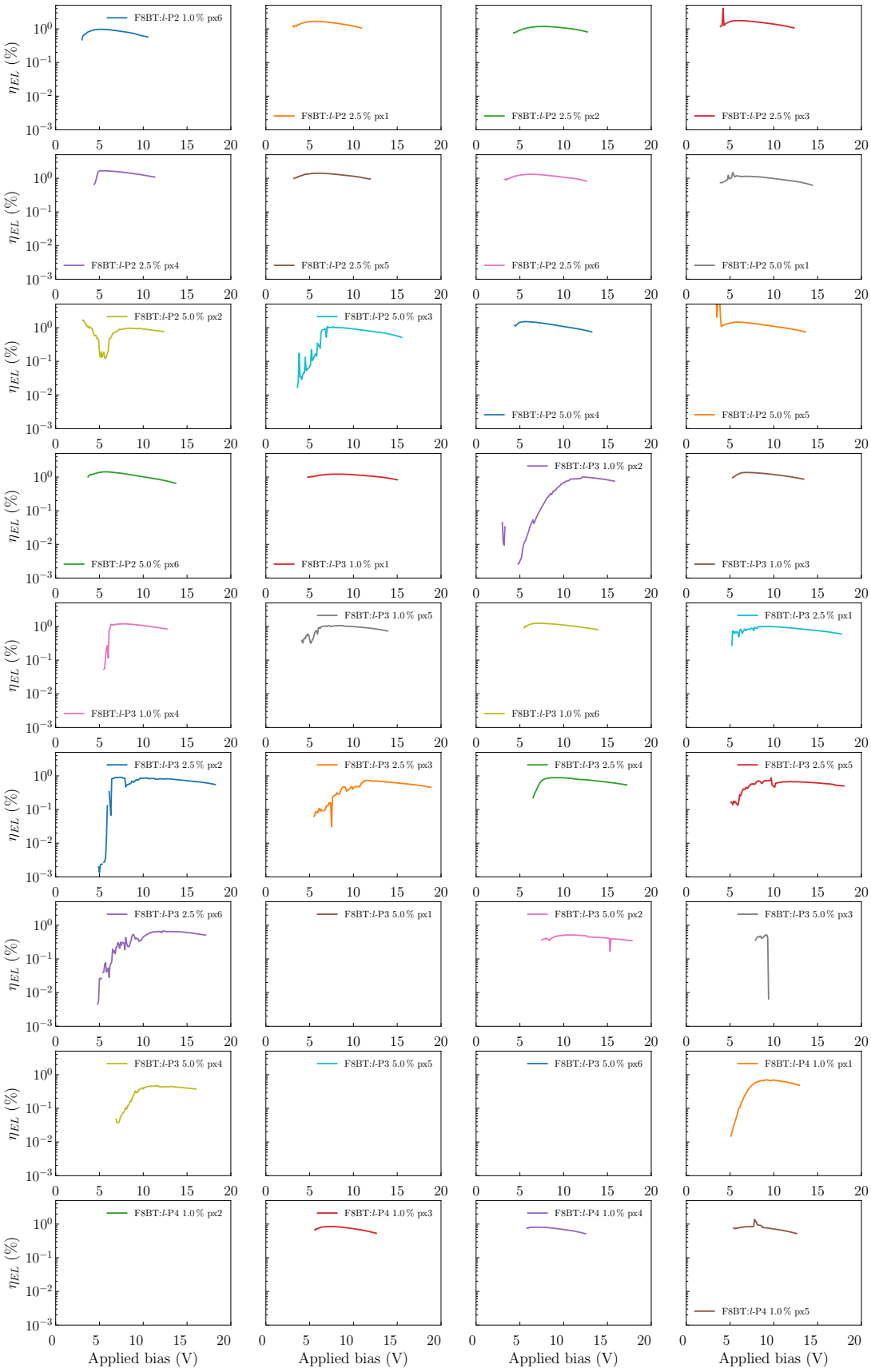

Figure C.3 | η_{EL} versus Applied bias curves for OLEDs (3).

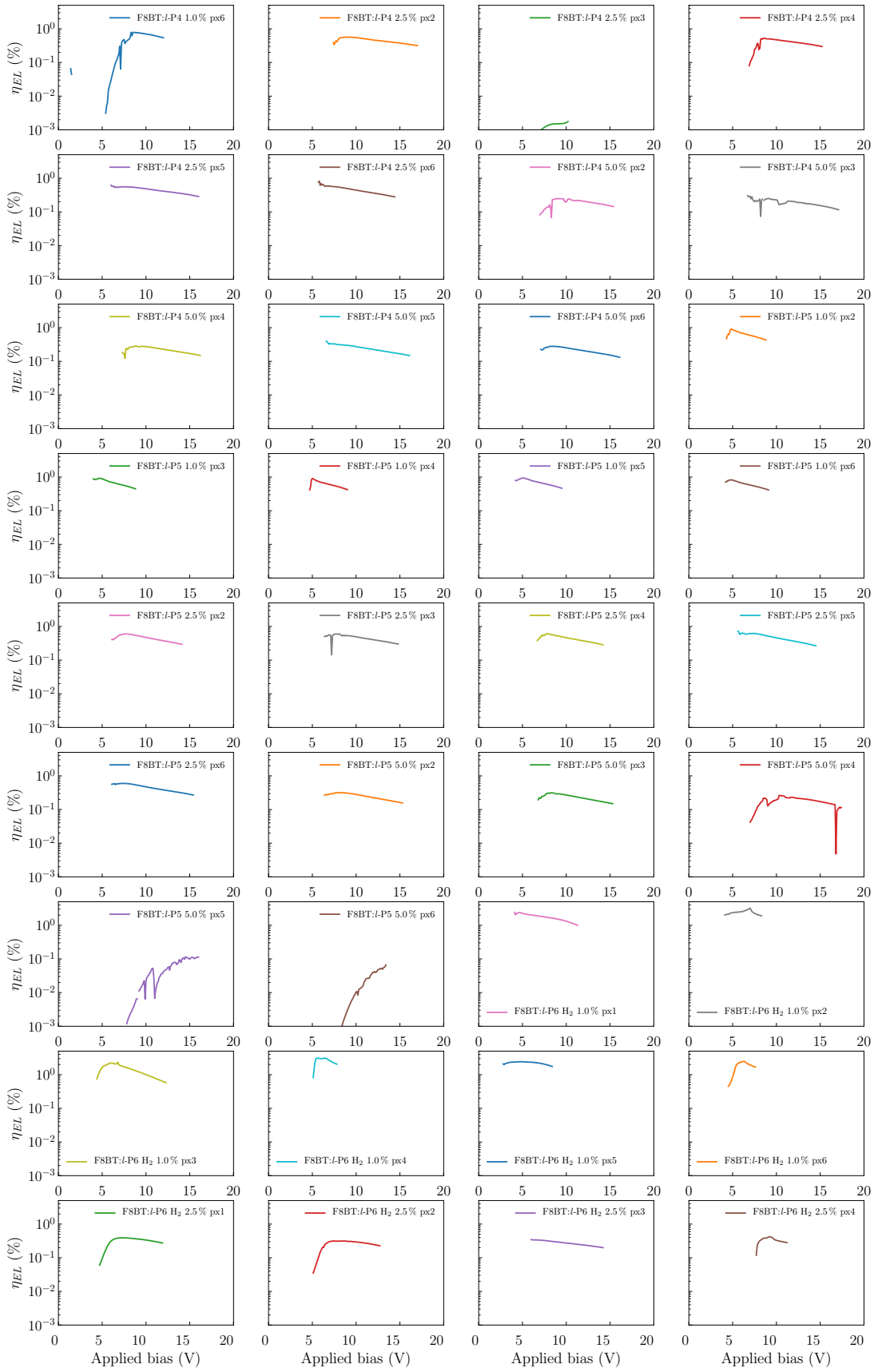

Figure C.4 | η_{EL} versus Applied bias curves for OLEDs (4).

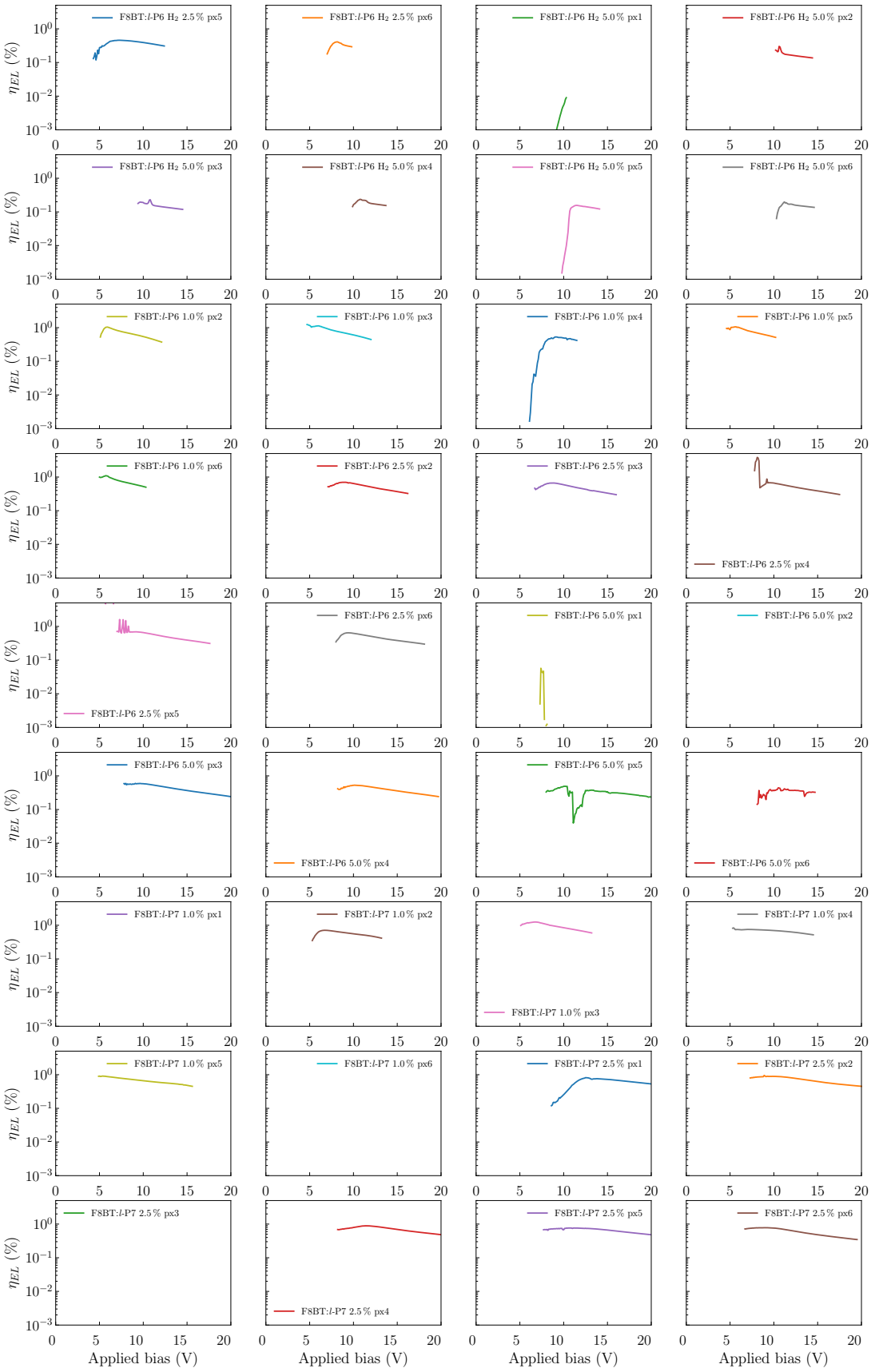

Figure C.5 | η_{EL} versus Applied bias curves for OLEDs(5).

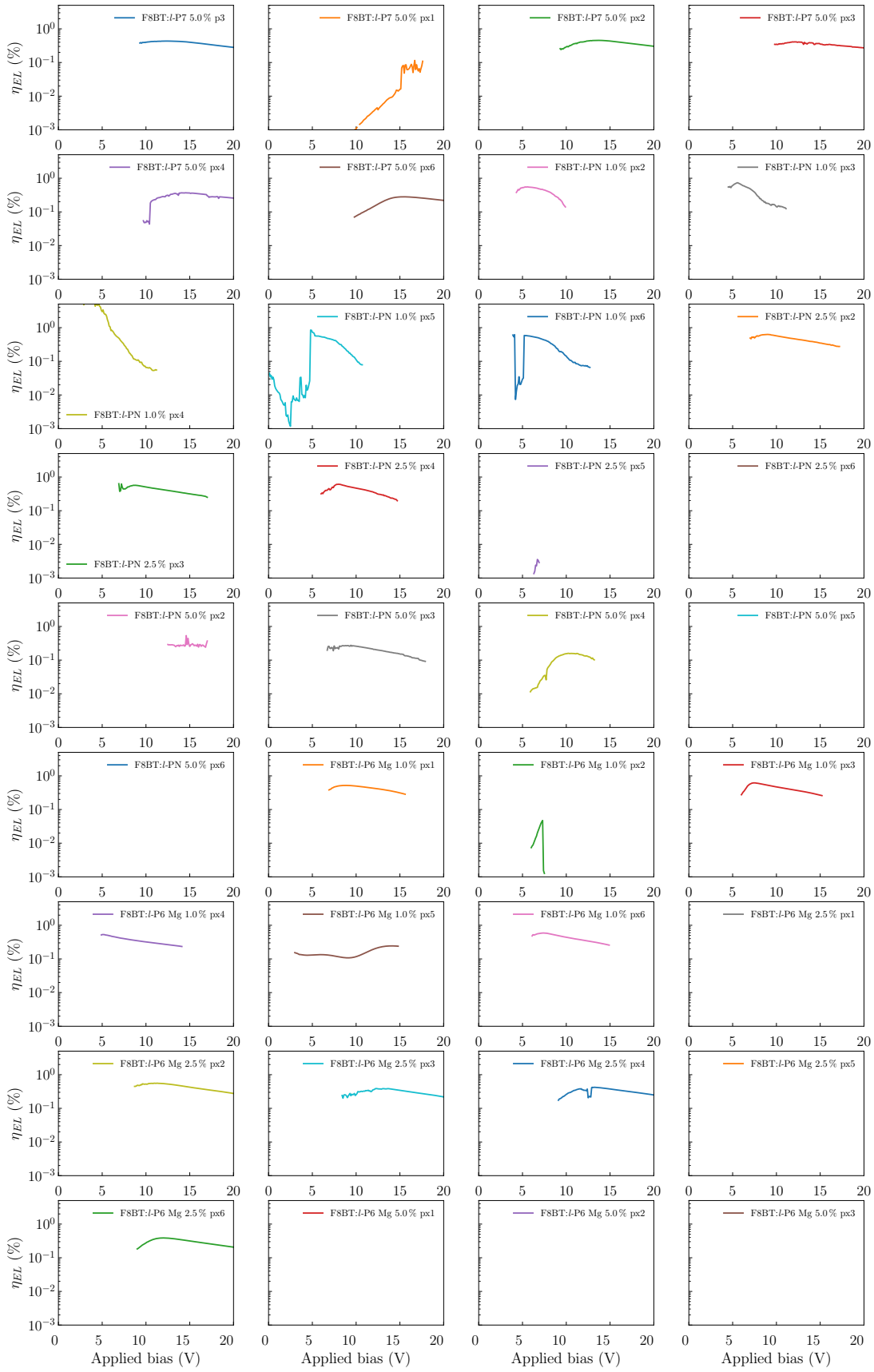

Figure C.6 | η_{EL} versus Applied bias curves for OLEDs (6).

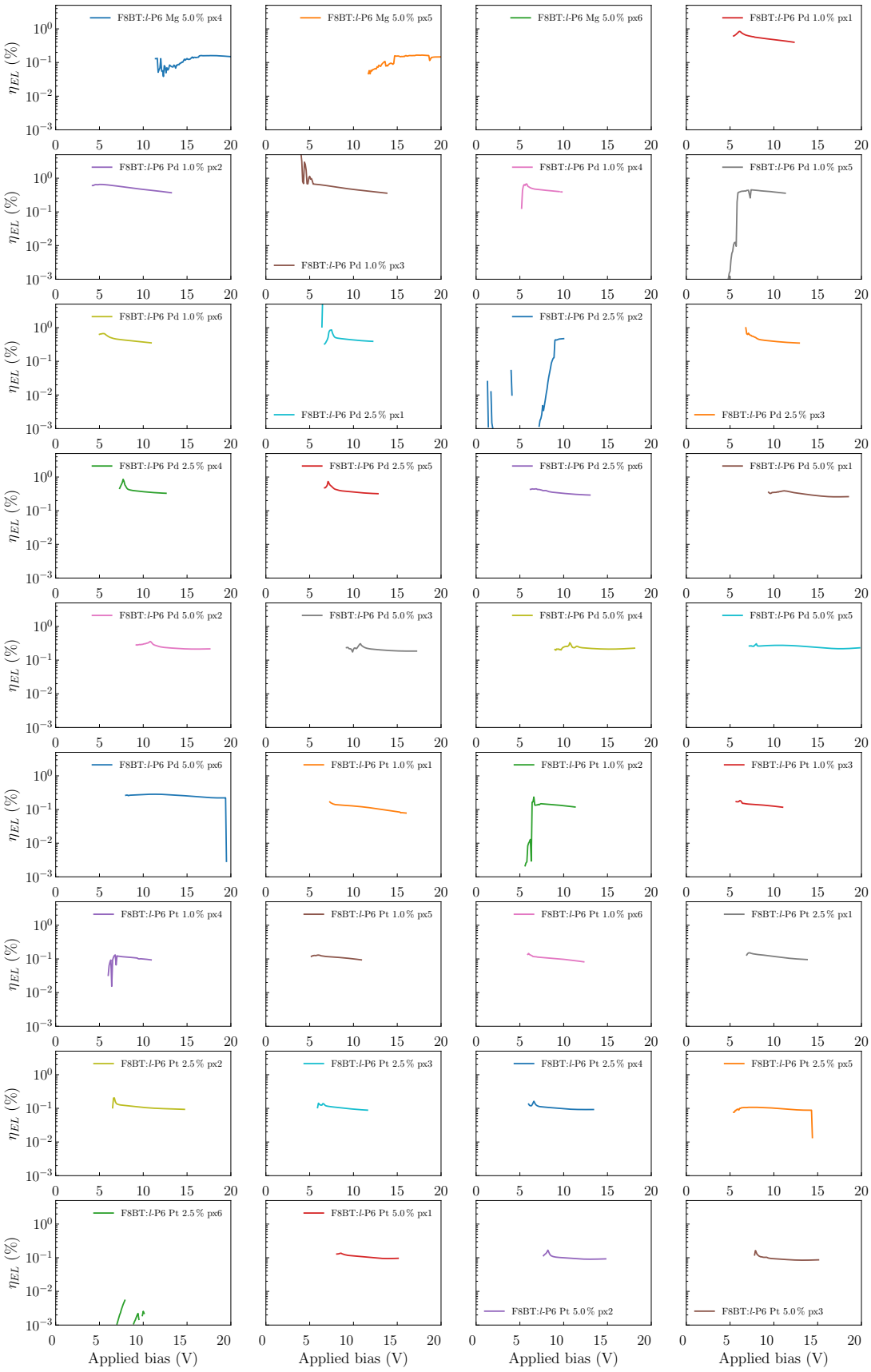

Figure C.7 | η_{EL} versus Applied bias curves for OLEDs (7).

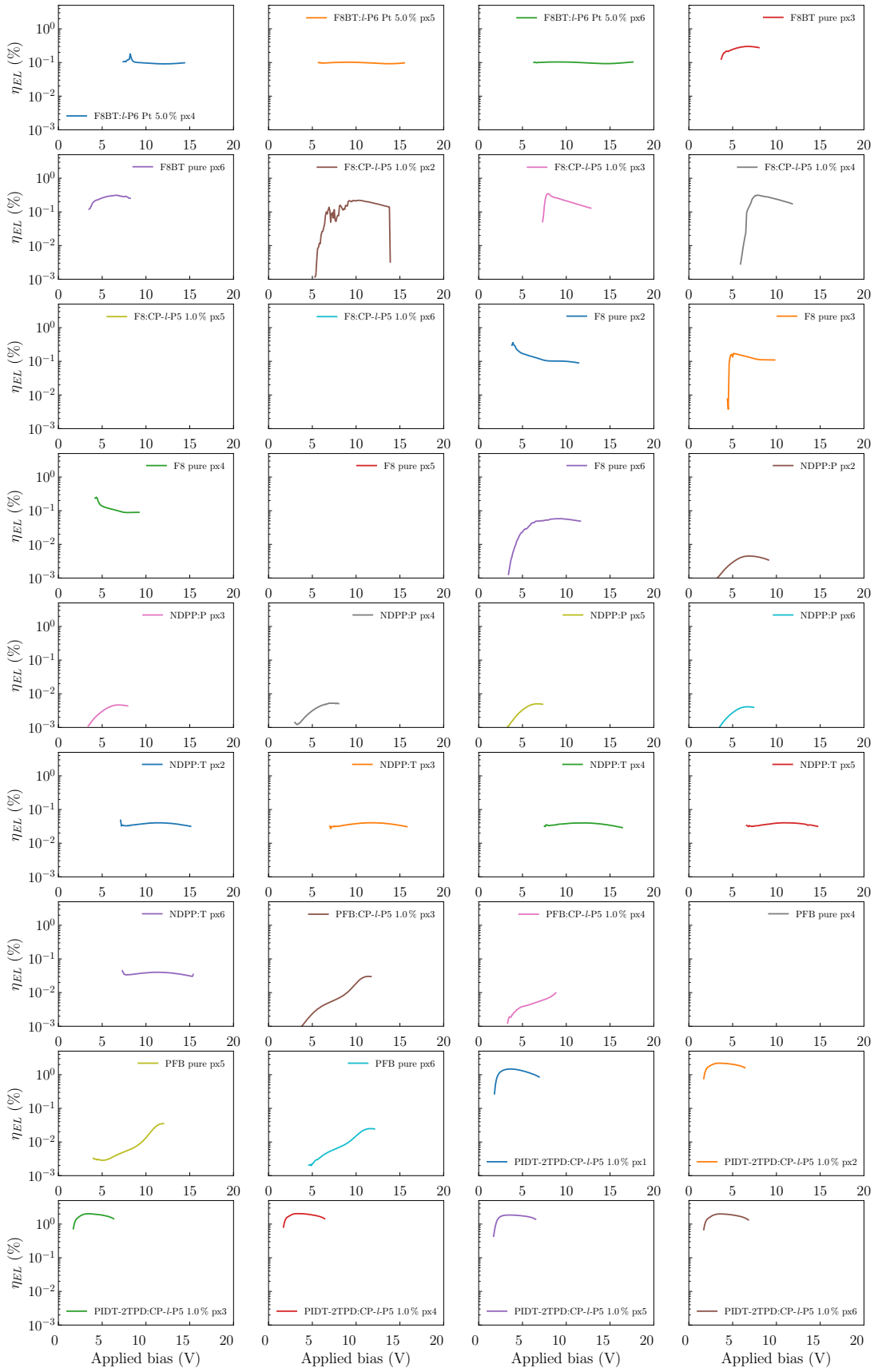

Figure C.8 | η_{EL} versus Applied bias curves for OLEDs (8).

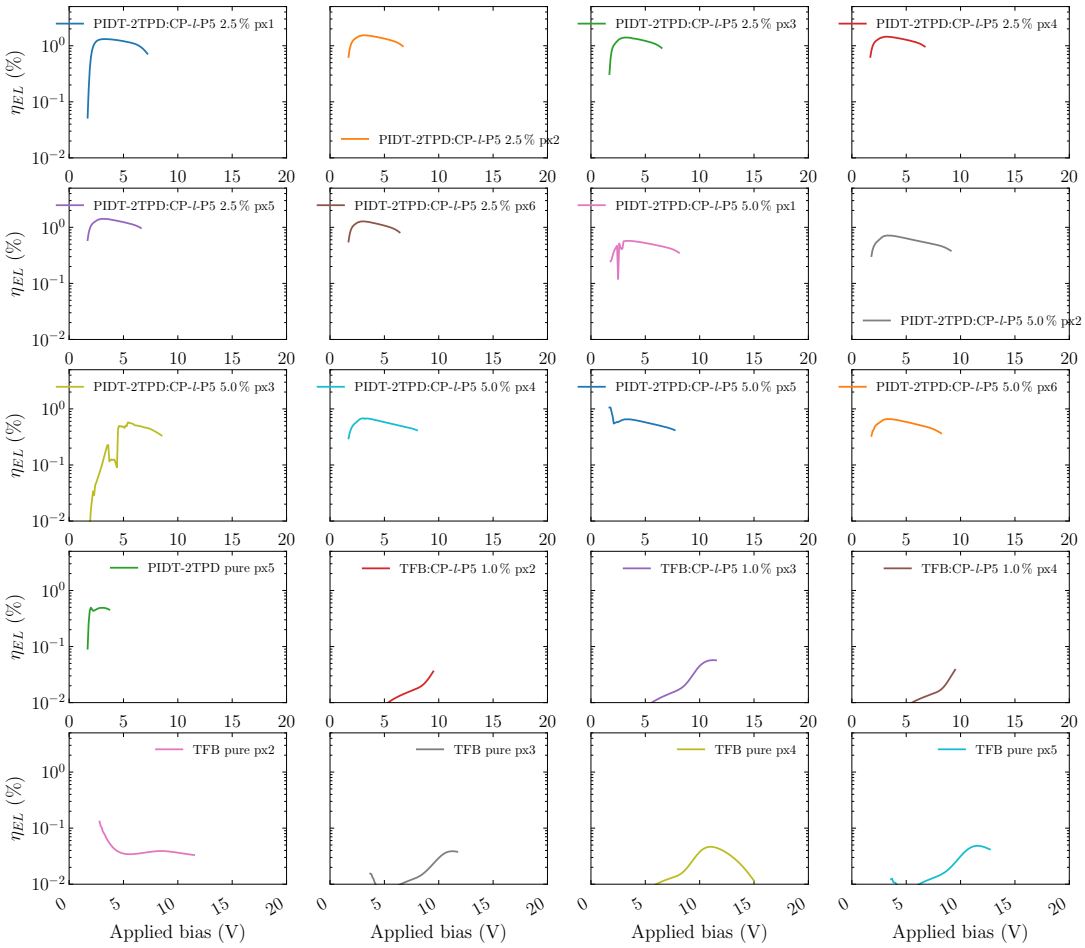

Figure C.9 | η_{EL} versus Applied bias curves for OLEDs (9).

D | Poster presentations

This appendix includes the posters that were presented in international conferences related to the work that was described in this thesis.

European Optical Society Bi-Annual Meeting (EOSAM) September 2016, Berlin, Germany

Near-Infrared Organic Light-Emitting Diodes based on Porphyrin Oligomers

A.G. Rapidis[1,‡], A. Minotto[1], I. Bulut[2], H.L. Anderson[2] and F. Cacialli[1]

[1]University College London, Department of Physics and Astronomy and London Centre for Nanotechnology, Gower Street, London, WC1E 6BT, U.K.
[2]University of Oxford, Department of Chemistry, Chemistry Research Laboratory, Mansfield Road, Oxford, OX1 3TA, U.K.

‡ a.rapidis@ucl.ac.uk

Abstract

We report the electro-optical characterisation of a series of near-infrared (NIR) emitting linear porphyrin hexamer (***l*-P6(THS)**) incorporated in polymer light-emitting diodes (PLEDs). We study the photoluminescence (PL) and the electroluminescence (EL) of the *l*-P6(THS) in blends with the commercial conjugated polymer poly(9,9′-dioctylfluorene-*alt*-benzothiadiazole) (F8BT) that demonstrated the highest external quantum efficiency (EQE) reported so far from a heavy-metal free and non-phosphorescent NIR emitter.

Introduction

NIR emitting materials have a wide range of applications:

- Medical (Photodynamic therapy) [1]
- Security and defence devices
- All optical communications (Li-Fi) [2]

- Novel linear porphyrin hexamer with different sidechains (THS) to prevent aggregation compared to previous work from our groups. [3]
- Solution processable materials w/o the need of high vacuum deposition techniques.

Optical Characterisation

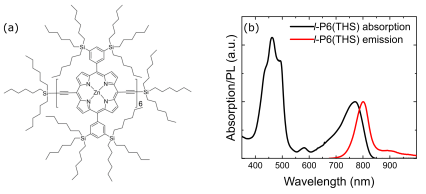

***(a)** Molecular structure of the porphyrins **(b)** Absorption and emission spectra of the l-P6(THS) in toluene solution at room temperature.*

- THS sidechains are limiting the π-π stacking
- >99 % of the photons are emitted in the NIR.

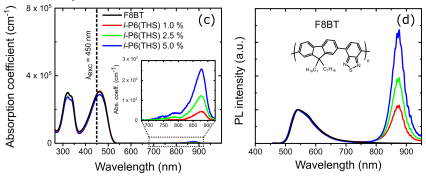

***(c)** Absorption and **(d)** emission spectra of the F8BT:l-P6(THS) blends in thin films (~100 nm), with different loadings of the l-P6(THS). The molecular structure of F8BT is shown.*

- F8BT emission spectrally overlaps with the *l*-P6(THS) absorption, permitting efficient energy transfer.
- At increasing loadings, the F8BT emission is quenched in favour of the oligomer.
- PLQY > 17 %, exceeding 32 % at lower concentrations.
- Focus on the 2.5 w/w% for the PLEDs

Sample	PLQY (%)	PL in NIR (%)
F8BT	54	3
1.0 % *l*-P6(THS)	17	52
2.5 % *l*-P6(THS)	13	62
5.0 % *l*-P6(THS)	6	83

Polymer Light-Emitting Diodes (PLEDs)

We fabricated PLEDs incorporating the F8BT:*l*-P6(THS) blends with the architecture shown below.

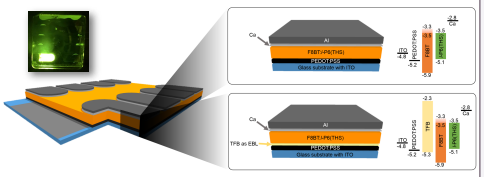

Illustration of the fabricated devices showing the cross-sections and the relative band diagrams. One of the fabricated devices switched-on incorporating pure F8BT as active layer and TFB as EBL is shown.

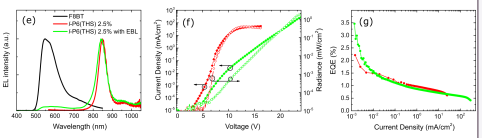

***(e)** EL spectra of the PLEDs incorporating pure F8BT and the F8BT:l-P6(THS) blends. **(f)** J-V-L characteristics of the PLEDs. **(g)** EQE versus current density curves of the PLEDs. EL collected at saturation voltage for each device.*

- Spectrally pure EL with >95 % of the photons in the NIR
- Peak of the emission at 850 nm
- Use of the commercial hole transporting polymer TFB to act as Electron Blocking Layer (EBL) [4]
- Substantial increase of the average max radiance and EQE, as well as the EQE_{MAX} obtained

Sample	V_{ON} (V)	Average R_{MAX} (mW/cm²)	EQE_{MAX} (%)	Average EQE_{MAX} (%)	EL in the NIR (%)
2.5 % w/o EBL	6.6±1.2	0.3±0.1	2.21	0.88±0.35	98
2.5 % with EBL	8.1±0.9	1.9±0.6	3.46	1.1±0.5	95

References

1. Jang, B. et al., *ACS Nano* 1086-1094 (2011)
2. Haigh, P. et al., *Opt Express* **22**, 2830-2838 (2014)
3. Fenwick, O. et al., *Nano Lett.* **11**, 2451-2456 (2011)
4. Kim, J. S. et al., *Appl. Phys. Lett.* **87**, 80-83 (2005)

Conclusions – Future work

❖ We characterised electro-optically the PL and EL of a novel conjugated linear porphyrin hexamer.
❖ We demonstrated the highest EL EQE = 3.46 % in the NIR from a non-phosphorescent and heavy-metals free material.
❖ The average maximum EQE is >1 % while remaining above 0.5 % at high current densities (>200 mA/cm²).
❖ The introduction of a thin (>10 nm) layer of TFB improves significantly the performance and characteristics of the device.

➢ Future optimisation of the multi-layered architecture with the introduction of a Hole Blocking Layer (HBL).
➢ Examine different lengths of the repeating porphyrin unit for colour tuning.

Acknowledgements

This work was funded from the European Community's Framework Programme for Research and Innovation Horizon 2020 as a Marie Skłodowska-Curie Action European Training Network (MSCA-ETN) under Grant Agreement No. 643238 (SYNCHRONICS).
Prof. Franco Cacialli is Royal Society Wolfson Research Merit Award Holder.

European Material Research Society (E-MRS) September 2017, Warsaw, Poland

Highly Efficient Near-Infrared Organic Light-Emitting Diodes based on Porphyrin Oligomers

A. G. Rapidis[1,‡], A. Minotto[1], I. Bulut[2], H. L. Anderson[2] and F. Cacialli[1]

[1]University College London, Department of Physics and Astronomy and London Centre for Nanotechnology, Gower Street, London, WC1E 6BT, U.K.
[2]University of Oxford, Department of Chemistry, Chemistry Research Laboratory, Mansfield Road, Oxford, OX1 3TA, U.K.

‡ a.rapidis@ucl.ac.uk

Abstract

Here we report the optical characterisation of a series of near-infrared (NIR) emitting porphyrin oligomers incorporated in organic light-emitting diodes (OLEDs). We characterised the optical properties both in solution and thin film and the electroluminescence external quantum efficiency (η_{EL}) of the oligomers in blends with the commercial conjugated polymers poly(9,9′-dioctylfluorene-alt-benzothiadiazole) (F8BT), that demonstrated high EQEs up to 3.8 %. We investigated different loadings of the porphyrins in the polymer matrix and carried-out optical characterisation by means of UV-VIS absorption, time-resolved emission spectroscopy (time-correlated single photon counting) and PL efficiency measurements (η_{PL}).

Introduction

NIR emitting materials have a wide range of applications

- ❑ Medical (Photodynamic therapy and Low Level Light Therapy) [1]
  - ➢ Low absorption from tissue and > 50 % CCD efficiency in the 700 – 950 nm window [2]
- ❑ All optical communications (Li-Fi) [3]

- Novel linear porphyrin hexamer with bulky sidechains (THS) to prevent aggregation
- Solution-processable materials w/o the need of high-vacuum deposition techniques.

Optical Characterisation

Optical characterisation includes UV-VIS-NIR absorption and ηPL measurements of the porphyrin oligomers.

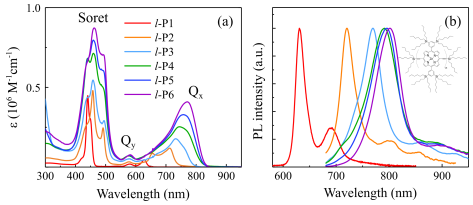

(a) *Absorption and* ***(b)*** *Emission spectra of the oligomers in toluene solution at room temperature. Inset in* ***(b)*** *shows the porphyrin structure.*

- THS sidechains are limiting the π-π stacking
- Monomer PL peaks at 630 nm while the hexamer has >99 % of the photons are emitted in the NIR.

Blending the hexamer (NIR emission) with the commercial conjugated polymer F8BT (good spectral overlap – efficient Förster Resonance Energy Transfer)

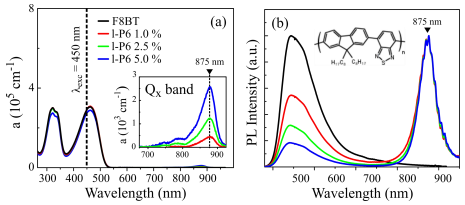

(a) *Absorption and* ***(b)*** *emission spectra of the F8BT:I-P6 blends in thin films (~100 nm). The molecular structure of F8BT is shown in* ***(b)****.*

- At increasing loadings, the F8BT emission is quenched in favour of the oligomer – up to 85 % NIR emission at 10 w/w % loading
- η_{PL} > 17 %, exceeding 32 % at lower concentrations.
- Focus on the 2.5 w/w% for the OLEDs

Organic Light-Emitting Diodes (OLEDs)

We fabricated OLEDs incorporating the F8BT:*I*-P6 blends with the architecture shown below.

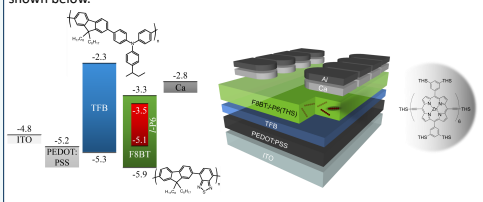

Illustration of the fabricated devices showing the cross-sections and the relative band diagrams..

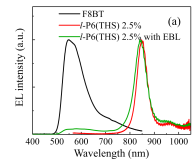

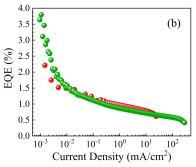

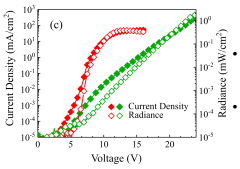

(a) *EL spectra of the OLEDs incorporating the F8BT:I-P6 blends.* ***(b)*** *η_{EL} versus Current Density curves with and w/o EBL.* ***(c)*** *Current Density – Voltage – Radiance curves of the OLEDs.*

Main focus on the 2.5 % as the best compromise between spectral purity and efficiency.

- ❑ Spectrally pure NIR emission with > 95 % of the photons at λ > 700 nm.
- ❑ EL peaking at 850 nm with 45 nm FWHM.
- ❑ η_{EL} up to 2.2 %.
- ❑ By adding the commercial conjugated polymer TFB to act as Electron Blocking Layer (EBL) the η_{EL} improved further to 3.8 %. [4]

- Average maximum η_{EL} remained > 1.1 % with the EBL and > 0.8 % w/o EBL.
- Average maximum radiance > 1.9 mW/cm² with EBL and > 0.3 mw/cm² w/o EBL

References

1. Jang, B. et al., *ACS Nano* 1086-1094 (2011)
2. Smith, A. M. et al., *Nature Nanotechnology*, 4, 710-711 (2009)
3. Tsonev, D. et al., Proc. Of SPIE, 9007, 900702 (2013)
4. Kim, J.-S. et al., APL, 87, 02356 (2005)

Conclusions – Future work

❖ We characterised electro-optically the PL and EL of a novel conjugated linear porphyrin hexamer.
❖ We demonstrated the highest η_{EL} = 3.8 % in the NIR from a non-phosphorescent and heavy-metal free material with a τ ~ ns, suitable for telecommunications applications.

➢ Improve the injected carrier balance by adding a Hole Blocking Layer (HBL).
➢ Harvest triplet emission by substituting with heavy metals (Pt, Pd) the Zn centre.

Acknowledgements

This work was funded from the European Community's Framework Programme for Research and Innovation Horizon 2020 as a Marie Skłodowska-Curie Action European Training Network (MSCA-ETN) under Grant Agreement No. 643238 (SYNCHRONICS).
Prof. Franco Cacialli is Royal Society Wolfson Research Merit Award Holder.

PRESENCE Workshop: PhD students as a bridge between science and society, Festival of Science October 2017, Genova, Italy

Flexible Electronics

Alexandros G. Rapidis‡

University College London, Department of Physics and Astronomy and London Centre for Nanotechnology
Gower Street, London, WC1E 6BT, U.K.

‡ **a.rapidis@ucl.ac.uk**

What is Flexible electronics?

The majority of electronics is built on top of silicon (Si) as a substrate. On certain occasions, glass can be used as an alternative to silicon. By using a flexible material as substrate, such as various kinds of plastic, and fabricating electronics on it, we end up with *flexible electronics!* Will the next Samsung Galaxy or Apple iPhone use flexible materials? Maybe…

Applications
Flexible screens and sensors – Next generation smartphones and laptops?

Many smartphone and laptop manufacturers have presented concepts and working prototypes of foldable and flexible devices.

Lenovo - using advanced material and new screen technologies to create a foldable laptop screen (concept 2016)


Lenovo

Cambridge Graphene Centre and Plastic Logic – Flexible e-ink type display using graphene electronics. (2014)

LG Display – A 810x1200 18" OLED foldable display with a reported $1.75 billion investment. With 0.18mm thick, it's rollable like a poster! (presented 2016).


Flexterra

Flexterra – A start-up comprised by physicists and chemists created a 24 mm x 30mm flexible screen for a smart "wrist band" called Wove Band. (2017)

Central Standard Timing - CST-01:A 0.8mm thick flexible wristwatch, with an e-ink (Kindle like) screen. The "world's thinnest watch" that weighs 12g. It raised over $1,000,000 on Kickstarter. (2013)

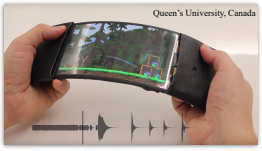

Queen's University, Canada – ReFlex: A flexible smartphone with useful features, but also fun! Bend it to launch the birds in *Angry Birds*!! It has a 720p OLED display by LG, Android OS and sensors to "feel" the bend. (2016)

Flexible sensors

To enable flexible devices, a flexible touchscreen is needed. Also, flexible and conformable electronics find applications in wearable sensors for bio-related applications.

University of British Columbia, Canada – A 5cm x 5cm prototype flexible sensor that can detect "touch" commands while bended or stretched. (2017)

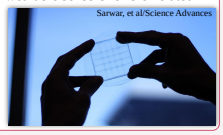

Applications
Flexible batteries and solar cells – Energy supply

Smartphones and laptops with flexible screens and flexible electronics are useless without a flexible source of energy. Batteries can be made flexible. A *greener* alternative? Flexible solar cells? Done!

Korean Universities – Flexible, ultra-thin solar cells that can be integrated to a number of devices and objects : smartwatches, clothes, bags, even glasses! (2016)

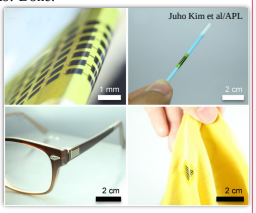

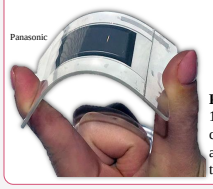
Panasonic

Panasonic – A flexible battery that can pass 1000 bend cycles and maintain 80% of the capacity. At 0.45 mm, it is very thin, but with a low max capacity of 60 mAh, much less than an iPhone 7 battery (~1900 mAh). (2017)

Our work for Flexible Electronics: Sensors!

Our approach to flexible sensors is "tattoo" electronics! Just like the "tattoos" found in snacks! All that is needed is just a wet cloth an the tattoo is transferred. Our driving force:

University of California-Berkley, US – All-organic sensor for pulse oximetry: Measure pulse rate and blood oxygenation by using light. Flexible substrate with two OLEDs and a detector. (2014)


Lochner et al, Nat. Commun. 2014

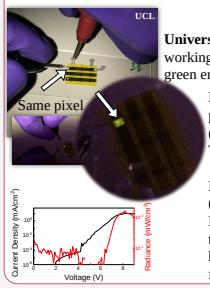

University College London, London – A tattoo-able working OLEDs on commercial tattoo paper with green emission – On-going work!

For this work we used a commercial tattoo paper, some bio-compatible "plastics" (polymers) to emit the light and aluminium! The device works (not ideally, yet!)!

Further optimisations are on the way! Our (Italian) collaborators at the Centre for Micro-BioRobotics (CMBR) in IIT are developing the detection part on the same tattoo paper and hopefully we can obtain a fully organic flexible OLED-detection system.

Conclusions

Flexible electronics are a major market, with a projected worth of up to $73.4 billion by 2027 for the printed, flexible and organic electronics markets, receiving a lot of investments from over 3000 companies and organisations ranging from multinational companies, such as LG and Samsung, to innovative start-ups and leading Universities around the world.

Acknowledgements

This work was funded by the European Community's Framework Programme for Research and Innovation Horizon 2020 as a Marie Skłodowska-Curie Action European Training Network (MSCA-ETN) under Grant Agreement No. 643238 (SYNCHRONICS).
Part of this work was in collaboration with J. Barsotti and V. Mattoli of the IIT-Pontedera.

Organic Light-Emitting Diodes based on Narrow Bandgap Encapsulated Diketopyrrolopyrrole Polymers

A. G. Rapidis[1,‡], A. Leventis[2], J. Royakkers[2], N. Goodeal[2] M. Corpinot[3], J. M. Frost[4], D.-K. Bučar[3], M. Blunt[2], H. Bronstein[4] and F. Cacialli[1]

[1]University College London, Department of Physics and Astronomy and London Centre for Nanotechnology, Gower Street, London, WC1E 6BT, U.K.
[2]University of Cambridge, Department of Chemistry & Physics, Lensfield Road, Cambridge, CB2 1EW, U.K.
[3]University College London, Department of Chemistry, 20 Gordon Street, London, WC1H 0AJ, U.K.
[4]Imperial College London, Department of Materials, Exhibition Road, London, SW7 2AZ, U.K.

‡ a.rapidis@ucl.ac.uk

1. Abstract

Here we report the optical and electro-optical characterisation of three encapsulated low-gap red-emitting conjugated polymers and their "naked" analogues, incorporated in organic light-emitting diodes (OLEDs). We characterised the optical properties both in solution and thin films, and the electroluminescence external quantum efficiency (η_{EL}) to evaluate the advantages of our encapsulation strategy which entails sheathing of the conjugated cores via covalently-bound and ring-shaped sidechain. The novel polymers exhibit high fluorescence quantum yields (η_{PL}), both in solution (> 70 %) and in thin films (> 20 %) as a result of reduced suppressed pi-pi aggregation and structural disorder.

2. Optical Characterisation

- ❑ Diketopyrrolopyrrole (DPP) motifs in: organic solar cells, transistor devices, as dyes in automotive industry (Ferrari)
- ❑ Luminescent applications limited due to the tendency of DPP to π-π stack

- ➢ Covalent approach to sheath the DPP core and prevent stacking effects
- ➢ Copolymerised with three different derivatives: fluorene (E-DPPF), thiophene (E-DPPT) and phenyl (E-DPPP) (Figure 1)

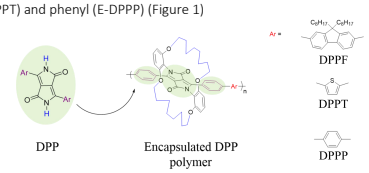

Figure 1: *Representation of the encapsulation strategy of the DPP core. The copolymerised derivatives are shown on the right.*

- ❑ Further explore the efficacy of the encapsulation strategy by comparing with the "naked" analogues
- ❑ PL spectra are compared in Figure 2

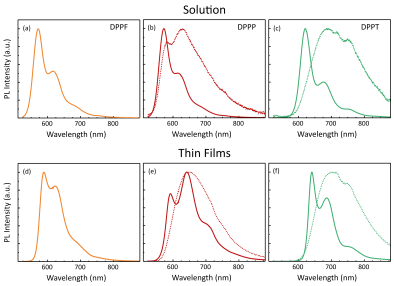

Figure 2: *Normalised photoluminescence spectra.* ***(a, b, c)*** *Dilute solution in chlorobenzene (~ 4 μg/ml).* ***(d, e, f)*** *Thin films (~ 100 nm thickness). Solid lines → encapsulated polymers, dashed lines → "naked" analogues.* ***(a, d)*** *DPPF,* ***(b, e)*** *DPPP and* ***(c, f)*** *DPPT.*

- ❑ ~20 nm red-shift from solution to thin films due to increased planarity "Naked" versus encapsulated polymers
- ❑ Spectral narrowing and blue-shift for the encapsulated polymers (FWHM narrowing of ~ 80 and ~ 40 nm for DPPP in solution and thin film respectively, ~ 130 and ~ 75 nm for DPPT)
- ❑ 3 times higher η_{PL} of the encapsulated polymers in both solution and thin films

Sample	$\eta_{PL}^{solution}$ (%)	η_{PL}^{film} (%)
E-DPPF	94.8 ± 1.1	19.8 ± 1.1
E-DPPP	74 ±1.2	22.6 ± 1.1
E-DPPT	73.6 ± 1.2	27.8 ± 1.3
N-DPPF		
N-DPPP	19 ± 3.3	8 ± 0.3
N-DPPT	18.2 ± 1.3	5.6 ± 0.5

3. Organic Light-Emitting Diodes (OLEDs)

- ❑ We fabricated OLEDs using the polymers as the active layer in a typical structure of ITO/PEDOT:PSS/Polymer/Calcium/Aluminium.

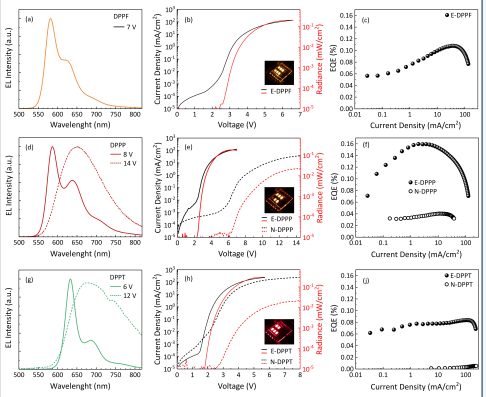

Figure 3: *(a, d, g) EL spectra,* ***(b, e, h)*** *current density – voltage – radiance (IVR) curves (black for current density and red for radiance) of E-DPPF, E-DPPP and E-DPPT (solid lines) and the "naked" analogues (dashed lines) respectively.* ***(c, f, j)*** *η_{EL} versus current density of E-DPPF, E-DPPP and E-DPPT (black balls) and the "naked" analogues (empty circles) respectively.*

- ❑ Electroluminescence (EL) FWHM increased by ~ 50 and ~ 140 nm respectively for DPPP and DPPT)
- ❑ Red-shift of ~ 70 nm for DPPP and ~ 50 nm for the DPPT
- ❑ External quantum efficiency (η_{EL}) of OLEDs shows 4 time increase for DPPP and 16 times for DPPT.
- ❑ Up to 10 times higher radiance (~ 0.2 mW/cm² and ~ 0.02 mW/cm² for encapsulated and "naked" respectively)
- ➢ All corroborate our claims for aggregation prevention of the encapsulated polymers

4. Conclusions

- ❖ Successful synthesis of three diketopyrrolopyrrole copolymers
- ❖ We characterised electro-optically the PL and EL of a novel conjugated insulated molecular wired DPP copolymer
- ❖ We compared the optical and electro-optical properties of the encapsulated polymers to their "naked" analogues to demonstrate the suppression of aggregation.
- ❖ First demonstration of a DPP copolymer with very high η_{PL} both in solution and thin film, paving the way for future applications where efficient red emitters are required.

5. References

A. Leventis et al., JACS, 2018, 140 (5), pp 1622–1626

Acknowledgements

This work was funded from the European Community's Framework Programme for Research and Innovation Horizon 2020 as a Marie Skłodowska-Curie Action European Training Network (MSCA-ETN) under Grant Agreement Nos. 643238 (SYNCHRONICS) and 679789-455 (CONTREX).
Prof. Franco Cacialli is Royal Society Wolfson Research Merit Award Holder.

European Material Research Society (E-MRS) June 2018, Strasbourg, France

Porphyrin oligomers as efficient low-bandgap emitters in Organic Light-Emitting Diodes

A. G. Rapidis[1,‡], R. Scowen[2], A. Minotto[1], G. Carnicella[1], I. Bulut[3], H. L. Anderson[3] and F. Cacialli[1]

[1]University College London, Department of Physics and Astronomy and London Centre for Nanotechnology, Gower Street, London, WC1E 6BT, U.K.
[2]University College London, Department of Electronic and Electrical Engineering, Torrington Place, London, WC1E 7JE, U.K.
[3]University of Oxford, Department of Chemistry, Chemistry Research Laboratory, Mansfield Road, Oxford, OX1 3TA, U.K.

‡ a.rapidis@ucl.ac.uk

1. Abstract

We characterised a series of low-gap zinc porphyrin oligomers and incorporated in organic light-emitting diodes (OLEDs). The modified bulky trihexylsilyl (THS) sidechains prevent π-π stacking, whereas an increase of the oligomer length increases the conjugation and hinders intersystem crossing. This allows the tuning of the emission from red to the near-infrared (NIR) (λ > 700 nm) and achieving high η_{EL}. When incorporated in OLEDs, porphyrins emit up to ~ 900 nm and show exceptionally high η_{EL}, up to 4.5 % and high radiances, up to 4 mw/cm², paving the way for applications where NIR emitters are required.

2. Introduction

NIR emitting materials have applications in:

- ❑ Medical (photodynamic therapy and low level light therapy)
  - ➢ Low absorption from tissue and > 50 % CCD efficiency in the 700 – 950 nm window
- ❑ All optical communications (Li-Fi)
- ❑ Defence and security

- ❖ Synthesised a series of zinc porphyrin oligomers with bulky sidechains to prevent aggregation
- ❖ Solution-processable materials w/o the need of high-vacuum deposition techniques
- ❖ Tuning of the emission by changing the oligomer length

3. Optical Characterisation

- ❑ Oligomers emit in the red and NIR region
- ❑ Peaks in solution from ~ 630 nm to ~800 > 80 % of the emission in the NIR

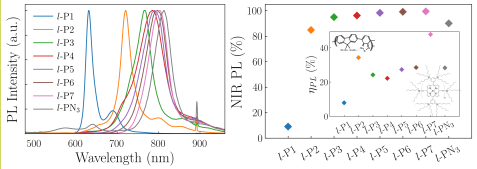

Figure 1: (left) *Normalised photoluminescence in dilute (10^{-6} M) toluene solution.* ***(right)*** *Percentage of the photoluminescence in the NIR region. Inset: Photoluminescence quantum yield (η_{PL}) of the oligomers in solution. Structures of F8BT (top left) and porphyrin (bottom right)*

- ❑ THS sidechains are limiting the π-π stacking
- ❑ Oligomers show high η_{PL} in solution, up to ~ 45 % for *l*-P7
- ❑ For n > 3, > 95 % in the NIR

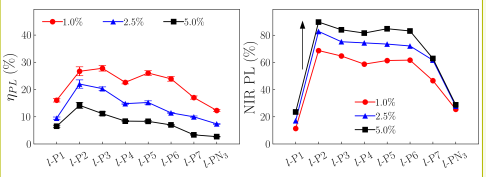

Figure 2: (left) *Photoluminescence quantum yield (η_{PL}) of the F8BT:Oligomers blends in thin films (~ 100 nm).* ***(right)*** *Percentage of the photoluminescence in the NIR region.*

- ❑ For solid-state applications, blends with a commercial conjugated polymer, F8BT
  - ➢ Excellent semiconducting properties
  - ➢ Good spectral overlap – efficient Förster Resonant Energy Transfer (FRET) expected
  - ➢ Blends with F8BT in three loadings: 1.0, 2.5 and 5.0 w/w%
- ❑ Good trade-off of NIR emission-high η_{PL} for the 2.5 w/w% loading and the mid-length oligomers
- ❑ Increasing the loading → increased quenching of F8BT → High NIR emission

4. Organic Light-Emitting Diodes (OLEDs)

- ❑ Multi-layered OLEDs fabrication incorporating the F8BT:*Oligomers* blends as active layer
- ❑ OLEDs architecture: ITO/PEDOT:PSS/Active Layer/Calcium/Aluminium
- ❑ OLEDs show almost complete quenching of the F8BT emission
  - ➢ > 90 % of the photons in the NIR
  - ➢ Type II heterojunction favours the emission from the low energy sites
  - ➢ Direct recombination rather than FRET

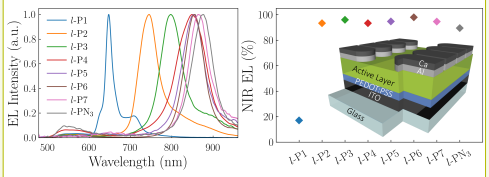

Figure 3: (left) *Normalised electroluminescence spectra of F8BT:Porphyrin blends.* ***(right)*** *Percentage of the electroluminescence in the NIR region. Both figures show the spectra and NIR EL of F8BT:Porphyrin 5.0 w/w% loading at the voltage where the maximum light emission was achieved. Inset: Illustration of the architecture of the fabricated OLEDs.*

- ❑ η_{EL} values represent some of the highest reported for heavy-metal free organic materials for this spectral range
  - ➢ η_{EL} max of 4.5 % for *l*-P2
  - ➢ > 1 % for all oligomers
- ❑ Average maximum η_{EL} remains > 0.5 % for all the oligomers

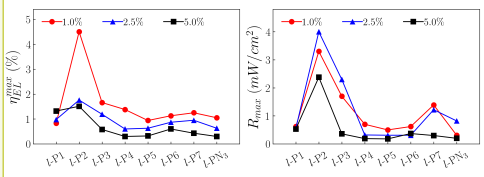

Figure 4: (left) *Maximum electroluminescence external quantum efficiency (η_{EL}) achieved.* ***(right)*** *Maximum radiance achieved.*

- ❑ Radiances exhibited by the oligomers up to ~ 4 mW/cm²
- ❑ Maximum radiance achieved at reasonable voltages (~ 15 V) for the 1.0 and 2.5 w/w% loadings

5. Conclusions – Future work

- ❖ We characterised electro-optically the PL and EL of a series novel conjugated linear porphyrin oligomers.
- ❖ We demonstrated very high η_{EL} = 4.5 % and radiance in the NIR from a non-phosphorescent and heavy-metal free material, suitable for applications in the NIR
- ❖ We showed the tuning of the emission by changing the oligomer length
- ➢ Use a different host polymer than F8BT
- ➢ Harvest triplet emission by substituting zinc with heavy metals (Pt, Pd) in the metal centre.

Acknowledgements

This work was funded from the European Community's Framework Programme for Research and Innovation Horizon 2020 as a Marie Skłodowska-Curie Action European Training Network (MSCA-ETN) under Grant Agreement No. 643238 (SYNCHRONICS).
Prof. Franco Cacialli is Royal Society Wolfson Research Merit Award Holder.

Bibliography

[1] F. Cacialli, "Organic semiconductors for the new millennium," *Philosophical Transactions of the Royal Society A: Mathematical, Physical and Engineering Sciences*, vol. 358, no. 1765, pp. 173–192, 2000.

[2] J. Clark and G. Lanzani, "Organic photonics for communications," *Nature Photonics*, vol. 4, no. 7, pp. 438–446, 2010.

[3] H. Sirringhaus, T. Kawase, R. H. Friend, T. Shimoda, M. Inbasekaran, W. Wu, and E. P. Woo, "High-Resolution Inkjet Printing of All-Polymer Transistor Circuits," *Science*, vol. 290, no. 5499, pp. 2123–2126, 2000.

[4] J. F. Maya-Vetencourt, D. Ghezzi, M. R. Antognazza, E. Colombo, M. Mete, P. Feyen, A. Desii, A. Buschiazzo, M. Di Paolo, S. Di Marco, F. Ticconi, L. Emionite, D. Shmal, C. Marini, I. Donelli, G. Freddi, R. MacCarone, S. Bisti, G. Sambuceti, G. Pertile, G. Lanzani, and F. Benfenati, "A fully organic retinal prosthesis restores vision in a rat model of degenerative blindness," *Nature Materials*, vol. 16, no. 6, pp. 681–689, 2017.

[5] M. H. Segler, M. Preuss, and M. P. Waller, "Planning chemical syntheses with deep neural networks and symbolic AI," *Nature*, vol. 555, no. 7698, pp. 604–610, 2018.

[6] K. T. Butler, D. W. Davies, H. Cartwright, O. Isayev, and A. Walsh, "Machine learning for molecular and materials science," *Nature*, vol. 559, no. 7715, pp. 547–555, 2018.

[7] A. Bernanose, M. Comte, and P. Vouaux, "Sur un nouveau mode d'émission lumineuse chez certains composés organiques," *J. Chim. Phys.*, vol. 50, pp. 64–68, 1953.

[8] A. Bernanose and G. Marquet, "Électroluminescence Du Carbazol Par Les Champs Électriques Alternatifs - Charactérisation De

L'Électrophotoluminescence Organique," *J. Chim. Phys.*, vol. 51, pp. 255–259, 1954.

[9] M. Pope, H. P. Kallmann, and P. Magnante, "Electroluminescence in Organic Crystals," *The Journal of Chemical Physics*, vol. 38, no. 8, pp. 2042–2043, 1963.

[10] C. K. Chiang, C. R. Fincher, Y. W. Park, A. J. Heeger, H. Shirakawa, E. J. Louis, S. C. Gau, and A. G. MacDiarmid, "Electrical conductivity in doped polyacetylene," *Physical Review Letters*, vol. 39, no. 17, pp. 1098–1101, 1977.

[11] H. Shirakawa, J. Louis, and A. G. Macdiarmid, "Synthesis of Electrically Conducting Organic Polymers : Halogene Derivatives of Polyacetylene, (CH)x," *J. C. S. Chem. Comm*, no. 578, pp. 578–580, 1977.

[12] G. E. Eperon, *Active Layer Control for High Efficiency Perovskite Solar Cells*. PhD thesis, University of Oxford, 2015.

[13] S. D. Stranks, *Investigating Carbon Nanotube – Polymer Blends for Organic Solar Cell Applications*. PhD thesis, University of Oxford, 2011.

[14] H. J. Snaith, "Estimating the maximum attainable efficiency in Dye-sensitized solar cells," *Advanced Functional Materials*, vol. 20, no. 1, pp. 13–19, 2010.

[15] L. Meng, Y. Zhang, X. Wan, C. Li, X. Zhang, Y. Wang, X. Ke, Z. Xiao, L. Ding, R. Xia, H.-L. Yip, Y. Cao, and Y. Chen, "Organic and solution-processed tandem solar cells with 17.3% efficiency," *Science*, vol. 2612, 2018.

[16] J. Burroughes, D. Bradley, A. R. Brown, R. N. Marks, K. Mackay, R. H. Friend, P. L. Burns, and A. B. Holmes, "Light-emitting diodes based on conjugated polymers," *Nature*, vol. 347, pp. 539–541, 1990.

[17] R. H. Friend, R. W. Gymer, A. B. Holmes, J. H. Burroughes, R. N. Marks, C. Taliani, D. D. C. Bradley, D. A. D. Santos, J. L. Bredas, M. Logdlund, and W. R. Salaneck, "Electroluminescence in conjugated polymers," *Nature*, vol. 397, no. 6715, pp. 121–128, 1999.

[18] I. D. W. Samuel and G. A. Turnbull, "Organic Semiconductor Lasers," *Chemical Reviews*, vol. 107, no. 4, pp. 1272–1295, 2007.

[19] N. Tessler, G. J. Denton, and R. H. Friend, "Lasing from conjugated-polymer microcavities," 1996.

[20] M. H. Song, D. Kabra, B. Wenger, R. H. Friend, and H. J. Snaith, "Optically-pumped lasing in hybrid organic-inorganic light-emitting diodes," *Advanced Functional Materials*, vol. 19, no. 13, pp. 2130–2136, 2009.

[21] J. J. M. Halls, C. A. Walsh, N. C. Greenham, E. A. Marseglia, R. H. Friend, S. C. Moratti, and A. B. Holmes, "Efficient photodiodes from interpenetrating polymer networks," *Nature*, vol. 376, no. 6540, pp. 498–500, 1995.

[22] H. Sirringhaus, P. J. Brown, R. H. Friend, M. M. Nielsen, K. Bechgaard, B. M. W. Langeveld-Voss, A. J. H. Spiering, R. A. J. Janssen, E. W. Meijer, P. Herwig, and D. M. de Leeuw, "Two-dimensional charge transport in self-organized, high-mobility conjugated polymers," *Nature*, vol. 401, no. 6754, pp. 685–688, 1999.

[23] B. O'Regan and M. Grätzel, "A low-cost, high-efficiency solar cell based on dye-sensitized colloidal TiO2 films," *Nature*, vol. 353, no. 6346, pp. 737–740, 1991.

[24] S. Mathew, A. Yella, P. Gao, R. Humphry-Baker, B. F. E. Curchod, N. Ashari-Astani, I. Tavernelli, U. Rothlisberger, M. K. Nazeeruddin, and M. Grätzel, "Dye-sensitized solar cells with 13% efficiency achieved through the molecular engineering of porphyrin sensitizers," *Nature Chemistry*, vol. 6, no. 3, pp. 242–247, 2014.

[25] H. J. Snaith, "Present status and future prospects of perovskite photovoltaics," *Nature Materials*, vol. 17, pp. 372–376, 2018.

[26] M. M. Lee, J. Teuscher, T. Miyasaka, T. N. Murakami, and H. J. Snaith, "Efficient Hybrid Solar Cells Based on Meso-Superstructured Organometal Halide Perovskites," *Science*, vol. 338, 2012.

[27] A. Kojima, K. Teshima, Y. Shirai, and T. Miyasaka, "Novel Photoelectrochemical Cell with Mesoscopic Electrodes Sensitized by Lead-halide Compounds (11)," *Meeting Abstracts*, vol. MA2006-02, 2006.

[28] A. Kojima, K. Teshima, Y. Shirai, and T. Miyasaka, "Organometal Halide Perovskites as Visible- Light Sensitizers for Photovoltaic Cells," *J. Am. Chem. Soc*, vol. 131, pp. 6050–6051, 2009.

[29] L. Serrano-Lujan, N. Espinosa, T. T. Larsen-Olsen, J. Abad, A. Urbina, and F. C. Krebs, "Tin- and lead-based perovskite solar cells under scrutiny: An environmental perspective," *Advanced Energy Materials*, vol. 5, no. 20, pp. 1–5, 2015.

[30] F. Giustino and H. J. Snaith, "Toward Lead-Free Perovskite Solar Cells," *ACS Energy Letters*, vol. 1, pp. 1233–1240, 2016.

[31] O. D. Miller, E. Yablonovitch, and S. R. Kurtz, "Intense internal and external fluorescence as solar cell approach the SQ efficiency limit," *Photovoltaics, IEEE Journal of*, vol. 2, no. 3, pp. 1–27, 2012.

[32] R. H. Partridge, "Electroluminescence from polyvinylcarbazole films: 1. Carbazole cations," *Polymer*, vol. 24, no. 6, pp. 733–738, 1983.

[33] C. W. Tang and S. A. Vanslyke, "Organic electroluminescent diodes," *Applied Physics Letters*, vol. 51, no. 12, pp. 913–915, 1987.

[34] C. Adachi, S. Tokito, T. Tsutsui, and S. Saito, "Organic electroluminescent device with a three-layer structure," *Japanese Journal of Applied Physics*, vol. 27, no. 4A, pp. L713–L715, 1988.

[35] D. Braun and A. J. Heeger, "Visible light emission from semiconducting polymer diodes," *Applied Physics Letters*, vol. 58, no. 18, pp. 1982–1984, 1991.

[36] G. Gustafsson, Y. Cao, G. M. Treacy, F. Klavetter, N. Colaneri, and a. J. Heeger, "Flexible Light-Emitting-Diodes Made from Soluble Conducting Polymers," *Nature*, vol. 357, no. 6378, pp. 477–479, 1992.

[37] S. D. Stranks and H. J. Snaith, "Metal-halide perovskites for photovoltaic and light-emitting devices," *Nature Nanotechnology*, vol. 10, no. 5, pp. 391–402, 2015.

[38] B. R. Sutherland and E. H. Sargent, "Perovskite photonic sources," *Nature Photonics*, vol. 10, no. 5, pp. 295–302, 2016.

[39] H. Cho, S.-H. Jeong, M.-H. Park, Y.-H. Kim, C. Wolf, C.-L. Lee, J. H. Heo, A. Sadhanala, N. Myoung, S. Yoo, S. H. Im, R. H. Friend, and T.-W. Lee, "Overcoming the Electroluminescence Efficiency Limitations of Perovskite Light-Eitting Diodes," *Science*, vol. 350, no. 6265, p. 1222, 2015.

[40] G. Xing, N. Mathews, S. S. Lim, N. Yantara, X. Liu, D. Sabba, M. Grätzel, S. Mhaisalkar, and T. C. Sum, "Low-temperature solution-processed wavelength-tunable perovskites for lasing," *Nature Materials*, vol. 13, no. 5, pp. 476–480, 2014.

[41] F. Deschler, M. Price, S. Pathak, L. E. Klintberg, D. D. Jarausch, R. Higler, S. Hüttner, T. Leijtens, S. D. Stranks, H. J. Snaith, M. Atatüre, R. T. Phillips, and R. H. Friend, "High photoluminescence efficiency

and optically pumped lasing in solution-processed mixed halide perovskite semiconductors," *Journal of Physical Chemistry Letters*, vol. 5, no. 8, pp. 1421–1426, 2014.

[42] G. Li, R. Zhu, and Y. Yang, "Polymer solar cells," *Nature Photonics*, vol. 6, no. 3, pp. 153–161, 2012.

[43] C. J. Brabec, N. S. Sariciftci, and J. C. Hummelen, "Plastic Solar Cells," *Advanced Functional Materials*, vol. 11, no. 1, pp. 15–26, 2001.

[44] C. W. Tang, "Two-layer organic photovoltaic cell," *Applied Physics Letters*, vol. 48, no. 2, pp. 183–185, 1986.

[45] G. Horowitz, "Organic field-effect transistors," *Advanced Materials*, vol. 10, no. 5, pp. 365–377, 1998.

[46] L. Hou, X. Zhang, G. F. Cotella, G. Carnicella, M. Herder, B. M. Schmidt, M. Pätzel, S. Hecht, F. Cacialli, and P. Samorì, "Optically switchable organic light-emitting transistors," *Nature Nanotechnology*, 2019.

[47] R. G. Sun, Y. Z. Wang, Q. B. Zheng, H. J. Zhang, and A. J. Epstein, "1.54 um Infrared Photoluminescence and Electroluminescence From an Erbium Organic Compound," *Journal of Applied Physics*, vol. 87, no. 10, pp. 7589–7591, 2000.

[48] D. Y. Kim, T.-H. Lai, J. W. Lee, J. R. Manders, and F. So, "Multi-spectral imaging with infrared sensitive organic light emitting diode," *Scientific Reports*, vol. 4, pp. 1–5, 2014.

[49] H. Suzuki, "Organic light-emitting materials and devices for optical communication technology," *Journal of Photochemistry and Photobiology A: Chemistry*, vol. 166, no. 1-3, pp. 155–161, 2004.

[50] S. E. Braslavsky and K. N. Houk, "Glossary of terms used in photochemistry (Recommendations 1988)," *Pure and Applied Chemistry*, vol. 60, no. 7, pp. 1055–1106, 1988.

[51] M. Kasha, "Characterization of Electronic Tran- Sitions in Complex Molecules," *Discuss. Faraday Soc.*, vol. 9, no. c, pp. 14–19, 1950.

[52] C. M. Marian, "Spin – orbit coupling and intersystem crossing in molecules," *Advanced Review*, vol. 2, pp. 187–203, 2012.

[53] D. Beljonne, Z. Shuai, G. Pourtois, and J. L. Bredas, "Spin - Orbit Coupling and Intersystem Crossing in Conjugated Polymers: A Configuration

Interaction Description," *The Journal of Physical Chemistry A*, vol. 105, no. 15, pp. 3899–3907, 2001.

[54] A. Kohler and H. Bassler, *Electronic Processes in Organic Semiconductors*. John Wiley & Sons, 2015.

[55] N. J. Turro, V. Ramamurthy, V. Ramamurthy, and J. C. Scaiano, *Principles of molecular photochemistry: an introduction*. University science books, 2009.

[56] Martin Pope and C. E. Swenberg, *Electronic Processes In Organic Crystals and Polymers*. Oxford University Press, second edi ed., 1999.

[57] M. Knupfer, "Exciton binding energies in organic semiconductors," *Applied Physics A: Materials Science and Processing*, vol. 77, no. 5, pp. 623–626, 2003.

[58] S. F. Alvarado, P. F. Seidler, D. G. Lidzey, and D. D. C. Bradley, "Direct determination of the exciton binding energy of conjugated polymers using a scanning tunneling microscope," *Physical Review Letters*, vol. 81, no. 5, pp. 1082–1085, 1998.

[59] F. Perrin, "Theorie de la fluorescence polarisée (influence de la viscosité)," *Compt. rend*, vol. 180, p. 581, 1925.

[60] F. Perrin, "Polarisation de la lumière de fluorescence. Vie moyenne des molécules dans l'etat excité," *Journal de Physique et le Radium*, vol. 7, pp. 390–401, 1926.

[61] Q. Pei and Y. Yang, "Efficient Photoluminescence and Electroluminescence from a Soluble Polyfluorene," *Journal of the American Chemical Society*, vol. 7863, no. 11, pp. 7416–7417, 1996.

[62] M. Grell, D. D. C. Bradley, M. Inbasekaran, and E. P. Woo, "A glass-forming conjugated main-chain liquid crystal polymer for polarized electroluminescence applications," *Advanced Materials*, vol. 9, no. 10, pp. 798–802, 1997.

[63] D. D. C. Bradley, "Conjugated polymer electroluminescence," *Synthetic Metals*, vol. 54, no. 1-3, pp. 401–415, 1993.

[64] T. M. Brown, J. S. Kim, R. H. Friend, F. Cacialli, R. Daik, and W. J. Feast, "Built-in field electroabsorption spectroscopy of polymer light-emitting diodes incorporating a doped poly(3,4-ethylene dioxythiophene) hole injection layer," *Applied Physics Letters*, vol. 75, no. 12, pp. 1679–1681, 1999.

[65] N. Aizawa, Y. J. Pu, M. Watanabe, T. Chiba, K. Ideta, N. Toyota, M. Igarashi, Y. Suzuri, H. Sasabe, and J. Kido, "Solution-processed multilayer small-molecule light-emitting devices with high-efficiency white-light emission," *Nature Communications*, vol. 5, pp. 1–7, 2014.

[66] P. Herguth, X. Jiang, M. Liu, and A. Jen, "Highly efficient fluorene-and benzothiadiazole-based conjugated copolymers for polymer light-emitting diodes," *Macromolecules*, pp. 6094–6100, 2002.

[67] Y. He, S. Gong, R. Hattori, and J. Kanicki, "High performance organic polymer light-emitting heterostructure devices," *Applied Physics Letters*, vol. 74, no. 16, pp. 2265–2267, 1999.

[68] J. S. Kim, B. Lägel, E. Moons, N. Johansson, I. D. Baikie, W. R. Salaneck, R. H. Friend, and F. Cacialli, "Kelvin probe and ultraviolet photoemission measurements of indium tin oxide work function: a comparison," *Synthetic Metals*, vol. 111, pp. 311–314, 2000.

[69] J. S. Kim, M. Granström, R. H. Friend, N. Johansson, W. R. Salaneck, R. Daik, W. J. Feast, and F. Cacialli, "Indium–tin oxide treatments for single- and double-layer polymeric light-emitting diodes: The relation between the anode physical, chemical, and morphological properties and the device performance," *Journal of Applied Physics*, vol. 84, no. 12, pp. 6859–6870, 1998.

[70] T. M. Brown, G. M. Lazzerini, L. J. Parrott, V. Bodrozic, L. Bürgi, and F. Cacialli, "Time dependence and freezing-in of the electrode oxygen plasma-induced work function enhancement in polymer semiconductor heterostructures," *Organic Electronics: physics, materials, applications*, vol. 12, no. 4, pp. 623–633, 2011.

[71] T. M. Brown and F. Cacialli, "Contact optimization in polymer light-emitting diodes," *Journal of Polymer Science, Part B: Polymer Physics*, vol. 41, no. 21, pp. 2649–2664, 2003.

[72] W. Hu, *Organic Optoelectronics*. John Wiley & Sons, 2013.

[73] P. W. M. Blom and M. C. J. M. Vissenberg, "Charge transport in poly(p-phenylene vinylene) light-emitting diodes," *Materials Science and Engineering*, vol. 27, no. March, pp. 53–94, 2000.

[74] M. A. Baldo, D. F. O'Brien, M. E. Thompson, and S. R. Forrest, "Excitonic singlet-triplet ratio in a semiconducting organic thin film," *Physical Review B*, vol. 60, no. 20, pp. 14422–14428, 1999.

[75] D. Y. Kondakov, "Triplet-triplet annihilation in highly efficient fluorescent organic light-emitting diodes: current state and future outlook," *Philosophical Transactions of the Royal Society A: Mathematical, Physical and Engineering Sciences*, vol. 373, no. 2044, pp. 20140321–20140321, 2015.

[76] M. V. Nemallapudi, S. Gundacker, R. M. Turtos, M. Vangeleyn, N. Brillouet, P. Lecoq, and E. Auffray, "Alternative Geometries for Improved Light Output of Inorganic Scintillating Crystals," *IEEE Transactions on Nuclear Science*, vol. 63, no. 2, pp. 649–655, 2016.

[77] F. So, *Organic Electronics: Materials, Processing, Devices and Applications*. CRC Press, 2010.

[78] Y. Sun and S. R. Forrest, "Organic light emitting devices with enhanced outcoupling via microlenses fabricated by imprint lithography," *Journal of Applied Physics*, vol. 100, no. 7, pp. 1–7, 2006.

[79] A. Zampetti, A. Minotto, and F. Cacialli, "Near-Infrared (NIR) Organic Light-Emitting Diodes (OLEDs): Challenges and Opportunities," *Advanced Functional Materials*, vol. 1807623, p. 1807623, 2019.

[80] F. C. Spano and C. Silva, "H- and J-Aggregate Behavior in Polymeric Semiconductors," *Annual Review of Physical Chemistry*, vol. 65, no. 1, pp. 477–500, 2014.

[81] R. Englman and J. Jortner, "The energy gap law for radiationless transitions in large molecules," *Molecular Physics*, vol. 18, no. 2, pp. 145–164, 1970.

[82] A. Nitzan, S. Mukamel, and J. Jortner, "Energy gap law for vibrational relaxation of a molecule in a dense medium," *The Journal of Chemical Physics*, vol. 63, no. 1, pp. 200–207, 1975.

[83] S. Anderson and H. Anderson, "Synthesis of a Water-Soluble Conjugated Rotaxane," *Angew. Chem., Int. Ed.*, vol. 35, no. 17, pp. 1956–1959, 1996.

[84] F. Cacialli, J. S. Wilson, J. J. Michels, C. Daniel, C. Silva, R. H. Friend, N. Severin, P. Samorì, J. P. Rabe, M. J. O'Connell, P. N. Taylor, and H. L. Anderson, "Cyclodextrin-threaded conjugated polyrotaxanes as insulated molecular wires with reduced interstrand interactions," *Nature Materials*, vol. 1, no. 3, pp. 160–164, 2002.

[85] A. Leventis, J. Royakkers, A. G. Rapidis, N. Goodeal, M. K. Corpinot, J. M. Frost, D. K. Bučar, M. O. Blunt, F. Cacialli, and H. Bronstein,

"Highly Luminescent Encapsulated Narrow Bandgap Polymers Based on Diketopyrrolopyrrole," *Journal of the American Chemical Society*, vol. 140, no. 5, pp. 1622–1626, 2018.

[86] J. Morgado, F. Cacialli, R. Iqbal, S. C. Moratti, A. B. Holmes, G. Yahioglu, L. R. Milgrom, and R. H. Friend, "Förster energy transfer and control of the luminescence in blends of an orangeemitting poly(pphenylenevinylene) and a redemitting tetraphenylporphyrin," *Journal of Materials Chemistry*, vol. 11, no. 2, pp. 278–283, 2001.

[87] O. Fenwick, J. K. Sprafke, J. Binas, D. V. Kondratuk, D. Stasio, H. L. Anderson, and F. Cacialli, "Linear and cyclic porphyrin hexamers as near infra-red emitters in organic light-emitting diodes," *Nano Letters*, vol. 11, pp. 2451–2456, 2011.

[88] M. Sassi, N. Buccheri, M. Rooney, C. Botta, F. Bruni, U. Giovanella, S. Brovelli, and L. Beverina, "Near-infrared roll-off-free electroluminescence from highly stable diketopyrrolopyrrole light emitting diodes," *Scientific Reports*, vol. 6, no. 1, p. 34096, 2016.

[89] A. Zampetti, A. Minotto, B. M. Squeo, V. G. Gregoriou, S. Allard, U. Scherf, C. L. Chochos, and F. Cacialli, "Highly Efficient Solid-State Near-infrared Organic Light-Emitting Diodes incorporating A-D-A Dyes based on α,β-unsubstituted "BODIPY" Moieties," *Scientific Reports*, vol. 7, no. 1, p. 1611, 2017.

[90] A. Minotto, P. Murto, Z. Genene, A. Zampetti, G. Carnicella, W. Mammo, M. R. Andersson, E. Wang, and F. Cacialli, "Efficient Near-Infrared Electroluminescence at 840 nm with "Metal-Free" Small-Molecule:Polymer Blends," *Advanced Materials*, vol. 1706584, no. July, p. 1706584, 2018.

[91] D. H. Kim, A. D'Aléo, X. K. Chen, A. D. Sandanayaka, D. Yao, L. Zhao, T. Komino, E. Zaborova, G. Canard, Y. Tsuchiya, E. Choi, J. W. Wu, F. Fages, J. L. Brédas, J. C. Ribierre, and C. Adachi, "High-efficiency electroluminescence and amplified spontaneous emission from a thermally activated delayed fluorescent near-infrared emitter," *Nature Photonics*, vol. 12, no. 2, pp. 98–104, 2018.

[92] Y. Sun, C. Borek, K. Hanson, P. I. Djurovich, M. E. Thompson, J. Brooks, J. J. Brown, and S. R. Forrest, "Photophysics of Pt-porphyrin electrophosphorescent devices emitting in the near infrared," *Applied Physics Letters*, vol. 90, no. 21, pp. 10–13, 2007.

[93] J. C. Ostrowski, K. Susumu, M. R. Robinson, M. J. Therien, and G. C. Bazan, "Near-infrared electroluminescent light-emitting devices based on ethyne-bridged porphyrin fluorophores," *Advanced Materials*, vol. 15, no. 15, pp. 1296–1300, 2003.

[94] O. Fenwick, S. Fusco, T. N. Baig, F. Di Stasio, T. T. Steckler, P. Henriksson, C. Flechon, M. R. Andersson, and F. Cacialli, "Efficient red electroluminescence from diketopyrrolopyrrole copolymerised with a polyfluorene," *APL Materials*, vol. 1, no. 3, 2013.

[95] L. H. Slooff, A. Polman, F. Cacialli, R. H. Friend, G. A. Hebbink, F. C. J. M. Van Veggel, and D. N. Reinhoudt, "Near-infrared electroluminescence of polymer light-emitting diodes doped with a lissamine-sensitized Nd3+ complex," *Applied Physics Letters*, vol. 78, no. 15, pp. 2122–2124, 2001.

[96] D. H. Kim, A. D'Aléo, X. K. Chen, A. D. Sandanayaka, D. Yao, L. Zhao, T. Komino, E. Zaborova, G. Canard, Y. Tsuchiya, E. Choi, J. W. Wu, F. Fages, J. L. Brédas, J. C. Ribierre, and C. Adachi, "Supplementary information of High-efficiency electroluminescence and amplified spontaneous emission from a thermally activated delayed fluorescent near-infrared emitter," *Nature Photonics*, vol. 12, no. 2, pp. 98–104, 2018.

[97] K. Tuong Ly, R.-W. Chen-Cheng, H.-W. Lin, Y.-J. Shiau, S.-H. Liu, P.-T. Chou, C.-S. Tsao, Y.-C. Huang, and Y. Chi, "Near-infrared organic light-emitting diodes with very high external quantum efficiency and radiance," *Nature Photonics*, vol. 11, no. 1, pp. 63–68, 2016.

[98] C. Borek, K. Hanson, P. I. Djurovich, M. E. Thompson, K. Aznavour, R. Bau, Y. Sun, S. R. Forrest, J. Brooks, L. Michalski, and J. Brown, "Highly Efficient , Near-Infrared Electrophosphorescence from a Pt – Metalloporphyrin Complex ** Zuschriften," *Angewandte Chemie (International ed. in English)*, vol. 119, pp. 1127–1130, 2007.

[99] C. Adachi, M. A. Baldo, M. E. Thompson, and S. R. Forrest, "Nearly 100% internal phosphorescence efficiency in an organic light emitting device," *Journal of Applied Physics*, vol. 90, no. 10, pp. 5048–5051, 2001.

[100] K. R. Graham, Y. Yang, J. R. Sommer, A. H. Shelton, K. S. Schanze, J. Xue, and J. R. Reynolds, "Extended conjugation platinum(II) porphyrins for use in near-infrared emitting organic light emitting diodes," *Chemistry of Materials*, vol. 23, no. 24, pp. 5305–5312, 2011.

[101] J. R. Sommer, R. T. Farley, K. R. Graham, Y. Yang, J. R. Reynolds, J. Xue, and K. S. Schanze, "Efficient near-infrared polymer and organic light-emitting diodes based on electrophosphorescence from (tetraphenyltetranaphtho[2,3]porphyrin)platinum(II)," *ACS Applied Materials and Interfaces*, vol. 1, no. 2, pp. 274–278, 2009.

[102] J. R. Sommer, A. H. Shelton, A. Parthasarathy, I. Ghiviriga, J. R. Reynolds, and K. S. Schanze, "Photophysical properties of near-infrared phosphorescent π-extended platinum porphyrins," *Chemistry of Materials*, vol. 23, no. 24, pp. 5296–5304, 2011.

[103] X. Gong, Z. Yang, G. Walters, R. Comin, Z. Ning, E. Beauregard, V. Adinolfi, O. Voznyy, and E. H. Sargent, "Highly efficient quantum dot near-infrared light-emitting diodes," *Nature Photonics*, vol. 10, no. 4, pp. 253–257, 2016.

[104] H. Uoyama, K. Goushi, K. Shizu, H. Nomura, and C. Adachi, "Highly efficient organic light-emitting diodes from delayed fluorescence," *Nature*, vol. 492, no. 7428, pp. 234–238, 2012.

[105] T. L. Wu, M. J. Huang, C. C. Lin, P. Y. Huang, T. Y. Chou, R. W. Chen-Cheng, H. W. Lin, R. S. Liu, and C. H. Cheng, "Diboron compound-based organic light-emitting diodes with high efficiency and reduced efficiency roll-off," *Nature Photonics*, vol. 12, no. 4, pp. 235–240, 2018.

[106] T.-A. Lin, T. Chatterjee, W.-L. Tsai, W.-K. Lee, M.-J. Wu, M. Jiao, K.-C. Pan, C.-L. Yi, C.-L. Chung, K.-T. Wong, and C.-C. Wu, "Sky-Blue Organic Light Emitting Diode with 37% External Quantum Efficiency Using Thermally Activated Delayed Fluorescence from Spiroacridine-Triazine Hybrid," *Advanced Materials*, vol. 28, no. 32, pp. 6976–6983, 2016.

[107] J. Li, T. Nakagawa, J. Macdonald, Q. Zhang, H. Nomura, H. Miyazaki, and C. Adachi, "Highly efficient organic light-emitting diode based on a hidden thermally activated delayed fluorescence channel in a heptazine derivative," *Advanced Materials*, vol. 25, no. 24, pp. 3319–3323, 2013.

[108] D. M. E. Freeman, A. J. Musser, J. M. Frost, H. L. Stern, A. K. Forster, K. J. Fallon, A. G. Rapidis, F. Cacialli, I. McCulloch, T. M. Clarke, R. H. Friend, and H. Bronstein, "Synthesis and Exciton Dynamics of Donor-Orthogonal Acceptor Conjugated Polymers: Reducing the Singlet–Triplet Energy Gap," *Journal of the American Chemical Society*, vol. 139, pp. 11073–11080, aug 2017.

[109] Y. Zhang, Y. Wang, J. Song, J. Qu, B. Li, W. Zhu, and W.-Y. Wong, "Near-Infrared Emitting Materials via Harvesting Triplet Excitons: Molecular Design, Properties, and Application in Organic Light Emitting Diodes," *Advanced Optical Materials*, vol. 1800466, p. 1800466, 2018.

[110] C. M. Lochner, Y. Khan, A. Pierre, and A. C. Arias, "All-organic optoelectronic sensor for pulse oximetry," *Nature Communications*, vol. 5, p. 5745, 2014.

[111] Y. Khan, A. E. Ostfeld, C. M. Lochner, A. Pierre, and A. C. Arias, "Monitoring of Vital Signs with Flexible and Wearable Medical Devices," *Advanced Materials*, vol. 28, no. 22, pp. 4373–4395, 2016.

[112] A. M. Smith, M. C. Mancini, and S. Nie, "Bioimaging: Second window for in vivo imaging," *Nature Nanotechnology*, vol. 4, no. 11, pp. 710–711, 2009.

[113] B. Jang, J.-y. Park, C.-h. Tung, I.-h. Kim, and Y. Choi, "Gold Nanorod-Photosensitizer Complex for Near-Infrared Fluorescence Imaging and Photodynamic/Photothermal Therapy In Vivo," *ACS nano*, vol. 5, no. 2, pp. 1086–1094, 2011.

[114] M. R. Hamblin and T. N. Demidova-Rice, "Cellular Chromophores and Signaling in Low Level Light Therapy," *SPIE Proceedings*, vol. 6428, pp. 642802–642802–14, 2007.

[115] S. Lim, "Phototherapy and the benefits of LEDs Applications of LEDs," *Journal of the SID*, pp. 882–887, 2011.

[116] C. Corsi, "History highlights and future trends of infrared sensors," *Journal of Modern Optics*, vol. 57, no. 18, pp. 1663–1686, 2010.

[117] P. A. Haigh, F. Bausi, Z. Ghassemlooy, I. Papakonstantinou, H. Le Minh, C. Fléchon, and F. Cacialli, "Visible light communications: real time 10 Mb/s link with a low bandwidth polymer light-emitting diode," *Optics Express*, vol. 22, no. 3, p. 2830, 2014.

[118] D. Tsonev, S. Videv, and H. Haas, "Light fidelity (Li-Fi): towards all-optical networking," *Proceedings of SPIE*, vol. 9007, p. 900702, 2013.

[119] A. W. Grice, D. D. C. Bradley, M. T. Bernius, M. Inbasekaran, W. W. Wu, and E. P. Woo, "High brightness and efficiency blue light-emitting polymer diodes," *Applied Physics Letters*, vol. 73, no. 5, pp. 629–631, 1998.

[120] Y. Shi, J. Liu, and Y. Yang, "Device performance and polymer morphology in polymer light emitting diodes: The control of thin film morphology

and device quantum efficiency," *Journal of Applied Physics*, vol. 87, no. 9, pp. 4254–4263, 2000.

[121] K. Rurack and M. Spieles, "Fluorescence quantum yields of a series of red and near-infrared dyes emitting at 600-1000 nm," *Analytical Chemistry*, vol. 83, no. 4, pp. 1232–1242, 2011.

[122] J. C. de Mello, H. F. Wittmann, and R. H. Friend, "An improved experimental determination of external photoluminescence quantum efficiency," *Advanced Materials*, vol. 9, no. 3, pp. 230–232, 1997.

[123] J. S. Kim, R. H. Friend, and F. Cacialli, "Improved operational stability of polyfluorene-based organic light-emitting diodes with plasma-treated indium–tin–oxide anodes," *Applied Physics Letters*, vol. 74, no. 21, pp. 3084–3086, 1999.

[124] S. E. Shaheen, G. E. Jabbour, M. M. Morrell, Y. Kawabe, B. Kippelen, N. Peyghambarian, M. F. Nabor, R. Schlaf, E. A. Mash, and N. R. Armstrong, "Bright blue organic light-emitting diode with improved color purity using a LiF/Al cathode," *Journal of Applied Physics*, vol. 84, no. 4, pp. 2324–2327, 1998.

[125] P. López Varo, J. A. Jiménez Tejada, J. A. López Villanueva, and M. J. Deen, "Space-charge and injection limited current in organic diodes: A unified model," *Organic Electronics: physics, materials, applications*, vol. 15, no. 10, pp. 2526–2535, 2014.

[126] A. Savitzky and M. J. Golay, "Smoothing and Differentiation of Data by Simplified Least Squares Procedures," *Analytical Chemistry*, vol. 36, no. 8, pp. 1627–1639, 1964.

[127] S. D. Stranks, J. K. Sprafke, H. L. Anderson, and R. J. Nicholas, "Electronic and mechanical modification of single-walled carbon nanotubes by binding to porphyrin oligomers," *ACS Nano*, vol. 5, no. 3, pp. 2307–2315, 2011.

[128] M. D. Peeks, P. Neuhaus, and H. L. Anderson, "Experimental and computational evaluation of the barrier to torsional rotation in a butadiyne-linked porphyrin dimer," *Phys. Chem. Chem. Phys.*, vol. 18, no. 7, pp. 5264–5274, 2016.

[129] H. L. Anderson, "Building molecular wires from the colours of life: conjugated porphyrin oligomers," *Chemical Communications*, vol. 0, no. 23, pp. 2323–2330, 1999.

[130] C. E. Tait, P. Neuhaus, M. D. Peeks, H. L. Anderson, and C. R. Timmel, "Transient EPR Reveals Triplet State Delocalization in a Series of Cyclic and Linear pi-Conjugated Porphyrin Oligomers," *Journal of the American Chemical Society*, vol. 137, no. 25, pp. 8284–8293, 2015.

[131] F. C. Grozema, C. Houarner-Rassin, P. Prins, L. D. A. Siebbeles, and H. L. Anderson, "Supramolecular Control of Charge Transport in Molecular Wires," *Journal of the American Chemical Society*, vol. 129, no. 44, pp. 13370–13371, 2007.

[132] M. U. Winters, J. Kärnbratt, M. Eng, C. J. Wilson, H. L. Anderson, and B. Albinsson, "Photophysics of a butadiyne-linked porphyrin dimer: Influence of conformational flexibility in the ground and first singlet excited state," *Journal of Physical Chemistry C*, vol. 111, no. 19, pp. 7192–7199, 2007.

[133] M. Hoffmann, J. Kärnbratt, M. H. Chang, L. M. Herz, B. Albinsson, and H. L. Anderson, "Enhanced π conjugation around a porphyrin[6] nanoring," *Angewandte Chemie - International Edition*, vol. 47, no. 27, pp. 4993–4996, 2008.

[134] J. K. Lee, I. Bulut, M. Rickhaus, Y. Sheng, X. Li, G. G. Han, G. A. D. Briggs, H. L. Anderson, and J. H. Warner, "Metal atom markers for imaging epitaxial molecular self-assembly on graphene by scanning transmission electron microscopy," *ACS Nano*, vol. 13, no. 6, pp. 7252–7260, 2019.

[135] G. Moise, L. Tejerina, M. Rickhaus, H. L. Anderson, and C. R. Timmel, "Spin Delocalization in the Radical Cations of Porphyrin Molecular Wires: A New Perspective on EPR Approaches," *Journal of Physical Chemistry Letters*, vol. 10, pp. 5708–5712, 2019.

[136] M. Rickhaus, A. Vargas Jentzsch, L. Tejerina, I. Grübner, M. Jirasek, T. D. Claridge, and H. L. Anderson, "Single-Acetylene Linked Porphyrin Nanorings," *Journal of the American Chemical Society*, vol. 139, no. 46, pp. 16502–16505, 2017.

[137] R. Haver, L. Tejerina, H. W. Jiang, M. Rickhaus, M. Jirasek, I. Grübner, H. J. Eggimann, L. M. Herz, and H. L. Anderson, "Tuning the Circumference of Six-Porphyrin Nanorings," *Journal of the American Chemical Society*, vol. 141, no. 19, pp. 7965–7971, 2019.

[138] Y. Murakami, J.-i. Kikuchi, Y. Hisaeda, and O. Hayashida, "Artificial Enzymes," *Chemical Reviews*, vol. 96, no. 2, pp. 721–758, 1996.

[139] R. J. Cogdell, A. Gall, and J. Köhler, "The architecture and function of the light-harvesting apparatus of purple bacteria: from single molecules to in vivo membranes.," *Quarterly reviews of biophysics*, vol. 39, no. 3, pp. 227–324, 2006.

[140] G. McDermott, S. M. Prince, a. a. Freer, a. M. Hawthornthwaite-Lawless, M. Z. Papiz, R. J. Cogdell, and N. W. Isaacs, "Crystal structure of an integral membrane light-harvesting complex from\n\tphotosynthetic bacteria," 1995.

[141] H. A. Collins, M. Khurana, E. H. Moriyama, A. Mariampillai, E. Dahlstedt, M. Balaz, M. K. Kuimova, M. Drobizhev, V. X. D. Yang, D. Phillips, A. Rebane, B. C. Wilson, and H. L. Anderson, "Blood-vessel closure using photosensitizers engineered for two-photon excitation," *Nature Photonics*, vol. 2, no. 7, pp. 420–424, 2008.

[142] V. V. Rozhkov, M. Khajehpour, and S. A. Vinogradov, "Luminescent Zn and Pd tetranaphthaloporphyrins," *Inorganic Chemistry*, vol. 42, no. 14, pp. 4253–4255, 2003.

[143] D. Beljonne, G. E. O'Keefe, P. J. Hamer, R. H. Friend, H. L. Anderson, and J. L. Brédas, "Investigation of the linear and nonlinear optical response of edge-linked conjugated zinc porphyrin oligomers by optical spectroscopy and configuration interaction techniques," *The Journal of Chemical Physics*, vol. 106, no. 23, pp. 9439–9460, 1997.

[144] T. Bessho, S. M. Zakeeruddin, C. Y. Yeh, E. W. G. Diau, and M. Gratzel, "Highly efficient mesoscopic dye-sensitized solar cells based on donor-acceptor-substituted porphyrins," *Angewandte Chemie - International Edition*, vol. 49, no. 37, pp. 6646–6649, 2010.

[145] J. M. Ball, N. K. S. Davis, J. D. Wilkinson, J. Kirkpatrick, J. Teuscher, R. Gunning, H. L. Anderson, and H. J. Snaith, "A panchromatic anthracene-fused porphyrin sensitizer for dye-sensitized solar cells," *RSC Advances*, vol. 2, no. 17, p. 6846, 2012.

[146] J. Rawson, A. C. Stuart, W. You, and M. J. Therien, "Tailoring porphyrin-based electron accepting materials for organic photovoltaics," *Journal of the American Chemical Society*, vol. 136, no. 50, pp. 17561–17569, 2014.

[147] M. Pawlicki, H. A. Collins, R. G. Denning, and H. L. Anderson, "Two-photon absorption and the design of two-photon dyes," *Angewandte Chemie - International Edition*, vol. 48, no. 18, pp. 3244–3266, 2009.

[148] J. H. Olivier, Y. Bai, H. Uh, H. Yoo, M. J. Therien, and F. N. Castellano, "Near-infrared-to-visible photon upconversion enabled by conjugated porphyrinic sensitizers under low-power noncoherent illumination," *Journal of Physical Chemistry A*, vol. 119, no. 22, pp. 5642–5649, 2015.

[149] H. L. Anderson, "Conjugated Porphyrin Ladders," *Inorganic Chemistry*, vol. 33, no. 5, pp. 972–981, 1994.

[150] M. Hoffmann, C. J. Wilson, B. Odell, and H. L. Anderson, "Template-directed synthesis of a π;-conjugated porphyrin nanoring," *Angewandte Chemie - International Edition*, vol. 46, no. 17, pp. 3122–3125, 2007.

[151] M. C. O'Sullivan, J. K. Sprafke, D. V. Kondratuk, C. Rinfray, T. D. W. Claridge, A. Saywell, M. O. Blunt, J. N. O'Shea, P. H. Beton, M. Malfois, and H. L. Anderson, "Vernier templating and synthesis of a 12-porphyrin nano-ring," *Nature*, vol. 469, no. 7328, pp. 72–75, 2011.

[152] D. V. Kondratuk, L. M. A. Perdigão, A. M. S. Esmail, J. N. O'Shea, P. H. Beton, and H. L. Anderson, "Supramolecular nesting of cyclic polymers," *Nature Chemistry*, vol. 7, no. 4, pp. 317–322, 2015.

[153] M. B. Wieland, L. M. Perdigão, D. V. Kondratuk, J. N. O'Shea, H. L. Anderson, and P. H. Beton, "Height dependent molecular trapping in stacked cyclic porphyrin nanorings," *Chemical Communications*, vol. 50, no. 55, pp. 7332–7335, 2014.

[154] D. V. Kondratuk, L. M. A. Perdigao, M. C. O'Sullivan, S. Svatek, G. Smith, J. N. O'Shea, P. H. Beton, and H. L. Anderson, "Two vernier-templated routes to a 24-porphyrin nanoring," *Angewandte Chemie - International Edition*, vol. 51, no. 27, pp. 6696–6699, 2012.

[155] T. V. Duncan, K. Susumu, L. E. Sinks, and M. J. Therien, "Exceptional near-infrared fluorescence quantum yields and excited-state absorptivity of highly conjugated porphyrin arrays," *Journal of the American Chemical Society*, vol. 128, no. 28, pp. 9000–9001, 2006.

[156] C.-K. Yong, P. Parkinson, D. V. Kondratuk, W.-H. Chen, A. Stannard, A. Summerfield, J. K. Sprafke, M. C. O'Sullivan, P. H. Beton, H. L. Anderson, and L. M. Herz, "Ultrafast delocalization of excitation in synthetic light-harvesting nanorings," *Chem. Sci.*, vol. 6, no. 1, pp. 181–189, 2015.

[157] B. S. Harrison, T. J. Foley, M. Bouguettaya, J. M. Boncella, J. R. Reynolds, K. S. Schanze, J. Shim, P. H. Holloway, G. Padmanaban,

and S. Ramakrishnan, "Near-infrared electroluminescence from conjugated polymer/lanthanide porphyrin blends," *Applied Physics Letters*, vol. 79, no. 23, pp. 3770–3772, 2001.

[158] J. Morgado, F. Cacialli, R. H. Friend, R. Iqbal, G. Yahioglu, L. R. Milgrom, S. C. Moratti, and A. B. Holmes, "Tuning the red emission of a soluble poly(p-phenylene vinylene) upon grafting of porphyrin side groups," *Chemical Physics Letters*, vol. 325, no. 5-6, pp. 552–558, 2000.

[159] P. N. Taylor, J. Huuskonen, C. Rumbles, R. T. Aplin, E. Williams, and H. L. Anderson, "Conjugated porphyrin oligomers from monomer to hexamer," *Chemical Communications*, no. 8, pp. 909–910, 1998.

[160] M. H. Chang, M. Hoffmann, H. L. Anderson, and L. M. Herz, "Dynamics of excited-state conformational relaxation and electronic delocalization in conjugated porphyrin oligomers," *Journal of the American Chemical Society*, vol. 130, no. 31, pp. 10171–10178, 2008.

[161] J. J. Piet, P. N. Taylor, B. R. Wegewijs, H. L. Anderson, a. Osuka, and J. M. Warman, "Photoexcitations of covalently bridged zinc porphyrin oligomers: Frenkel versus Wannier-Mott type excitons," *The Journal of Physical Chemistry B*, vol. 105, pp. 97–104, 2001.

[162] A. Endo, K. Sato, K. Yoshimura, T. Kai, A. Kawada, H. Miyazaki, and C. Adachi, "Efficient up-conversion of triplet excitons into a singlet state and its application for organic light emitting diodes," *Applied Physics Letters*, vol. 98, no. 8, 2011.

[163] O. Fenwick, S. Fusco, T. N. Baig, F. Di Stasio, T. T. Steckler, P. Henriksson, C. Flechon, M. R. Andersson, and F. Cacialli, "Efficient red electroluminescence from diketopyrrolopyrrole copolymerised with a polyfluorene," *APL Materials*, vol. 1, no. 3, 2013.

[164] S. Janietz, D. D. Bradley, M. Grell, C. Giebeler, M. Inbasekaran, and E. P. Woo, "Electrochemical determination of the ionization potential and electron affinity of poly(9,9-dioctylfluorene)," *Applied Physics Letters*, vol. 73, no. 17, pp. 2453–2455, 1998.

[165] F. So and D. Kondakov, "Degradation mechanisms in small-molecule and polymer organic light-emitting diodes," *Advanced Materials*, vol. 22, no. 34, pp. 3762–3777, 2010.

[166] G. Polito, S. Surdo, V. Robbiano, G. Tregnago, F. Cacialli, and G. Barillaro, "Synergic integration of conjugated luminescent polymers

and three-dimensional silicon microstructures for the effective synthesis of photoluminescent light source arrays," *Lecture Notes in Electrical Engineering*, vol. 319, no. 12, pp. 243–247, 2015.

[167] T. T. Steckler, M. J. Lee, Z. Chen, O. Fenwick, M. R. Andersson, F. Cacialli, and H. Sirringhaus, "Multifunctional materials for OFETs, LEFETs and NIR PLEDs," *Journal of Materials Chemistry C*, vol. 2, no. 26, pp. 5133–5141, 2014.

[168] J. Zaumseil, C. R. McNeill, M. Bird, D. L. Smith, P. Paul Ruden, M. Roberts, M. J. McKiernan, R. H. Friend, and H. Sirringhaus, "Quantum efficiency of ambipolar light-emitting polymer field-effect transistors," *Journal of Applied Physics*, vol. 103, no. 6, 2008.

[169] M. C. Gwinner, D. Kabra, M. Roberts, T. J. Brenner, B. H. Wallikewitz, C. R. McNeill, R. H. Friend, and H. Sirringhaus, "Highly efficient single-layer polymer ambipolar light-emitting field-effect transistors," *Advanced Materials*, vol. 24, no. 20, pp. 2728–2734, 2012.

[170] J. S. Kim, R. H. Friend, I. Grizzi, and J. H. Burroughes, "Spin-cast thin semiconducting polymer interlayer for improving device efficiency of polymer light-emitting diodes," *Applied Physics Letters*, vol. 87, no. 2, pp. 58–61, 2005.

[171] G. M. Lazzerini, F. Di Stasio, C. Flechon, D. J. Caruana, and F. Cacialli, "Low-temperature treatment of semiconducting interlayers for high-efficiency light-emitting diodes based on a green-emitting polyfluorene derivative," *Applied Physics Letters*, vol. 99, no. 24, pp. 2–4, 2011.

[172] D. Han, Y. Khan, J. Ting, S. M. King, N. Yaacobi-Gross, M. J. Humphries, C. J. Newsome, and A. C. Arias, "Flexible Blade-Coated Multicolor Polymer Light-Emitting Diodes for Optoelectronic Sensors," *Advanced Materials*, vol. 1606206, pp. 1–8, 2017.

[173] M. Sessolo and H. J. Bolink, "Hybrid organic-inorganic light-emitting diodes," *Advanced Materials*, vol. 23, no. 16, pp. 1829–1845, 2011.

[174] G. Tregnago, C. Flechon, S. Choudhary, C. Gozalvez, A. Mateo-Alonso, and F. Cacialli, "Virtually pure near-infrared electroluminescence from exciplexes at polyfluorene/hexaazatrinaphthylene interfaces," *Applied Physics Letters*, vol. 105, no. 14, 2014.

[175] J. Gruner, H. F. Wittmann, P. J. Hamer, R. H. Friend, J. Huber, U. Scherf, K. Mullen, S. C. Moratti, and A. B. Holmes, "Electroluminescence and

photoluminescence investigations of the yellow emission of devices based on ladder-type oligo(para-phenylene)s," *Synthetic Metals*, vol. 67, no. 1-3, pp. 181–185, 1994.

[176] J. Kärnbratt, M. Gilbert, J. K. Sprafke, H. L. Anderson, and B. Albinsson, "Self-assembly of linear porphyrin oligomers into well-defined aggregates," *Journal of Physical Chemistry C*, vol. 116, no. 37, pp. 19630–19635, 2012.

[177] G. G. Malliaras and J. C. Scott, "The roles of injection and mobility in organic light emitting diodes," *Journal of Applied Physics*, vol. 83, no. 10, pp. 5399–5403, 1998.

[178] E. Moons, "Conjugated polymer blends: linking film morphology to performance of light emitting diodes and photodiodes," *Journal of Physics: Condensed Matter*, vol. 12235, no. 14, pp. 12235–12260, 2002.

[179] W. H. Flora, H. K. Hall, and N. R. Armstrong, "Guest emission processes in doped organic light-emitting diodes: Use of phthalocyanine and naphthalocyanine near-IR dopants," *Journal of Physical Chemistry B*, vol. 107, no. 5, pp. 1142–1150, 2003.

[180] R. J. Holmes, S. R. Forrest, T. Sajoto, A. Tamayo, P. I. Djurovich, and M. E. Thompson, "Reduced geminate recombination in iridium-based electrophosphorescent materials," *Organic Electronics*, vol. 7, pp. 163–172, 2006.

[181] M. A. Baldo, C. Adachi, and S. R. Forrest, "Transient analysis of organic electrophosphorescence. II. Transient analysis of triplet-triplet annihilation," *Physical Review B - Condensed Matter and Materials Physics*, vol. 62, no. 16, pp. 10967–10977, 2000.

[182] M. A. Baldo, D. F. O 'brien, Y. You, A. Shoustikov, S. Sibley, M. E. Thompson, and S. R. Forrest, "Highly efficient phosphorescent emission from organic electroluminescent devices," *Nature*, vol. 395, no. September, pp. 151–154, 1998.

[183] C. Murawski, K. Leo, and M. C. Gather, "Efficiency roll-off in organic light-emitting diodes," *Advanced Materials*, vol. 25, no. 47, pp. 6801–6827, 2013.

[184] X. Gong, M. R. Robinson, J. C. Ostrowski, D. Moses, G. C. Bazan, and A. J. Heeger, "High-Efficiency Polymer-Based Electrophosphorescent Devices," *Advanced Materials*, vol. 14, no. 8, pp. 581–585, 2002.

[185] N. Tessler, V. Medvedev, M. Kazes, S. H. Kan, and U. Banin, "Efficient near-infrared polymer nanocrystal light-emitting diodes," *Science*, vol. 295, no. 5559, pp. 1506–1508, 2002.

[186] G. Latini, A. Downes, O. Fenwick, A. Ambrosio, M. Allegrini, C. Daniel, C. Silva, P. G. Gucciardi, S. Patane, R. Daik, W. J. Feast, and F. Cacialli, "Optical probing of sample heating in scanning near-field experiments with apertured probes," *Applied Physics Letters*, vol. 86, no. 1, 2005.

[187] S. F. Lim, R. H. Friend, I. D. Rees, J. Li, Y. Ma, K. Robinson, A. B. Holmes, E. Hennebicq, D. Beljonne, and F. Cacialli, "Suppression of green emission in a new class of blue-emitting polyfluorene copolymers with twisted biphenyl moieties," *Advanced Functional Materials*, vol. 15, no. 6, pp. 981–988, 2005.

[188] E. J. W. List, R. Guentner, P. Scanducci de Freitas, and U. Scherf, "The Effect of Keto Defect Sites on the Emission Properties of Polyfluorene-Type Materials**," *Advanced Materials*, vol. 14, no. 5, pp. 374–378, 2002.

[189] D. V. Khramtchenkov, H. Bassler, and V. I. Arkhipov, "A model of electroluminescence in organic double-layer light-emitting diodes," *Journal of Applied Physics*, vol. 79, no. 12, p. 9283, 1996.

[190] H. Xiang, L. Zhou, Y. Feng, J. Cheng, D. Wu, and X. Zhou, "Tunable Fluorescent/Phosphorescent Platinum(II) Porphyrin-Fluorene Copolymers for Ratiometric Dual Emissive Oxygen Sensing," *Inorganic Chemistry*, vol. 51, no. 9, pp. 5208–5212, 2012.

[191] D. Y. Kondakov, T. D. Pawlik, T. K. Hatwar, and J. P. Spindler, "Triplet annihilation exceeding spin statistical limit in highly efficient fluorescent organic light-emitting diodes," *Journal of Applied Physics*, vol. 106, no. 12, 2009.

[192] A. S. Dhoot and N. C. Greenham, "Triplet formation in polyfluorene devices," *Advanced Materials*, vol. 14, no. 24, pp. 1834–1837, 2002.

[193] A. Dey, A. Rao, and D. Kabra, "A Complete Quantitative Analysis of Spatio-Temporal Dynamics of Excitons in Functional Organic Light-Emitting Diodes," *Advanced Optical Materials*, 2016.

[194] F. Cacialli, R. H. Friend, S. C. Moratti, and A. B. Holmes, "Characterization Of Properties Of Polymeric Light-Emitting-Diodes Over Extended Periods," *Synth. Met.*, vol. 67, no. 1-3, pp. 157–160, 1994.

[195] R. Y. Yang and X. A. Cao, "Thermal and nonthermal factors affecting the lifetime of blue phosphorescent organic light-emitting diodes," *IEEE Transactions on Electron Devices*, vol. 65, no. 8, pp. 3300–3304, 2018.

[196] S. Scholz, D. Kondakov, B. Lüssem, and K. Leo, "Degradation Mechanisms and Reactions in Organic Light-Emitting Devices," *Chemical Reviews*, vol. 115, no. 16, pp. 8449–8503, 2015.

[197] W. Song, T. Kim, Y. Lee, and J. Y. Lee, "A stepwise energy level doping structure for improving the lifetime of phosphorescent organic light-emitting diodes," *Journal of Materials Chemistry C*, vol. 5, no. 16, pp. 3948–3954, 2017.

[198] H. J. Shin, M. C. Jung, J. Chung, K. Kim, J. C. Lee, and S. P. Lee, "Degradation mechanism of organic light-emitting device investigated by scanning photoelectron microscopy coupled with peel-off technique," *Applied Physics Letters*, vol. 89, no. 6, pp. 3–5, 2006.

[199] P. Tyagi, R. Srivastava, L. I. Giri, S. Tuli, and C. Lee, "Degradation of organic light emitting diode: Heat related issues and solutions," *Synthetic Metals*, vol. 216, pp. 40–50, 2016.

[200] D. Y. Kondakov, W. C. Lenhart, and W. F. Nichols, "Operational degradation of organic light-emitting diodes: Mechanism and identification of chemical products," *Journal of Applied Physics*, vol. 101, no. 2, 2007.

[201] T. M. Brown, R. H. Friend, I. S. Millard, D. J. Lacey, J. H. Burroughes, and F. Cacialli, "Efficient electron injection in blue-emitting polymer light-emitting diodes with LiF/Ca/Al cathodes," *Applied Physics Letters*, vol. 79, no. 2, pp. 174–176, 2001.

[202] J. J. Michels, M. J. O'Connell, P. N. Taylor, J. S. Wilson, F. Cacialli, and H. L. Anderson, "Synthesis of Conjugated Polyrotaxanes," *Chemistry - A European Journal*, vol. 9, no. 24, pp. 6167–6176, 2003.

[203] M. J. Frampton and H. L. Anderson, "Insulated molecular wires," *Angewandte Chemie - International Edition*, vol. 46, no. 7, pp. 1028–1064, 2007.

[204] M. M. Mróz, S. Perissinotto, T. Virgili, G. Gigli, M. Salerno, M. J. Frampton, G. Sforazzini, H. L. Anderson, and G. Lanzani, "Laser action from a sugar-threaded polyrotaxane," *Applied Physics Letters*, vol. 95, no. 3, pp. 1–4, 2009.

[205] K. Sugiyasu, Y. Honsho, R. M. Harrison, A. Sato, T. Yasuda, S. Seki, and M. Takeuchi, "A self-threading polythiophene: Defect-free insulated molecular wires endowed with long effective conjugation length," *Journal of the American Chemical Society*, vol. 132, no. 42, pp. 14754–14756, 2010.

[206] C. Pan, K. Sugiyasu, Y. Wakayama, A. Sato, and M. Takeuchi, "Thermoplastic fluorescent conjugated polymers: Benefits of preventing π-π Stacking," *Angewandte Chemie - International Edition*, vol. 52, no. 41, pp. 10775–10779, 2013.

[207] S. Brovelli and F. Cacialli, "Optical and electroluminescent properties of conjugated polyrotaxanes," *Small*, vol. 6, no. 24, pp. 2796–2820, 2010.

[208] K. Becker, P. G. Lagoudakis, G. Gaefke, S. Höger, and J. M. Lupton, "Exciton accumulation in π-conjugated wires encapsulated by light-harvesting macrocycles," *Angewandte Chemie - International Edition*, vol. 46, no. 19, pp. 3450–3455, 2007.

[209] P. Taylor, M. O'Connell, L. McNeill, M. Hall, R. Aplin, and H. Anderson, "Insulated Molecular Wires: Synthesis of Conjugated Polyrotaxanes by Suzuki Coupling in Water We are grateful to Carol A. Stanier for valuable discussion and to Professor Christopher J. Schofield for providing facilities for gel electrophoresis. Disodium 1," *Angewandte Chemie (International ed. in English)*, vol. 39, no. 19, pp. 3456–3460, 2000.

[210] L. Zalewski, M. Wykes, S. Brovelli, M. Bonini, T. Breiner, M. Kastler, F. Dotz, D. Beljonne, H. L. Anderson, F. Cacialli, and P. Samorì, "A Conjugated Thiophene-Based Rotaxane: Synthesis, Spectroscopy, and Modeling," *Chemistry - A European Journal*, vol. 16, no. 13, 2010.

[211] T. M. Swager, "The Molecular Wire Approach to Sensory Signal Amplification," *Accounts of Chemical Research*, vol. 31, no. 5, pp. 201–207, 1998.

[212] H. Bronstein, Z. Chen, R. Shahid Ashraf, W. Zhang, J. Du, J. R. Durrant, P. Shakya Tuladhar, K. Song, S. E. Watkins, Y. Geerts, M. M. Wienk, R. A. J Janssen, T. Anthopoulos, H. Sirringhaus, M. Heeney, and I. McCulloch, "Thieno[3,2-b]thiophene-Diketopyrrolopyrrole-Containing Polymers for High-Performance Organic Field-Effect Transistors and Organic Photovoltaic Devices," *J. Am. Chem. Soc*, vol. 133, pp. 3272–3275, 2011.

[213] I. Meager, R. S. Ashraf, S. Rossbauer, H. Bronstein, J. E. Donaghey, J. Marshall, B. C. Schroeder, M. Heeney, T. D. Anthopoulos, and

I. McCulloch, "Alkyl Chain Extension as a Route to Novel Thieno[3,2-b]thiophene Flanked Diketopyrrolopyrrole Polymers for Use in Organic Solar Cells and Field Effect Transistors," *Macromolecules*, vol. 46, pp. 5961–5967, 2013.

[214] Z. Chen, M. J. Lee, R. Shahid Ashraf, Y. Gu, S. Albert-Seifried, M. Meedom Nielsen, B. Schroeder, T. D. Anthopoulos, M. Heeney, I. McCulloch, and H. Sirringhaus, "High-performance ambipolar diketopyrrolopyrrole-thieno[3,2-b]thiophene copolymer field-effect transistors with balanced hole and electron mobilities," *Advanced Materials*, vol. 24, no. 5, pp. 647–652, 2012.

[215] Z. Qiao, Y. Xu, S. Lin, J. Peng, and D. Cao, "Synthesis and characterization of red-emitting diketopyrrolopyrrole-alt-phenylenevinylene polymers," *Synthetic Metals*, vol. 160, no. 13-14, pp. 1544–1550, 2010.

[216] C. B. Nielsen, M. Turbiez, and I. McCulloch, "Recent advances in the development of semiconducting DPP-containing polymers for transistor applications," *Advanced Materials*, vol. 25, no. 13, pp. 1859–1880, 2013.

[217] Y. Xu, Y. Jin, W. Lin, J. Peng, H. Jiang, and D. Cao, "Syntheses and eletroluminescence properties of red emitting copolymers with different lengths of diketopyrrolopyrrole units," *Synthetic Metals*, vol. 160, no. 19-20, pp. 2135–2142, 2010.

[218] D. Cao, Q. Liu, W. Zeng, S. Han, and J. Peng, "Diketopyrrolopyrrole-Containing Polyfluorenes : Facile Method To Tune Emission Color and Improve Electron Affinity," *Macromolecules*, vol. 39, no. 24, pp. 8347–8355, 2006.

[219] S. Stas, J. Y. Balandier, V. Lemaur, O. Fenwick, G. Tregnago, F. Quist, F. Cacialli, J. Cornil, and Y. H. Geerts, "Straightforward access to diketopyrrolopyrrole (DPP) dimers," *Dyes and Pigments*, vol. 97, no. 1, pp. 198–208, 2013.

[220] K. Zhang and B. Tieke, "Highly Luminescent Polymers Containing the 2,3,5,6-Tetraarylated Pyrrolo [3,4-c] pyrrole-1,4-dione (N-Aryl DPP) Chromophore in the Main Chain," *Macromolecules*, vol. 41, no. 20, pp. 7287–7295, 2008.

[221] D. Cao, Q. Liu, W. Zeng, H. Han, J. Peng, and S. Liu, "Synthesis and Characterization of Novel Red-Emitting Alternating Copolymers Based on Fluorene and Diketopyrrolopyrrole Derivatives," *Journal of Polymer Science: Part A: Polymer Chemistry*, vol. 44, no. 8, pp. 2395–2405, 2006.

[222] L. C. Palilis, D. G. Lidzey, M. Redecker, D. D. C. Bradley, M. Inbasekaran, E. P. Woo, and W. W. Wu, "Bright and efficient blue and green light-emitting diodes based on conjugated polymer blends," *Synthetic Metals*, vol. 111, pp. 159–163, 2000.

[223] J. Gierschner, H. G. Mack, D. Oelkrug, I. Waldner, and H. Rau, "Modeling of the Optical Properties of Cofacial Chromophore Pairs: Stilbenophane," *Journal of Physical Chemistry A*, vol. 108, no. 2, pp. 257–263, 2004.